Scale interactions between the lower atmosphere and the urban canopy

Karin Blackman

UNIVERSITE BRETAGNE LOIRE

CENTRALE NANTES

Thèse de Doctorat

Karin BLACKMAN

Mémoire présenté en vue de l'obtention
du grade de Docteur de l'Ecole Centrale de Nantes
Sous le label de l'UNIVERSITÉ BRETAGNE LOIRE

École doctorale : Sciences pour l'Ingénieur, Géosciences, Architecture

Discipline : Mécanique des milieux fluides
Unité de recherche : Laboratoire de recherche en Hydrodynamique, Énergétique et Environnement Atmosphérique

Soutenue le 23 Octobre, 2017

Interactions multi-échelles entre la basse atmosphère et la canopée urbaine

Scale interactions between the lower atmosphere and the urban canopy

JURY

Président :	**Laurent DAVID**, Professeur des Universités, Université de Poitiers
Rapporteurs :	**Fabien ANSELMET**, Professeur des Universités, Ecole Centrale Marseille **Serge SIMOENS**, Directeur de Recherche CNRS, Ecole Centrale Lyon
Examinateurs:	**Carlo COSSU**, Directeur de Recherche CNRS, INP Toulouse
Directeur de thèse :	**Isabelle CALMET**, Maître de conférences HDR, École Centrale Nantes
Co-encadrant de thèse :	**Laurent PERRET**, Maître de conférences, École Centrale Nantes

Acknowledgements

First, I would like to thank my thesis director Dr. Isabelle Calmet and co-encadrent Dr. Laurent Perret for their invaluable knowledge and guidance during my Ph.D. program. I would also like to thank my defense jury Dr. Laurent David, Dr. Carlo Cossu, Dr. Fabien Anselmet and Dr. Serge Simoëns for their positive encouragement. I would like to acknowledge the financial support of the French National Research Agency through research Grant URBANTURB No. ANR-14-CE22-0012-01. My thanks also go to Mr. Thibaud Piquet for his technical support during the experimental program and Dr. Cedric Rivet who provided supplementary wind tunnel data. I would like to offer my sincere thanks to Dr. Eric Savory for his continuous support and insightful comments. Finally, I would like to thank my husband, Jérémie, without whom this thesis would never have been written.

Contents

List of Tables

List of Figures

Nomenclature

α	power law exponent	-
α_{AM}	coefficient of superposition	-
β	coefficient of amplitude modulation	-
δ	boundary layer thickness	m
ε	mean dissipation	$m^2 s^{-3}$
η	Kolmogorov microscale	m
θ	angle of inclination	°
λ	Taylor microscale	m
λ_{ci}	swirling strength	-
λ_p	plan area packing density	-
λ_f	frontal area packing density	-
ν	kinematic viscosity	$m^2.s^{-1}$
ξ	kinetic energy from large-scales	$m^2 s^{-2}$
ρ	fluid density	$kg.m^{-3}$
σ_i	standard deviation of variable i	-
τ	time delay	s
τ_{ij}	sub-grid scale stress tensor	$m^2.s^{-2}$
τ_w	wall shear stress	Pa
ψ	pressure transport	$m^2 s^{-3}$
A_i^n	LSE coefficients	-
A_d	total plan area	m^2
A_f	frontal area of obstacles	m^2
A_p	plan area of obstacles	m^2
Adv	advection	$m^2 s^{-3}$
AR	aspect ratio	-
AR_b	aspect ratio of 3D obstacles	-
d	displacement height	m

D_μ	viscous transport	$m^2 s^{-3}$
ϵ	instantaneous dissipation	$m^2 s^{-3}$
E	kinetic energy from movement of the mean flow	$m^2 s^{-2}$
e	kinetic energy from small-scales	$m^2 s^{-2}$
f	frequency	Hz
h	obstacle height	m
h_{avg}	average building height	m
I	energy transfer from movement of the mean to small-scales	$m^2 s^{-3}$
II	energy transfer from movement of the mean flow to large-scales	$m^2 s^{-3}$
III	energy transfer from large- to small-scales	$m^2 s^{-3}$
κ	von Karman constant, 0.42	-
K	pressure gradient indicator	-
k	turbulent kinetic energy	$m^2 s^{-2}$
ℓ	wavelength	m
ℓ_c	critical wavelength	m
$\mathcal{L}$	wavenumber	rad/m
L	street canyon length	m
L_b	length of 3D obstacles	m
L_i	integral length scale	m
N_{ref}	number of reference locations	-
P	pressure	Pa
P_d	production	$m^2 s^{-3}$
Q2	ejection event	-
Q4	sweep event	-
Re	Reynolds number	-
R_{ii}	correlation coefficient	-
S_{ij}	resolved strain rate tensor	s^{-1}
t	time	s
t^*	ν/u_*^2	-
T	turbulent transport	$m^2 s^{-3}$

U_∞	freestream velocity	$m.s^{-1}$
U_g	geostrophic velocity	$m.s^{-1}$
u_*	friction velocity	$m.s^{-1}$
U, V, W	streamwise, spanwise and vertical velocity	$m.s^{-1}$
u', v', w'	streamwise, spanwise and vertical fluctuating velocity	$m.s^{-1}$
u'_L	large-scale streamwise fluctuation	$m.s^{-1}$
u'_S	small-scale streamwise fluctuation	$m.s^{-1}$
u'^{NW}	near-wall streamwise fluctuation	$m.s^{-1}$
u'^{BL}_L	boundary layer large-scale fluctuation	$m.s^{-1}$
$\hat{u}$	universal signal of fluctuating velocity	$m.s^{-1}$
$\tilde{u}$	predicted fluctuation velocity	$m.s^{-1}$
v	reference velocity signal	$m.s^{-1}$
W_b	width of 3D obstacles	m
W	width of canyon	m
x, y, z	streamwise, spanwise and vertical coordinates	m
y^*	viscous length scale	m
z_o	roughness length	m
Δ	spatial filter size	mm
Δ_x	Particle Image Velocimentry spatial resolution in the x-direction	mm
$\overline{\quad}$	temporal average	-
$\langle \quad \rangle$	spatial average	-
$\sim$	spatial filtering	-
$\lceil \quad \rceil$	large-scale filter	-

Acronyms

2D	two-dimensional
3D	three-dimensional
ABL	atmospheric boundary layer
ESDU	Engineering Sciences Data Unit
HWA	Hot-Wire Anemometry
LES	large-eddy simulation
LSE	Linear Stochastic Estimation
PIV	particle image velocimetry
RSL	roughness sublayer
TKE	turbulent kinetic energy
UBL	urban boundary layer
UCL	urban canopy layer
VLSM	very large scale motion

Introduction

Pour la première fois dans l'histoire, le nombre de personnes vivant en milieu urbain dépasse la population rurale. Cette urbanisation mondiale conduit à un paysage urbain en constante évolution, ce qui entraîne des défis importants en termes de climat, de météorologie et de pollution. Plus précisément, dans les zones urbaines, la mauvaise qualité de l'air liée aux rejets de polluants depuis les vehicules et les bâtiments est une préoccupation importante pour la santé humaine. L'Organisation mondiale de la santé (2014) estime que 1,3 millions de décès surviennent dans le monde en raison de la mauvaise qualité de l'air. Les particules émises lors de la combustion des combustibles fossiles, l'ozone formé par transformation des oxydes d'azote, le dioxyde d'azote et le dioxyde de soufre, sont autant de polluants qui augmentent le risque de problèmes de santé graves tels que les maladies cardiovasculaires et respiratoires, le cancer du poumon et l'asthme. Les zones urbaines sont particulièrement sensibles à la pollution atmosphérique, car elles sont généralement densément baties et ont une circulation aérienne accrue. Des ressources financières significatives dans le monde ont été allouées pour améliorer la qualité de l'air en milieu urbain, et plus généralement réduire les impacts de la pollution dans la couche limite atmosphérique.

La turbulence et plus particulièrement les structures turbulentes cohérentes jouent un rôle important dans la ventilation et la dispersion des polluants dans les zones urbaines. Les structures cohérentes importantes pour la ventilation des zones urbaines sont identifiées comme étant des régions de basse vitesse et des tourbillons en épingle à cheveux associés aux processus de balayage et d’éjection. La compréhension de ces structures cohérentes et de leur organisation est particulièrement intéressante car elles régissent le transport de chaleur, de quantité de mouvement et de polluants (Takimoto et al., 2011; Perret et Savory, 2013). De nombreux travaux ont été faits pour classer et définir les structures cohérentes afin de produire un modèle conceptuel décrivant l'organisation de la couche limite turbulente (Adrian et al., 2000). Au sein de la couche limite turbulente développée

sur une paroi lisse (Mathis et al., 2009) et sur une paroi rugueuse (Nadeem et al., 2015; Anderson, 2016; Squire et al., 2016), les structures de grande echelle et de basse vitesse qui existent dans la couche limite ont pu être reliées aux petites structures de proche paroi au travers d'un mécanisme non linéaire. Cependant, les travaux antérieurs sont limités à un ou deux types de rugosité et cette relation n'a pas été confirmée pour la couche limite urbaine. Les structures cohérentes ont été bien identifiées qualitativement, mais la façon dont elles interagissent, d'un point de vue fondamental ne sont pas entièrement comprises.

Le travail de recherche présenté vise à utiliser des données expérimentales en soufflerie pour améliorer la compréhension de la physique qui gouverne le transport des polluants dans la couche limite urbaine. Il s'agit en particulier de

1) Quantifier la relation entre les structures cohérentes à grande échelle qui se développent dans la couche de surface atmosphérique et les petites échelles générées par les rugosités typiques de la surface urbaine;
2) Comprendre l'influence de la configuration de rugosité présente en amont de la canopé étudiée sur les interactions dynamiques entre échelles considérées.
3) Quantifier la production et la dissipation d'énergie cinétique turbulente associée à ces structures cohérentes;

Le premier chapitre dresse un état de l'art sur les caractéristiques importantes et les structures d'écoulement considérées lors de l'étude de la couche de limite urbaine. Celui-ci fournit un contexte général du travail, tandis qu'une revue bibliographique détaillé pour chaque sujet spécifique est introduite dans le chapitre concerné. Le Chapitre 2 décrit les détails expérimentaux sur lesquels s'appuie le présent travail ainsi que les principales caractéristiques statistiques de la couche limite urbaine modélisée dans la soufflerie. Le chapitre 3 décrit la méthodologie adoptée pour accéder à une information résolue en temps sur les grandes échelles présentes dans la sous-couche rugueuse et permettre ensuite d'analyser les interactions non linéaires entre les grandes et les petites échelles. Ce chapitre présente en particulier, le modèle d'estimation stochastique qui sera la base des chapitres suivants portant sur l'analyse des interactions dynamiques entre échelles. Dans le chapitre 4, la relation non linéaire entre échelles est analysée dans le cas particulier d'une canopée de type urbain constituée d'un réseau de cubes décalés. Le

Chapitre 5 porte sur l'influence de la rugosité en amont et du rapport d'aspect de la rue canyon sur cette relation non linéaire, en utilisant des réseaux simplifiés de rugosité et des canyons nominalement bidimensionnels. Le Chapitre 6 est un examen du bilan d'énergie cinétique turbulente (TKE) à l'intérieur et au-dessus de la canopée urbaine constituée de cubes, comprenant en particulier la quantification de la dissipation par le biais d'un modèle de sous-maille. Le Chapitre 7 combine les méthodes présentées au Chapitre 3 et utilisées dans les Chapitres 4 et 6 pour étudier les transferts non linéaires d'énergie cinétique turbulente entre les échelles. Enfin, des conclusions et perspectives sont proposes, sur la base des résultats de ce travail de thèse, en mettant en avant les connaissances qu'elles fournissent pour comprendre les relations qui régissent le transport des polluants dans la couche de limite urbaine.

Introduction

For the first time in history the number of people living in urban areas outweighs the rural population. This global urbanization leads to a constantly changing urban landscape resulting in significant challenges in terms of climate, meteorology and pollution. Specifically, within urban areas poor air quality as a result of vehicle and building exhaust entrainment and re-circulation is a significant concern for human health. The World Health Organization (2014) estimates that 1.3 million deaths occur worldwide per year due to poor air quality. The burning of fossil fuels such as in vehicular combustion engines produces particulate matter, ozone formed from nitrogen oxides, nitrogen dioxide and sulfur dioxide and it is well known that these pollutants increase the risk of serious health conditions such as cardiovascular and respiratory diseases, lung cancer and asthma. Urban areas are particularly susceptible to air pollution as they typically have a dense packing structure and increased vehicular traffic. Worldwide significant monetary resources have been allocated to help mitigate the effects of poor air quality, but in order to reduce the impacts of poor air quality one must first understand the fundamental processes that govern the transport of pollutants within the atmospheric boundary layer.

Turbulence and more specifically turbulent coherent structures play an important role in the ventilation and transport of pollutants in urban areas. The coherent structures important to the ventilation of urban areas are classified as low momentum regions, hairpin vortices and sweeps and ejections. Understanding these coherent structures and their organization are of particular interest as they govern the transport of heat, momentum and pollution (Takimoto et al., 2011; Perret and Savory, 2013). Much effort has been made to classify and define coherent structures in order to produce a conceptual model for the organization of the turbulent boundary layer (Adrian et al. 2000). Within the turbulent boundary layer developing over a smooth-wall (Mathis et al., 2009) and rough-wall (Nadeem et al., 2015; Anderson, 2016; Squire et al., 2016) the large-scale low momentum regions occurring within the overlying boundary have been linked through a non-linear mechanism to the near-wall small-scales. However, previous work is limited

to one or two types of roughness and this relationship has not been confirmed to occur within the urban boundary layer. Furthermore, the transfer of energy between these structures as a result of their interactions has yet to be investigated. Coherent structures have been well identified qualitatively, but their quantitative relationships and how they interact and influence one another at a fundamental level is not fully understood.

This research program aims to use experimental evidence to improve the understanding of the fundamental physics governing pollutant transport in the urban boundary layer by

1) quantifying the relationship between large-scale coherent structures and small-scales generated by the urban roughness,
2) understanding the effects of upstream roughness configuration on this relationship and,
3) quantifying the energy production and dissipation of the coherent structures.

The first chapter provides a bibliographic review of the important features and flow structures considered when studying the urban boundary layer. This will provide a general context of the work while a detailed bibliographic review for each specific topic will be included in the applicable chapter. Chapter 2 describes the experimental details of the present work and the characteristics of the wind tunnel model boundary layer. Chapter 3 provides a detailed description of the Linear Stochastic Estimation methodology, which is used to obtain temporally resolved large-scale fluctuations within the roughness sublayer allowing for the investigation of non-linear interactions between large- and small-scales. This methodology is then used for the analysis presented in Chapters 4, 5 and 7. Chapter 4, is an investigation of the non-linear relationship between large-scale momentum regions and small-scales induced by the presence of the roughness within a staggered cube array. Chapter 5 is an investigation of the effect of upstream roughness array configuration and canyon aspect ratio on this non-linear relationship using simplified roughness arrays and nominally two-dimensional canyons. Chapter 6 is an examination of the Turbulent Kinetic Energy (TKE) budget within and above a staggered cube array including quantification of the dissipation using a sub-grid scale model. Chapter 7 combines the methods presented in Chapters 3 and 6 to investigate the non-linear energy transfer between scales. A final chapter (Conclusions and Perspectives)

discusses the results of the previous chapters and the insights they provide into understanding the fundamental relationships that govern the transport of pollutants in the urban boundary layer.

Résumé du Chapitre 1: La couche limite urbaine

Ce chapitre dresse un panorama des connaissances sur la couche limite urbaine et la façon de représenter et modéliser l'atmosphère urbaine. Une attention particulière est portée sur les schémas conceptuels qui permettent de relier les structures cohérentes présentes dans la couche de surface atmosphérique et les processus de ventilation de la canopée urbaine et d'échanges entre canopée et atmosphère. Un résumé (en français) de ce chapitre est proposé ci-après.

Dans les zones urbaines, la mauvaise qualité de l'air est néfaste à la santé, mais les processus qui expliquent le transport des polluants dans la couche limite atmosphérique sont encore mal compris. La couche limite atmosphérique (CLA) est une région complexe située entre la surface de la terre et l'atmosphère libre où l'effet du frottement à la surface peut être négligé. La CLA est représentée verticalement par une succession de sous-couches: la sous-couche de rugosité, la sous-couche inertielle et la couche d'Ekman. La CLA peut être définie comme la couche de l'atmosphère dans laquelle la turbulence joue un rôle primordial dans les échanges entre la surface et l'atmosphère.

La turbulence est responsable du transport de l'énergie, de la quantité de mouvement, de la chaleur et des polluants dans la CLA. La turbulence est constituée de tourbillons de tailles et de fréquences caractéristiques qui s'étendent sur une large gamme d'échelles. Il existe plusieurs définitions des échelles de longueur utilisées pour définir la taille d'un tourbillon. L'échelle de longueur intégrale définit les plus grands tourbillons (énergétiques) présents dans l'écoulement, la micro-échelle de Taylor est l'échelle de longueur des plus gros tourbillons dissipatifs et enfin, l'échelle de longueur de Kolmogorov est celle des plus petits tourbillons dissipatifs. Les spectres de turbulence sont une mesure de l'énergie contenue dans les tourbillons pour chaque échelle et, permet en conséquence, une mesure de la fréquence caractéristique de ces tourbillons (Cook, 1985).

Pour étudier la qualité de l'air en milieu urbain, il faut étudier la couche limite urbaine (CLU) qui est définie comme la partie de la CLA qui est influencée par la présence de la zone urbaine (Roth, 2000). Il existe plusieurs régions d'importance dans la CLU. La

première est la couche de canopée urbaine (CCU) comprise entre le sol et le sommet des bâtiments. L'écoulement y est directement influencé par les caractéristiques de la rugosité au niveau micro-échelle, et est généralement très complexe. La sous-couche de rugosité, qui comprend la CCU, est définie par les échelles de longueur associées aux caractéristiques de surface. Enfin, la couche mélangée est la région où la turbulence n'est plus directement influencée par les caractéristiques de la surface.

L'usage de la soufflerie est fréquent pour modéliser la CLU en tant que la couche limite. Les conditions d'entrée peuvent être contrôlées et les techniques de mesure peuvent permettre d'obtenir des champs d'écoulement en 2D avec les trois composantes de vitesse. Lors de la modélisation de la CLU dans la soufflerie, la mise à l'échelle de la couche limite est de la plus haute importance et elle prend en compte trois aspects de la similitude du modèle: géométrique, cinématique et dynamique.

La similitude géométrique est la mise à l'échelle de toutes les dimensions du modèle qui permet d'établir un rapport constant avec les dimensions à l'échelle réelle (Cook, 1985). La similitude cinématique consiste en la mise à l'échelle du temps, tout comme la similitude géométrique et dynamique permettent la mise à l'échelle de toutes les forces, qui est obtenue en faisant correspondre le nombre de Reynolds, Re. Bien que cela soit difficile à réaliser à petite échelle, il a été montré que l'écoulement sur les corps non-profilés, tels que ceux rencontrés dans les zones urbaines, ne dépend pas fortement du nombre de Reynolds. La similitude est donc réalisée dès lors qu'un Re suffisant est atteint pour générer un écoulement turbulent.

De nombreux travaux ont été réalisés pour classifier et définir des structures cohérentes afin de proposer un modèle conceptuel pour l'organisation de la couche limite turbulente (Adrian et al., 2000). Dans ce modèle, les structures cohérentes et les mouvements cohérents peuvent être classés comme des régions de basse vitesse, des tourbillons en épingle à cheveux et des balayages et éjections. Les régions de basse vitesse sont constituées de structures allongées de vitesses inférieures à la vitesse moyenne de l'écoulement. La présence de régions à basse vitesse est toujours contrebalancée par la présence de régions à haute vitesse (Takimoto et al., 2013). Les deux types de régions

peuvent avoir des dimensions allant jusqu'à 1000^+ de long, 20^+ à 40^+ de large et de 5 à 10^+ de haut (où $^+$ sont les unités de paroi déterminées à l'aide de la vitesse frottement u_* et de la viscosité cinématique ν) (Robinson, 1991). Ces structures ont souvent été identifiées dans la littérature, y compris grâce à des études de terrain (Inagaki et Kanda 2008), démontrant ainsi leur nature persistante et cohérente. Une hypothèse est que les régions de basse vitesse sont le résultat de groupes de tourbillons en épingle à cheveux (Coceal et al., 2007b). La génération d'un tourbillon en épingle à cheveux n'est pas pleinement comprise à ce jour, si ce n'est qu'elle provient d'une perturbation qui crée une poche de basse vitesse, comme un événement d'éjection. Cela limite les jambes de tourbillon en épingle à cheveux dans la direction transverse, qui sont ensuite tournées et étirées par le cisaillement moyen (Coceal et al., 2007b). Enfin, ce tourbillon produit de fortes éjections en répétant le processus, créant ainsi un groupe de tourbillons en épingle à cheveux. Le processus entraîne l'apparition d'une région de basse vitesse qui est beaucoup plus longue que l'échelle de longueur d'un tourbillon en épingle à cheveux.

Les événements de balayage sont le processus de transfert du fluide depuis les zones de haute vitesse dans la couche limite sus-jacente vers les zones de basse vitesse dans la canopée, tandis que les événements d'éjection sont le processus de transfert du fluide à partir des zones de haute vitesse dans la canopée vers les zones de basse vitesse dans la couche limite sus-jacente. Il a été montré que les régions de basse vitesse influencent la concentration de polluants dans les canopées 3D et 2D (Michioka et Sato, 2012; Michioka et al., 2014) et sont corrélées avec les événements d'éjection (Takimoto et al., 2011; Inagaki et al., 2012). En outre, grâce à à la simulation des grandes échelles (LES), on a constaté que des événements de balayage se situaient sous des zones de haute vitesse (Inagaki et al., 2012). Ainsi, il est clair que les régions de basse vitesse et haute vitesse présentes dans la couche limite sus-jacente ont une relation importante avec les événements de balayage et d'éjection qui ventilent la canopée (Takimoto et al., 2011; Inagaki et al., 2012).

Ainsi, le transport de polluants dans les canopées urbaines pourrait-il être décrit de manière conceptuelle par la Figure 1.13 (Coceal et al., 2007b). Cette figure montre trois régions. La première est une région située dans la couche limite, au-dessus de la canopée,

où l'on trouve les structures de basse et haute vitesse et les tourbillons en épingle à cheveux (bleu foncé et rouge foncé). Les événements d'éjection et de balayage dans cette région sont responsables de l'échange intermittent de polluants entre la canopée et la couche limite supérieure. La deuxième région est une couche de fort cisaillement qui se forme le long de l'obstacle amont (blanc) et la troisième région est une région de recirculation à l'intérieur de la canopée (noir).

Ces trois régions interagissent pour influencer la ventilation de la canopée. Ce n'est qu'un modèle conceptuel simplifié qui ne décrit pas complètement la complexité de l'écoulement, mais qui permet de donner un résumé qualitatif des structures de l'écoulement qui ont un rôle dans les échanges entre les canopées urbaines et la couche limite. La ventilation des canopées urbaines régit la qualité globale de l'air de l'environnement urbain. Ainsi, il est important d'étudier quantitativement les rôles et les relations entre les structures turbulentes et les processus qui régissent la ventilation des zones urbaines.

La qualité de l'air est une préoccupation importante pour la santé humaine, en particulier dans les zones urbaines où il y a une augmentation substantielle des émissions de polluants atmosphériques (Organisation mondiale de la santé, 2014). Bien que beaucoup de travaux aient été consacrés à l'étude de la couche limite urbaine en utilisant des expériences de terrain, des expériences en soufflerie et des modèles numériques tels que la LES, les processus fondamentaux régissant le transport de chaleur, de quantité de mouvement et de pollution sont encore mal compris. Plus précisément, les structures cohérentes telles que les régions de basse vitesse et les tourbillons en épingle à cheveux ont été bien identifiées qualitativement, mais les relations quantitatives régissant les interactions entre les échelles sont encore méconnues.

1 The Urban Boundary Layer

Poor air quality is detrimental to human health, but the processes that govern the transport of pollutants within the atmospheric boundary layer are still poorly understood. The following describes the general structure of the atmospheric boundary followed by a description of the urban boundary layer and how it is modeled. Finally, the flow structures important to the transport of pollutants in urban areas and their organization are discussed.

1.1 The Atmospheric Boundary Layer

The atmospheric boundary layer (ABL) is a complex region between the free atmosphere, where the effect of the earth's friction can be neglected, and the surface of the earth. The free atmosphere is characterized by the freestream velocity (U_∞) or geostrophic wind speed (U_g), which is the velocity at a height that is no longer influenced by the surface friction. There are several sub-regions within the ABL. The first, the roughness sublayer (RSL), is the region where air flows around surface obstacles and the second, the surface layer, which consists of the inertial layer and the RSL, is the region where turbulence is influenced by the surface characteristics and is typically 100 m thick. Finally, the Ekman layer or well-mixed layer, is where flow is influenced by a combination of pressure gradient, turbulent drag and the Coriolis effect (Wyngaard, 2010).

The Coriolis effect is a force exerted on the wind from the rotation of the earth where the wind is deflected either clockwise in the northern hemisphere or counter-clockwise in the southern hemisphere. This phenomenon is responsible for the formation of large cyclones in the atmosphere, however, this occurs on a grand scale and is only noticeable for air traveling over large distances and long time periods.

The most important feature of the ABL is the generation of turbulence. Turbulence is responsible for the transport of energy, momentum, heat and pollutants within the ABL and due to the mixing mechanisms turbulence induces it tends to homogenize the

properties of the atmosphere faster than in laminar flow. Turbulence is generated by the wind shear existing over the height of the ABL, which is generally geostrophic at the top of the ABL and zero at the surface. Finally, temperature greatly influences the structure of the ABL as it can either generate or suppress turbulence. When there is a difference in temperature between the surface and the air a heat flux is created, which results in a transfer of energy between the air and the surface. The temperature gradient across the ABL determines the stability of the atmosphere.

Figure 1.1 shows the ABL under various stability conditions throughout the duration of one day. In neutral stability, the temperature of the surface is equal to the temperature of the air, thus, turbulence and mixing is not generated through temperature gradients. Under neutral conditions the surface layer can be defined by a logarithmic profile. In the unstable ABL the temperature of the surface is greater than the temperature of the air resulting in buoyancy forces which increase turbulence. In this case the surface layer has a strong wind shear and super adiabatic temperature gradient while the mixed layer has a constant potential temperature and an entrainment zone with a temperature inversion. This stability case typically occurs during the daytime when solar heating is strong. Finally, stable ABL conditions occur when the surface temperature is lower than the air temperature, which typically occurs at night. The stability suppresses the turbulence generated at the surface and the surface layer has a sub-adiabatic temperature gradient.

The ABL is a complex region where turbulence generation, whether through surface characteristics or stability conditions, is an important factor to understanding pollutant transport.

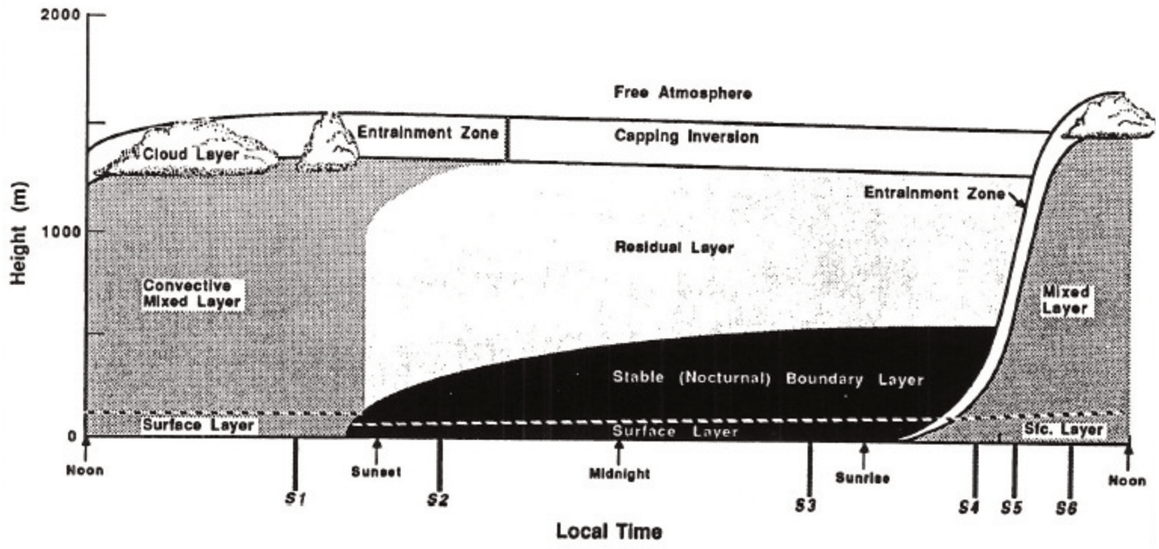

Figure 1.1. The atmospheric boundary layer throughout the duration of one day (Stull, 1988).

1.2 Turbulence in the ABL

The Navier-Stokes equations for momentum (Equation 1.1) and continuity describe flow in the turbulent boundary layer. As the equations have no exact solution for fully turbulent flows Reynolds decomposition (Equation 1.2) is often used to separate the mean portion of the flow ($\overline{U}$) from the turbulent fluctuations (u'). This decomposition provides a simplification of the Navier-Stokes equations to the Reynolds-averaged Navier-Stokes equations (not presented) which can be used to investigate the mean flow. Within this equation the term Reynolds stress ($\overline{u_i' u_j'}$) represents the influence of turbulence on the mean flow.

$$\frac{\partial U_i}{\partial t} + U_j \frac{\partial U_i}{\partial x_j} = -\frac{1}{\rho}\frac{\partial P}{\partial x_i} + \nu \frac{\partial^2 U_i}{\partial x_j \partial x_j} \tag{1.1}$$

$$U = \overline{U} + u' \tag{1.2}$$

Turbulence is made up of eddies, which are rotating packets of turbulence, occurring at a wide range of scales, which are defined by length scales. There are several definitions of length scale used to describe turbulent flow with the most common being the integral length scale (L_u), which defines the largest eddies in the flow. Integral scales can be estimated using temporal ($R_{uu}(\tau)$) or spatial correlations ($R_{uu}(x, z)$). When using spatial

correlation, the integral length scale can be directly determined from the correlation, but when using temporal correlation Taylor's hypothesis of frozen turbulence is used (Equation 1.3). This hypothesis states that the advection contributed by the turbulent circulations is negligible and therefore, the advection of turbulence past a fixed point is due solely to the mean flow. However, this hypothesis is only valid for flows where the variation of the wind speed due to turbulence is less than one half of the mean wind speed.

$$L_u(z) = \int R_{uu}(\tau) d\tau * \overline{U}(z) \tag{1.3}$$

Taylor microscales (λ) are the intermediate length scales and are the smallest scale within the inertial range where energy is passed between large-scales and microscales without dissipation. Finally, the Kolmogorov length scales (η) are the smallest scales and occur within the viscous sub-layer, which is the region where the rate of change of Turbulent Kinetic Energy (TKE) equals the dissipation rate per unit mass. In this region the turbulence is both isotropic and homogeneous.

1.2.1 Turbulence Spectra

As described above turbulence is made up of eddies occurring at a wide range of scales from large integral scales to small Kolmogorov scales. The turbulence spectra are a measure of the energy contained within eddies at each scale and, therefore, frequency (Cook, 1985). The flow consists of three scales of eddies; 1) the largest eddies or the production range; 2) energy containing eddies or the inertial range and 3) small scale eddies or the dissipation range. The largest eddies contain approximately 20% of the total energy but occur at low frequency, whereas the small-scale eddies contain very little energy, approximately 10%, but occur at high frequency. That leaves the energy containing eddies, where approximately 70% of the energy is contained. Energy in the flow is transferred between scales through non-linear inertial interactions. Large-scale structures are created, which then produce smaller scale structures and so on until the scale is small enough that viscous effects become important. At this scale viscosity causes inertial energy from the flow to be converted to heat energy thereby dissipating

the energy of the small-scales preventing the generation of infinitely small-scales. This interaction is called the ‘energy cascade’ (Figure 1.2) (Cook, 1985).

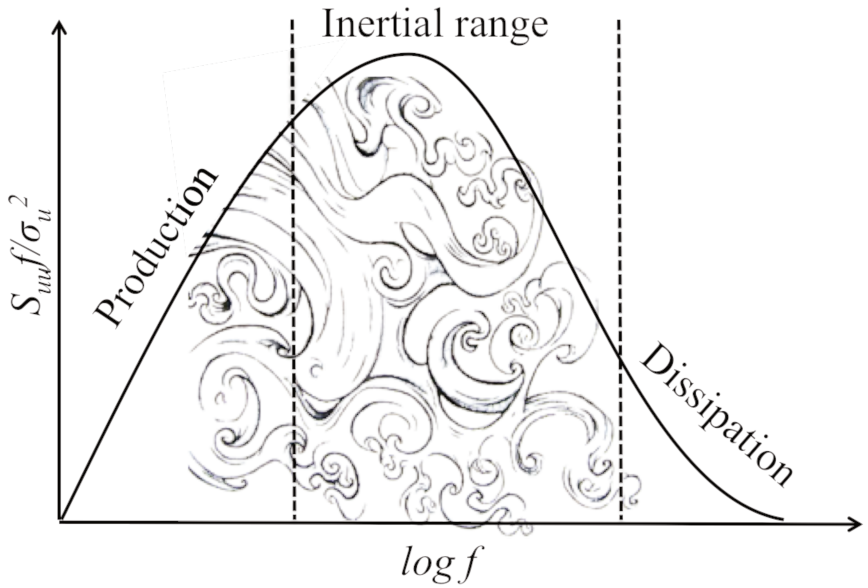

Figure 1.2. The turbulence spectra

1.3 The Urban Boundary Layer

Due to experimental restraints, wind tunnel studies of the urban boundary layer (UBL) are typically restricted to those under neutral conditions. This excludes the effects of temperature, which although important to atmospheric flow, simplifies the problem to turbulence generated from surface structure only. Roth (2000) defines the UBL as the portion of the ABL that is influenced by the presence of the urban area (Figure 1.3). There are several regions of importance in the UBL, the first, the urban canopy layer (UCL), is the region that is directly influenced by the site characteristics in the microscale and flow is generally very complex. The RSL, which includes the UCL, is defined by the length scales associated with the surface characteristics, such as the integral length scales. The inertial layer can be defined by the log law or power law, which are defined later and finally, the mixed layer, is the region where turbulence is no longer influenced by the surface characteristics.

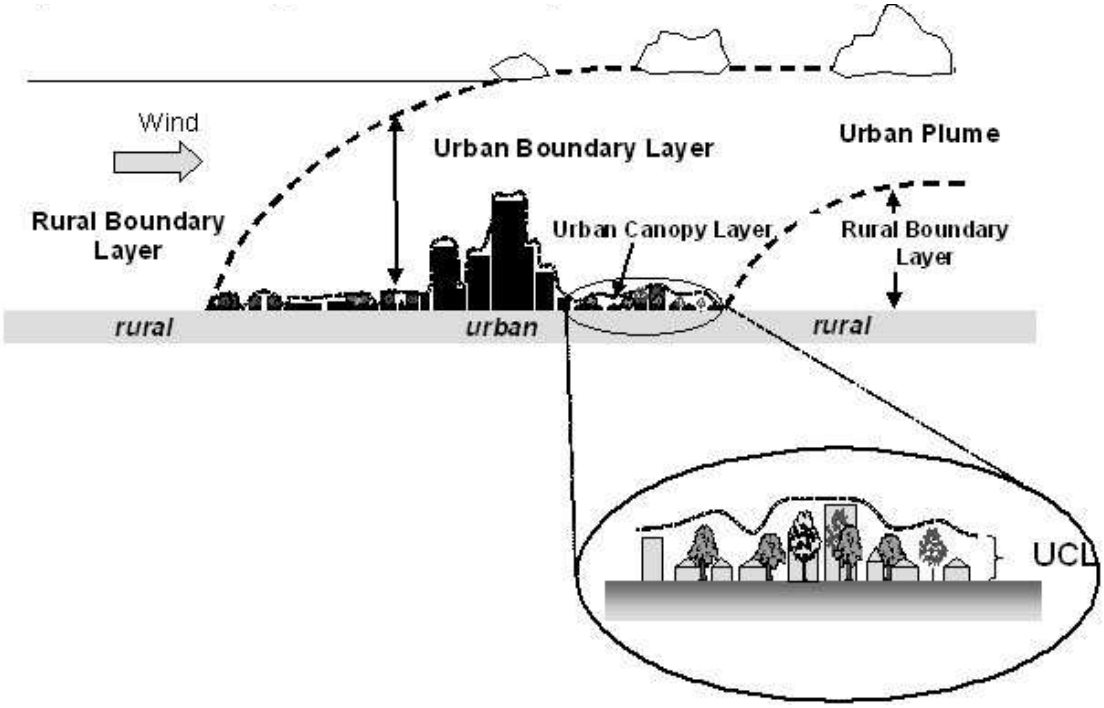

Figure 1.3. The urban atmosphere and its main regions (Roth, 2000).

1.3.1 Defining the urban canopy

The urban environment is a complex terrain with typical urban areas having varied building width, height, shape, density and arrangement. Therefore, when conducting experimental studies on urban areas, one is faced with the challenge of defining these areas using a simplistic universal parameter.

Stewart and Oke (2009) suggest defining urban areas using sub-classes based on surface cover, such as built fraction, soil moisture and albedo, surface structure, such as sky view factor and roughness height, and cultural activity, such as anthropogenic heat flux. However, in experimental studies urban canopies are typically defined by the universal parameters average building height (h_{avg}), plan area packing density (λ_p), frontal area packing density (λ_f), roughness length (z_o), zero-plane displacement height (d) and friction velocity (u_*), which are defined below.

Normally, within the wind tunnel building terrain is simulated using upstream roughness arrays composed of simplified obstacles such as cubes. These arrays consisting of a series of elements initiate and develop the approaching boundary layer. These arrays can be of

any configuration or size, but generally there are three configurations used which are (1) three-dimensional (3D) staggered blocks, (2) 3D aligned blocks or (3) two-dimensional (2D) bars (Figure 1.4). The aspect ratio (AR_b) of the 3D blocks is defined as the ratio of width to length (W_b/L_b). The plan area packing density (λ_p) of the roughness array is defined as the ratio of the plan area of the obstacles (A_{pi}) to the total plan area (A_d) (Equation 1.4). If the roughness elements are periodic the ratio can be reduced to that shown in Figure 1.4.

$$\lambda_p = \frac{\sum_{i=1}^{n} A_{pi}}{A_d} \tag{1.4}$$

Another parameter, the frontal area packing density (λ_f), which is the ratio of the frontal area of the obstacles (A_{fi}) to the total plan area (A_d), is used to define the upstream roughness (Equation 1.5).

$$\lambda_f = \frac{\sum_{i=1}^{n} A_{fi}}{A_d} \tag{1.5}$$

The average building height (h_{avg}) allows for a representative definition of the height for an urban area based on the height of the individual buildings and the building footprint. It is defined by Equation 1.6, where h_i is the height of each individual building and A_{pi} is the footprint of each building.

$$h_{avg} = \frac{\sum_{i=1}^{n} h_i A_{pi}}{\sum_{i=1}^{n} A_{pi}} \tag{1.6}$$

a)

b)

c)

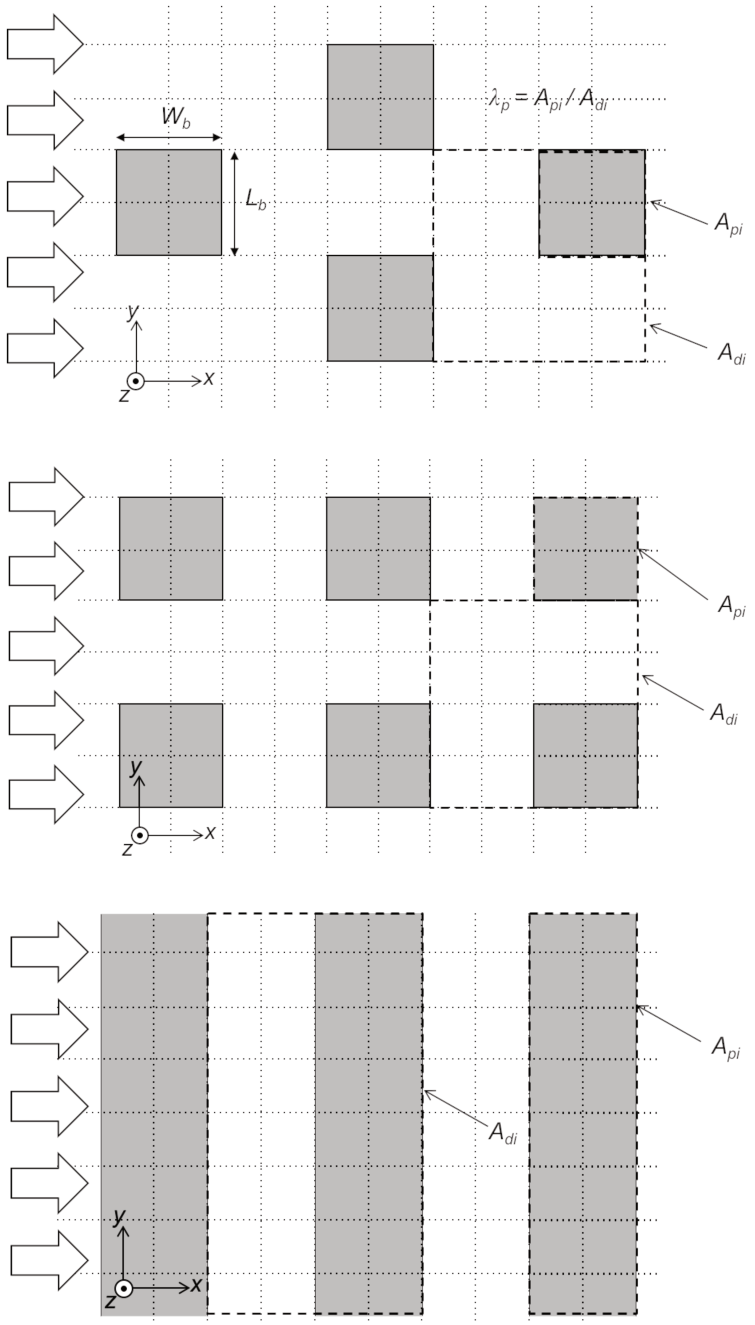

Figure 1.4. Upstream roughness array configurations; a) 2D bars; b) 3D staggered cubes; c) 3D aligned cubes.

The zero-plane displacement height (d) is the distance above ground level that the wind is displaced upwards by the surface roughness. The roughness length (z_o) is used to characterize the roughness of the surface and finally, the friction velocity (u_*) is a definition of shear stress in units of velocity. All three of these parameters are used in the

log law (Equation 1.7) to estimate velocity ($\overline{U}(z)$) at a height (z) and are also used to determine kinematic similarity between full-scale and model-scale.

$$\overline{U}(z) = \frac{u_*}{\kappa}\left[ln\left(\frac{z-d}{z_o}\right)\right] \quad (1.7)$$

The friction velocity (u_*) is related to the wall shear (τ_w) (Equation 1.8), which is the drag force per unit area. Within the urban boundary layer drag is a function of both viscous drag and pressure drag. As τ_w is directly related to shear stress ($\overline{u'w'}$) in the urban boundary layer it can be determined from the vertical profile of shear stress near the wall in the region of constant shear stress.

$$u_* = \sqrt{\frac{\tau_w}{\rho}} \quad (1.8)$$

As both d and z_o describe the surface roughness these can be estimated using either the friction velocity and log law or from definitions based on surface type such as those from ESDU (1982; 1985), shown in Figure 1.5. As well, much work has been conducted, such as that by Grimmond and Oke (1999), to attempt to define these parameters based on λ_p and λ_f (Figure 1.6). However, as shown by Blackman (2014) these parameters depend not only on the λ_p, but also on the geometry of the roughness configuration, such as aligned or staggered 3D arrays or 2D arrays.

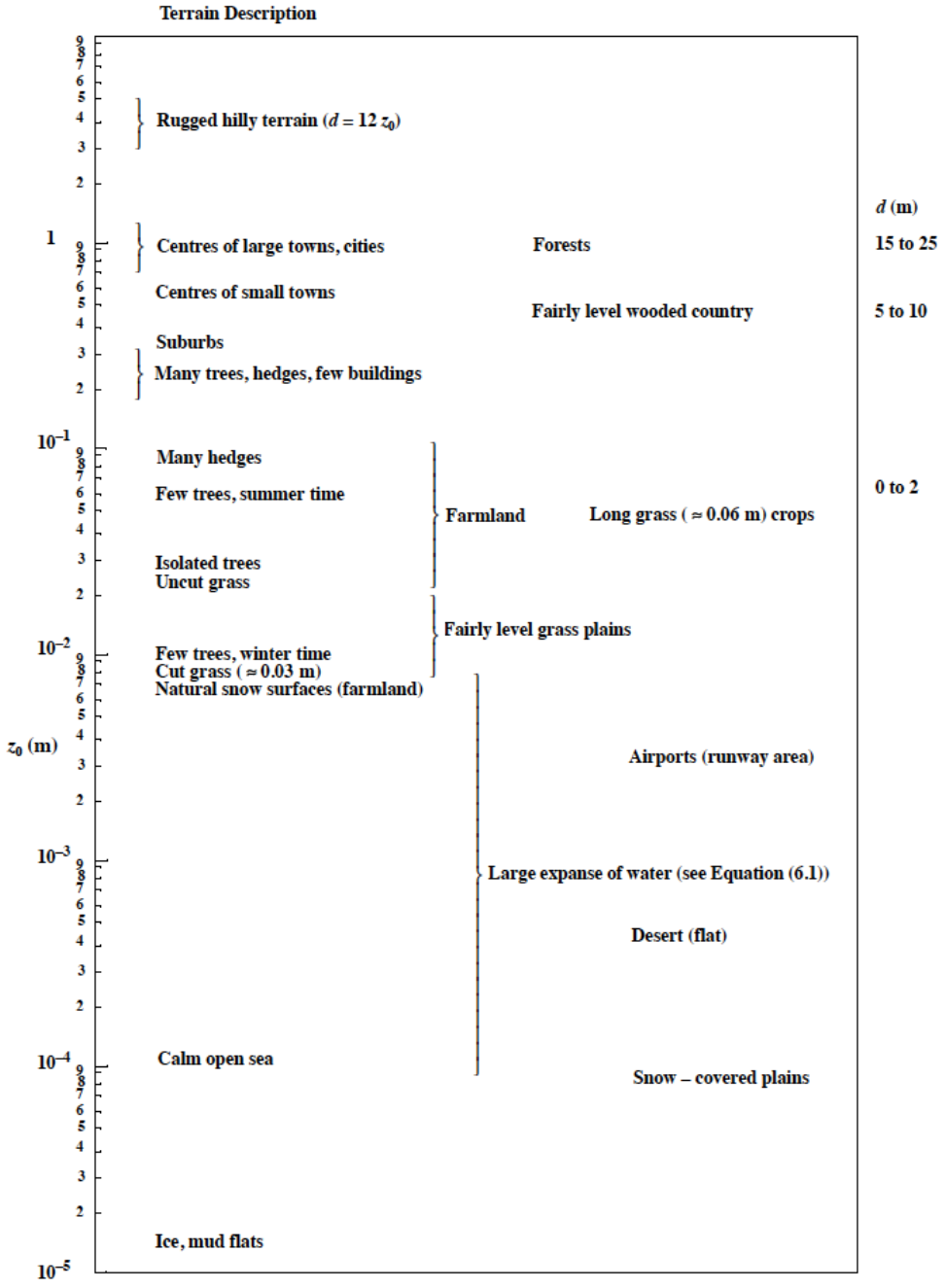

Figure 1.5. Roughness length (z_o) from terrain type (ESDU, 1982; 1985).

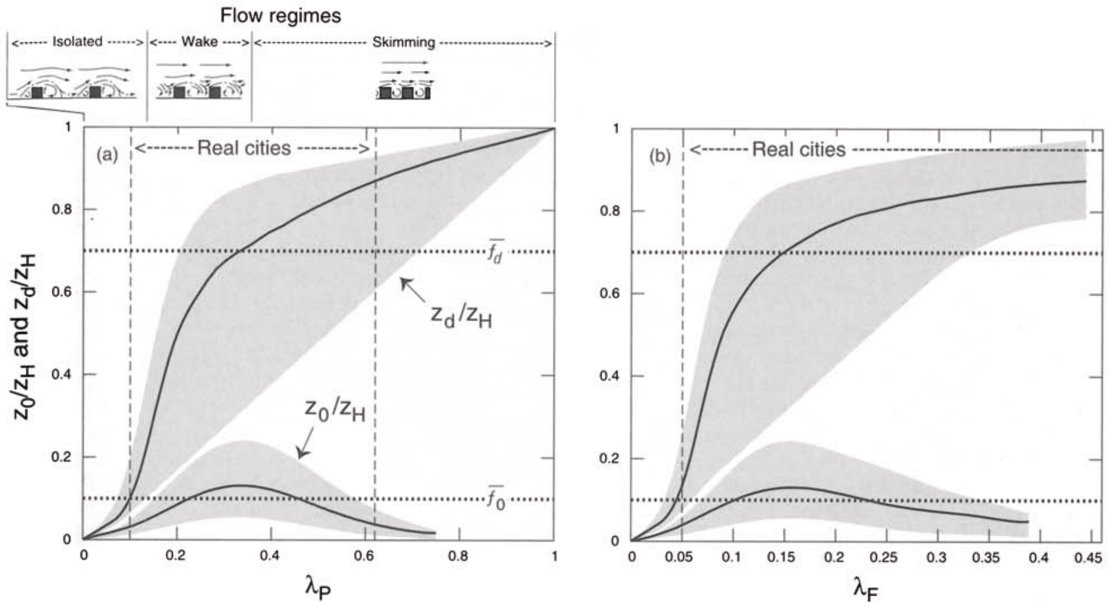

Figure 1.6. Roughness length (z_o) and zero-plane displacement height (d) based on λ_p and λ_f (Grimmond and Oke, 1999).

Finally, urban canopy arrays can be described using the flow regimes defined by Oke (1988) as skimming flow, wake interference flow and isolated flow (Figure 1.7). In the skimming flow regime flow that separates above the obstacles creates a shear layer. However, due to the close spacing of obstacles there is no penetration of the shear layer into the opening between obstacles, which causes a decoupling between the overlying boundary layer, shear layer and the flow within the canopy. In the wake interference regime, the shear layer penetrates into the opening inducing mixing between the boundary layer and the canopy while the downstream obstacle influences the wake of the upstream obstacle. Finally, in the case of the isolated flow regime the shear layer completely penetrates the space between obstacles and there is no interference between the wake of the upstream obstacle and the downstream obstacle. Using these geometric and flow definitions to describe urban canopies it is possible to classify and compare configurations of simplified models.

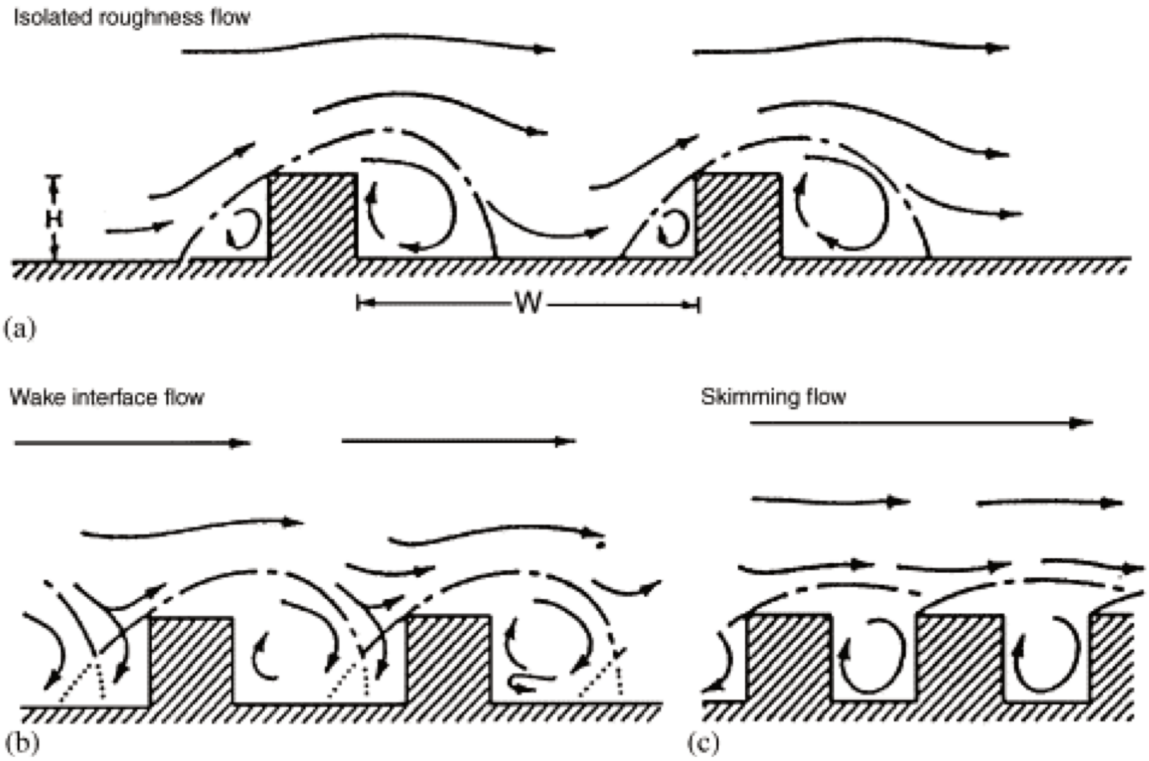

Figure 1.7. Flow regimes a) isolated roughness flow; b) wake interference flow; c) skimming flow (Oke, 1988).

1.4 Modeling the Urban Boundary Layer

The urban boundary layer is a complex region that is of interest for many applications. Studying this region is typically conducted using wind tunnel or field experiments as well as using numerical modeling techniques such as Large-Eddy simulation.

In-situ field measurements provide site-specific information, which can then be directly interpreted. Although flow dynamics are dependent on local building structure, in-situ measurements can still be used to understand the fundamental processes governing the transport of heat, momentum and pollutants (Rotach et al., 2005; Klein and Clark, 2007). Homogeneous field models using simplified blocks to simulate ground roughness can be used to study fundamental processes without the effects of local building structure, however like in-situ measurements they require long data logging times, depend heavily on weather conditions and require stringent data selection and pre-treatment (Liu et al., 2014; Blackman et al., 2015b).

Large-eddy simulation (LES) is a mathematical modeling method wherein low-pass filtering is applied to the Navier-Stokes equations which eliminates small-scale structures, thus reducing the computational cost of the model. LES has great advantage over experimental models as it has both high spatial and temporal resolution. This allows for detailed investigation of the turbulent dynamics throughout the boundary layer. However, due to the low-pass filtering used in LES the small-scales are not directly resolved, but estimated using further models.

The final method used to model the urban boundary layer, the wind tunnel experiment, can be used to provide insight into the fundamental physics governing the urban boundary layer and is described in the following section.

1.4.1 Wind tunnel models

The wind tunnel is frequently used to model the UBL as the boundary layer and inlet conditions can be controlled and measurement techniques are able to obtain 2D fields of three velocity components. However, as noted by Savory et al. (2013) many studies conducted within the wind tunnel are not representative of full-scale boundary layers. As the flow dynamics are highly sensitive to the approaching boundary layer flow it is imperative to accurately scale the boundary layer to realistic conditions.

1.4.1.1 Scaling of the boundary layer

When modeling the ABL in the wind tunnel for either site-specific or simplified geometries appropriately scaling the approaching boundary is of the utmost importance. Scaling takes into account three aspects of model similarity: geometric, kinematic, and dynamic. Geometric similarity is the scaling of all model dimensions to be a consistent ratio with that of the full-scale dimensions (Cook, 1985). Kinematic similarity is the scaling of time as well as geometry and is achieved in the wind tunnel by matching Jensen number, Je, integral length scales and turbulence spectra. The Jensen number, which is the ratio between the height of the obstacles, h, and the roughness length, z_o, and the integral length scales, of the streamwise (L_u), spanwise (L_v) and vertical (L_w) velocity, characterize the boundary layer. Finally, the turbulence spectra, which describes the distribution of the energy containing turbulent eddies, should match full-scale when

normalized. Dynamic similarity is the scaling of all forces and is achieved by matching the dimensionless number Reynolds number, Re. This is difficult to achieve at small scales, but it has been shown that flow over sharp edged bodies, such as those in urban areas, are not strongly Re dependent and similarity is achieved as long as sufficient Re is attained to generate turbulent flow.

As previously mentioned, the roughness length, z_o, can be determined from the log law (Equation 1.7), which describes the boundary layer wind profile. Another common law used to describe the boundary layer wind profile is the power law (Equation 1.9). The exponent (α) can also be used to scale the wind tunnel boundary layer with that of full-scale, but this method is not as robust as using the log law.

$$\frac{U}{U_{10}} = \left(\frac{z}{z_{10}}\right)^{\alpha} \tag{1.9}$$

If full-scale data is available scaling is achieved by directly comparing normalized profiles from the field and wind tunnel. However, in the case that wind tunnel models are conducted using simplified arrays these similarity requirements can be achieved using the guidelines specified by the Engineering Sciences Data Unit (ESDU). ESDU provides empirically derived boundary layer profiles, including mean streamwise velocity, turbulence intensities, shear stress, integral length scales and turbulence spectra, for different terrain based on accumulated field data (ESDU, 1982; 1985). These profiles can then be reproduced within the wind tunnel using simplified arrays and turbulence generators, such as spires and fences, to achieve similarity.

1.4.1.2 Simplification of the model

Modeling the urban boundary layer in the wind tunnel is a challenge as many factors such as terrain, building features and temperature gradient are important to the flow dynamics. Site-specific models include important building features and surrounding urban area as well as terrain and typically yield realistic results. However, the flows are difficult to interpret dynamically, thus rendering this approach unsuitable for understanding fundamental processes. Therefore, in order to understand the fundamental flow dynamics in urban areas it is necessary to simplify the urban model.

The first simplification is the simplification of the obstacle features. Building features such as courtyards, peaked roofs and chimneys, all contribute to the complexity of the flow. Within the wind tunnel it is common to simplify buildings to either 3D blocks or 2D bars. This reduces the complexity of the flow while still maintaining the turbulent flow structures responsible for the transport of heat, momentum and pollutants in urban areas (Savory et al., 2013). Additionally, depending on the interest of the study, terrain features, such as hills and valleys, are also simplified (Dupont et al., 2008). Finally, as discussed previously, temperature gradients result in changes to stability and are difficult to reproduce within the wind tunnel; therefore, neutral stability conditions are typically modeled.

All of the above modeling methods are able to reproduce the important features of turbulence within the UBL. The following sections will discuss the coherent flow structures that occur within both complex and simplified roughness arrays.

1.5 Coherent Structures

Much effort has been made to classify and define coherent structures in order to produce a conceptual model for the organization of the turbulent boundary layer (Adrian et al. 2000). Within this model coherent structures and motions can be classified as low momentum regions, hairpin vortices and sweeps and ejections. However, there is some question as to how to identify and quantify these coherent structures (Marusic et al., 2010). Coherent structures are defined by Hussain (1986) as ‘a connected turbulent fluid mass with instantaneously phase-correlated vorticity over its spatial extent’. This means that although turbulence itself is a 3D random process, coherent structures have a large-scale vorticity component that is instantaneously consistent over the spatial extent of the structure. This large-scale vorticity component is called the coherent vorticity and is the primary identifier of coherent structures (Hussain, 1986). Marusic et al. (2010) simply define coherent structures as ‘organized motions that are persistent in time and space and contribute significantly to the transport of heat, mass and momentum’. Although the definition of coherent structures is somewhat imprecise, identifying and quantifying these structures is of the utmost importance to understanding the turbulent dynamics in urban

areas. The following sections will describe current knowledge of coherent structures governing the transport of heat, momentum and pollutants in urban areas.

1.5.1 Low momentum regions

Coherent structures are often associated with low momentum regions, which are elongated regions moving at a velocity lower than that of the bulk flow. Work by Coceal et al. (2007b) using Direct Numerical Simulation (DNS) to study a cube array shows the presence of large-scale structures described as low momentum regions or low speed streaks (Figure 1.8). Michioka and Sato (2012) also found these regions just above both 2D and 3D canopies at a height of $z/h = 1.1$ and noted that pollutant concentrations below these regions were lower than the surroundings. This was confirmed by a second study of street canyons with various canyon widths, which showed that the presence of low-momentum regions increased pollutant removal from the canyon regardless of canyon aspect ratio (Michioka et al., 2014).

The presence of low momentum regions is always balanced by the presence of high momentum regions, which have a velocity greater than that of the bulk flow (Takimoto et al., 2013). Both types of regions can have dimensions of up to 1000^+ long, 20^+ to 40^+ wide and 5^+ to 10^+ high, where $^+$ are wall units determined using u_* and kinematic viscosity (ν) (Robinson, 1991).

Very Large-Scale Motions (VLSMs) have been identified within the smooth-wall boundary layer using DNS (Adrian, 2007; Lee and Hyung, 2011). These regions are either high or low momentum and exhibit large shear stress and TKE especially for flows with high Reynolds number demonstrating their importance to turbulence production and transport of momentum in the log layer (Adrian, 2007; Marusic et al., 2010; Lee and Hyung, 2011; Smits et al., 2011). Finally, VLSMs have been shown to influence the small-scale structures close to the wall through a non-linear relationship, which will be discussed further in Chapter 4 (Smits et al., 2011).

Low and high momentum regions have been consistently identified throughout the literature including field studies (Inagaki and Kanda, 2008), thus, demonstrating their

persistent, coherent nature. Their importance to the ventilation of urban areas is yet quantitatively unknown, but it is qualitatively clear that these structures influence the transport of pollutants (Michioka and Sato, 2012; Michioka et al., 2014). Furthermore, the presence of VLSMs has been confirmed, but their relationship to other coherent structures, such as hairpin vortices is yet to be established (Adrian, 2007).

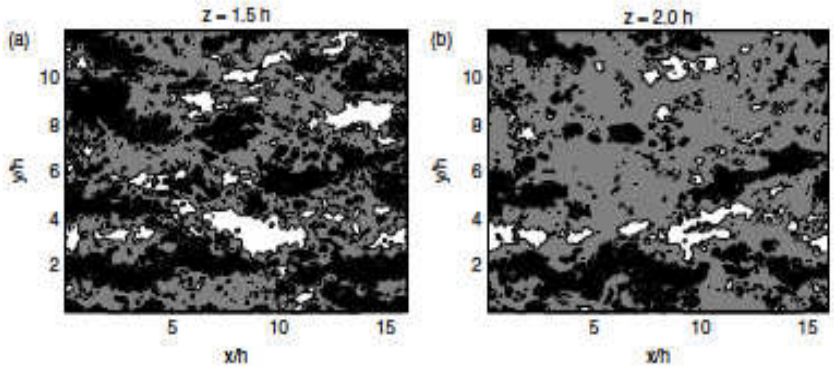

Figure 1.8. Instantaneous flow visualization of low momentum regions in a horizontal plane above a cubical array with black regions $u < 0.8u_m$ white regions $u > 1.2u_m$ where u_m is the local mean velocity (Coceal et al., 2007b).

1.5.2 Hairpin Vortices

It is hypothesized that low momentum regions and VLSMs are the result of groups of coherent hairpin vortices (Coceal et al., 2007b). Figure 1.9 shows an idealized hairpin vortex including the head, neck and legs. Hairpin vortices are described by the following features: i) a spanwise vortex core present in the head rotating in the same direction as the mean circulation; ii) below, a region of low momentum fluid which is a result of the vorticity in the head and neck; iii) an inclination of 35-50^o to the horizontal plane (Adrian et al., 2000; 2007). The legs of the hairpin vortex stretch in the streamwise direction and become quasi-streamwise vortices (Adrian et al., 2000; 2007).

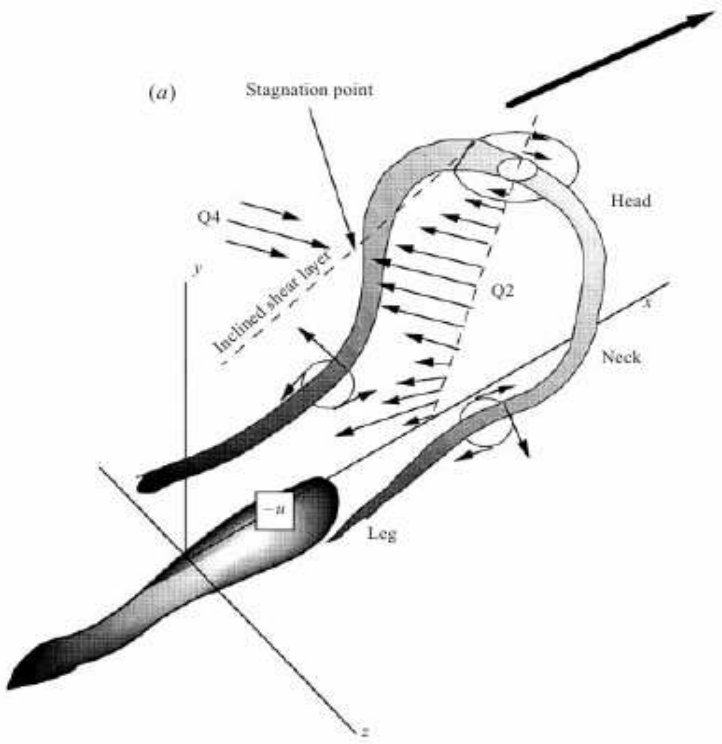

Figure 1.9. Illustration of an idealized hairpin vortex (Adrian et al., 2000).

Hairpin vortices frequently occur in groups, traveling at nearly the same streamwise velocity, thus, creating a packet of hairpin vortices (Adrian et al., 2000; 2007). It has also been noted by Adrian et al. (2000) that packets of hairpin vortices can align with other packets creating even longer zones of low momentum. The generation of a hairpin vortex is not fully understood except that it originates from a disturbance that creates a pocket of low momentum, such as an ejection event. This restricts the spanwise vortex lines, which are then rotated and stretched by the mean shear (Coceal et al. 2007b). Finally, this vortex then produces strong ejections repeating the process and creating a group of hairpin vortices. This process results in the appearance of a low momentum region that is much longer than the length scale of the individual hairpin vortex. From DNS Adrian (2007) noted that hairpin vortices experience a non-linear process called ‘auto-generation’. A primary hairpin vortex forms two other vortices. First, the downstream hairpin vortex (DHV) is formed from protrusions on the downstream face of an eddy which is then pulled into a pair of streamwise vortices that induce upward flow causing an arch. A secondary hairpin vortex (SHV) is created through interaction of the low-speed fluid that

occurs between the legs of the primary hairpin vortex and the high speed fluid above leading to a vortex roll-up that forms an arch.

It has been suggested by Adrian et al. (2000) that in a smooth-wall boundary layer hairpin vortex packets consist of eddies that form together close to the wall and travel at a 'packet convection speed'. These structures have a small angle of inclination near the wall, which increases to between 35-50^{o} close to the head of the hairpin vortex. Within the boundary layer there are several packets of hairpin vortices existing at once. Younger packets, which are small and have slower formation than larger packets, exist within larger packets or may be overtaken by the larger packets resulting in a constantly changing flow pattern as shown in Figure 1.10. The mechanism of merging packets was investigated by Tomkins and Adrian (2003) and is shown in Figure 1.11. The spanwise scale of hairpin vortices increases linearly with distance from the wall. The spanwise growth occurs from the merging of vortex packets and, therefore, low momentum regions. These then in turn form larger hairpin vortices with larger low momentum regions having a slightly higher packet convection speed. This phenomenon was confirmed by Lee and Hyung (2011) through DNS of a smooth-wall who also noted that hairpin vortex packets induced significantly elongated high and low momentum VLSMs in the logarithmic layer.

Although the process of generation of these hairpin vortices is not fully understood, the significance of these structures and low momentum regions to the frequency and strength of sweep and ejection events is well documented and discussed below (Michioka and Sato, 2012).

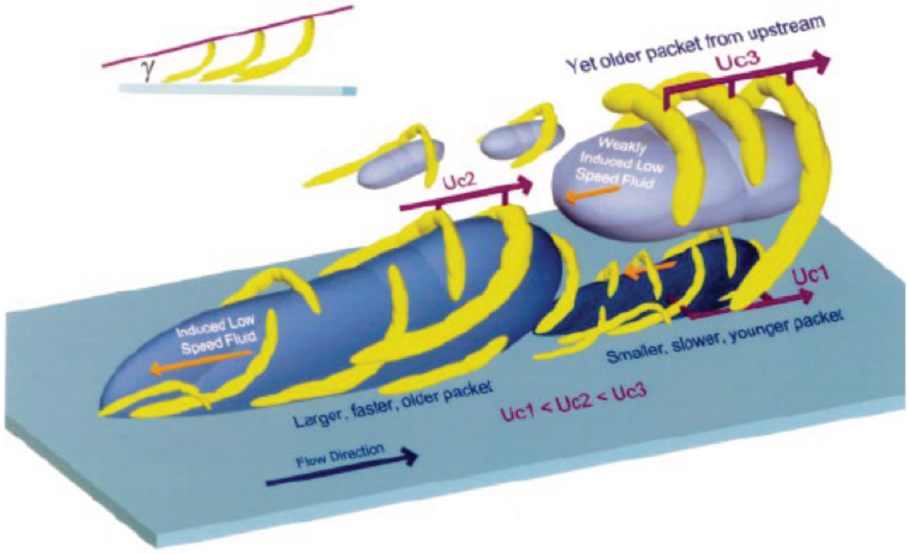

Figure 1.10. Conceptual model of nested packets of hairpin vortices growing from the wall in the turbulent boundary layer (Adrian et al., 2000).

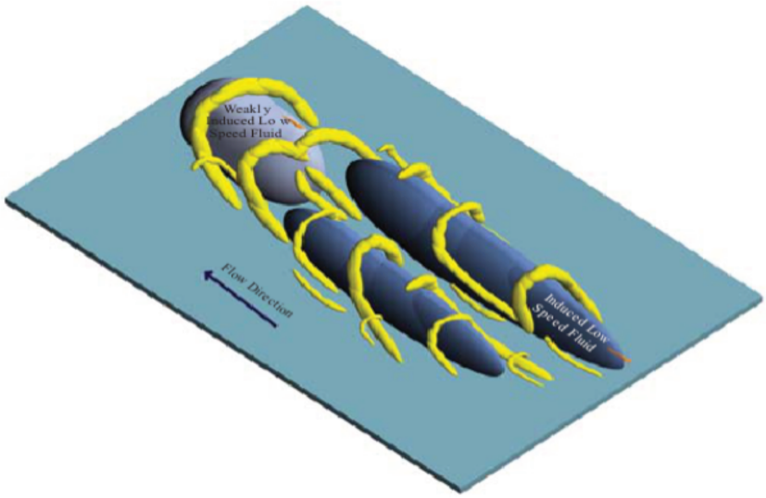

Figure 1.11. Conceptual model of scale growth of vortex packets through re-connection and packet merging (Adrian et al., 2000).

1.5.3 Sweeps and ejections

Sweep events are the process of transferring fluid from areas of high momentum within the overlying boundary layer to areas of low momentum within the canopy, while ejection events are the process of transferring fluid from areas of high momentum within the canopy to areas of low momentum within the overlying boundary layer (Figure 1.12).

These movements are classified using quadrant analysis and each of the four quadrants are defined as:

$$\begin{aligned} Q1&: u' > 0, w' > 0 \\ Q2&: u' < 0, w' > 0 \\ Q3&: u' < 0, w' < 0 \\ Q4&: u' > 0, w' < 0 \end{aligned} \tag{1.10}$$

where, Q1 and Q3 events are generally rare, weak events, Q2 events are ejections and Q4 events are sweeps (Coceal et. al., 2007a). Kellnerova et al. (2012) employed quadrant analysis to investigate the frequency and duration of sweep and ejection events. It was shown that within a 2D street canyon array at a height of $z/h = 1$ sweep events are more frequent, but shorter lived while ejections are less frequent with a longer duration (Kellnerova et. al., 2012). However, from DNS of a staggered cube array Coceal et al. (2007a) found that close to the obstacle fewer sweeps contributed more to the mean shear stress than more frequent ejections agreeing with the work of Castro et al. (2006) who conducted wind tunnel experiments of a staggered cube array. Away from the wall the opposite was found with fewer ejections contributing more to the Reynolds stresses (Coceal et al., 2007a). It was also shown through analysis of their spatial distribution that these events don't occur randomly throughout the boundary layer, but tend to occur in groups over a wide range of scales (Coceal et al., 2007a).

As discussed above regions of low momentum have been shown to influence pollutant concentration within 3D and 2D canopies (Michioka and Sato, 2012; Michioka et al., 2014). Wind tunnel experiments of an aligned cube array showed that large-scale upward flushing motions or ejections, which act to ventilate the canopy, are correlated with low momentum regions occurring above the canopy (Takimoto et al., 2011). Inagaki et al. (2012) used LES to model an aligned cube array and found that ejection events within the shear layer tend to occur beneath areas of low momentum in the inertial sublayer. Since sweep events were concentrated along the axis of the street, cavity eddy events were used as an indicator and showed a weak tendency to occur beneath areas of high momentum. However, this weak tendency is likely due to the cavity eddy being a subordinate of the

sweep event. Thus, it is clear that low momentum and high momentum regions present within the overlying boundary layer have an important relationship with sweep and ejection events that occur within the canopy (Takimoto et al., 2011; Inagaki et al., 2012). What is still unknown is how the coherent structures, including hairpin vortices, low momentum regions and ejections, are organized within the boundary layer and how their interactions can be quantified.

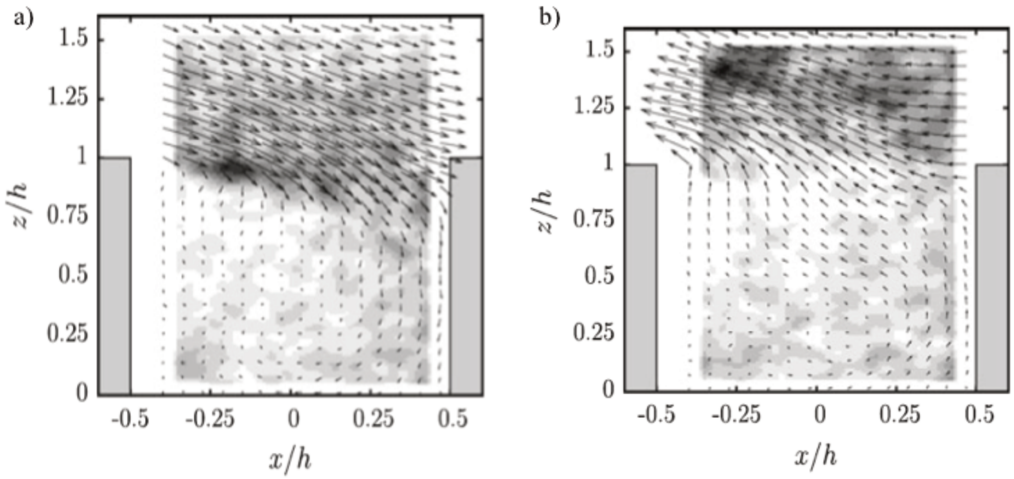

Figure 1.12. Example of phase averaged velocity fields corresponding to a) sweep event; b) ejection event. Where the approach flow is left to right, the arrows represent the velocity vectors and the contours are the phase-averaged swirling strength from white as zero to black as high value (Perret and Savory, 2013).

1.5.4 Organization of Coherent Structures

The transport of heat, momentum and pollutants from urban canopies has been shown to be a result of sweep and ejection events (Takimoto et al., 2011; Inagaki et al. 2012; Michioka and Sato, 2012; Michioka et al., 2014). The concept of organized groups of hairpin vortices has been discussed and has been shown to produce low momentum regions, which are in turn responsible for ejection events (Adrian et al., 2000; Coceal et al., 2007b). Therefore, understanding the organization of these coherent groups and their relationship to one another is crucial to understanding the ventilation of urban areas.

Of particular interest is the interaction between the shear layer and the overlying boundary layer as this interaction is believed to govern momentum transport between the urban canopy and the flow above (Perret and Savory, 2013). Examining the momentum

flux across the canopy it is clear that the turbulent momentum, such as that from sweep and ejection events, accounts for the majority of all momentum transport (Inagaki et al., 2012). Furthermore, it is shown that momentum transfer between the canopy and the overlying boundary layer is primarily due to a coupling between large-scale low and high momentum regions in the overlying boundary layer and the structure of the shear layer. To verify, the relationship between sweep and ejection events and the overlying boundary layer was investigated by Perret and Savory (2013) through conditional averages of the swirling strength. Conditional averages based on sweep or ejection events within the shear layer showed a high correlation with clockwise rotating vortices, however when using a reference location within the overlying boundary layer the swirling strength was found to be independent of the events suggesting the events are mainly driven by the shear layer dynamics. POD analysis was used to link the large-scale structures within the overlying boundary layer to the flow within the canopy and it was found that the large-scale structures are linked, non-linearly, to the intermittent flow in the canopy (Perret and Savory, 2013). In agreement with those of Salizzoni et al. (2011), these results suggest there is a coupling between the overlying boundary layer and the shear layer, which then drives the production of intermittent sweep and ejection events (Perret and Savory, 2013).

In summary, the transport of pollutants within urban canopies can be conceptually described by Figure 1.13 (Coceal et al., 2007b). This figure shows three regions, the first is turbulent organized structures along with hairpin vortices within the inertial layer above the canopy (dark blue and dark red). The Q2 or ejection and Q4 or sweep events in this region are responsible for the intermittent exchange of pollutants between the canopy and the overlying boundary layer. The second region is a strong shear layer that forms along the top of the upstream obstacle (white) and the third is a recirculation region within the canopy (black). These three regions interact to influence the ventilation of the canopy. This is only a simplified conceptual model and does not fully describe the complexity of the flow, but acts to give a qualitative summary of the flow structures that play a role in the ventilation of urban canopies. The ventilation governs the overall air quality of an urban environment. Thus, it is important to study the roles and relationships between the turbulent structures and processes that govern the ventilation of urban areas quantitatively.

1.6 Summary

Air quality is a significant concern for human health, particularly in urban areas where there is a substantial increase in air pollution emissions (World Health Organization, 2014). Although much work has been devoted to investigating the urban boundary layer using field experiments, wind tunnel experiments and numerical models such as LES, the fundamental processes governing the transport of heat, momentum and pollution are still poorly understood. Specifically, the coherent structures such as, low momentum regions and hairpin vortices, have been well identified qualitatively, but the quantitative relationships governing the interactions between scales are still unknown. In the present work the relationships between coherent structures will be studied quantitatively by first, within Chapter 4, studying the non-linear relationship between low and high momentum regions and the small-scale structures close to the roughness. Chapter 5 will expand the investigation of this non-linear relationship to street canyon flow. Within Chapter 6, the TKE budget, including dissipation, will be quantified to determine which coherent structures are most important to energy production and dissipation. Finally, the link between the non-linear relationship between large- and small-scales and energy transfer between those scales will be investigated quantitatively to determine how the organization of coherent structures relates to energy transfer. The following chapter will describe the experimental campaign undertaken to study these fundamental flow dynamics in the urban boundary layer.

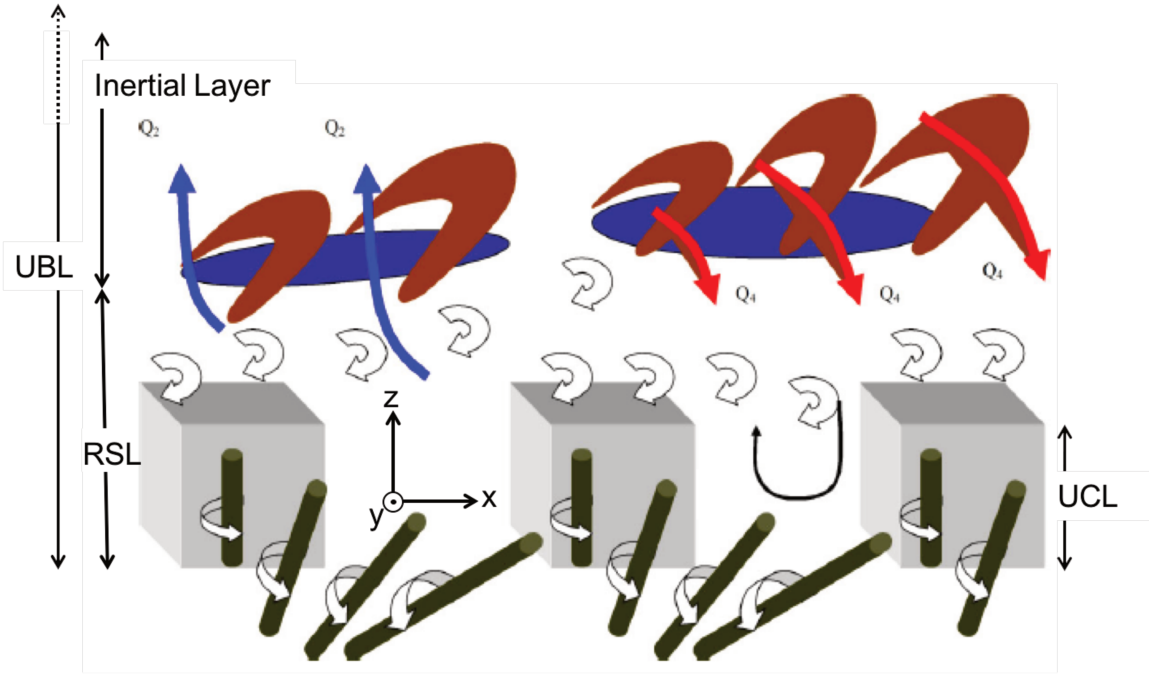

Figure 1.13. Conceptual cartoon summarizing the unsteady flow dynamics above and within street canyons. Above the canyon turbulent organized structures in the form of low momentum regions (dark blue) and hairpin vortices (dark red) dominate transport. Q2 is an ejection event and Q4 is a sweep event. Eddies (dark green) are shed off of the vertical sides of the building. A shear layer (white) is created by eddies forming along the roof of the building, which drives the recirculation zone (black) within the canyon (Coceal et al., 2007b).

Résumé du Chapitre 2: Détails expérimentaux

Ce chapitre décrit les campagnes expérimentales en soufflerie et les données qui ont été utilisées pour les analyses réalisées dans le cadre de cette thèse. La soufflerie du LHEEA est présentée, ainsi que la description des cas d'étude et les techniques de mesures. Enfin, les principales caractéristiques de la couche limite urbaine modélisée en soufflerie sont présentées. Un résumé (en français) de ce chapitre est proposé ci-après.

Les expériences ont été menées dans une soufflerie à couche limite atmosphérique, à aspiration basse et à faible vitesse. Les dimensions des sections de travail sont de 2 m en largeur, 2 m en hauteur et 24 m en longueur. Le développement de la couche limite est initié à l'aide de cinq générateurs de turbulence verticaux de 800 mm situées immédiatement en aval du convergent, et suivis d'une barrière solide de 200 mm située 750 mm en aval. Ces générateurs de turbulence sont ensuite suivis par des éléments de rugosité disposés sur le plancher de la soufflerie. Les expériences ont été effectuées avec une vitesse d'écoulement libre $\overline{U}_\infty$ = 5.8 m/s.

Au total, 7 configurations de rugosité ont été étudiées dans le cadre de la thèse. La première consiste en une canopée de cubes décalés de hauteur 50 mm et de densité surfacique $\lambda_p = 25\%$. Les configurations restantes ont été conçues pour étudier l'écoulement de la rue canyon. La région initiale de cubes décalés de 50 mm avec $\lambda_p = 25\%$ s'étend de 1 m à 14 m en aval de l'entrée. La dernière partie de la soufflerie en amont de la zone d'étude (entre 14 m et 19 m) est couverte soit par des cubes de 50 mm disposés en quinconce avec $\lambda_p = 25\%$, soit par des barres bidimensionnelles de hauteur h= 50 mm qui couvrent la largeur de la soufflerie, avec un espacement entre éléments de $1h$ ($\lambda_p = 50\%$) ou $3h$ ($\lambda_p = 25\%$). Dans ces configurations d'écoulement, une rue canyon de hauteur $h = 50$ mm et de longueur L = $30h$ est située à 19.5 m en aval de l'entrée de la soufflerie. Le rapport d'aspect de la rue est $W/h = 1$ ou 3. Chaque largeur de rue canyon a été étudiée en combinaison avec les 3 configurations de rugosité amont, donnant au total 6 configurations de rue canyon étudiées.

Les mesures de vitesse dans toutes les configurations décrites ci-dessus ont été effectuées en utilisant un système de Vélocimétrie par Image de Particules de Dantec (PIV) en configuration stéréoscopique et situé sous le plancher de la soufflerie pour mesurer les trois composantes de la vitesse. Les particules d'ensemencement constituées de gouttelettes d'eau glycol et générées à l'aide d'un générateur de fumée commercial sont éclairées par une nappe lumineuse générée par un laser Nd-YAG double cavité Litron (2 200 mJ). Deux caméras CCD 2048 × 2048 équipées chacune d'un objectif sont utilisées pour capturer des images. Dans plusieurs des configurations, une sonde anémomètre à fil chaud (HWA) a permis de mesurer la vitesse à une hauteur de $4h$ et à une fréquence de 10 kHz pour obtenir les informations temporelles de l'écoulement au-dessus de la canopée.

Les caractéristiques de la couche limite calculées à l'aide de la mesure PIV dans chaque type de rugosité montrent que la configuration de rugosité, que ce soit 3D ou 2D, et λ_p ont un impact significatif sur les statistiques de turbulence. Les trois couches limites ont un skewness de vitesse longitudinale, verticale et transversale similaire. Dans le présent travail, les trois couches limites présentent un fort skewness longitudinal positif et un skewness vertical négatif dans la couche de cisaillement, qui est lié à des événements de balayage fort (Brunet et al., 1994). Ces événements dominent le transport dans la couche de cisaillement, mais au-dessus, des éjections commencent à régir le transport. Les similitudes entre les profils de skewness des trois couches limites suggèrent que la nature du mécanisme régissant le transport reste la même.

2 Experimental Details

The following chapter describes the experimental campaigns used for the analysis of the present work. The two campaigns were completed as part of the requirements for a PhD thesis (Rivet, 2014) and a MESc thesis (Blackman, 2014). First a detailed description of the wind tunnel is presented, followed by a description of the roughness configurations used, the measurement techniques employed and finally, the boundary layer characteristics.

2.1 Boundary Layer Wind Tunnel

The experiments were conducted in a low-speed, suction type boundary layer wind tunnel with working section dimensions of 2 m (width) × 2 m (height) × 24 m (length) and a 5:1 ratio inlet condition. The wind tunnel has a wind speed range of 3-10 m/s and within the empty wind tunnel there is a freestream turbulence intensity of 0.5% with spanwise uniformity to within ±5% (Savory et al., 2013). Boundary layer development was initiated using five 800 mm vertical tapered spires located immediately downstream of the contraction followed by a 200 mm solid fence located 750 mm downstream of the spires (Figure 2.1). These turbulence generators were then followed by the roughness elements whose configurations are described in the following section. The experiments were performed with a freestream velocity $\overline{U}_\infty = 5.8$ m/s measured with a pitot-static tube 15 m downstream of the inlet at a height of $z = 1.5$ m at the centre of the wind tunnel.

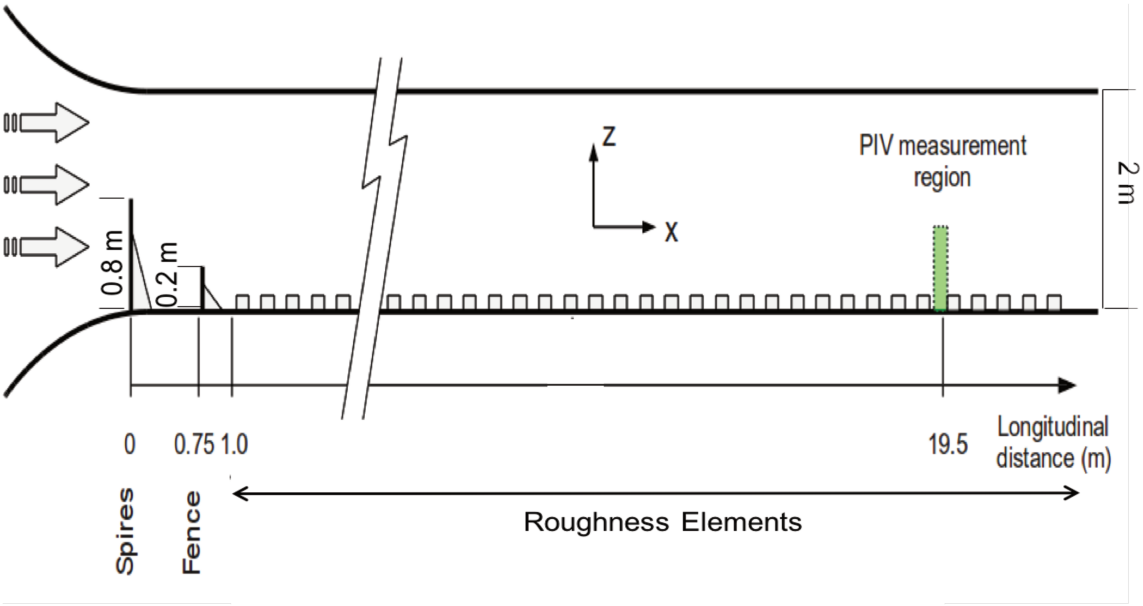

Figure 2.1. Wind tunnel set-up.

2.2 Roughness Configurations

In total 7 roughness configurations were studied in the present work. The first consisted of a staggered cube array with roughness height of 50 mm and packing density, $\lambda_p =$ 25% starting from 1 m downstream of the wind tunnel inlet (Figure 2.2a). The remaining configurations, which were designed to study street canyon flow, consisted of an initial fetch of 50 mm staggered cubes with $\lambda_p = 25\%$ from 1 m to 14 m downstream of the inlet. The last portion of the wind tunnel floor was covered by either 50 mm cubes arranged in a staggered array with $\lambda_p = 25\%$ (Figure 2.2b) or 50 mm square section, two-dimensional (2D) bars that spanned the width of the tunnel, with an element spacing of either $1h$ ($\lambda_p = 50\%$) (Figure 2.2c) or $3h$ ($\lambda_p = 25\%$) (Figure 2.2d). Within these flow configurations a street canyon of length L $= 30h$ and height h $=$ 50 mm was located 19.5 m downstream of the wind tunnel inlet and had an aspect ratio (AR $=$ W/h) of 1 or 3. Each street canyon width was studied using the 3 upstream roughness configurations giving a total of 6 street canyon configurations. The measurement canyons are referred to as Cnh with n = 1 or 3, and the upstream roughness (Rm) is staggered cubes (m = cu) or 2D bars with m = 1h or 3h.

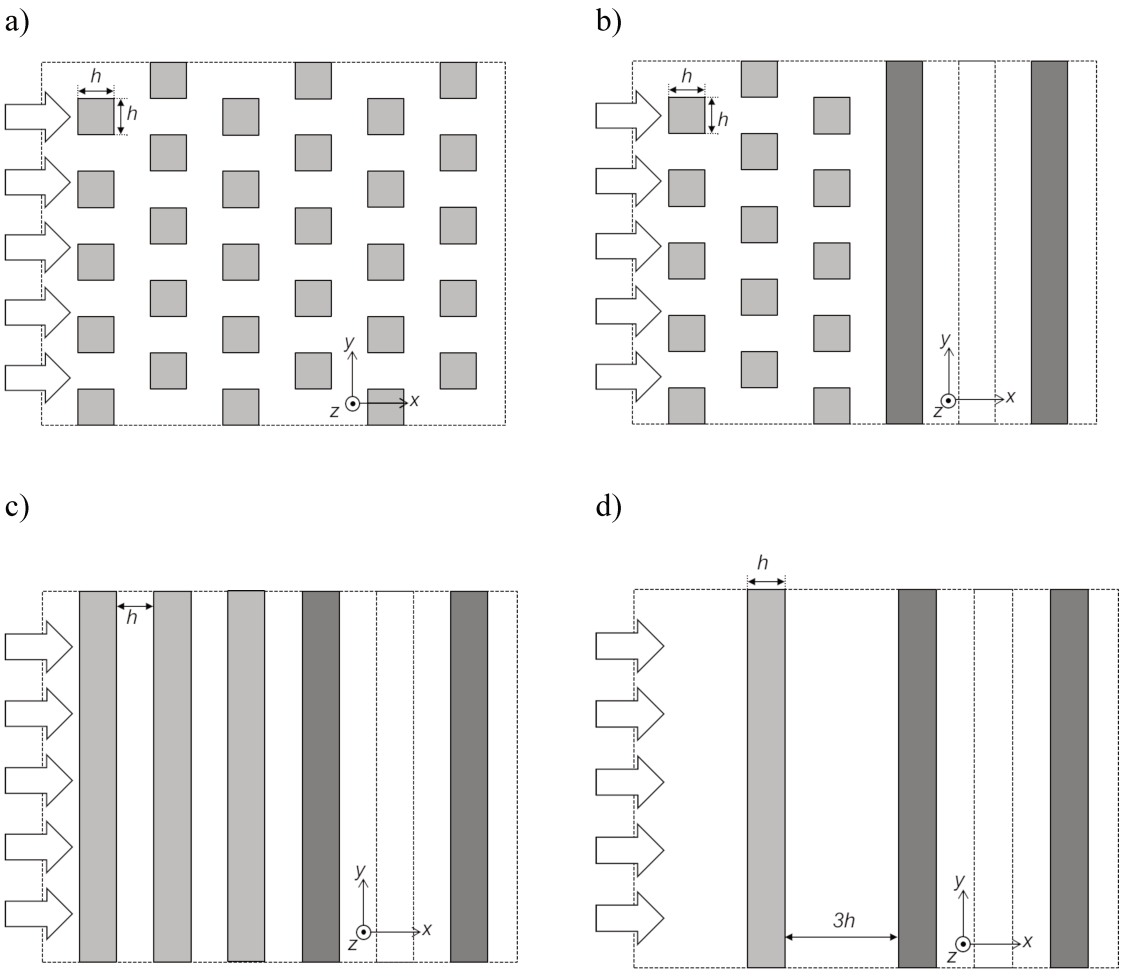

Figure 2.2. Canyon and roughness configurations a) Rcu; b) C1hRcu and C3hRcu; c) C1hR1h and C3hR1h; d) C1hR3h and C3hR3h.

2.3 Measurement Techniques

2.3.1 Particle Image Velocimetry

The flow measurements in all 7 roughness configurations described above were conducted using a Dantec Particle Image Velocimetry (PIV) system located under the wind tunnel floor and set up in stereoscopic configuration to measure all three components of velocity. Seeding particles consisting of water-glycol droplets generated using a commercially available smoke generator were introduced just downstream of the wind tunnel contraction to ensure proper seeding of the lower part of the boundary layer and had a diameter with distribution mean of 1 μm. To illuminate the particles a light

sheet generated by a Litron double cavity Nd-YAG laser (2 × 200 mJ) was used along with two CCD 2048 × 2048 cameras each equipped with an objective lens to capture images. Both the laser and the cameras were located beneath the wind tunnel floor where a glass panel allowed for the passage of light. Two camera configurations were used depending on the alignment of the laser sheet and are shown in Figure 2.3 below for streamwise aligned (Figure 2.3a) and spanwise aligned (Figure 2.3b) PIV measurements. The synchronization of the cameras and laser was controlled using Dantec Dynamic Studio software, which was also used to perform the PIV analysis of the recorded images described below. The PIV measurement plane extent and location in each of the roughness configurations studied in the present work is also presented below.

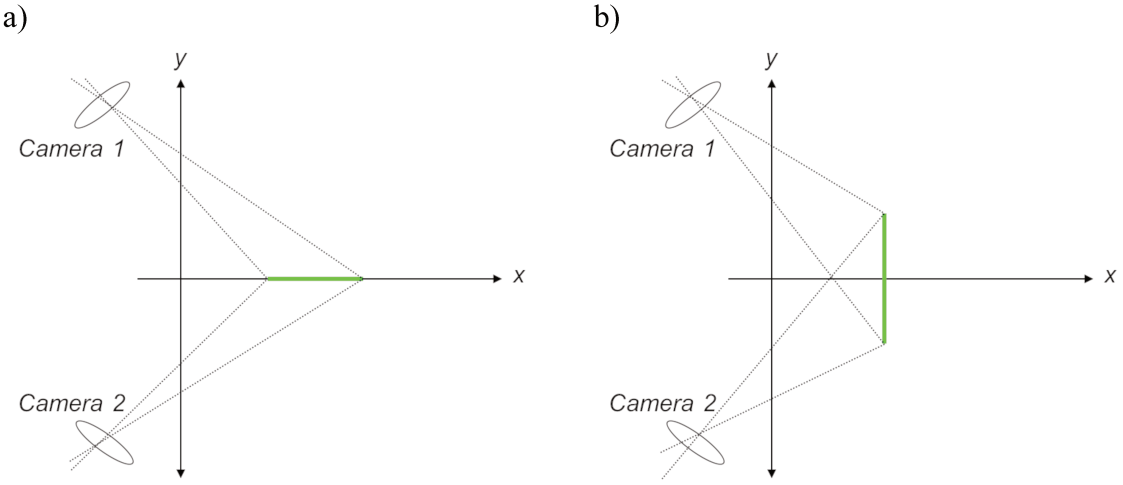

Figure 2.3. Wind tunnel stereoscopic PIV camera set-up of a) streamwise aligned measurements and b) spanwise aligned measurements with PIV measurement region (—).

Three measurement sets were conducted within the Rcu configuration. The first and second were conducted in a vertical plane aligned in the streamwise direction with a width of either $1h$ (Figure 2.4a) or $3h$ (Figure 2.4b) and a height of $5h$. The third consisted of three parallel, vertical planes aligned with the spanwise flow direction at three locations in the streamwise direction, $x/h = 0.7$, 1 and 1.3 downstream of a cube obstacle (Figure 2.4c). The measurements of each of the planes were performed separately allowing for the computation of mean statistical gradients of all three velocity components. Of these measurements the first was completed by Blackman (2014) as part of the requirements for a MESc thesis (Figure 2.4a) while the remaining two were completed by Rivet (2014) as part of the requirements for a PhD thesis (Figure 2.4b,c).

Each of the measurement configurations were conducted to study different flow phenomena within a staggered cube array. The first configuration (Figure 2.4a) combines spatially resolved PIV measurements and temporally resolved Hot-Wire Anemometry (HWA) measurements, which are detailed below, to study the non-linear interactions between large- and small-scales, which is described in Chapter 4. The second configuration (Figure 2.4b) along with the spanwise aligned measurements (Figure 2.4c) are used to study the Turbulent Kinetic Energy (TKE) budget, which is described in Chapter 6, as they provide large spatial extent and the mean velocity gradients required for the computation of the budget.

Within the six street canyon configurations a vertical plane aligned with the streamwise direction was used to measure velocity at the centre of the street canyon (Figure 2.5). The velocity fields had a width of either $1h$ or $3h$ depending on the width of the street canyon and a height of $5h$. These configurations were performed as part of the requirements for a MESc thesis (Blackman, 2014) and used in the present work to determine the influence of the upstream roughness and canyon geometry on the non-linear interactions between large- and small-scales, which is detailed in Chapter 5.

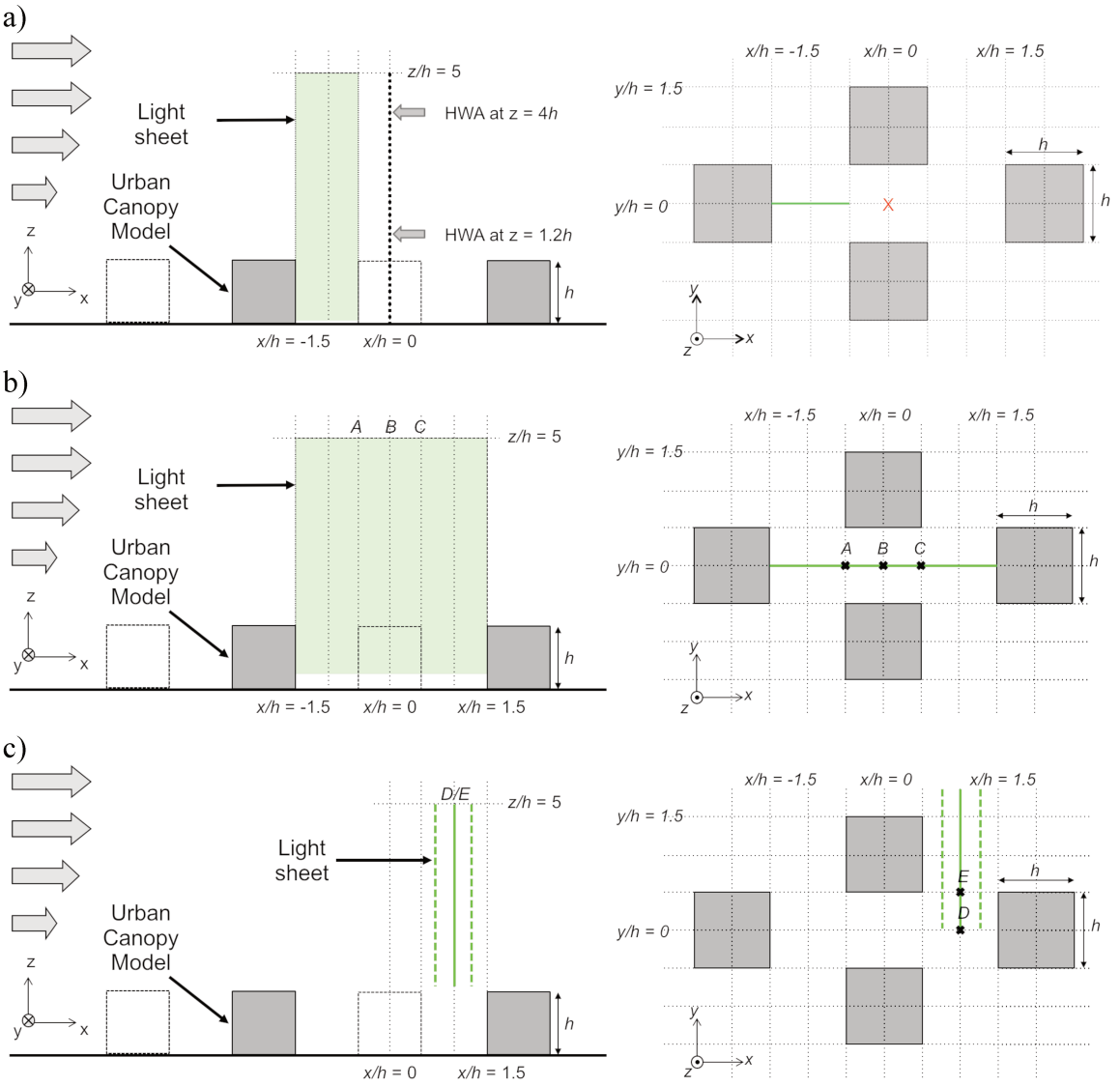

Figure 2.4. Side view (left column) and plan view (right column) of wind tunnel stereoscopic PIV set-up with PIV measurement region (—) and HWA (×) of a) streamwise aligned PIV measurements of width 1h; b) streamwise aligned PIV measurements of width 1h c) three parallel spanwise aligned PIV measurement regions.

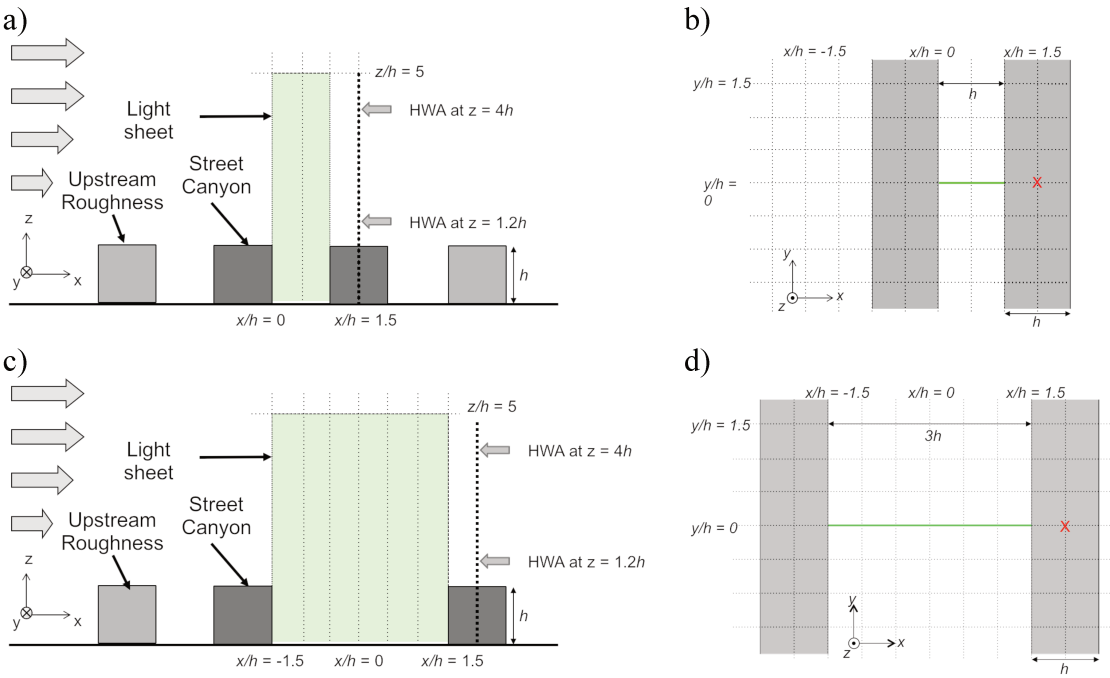

Figure 2.5. Wind tunnel stereoscopic PIV set-up of streamwise aligned street canyon measurements with PIV measurement region (—) and HWA (×) of C1h a) side view and b) plan view; C3h c) side view and d) plan view.

In all 7 configurations, the final 3-component velocity fields were obtained by first using a multi-pass adaptive correlation algorithm to compute the 2-component vector fields from each camera. These were performed with an initial interrogation window size of 256 × 256 to a final interrogation window size of either 16 × 16 or 32 × 32 (see Table 2.1) with an overlap of 50%. To avoid any peak locking and allow for accurate displacement estimation a subpixel refinement was used. Using a pinhole camera model these two-component vector fields were then combined using stereoscopic PIV to obtain three-component vector fields. Other experimental details such as the frequency between pairs of pulses of the laser, time-delay between two images of the same pair, number of pairs of images recorded and final spatial resolution of the measurements are listed in Table 2.1.

Table 2.1. PIV measurement details

	Plane	PIV width	Camera lens	Frequency (Hz)	Time delay (μs)	Images	Resolution mm^2	Final Interrogation Window
Rcu	x-z	$1h$[1]	60	7	400	5000	0.83×1.68	16×16
	x-z	$3h$[2]	105	5	400	4000	1.7×2.2	32×32
	y-z	$2h$[2]			200	4000	3.1×1.9	
C1h	x-z	$1h$[1]	60	7	400	5000	0.83×1.68	16×16
C3h	x-z	$3h$[1]	60	7	400	5000	0.83×1.68	16×16

[1]Data from Blackman (2014).
[2]Data from Rivet (2014).

2.3.2 Hot-Wire Anemometry

Within the street canyon configurations (Figure 2.5) and the staggered cube configuration with PIV width of $1h$ (Figure 2.4a) described above two hot-wire anemometer probes measured the velocity at heights of $1.2h$ and $4h$. These measurements were conducted at a frequency of 10 kHz to obtain temporal information of the flow. The HWA used was a single platinum-plated tungsten wire Dantec SSP11 sensor of diameter 5 μm and length 1.25 mm with straight prongs. The HWA had a 235 mm long straight probe support with diameter of 4 mm operated in constant temperature mode using two DISA 55M05 conditioners. To allow for accurate correlation these measurements were conducted at the same time and synchronized with the PIV system using the camera-triggering signal from the timer board of the PIV system recorded at the same time as the HWA signal.

2.4 Boundary layer characteristics

In the present work the turbulence quantities are defined as follows. The instantaneous velocity components in the x, y and z directions are streamwise (U), spanwise (V) and vertical (W), respectively. Ensemble averages are denoted as $\overline{\ }$, the standard deviation of the velocity is $\sigma_u = \left(\overline{(U(t)-\overline{U})^2}\right)^{1/2}$ and the shear stress is $\overline{u'w'} = \overline{(U(t)-\overline{U})*(W(t)-\overline{W})}$. Spatial averages, denoted as $\langle\ \rangle$, are used to reduce the

variability and applied after computation of the statistics. For instance, $\langle \sigma_u^3 \rangle = \langle \left(\overline{(U(t) - \overline{U})^2} \right)^{3/2} \rangle$.

Figure 2.6 shows the boundary layer profiles of the three roughness configurations (Rcu, R1h and R3h) including mean streamwise velocity, streamwise, vertical and spanwise standard deviation, shear stress $\overline{u'w'}$ and streamwise, vertical and spanwise skewness. Within Figure 2.6 the shaded areas represent the 99% confidence interval using the standard deviations of the main PIV statistics due to statistical error, which are listed for a height of $z/h = 3$ in Table 2.2 for each roughness configuration studied in the present work. These were estimated using the assumption of a normal distribution and the number of independent samples, considering that a time separation of two integral time scales between two samples is needed to ensure their independence (Tropea et al., 2007).

Table 2.2. Standard deviation of PIV statistics due to statistical error.

	Samples	$\overline{U}$ (m/s)	σ_u (m/s)	σ_v (m/s)	σ_w (m/s)	$\overline{u'w'}$ (m/s)	$\overline{u'^3}/\sigma_u^3$	$\overline{v'^3}/\sigma_v^3$	$\overline{w'^3}/\sigma_w^3$
Rcu$^{\perp}$	2659	0.041	0.029	0.017	0.016	0.029	0.033	0.015	0.015
R1h	2788	0.012	0.012	0.010	0.006	0.009	0.024	0.012	0.009
R3h	1730	0.022	0.016	0.027	0.027	0.018	0.052	0.022	0.022

$^{\perp}$Computed from Rcu set-up in x-z plane with width of $1h$.

As shown in Figure 2.6 the thickness of the approaching boundary layer results in a large region of constant shear stress above the canopy (Figure 2.6e), which is seldom achieved in the literature (Castro et al., 2006). As discussed in Blackman et al. (2015a) the roughness configuration, whether 3D or 2D, and λ_p has a significant impact on the turbulence statistics. The skimming flow regime (R1h) is shown to increase $\overline{U}$, σ_u, σ_w and σ_v, while $\overline{u'w'}$ decreases compared to the wake interference regime (R3h). The 3D roughness (Rcu) falls between the skimming and wake interference flow regimes except

within the σ_w and σ_v profiles, which are similar to wake interference profiles. Interestingly, other than a difference in magnitude of the streamwise skewness within the shear layer, all three boundary layers have similar streamwise, vertical and spanwise skewness profiles. The skewness profiles can provide insight into momentum transfer events such as sweeps and ejections. In the present work, all three boundary layers exhibit strong positive streamwise skewness and negative vertical skewness within the shear layer, which has been previously linked to energetic downward sweeping events (Brunet et al., 1994). These events dominate transport within the shear layer but above $z/h = 2$ ejections start to govern transport. Although R1h exhibits a larger magnitude of skewness within the shear layer and, therefore, a larger relative strength of sweep events, the similarities between the skewness profiles of all three boundary layers suggest that the nature of the mechanism governing transport remains the same.

a)

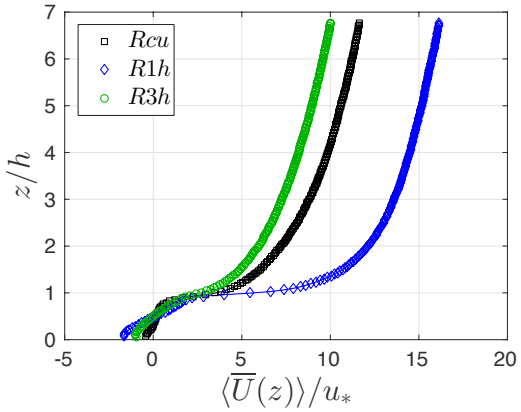
Rcu
R1h
R3h
z/h
⟨U(z)⟩/u*

b)

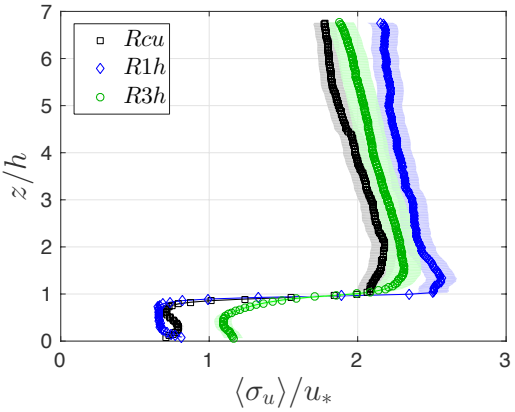
Rcu
R1h
R3h
z/h
⟨σu⟩/u*

c)

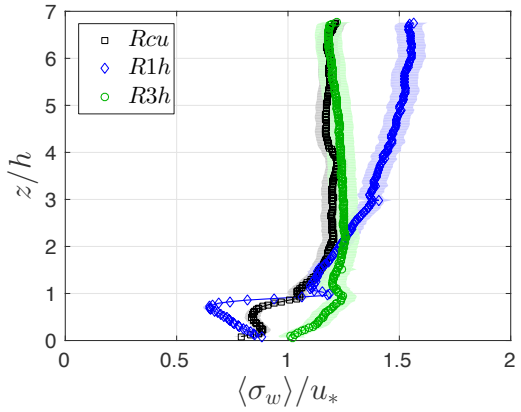
Rcu
R1h
R3h
z/h
⟨σw⟩/u*

d)

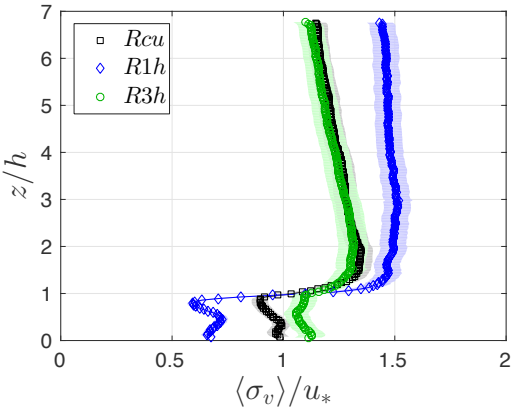
Rcu
R1h
R3h
z/h
⟨σv⟩/u*

e)

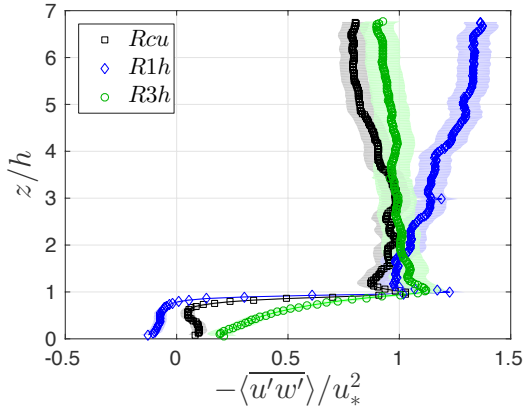
Rcu
R1h
R3h
z/h
−⟨u′w′⟩/u*²

f)

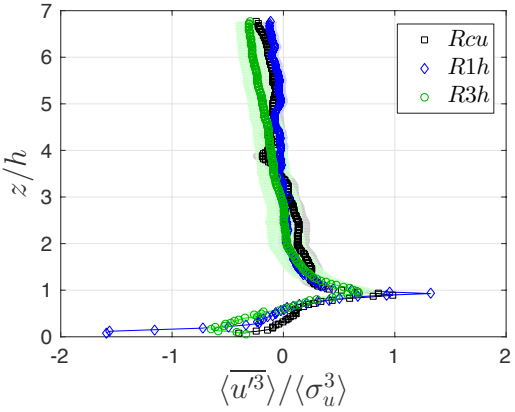
Rcu
R1h
R3h
z/h
⟨u′³⟩/⟨σu³⟩

g) h)

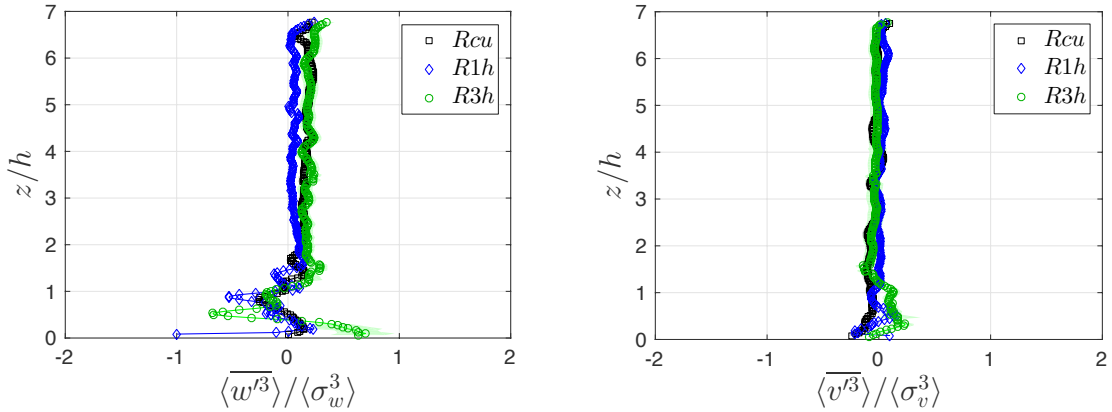

Figure 2.6. Spatially averaged PIV statistics a) mean streamwise velocity normalized by u_*; b) standard deviation of the streamwise velocity component; c) vertical component; d) spanwise component and e) shear stress normalized by u_* and f) skewness of the streamwise velocity component; g) vertical component and h) spanwise component.

Table 2.3 lists important flow and scaling parameters measured at $x = 19.5$ m except $\overline{U}_\infty$, which was measured at $x = 15$ m. The log law parameters z_o and d were determined by fitting the vertical streamwise velocity profile to the log law equation (Equation 1.7) while the friction velocity, u_*, was estimated from the vertical profile of the shear stress in the region of constant shear stress located just above the roughness height. The pressure gradient within the wind tunnel was tested using the Rcu roughness and found to be non-zero, but weak along the longitudinal direction in the boundary layer (Rivet, 2014). An indicator (K) is used to determine the importance of the pressure gradient,

$$K = -\frac{\nu}{\rho U_\infty^3}\frac{\partial P}{\partial x} \tag{2.1}$$

where ν is the kinematic viscosity and ρ is the density (DeGraaff and Eaton, 2000). For Rcu $K = 2.4\times10^{-8}$, therefore the pressure gradient is considered negligible for all roughness configurations (DeGraaff and Eaton, 2000).

Table 2.3 Scaling parameters.

	λ_p (%)	$u_*/\overline{U}_\infty$	$\overline{U}_\infty$ (m/s)	h (m)	δ (m)	Re_h^*	Re_δ (u_*)	d/h	z_o/h	$\partial P/\partial x$ (Pa m-1)
Rcu	25	0.064	5.800	0.050	0.975	$1.2\text{x}10^3$	2.4×10^4	0.900	0.061	-0.37
R1h	50	0.049				$1.2\text{x}10^3$		0.927	0.015	
R3h	25	0.070				$1.6\text{x}10^3$		0.725	0.125	

2.5 Summary

The present work uses data from two experimental campaigns completed as part of the requirements for a PhD thesis (Rivet, 2014) and a MESc thesis (Blackman, 2014). A combination of spatially resolved PIV and temporally resolved HWA measurements are used in Chapter 4 to study the non-linear interactions between large- and small-scales within a staggered cube array. This combined PIV and HWA set-up is then used within six street canyon configurations to determine the influence of upstream roughness and canyon geometry on the non-linear interaction, which is described in Chapter 5. The TKE budget is investigated in Chapter 6 using PIV measurements with a staggered cube array (Rivet, 2014) as they provide mean velocity gradients in three directions of space which are required for the computation of the budget. Finally, the combined PIV and HWA measurements within a staggered cube array are used to investigate the relationship between the non-linear interactions and energy transfer in Chapter 7. The following chapter will describe the Linear Stochastic Estimation (LSE) method that is applied using the combined spatially resolved PIV and temporally resolved HWA to decompose the flow and study the non-linear interactions.

Résumé du Chapitre 3: Méthodologie pour l'analyse des interactions multi-échelles

Le chapitre 3 présente la méthodologie utilisée pour étudier les interactions dynamiques entre les structures de grande échelle présentes dans la couche limite et les structures de plus petites échelles générées par les éléments de rugosités. Cette méthodologie, qui sera mise en œuvre pour les analyses présentées aux chapitres 4, 5 et 7 est brièvement résumée ici.

Pour étudier l'interaction entre les structures de différentes échelles qui existent dans une couche limite de paroi rugueuse, on utilise une décomposition triple. La décomposition triple a d'abord été introduite par Hussain (1983; 1986) pour étudier des structures cohérentes et est utilisée ici pour décomposer la vitesse instantanée (U) en la somme d'une moyenne temporelle ($\overline{U}$), d'une fluctuation de grande échelle (u'_L) et d'une fluctuation de petite échelle (u'_S).

Dans la couche limite de paroi lisse (Hutchins et Marusic, 2007; Mathis et al., 2009; Mathis et al., 2011a; Mathis et al., 2011b; Marusic et al., 2011; Inoue et al., 2012) et de paroi rugueuse (Nadeem et al., 2015; Squire et al., 2016), des interactions non linéaires ont pu être reliées à un mécanisme de modulation d'amplitude. L'analyse de la modulation d'amplitude selon la méthode proposée par Mathis et al. (2009a; 2011) nécessite d'avoir accès, conjointement et de façon bien résolue temporellement, à la dynamique de grande échelle dans la couche limite et aux signaux de petite échelle proche de la paroi. En raison des niveaux élevés de turbulence que l'on rencontre près des éléments de rugosité, l'anémométrie à fil chaud (Hot-Wire Anemometry, HWA) à proximité de la paroi n'est pas possible dans le présent travail. En outre, les mesures PIV réalisées dans le présent travail prés des éléments de rugosité ont une faible résolution temporelle. Par conséquent, une nouvelle approche utilisant l'estimation stochastique linéaire (LSE) est utilisée pour décomposer l'écoulement.

Dans la méthode de l'estimation stochastique montré en Figure 3.1, la vitesse fluctuante est calculée à chaque endroit d'intérêt à partir d'un coefficient et d'un signal de vitesse de

référence. Les coefficients sont déterminés à partir de la corrélation croisée du signal de référence et du signal de vitesse à l'endroit d'intérêt, ainsi que de l'auto-corrélation du signal de référence. Dans notre étude, la HWA, qui est située dans la couche limite supérieure à $z/h = 4$ avec une fréquence d'acquisition de 10 kHz, est utilisée pour capturer l'information de la couche limite, déterminer les coefficients et exécuter le modèle d'estimation stochastique. Tout d'abord, le signal HWA est filtré pour s'assurer que le signal de référence ne contient que des fluctuations à grande échelle et à basse fréquence. Les fluctuations à grande échelle filtrées (u'^{BL}_L) et le signal PIV proche de la rugosité sont ensuite utilisés pour déterminer les coefficients LSE (A^i_n). Un délai temporel est introduit dans ces corrélations pour préserver la séparation temporelle des événements conditionnels et inconditionnels. Une fois que les coefficients sont déterminés, ils sont utilisés avec le signal filtré de référence (u'^{BL}_L) pour prédire les fluctuations à grande échelle à proximité de la rugosité à une fréquence de 5 kHz.

3 Methodology for the analysis of scale interactions

The following chapter describes the Linear Stochastic Estimation (LSE) methodology that is used for the analysis of scale interactions in Chapters 4, 5, and 7. First an introduction is provided, followed by a detailed description of the LSE method used in the present work.

3.1 Introduction

To investigate the interactions between scales in a rough-wall boundary layer one must first separate the flow by scale, which can be done using triple decomposition. Triple decomposition was first introduced by Hussain (1983; 1986) to investigate coherent structures and is used here to decompose the instantaneous velocity (U) into a time-averaged mean ($\overline{U}$), large-scale fluctuations (u'_L) and small-scale fluctuations (u'_S) (Equation 3.1).

$$U = \overline{U} + u'_L + u'_S \tag{3.1}$$

Skewness, a third order statistic, can then be used to examine the non-linear interactions between scales in the flow. The third order moment can be decomposed as in Equation 3.2,

$$\overline{u'^3} = \overline{u'^3_L} + 3\overline{u'^2_L u'_S} + 3\overline{u'_L u'^2_S} + \overline{u'^3_S} \tag{3.2}$$

where $\overline{u'^3}$ becomes skewness once normalized by σ_u^3 and the cross-terms $\overline{u'_L u'^2_S}$ and $\overline{u'^2_L u'_S}$ represent the non-linear influence of the large-scales onto the small-scales and the small-scales onto the large-scales, respectively (Schlatter and Orlü, 2010; Mathis et al., 2011b).

Within the smooth-wall boundary layer (Hutchins and Marusic, 2007; Mathis et al., 2009; Mathis et al., 2011a; Mathis et al., 2011b; Marusic et al., 2011; Inoue et al., 2012) and rough-wall boundary layer (Nadeem et al., 2015; Squire et al., 2016) the non-linear interaction ($\overline{u'_L u'^2_S}$) has been linked to a mechanism of amplitude modulation. The amplitude modulation of the small-scales is described in Equation 3.3,

$$u'^{NW} = \hat{u}(1 + \beta u'^{BL}_L) + \alpha_{AM} u'^{BL}_L \tag{3.3}$$

where $\hat{u}$ is a universal signal of fluctuating velocity in the absence of any large-scale modulation, β is the coefficient of amplitude modulation and α_{AM} is the coefficient of superposition (Mathis et al., 2009, Mathis et al., 2011a).

Analysis of amplitude modulation using Equation 3.3 requires access to the temporally resolved large-scale boundary layer and near-wall small-scale signals. Due to the high levels of turbulence close to the roughness temporally resolved near-wall Hot-Wire Anemometry (HWA) is not feasible in the present work. Furthermore, classical methods used for triple decomposition, such as temporal and spatial filters, cannot be used as the PIV measurements are not temporally resolved and do not have a large spatial extent. Therefore, a novel approach using LSE described in the following section is used to decompose the flow.

3.2 Linear Stochastic Estimation

Stochastic Estimation was first introduced by Adrian (1977) as a method of approximation of the conditional averages in order to identify coherent structures in turbulent flows. Other researchers extended the method to include an estimation of the time-evolution of a two-dimensional (2D) velocity field by using the time history of an instantaneous signal such as velocity (Bonnet at al., 1994; Druault et al., 2004) or pressure (Picard and Delville, 2000; Naguib et al., 2001) as the condition. Recently, a novel application of Stochastic Estimation has been developed to combine field and wind tunnel measurements allowing for the detailed spatio-temporal analysis of the flow physics within a street-canyon immersed in the atmospheric boundary layer (Perret et al., 2016).

In the Stochastic Estimation method the fluctuating velocity ($\tilde{u}$) is calculated at each location of interest from a coefficient and a reference velocity signal (v) (Equation 3.4). The coefficients (A_i^n) are determined from the cross-correlation of the reference signal and the velocity signal at the location in space (x, y, z) that is to be predicted, as well as the auto-correlation of the reference signal (Equation 3.5). It has been shown by Tinney et al. (2006) that when the conditional event, in the present case the small-scale fluctuations close to the roughness, and unconditional source, large-scale momentum regions, are separated in time, spectral based coefficients should be used in the estimate to preserve this time separation. A similar method is employed in the present work where multi-time delay coefficients are used to preserve the time separation of events. The predictive model reference signals are time-lagged ($\Delta\tau$) and combined by summation of the velocity predictions from each reference location at each time (t), where N_{ref} is the number of reference locations and $2N_t+1$ is the number of time lags used.

$$\tilde{u}(x,y,z,t) = \sum_{i=1}^{N_{ref}} \sum_{m=-N_t}^{N_t} A_i^n v(x_i, y_i, z_i, t + m\Delta\tau) \tag{3.4}$$

$$\overline{\tilde{u}(x,y,z,t)v\left(x_j, y_j, z_j, t + m\Delta\tau\right)} = \sum_{i=1}^{N_{ref}} \sum_{n=-N_t}^{N_t} A_i^n \overline{v(x_i, y_i, z_i, t + n\Delta\tau)v(x_i, y_i, z_i, t + m\Delta\tau)}\,, j \in \left[1, N_{ref}\right], m \in [-N_t, N_t] \tag{3.5}$$

Considering amplitude modulation as described by Mathis et al. (2009) the near-wall turbulence (u'^{NW}) can be defined using a universal signal of fluctuating velocity ($\hat{u}$) which is the signal that would exist in the absence of any large-scale modulation and a large-scale signal from the overlying boundary layer ($u_L'^{BL}$) as well as a coefficient of superposition (α_{AM}) and coefficient of amplitude modulation (β) (Equation 3.3). In this case, the first half of the right-hand side of Equation 3.3 is equivalent to the small-scale fluctuation signal (u'_S) (Equation 3.6).

$$u'^{NW} = u'_S + \alpha_{AM} u_L'^{BL} \tag{3.6}$$

Multiplying both sides of this equation by u'^{BL}_L and ensemble-averaging we obtain the expression Equation 3.7. However, according to triple decomposition theory we know that the cross-correlation between large- and small-scales is zero and our final expression then becomes Equation 3.8 (Hussain, 1983; 1986). Thus, the coefficient α_{AM} can be determined from the cross-correlation between a near-wall signal and a large-scale signal within the overlying boundary layer and the auto-correlation of the large-scale signal.

$$\overline{u'^{NW}u'^{BL}_L} = \overline{u'_S u'^{BL}_L} + \alpha_{AM}\overline{u'^{BL^2}_L} \tag{3.7}$$

$$\overline{u'^{NW}u'^{BL}_L} = \alpha_{AM}\overline{u'^{BL^2}_L} \tag{3.8}$$

Equation 3.8 relates directly to the Stochastic Estimation method outlined in Equation 3.5 where a series of coefficients (A_i^n) are determined from the cross-correlation between a signal in the boundary layer (u'^{BL}_L, equivalent to v in Equation 3.5) and a near-wall signal (u'^{NW}, equivalent to $\tilde{u}$ in Equation 3.5) and the autocorrelation of the boundary layer signal. In the Stochastic Estimation method these coefficients are then used to calculate the fluctuating velocity at each location of interest (Equation 3.4). Therefore, Stochastic Estimation can be used to determine the large-scale component of the near the wall signal (u'^{NW}_L) using a series of coefficients (α_{AM}) as in Equation 3.9.

$$u'^{NW}_L = \alpha_{AM}u'^{BL}_L \tag{3.9}$$

In the present work a HWA located within the overlying boundary layer at $z/h = 4$ (Figure 2.4 and Figure 2.5) with an acquisition frequency of 10 kHz is used to capture the information from the boundary layer, determine the coefficients (A_i^n, Equation 3.5) and run the Stochastic Estimation model (Equation 3.4). The Stochastic Estimation process used to decompose the flow is outlined in Figure 3.1. First, the HWA signal is low-pass filtered to ensure the reference signal contains only low frequency, large-scale fluctuations (u'^{BL}_L). This ensures that the large-scale fluctuations predicted by the model will be uncorrelated with the small-scales, thus in agreement with the method of Mathis et al. (2009) and triple decomposition (Hussain, 1983; 1986) as outlined above.

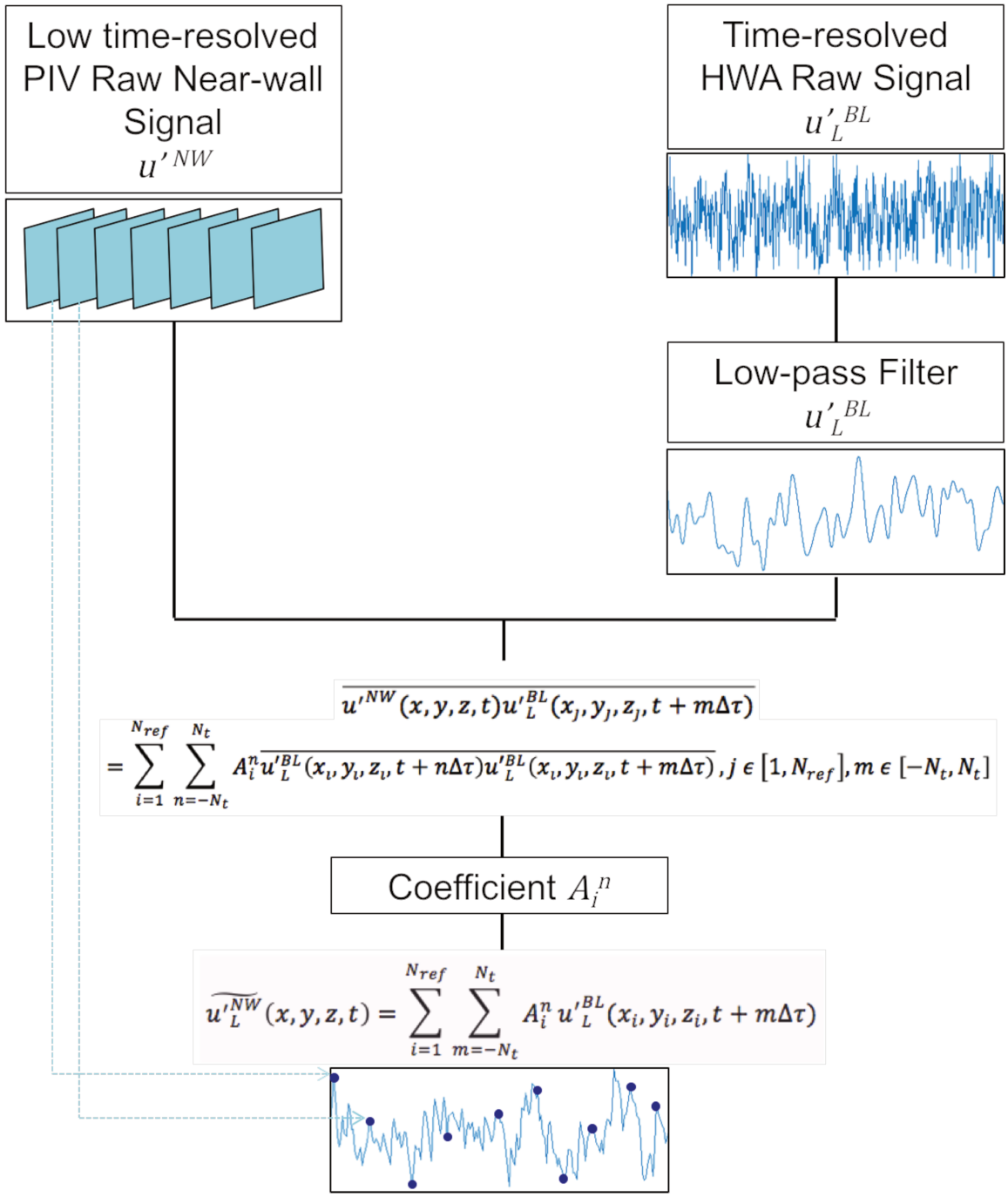

Figure 3.1. Schematic of process used for Stochastic Estimation decomposition.

The cut-off wavelength for the filter is determined for each roughness configuration separately. For the Rcu case HWA measurements conducted by Rivet (2014) at various heights within the boundary layer are used to calculate the spectra of streamwise velocity. The cut-off wavelength is chosen so as to separate the most energetic scales present in the logarithmic layer ($z = 4h$) and those near the canopy (Figure 3.2). This method

corresponds to the method used by Mathis et al. (2009) and results in the same cut-off wavelength of $\ell_c = \delta$ or approximately 20h. The peak spectral energy of the near-wall fluctuations in the present work differs significantly from that of Nadeem et al. (2015) who used sparsely spaced 2D roughness. In the present work this peak occurs at $z/h = 0.975$ whereas in the 2D rough-wall boundary layer it occurs at $z/h = 0.286$, a difference of 70% (Nadeem et al., 2015). However, the inner peak of the present work occurs on the edge of the HWA measurement region, thus, the actual location may be lower. In the case of the R1h and R3h configurations the cut-off wavelength for the filter was determined from the spectra of streamwise velocity at heights $z = 1.2h$ and $z = 4h$ measured in each boundary layer (Figure 2.5) as full HWA measurements were not available. This results in a cut-off wavelength of approximately $\ell_c = 31h$ and $24h$ for the R1h and R3h configurations, respectively. The differences in cut-off wavelength between configurations are a result of the spectral composition of the flow, thus, the skimming flow regime (R1h) is shown to have larger structures compared to the wake interference regime (Rcu and R3h).

The low-pass filtered large-scale fluctuations ($u_L'^{BL}$) and the raw near-wall PIV signal (u'^{NW}) are then used to determine the LSE coefficients (A_i^n) (Equation 3.10).

$$\overline{u'^{NW}(x,y,z,t)u_L'^{BL}\left(x_j,y_j,z_j,t+m\Delta\tau\right)} = \sum_{i=1}^{N_{ref}}\sum_{n=-N_t}^{N_t} A_i^n \overline{u_L'^{BL}(x_\iota,y_\iota,z_\iota,t+n\Delta\tau)u_L'^{BL}(x_\iota,y_\iota,z_\iota,t+m\Delta\tau)}, j \in [1,N_{ref}], m \in [-N_t,N_t] \quad (3.10)$$

A time-delay is introduced to these correlations to preserve the time separation of the conditional and unconditional events so that each coefficient represents the correlation between events at a specific instance in time. In the present work a time-delay of $\Delta\tau = 0.1$s is used for the Rcu configuration while $\Delta\tau = 0.2$s is used for the R1h and R3h configurations. This modification is required to prevent the production of a mathematically singular matrix which cannot be inversed for use in the LSE model. The time delays must be sufficiently separated within the correlation used to produce the matrix to capture both the correlation peaks and valleys. In all configurations a time-lag

with a maximum delay of t = -1s to 1s is introduced to these correlations to fully capture the time separation of the conditional and unconditional events.

Once the coefficients are determined they are used along with the reference low-pass signal u'^{BL}_L to predict the large-scale near-wall fluctuations ($\widetilde{u'^{NW}_L}$ or $\widetilde{u'_L}$) through summation of the velocity predictions at each location in time (Equation 3.11).

$$\widetilde{u'^{NW}_L}(x,y,z,t) = \sum_{i=1}^{N_{ref}} \sum_{m=-N_t}^{N_t} A_i^n u'^{BL}_L(x_i, y_i, z_i, t + m\Delta\tau) \tag{3.11}$$

In the present work this process is used to predict the large-scale component of both the streamwise and vertical fluctuating velocities at each location within the canopy and roughness sub-layer up to a height of $z/h = 3$ to include the roughness sub-layer and the beginning of the inertial layer where important scale interactions are expected to occur.

The spanwise velocity fluctuations are not predicted using this method as the PIV measurements are performed in the symmetry plane of a cube (in the spanwise direction) resulting in a statistically homogeneous flow in the spanwise direction. The positive and negative contributions of the fluctuating spanwise component v' to cross-statistics (such as $\langle\overline{u'v'}\rangle$) or odd-order moments of v' cancel each other out from a statistical point of view, therefore, the cross-correlation between a streamwise velocity in the overlying boundary layer and the spanwise velocity in the roughness sublayer will be zero. This renders the Stochastic Estimation ineffective for decomposing the spanwise velocity and is a shortcoming of the model proposed in the present work.

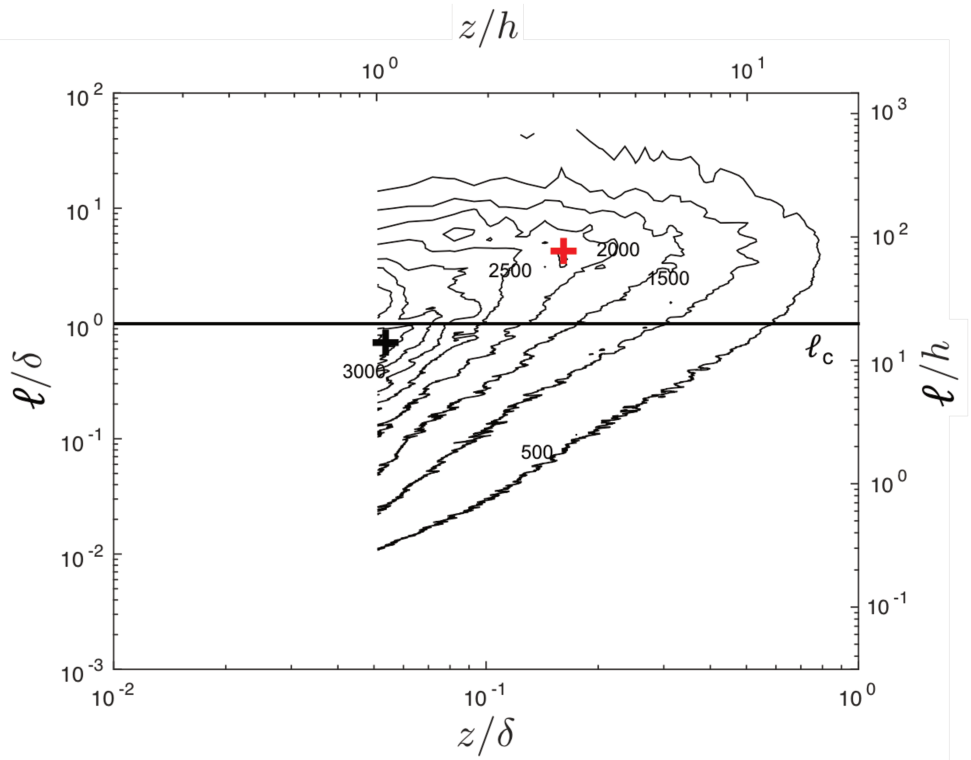

Figure 3.2. Spectra of streamwise velocity fluctuations $k\phi_{uu}/u_*^2$ measured in Rcu configuration and shown in contour representation where + marks the outer peak at $z/\delta = 0.16$, $\ell/\delta = 3.90$, + marks the inner peak at $z/\delta = 0.05$, $\ell/\delta = 0.57$ and the black line shows the location of the spectral filter (ℓ_c/δ).

3.3 Summary

Previous work in the smooth-wall (Hutchins and Marusic, 2007; Mathis et al., 2009; Mathis et al., 2011a; Mathis et al., 2011b; Marusic et al., 2011; Inoue et al., 2012) and rough-wall (Nadeem et al., 2015; Squire et al., 2016) boundary layers has linked non-linear interactions to amplitude modulation. However, previous work has relied on temporally resolved large-scale boundary layer and near-wall small-scale signals to investigate these non-linear interactions (Mathis et al., 2009). As temporally resolved near-wall measurements are not feasible in the present work a novel LSE approach is used to decompose the flow. In the following chapter this approach will be applied to a staggered cube array to investigate the non-linear interactions between large-scales within the overlying boundary layer and small-scales induced by the presence of the roughness.

Résumé du Chapitre 4: Interactions non linéaires entre une canopée de cubes et la couche limite au-dessus

Le Chapitre 4 présente les résultats de l'analyse réalisée en utilisant la décomposition triple et le modèle d'estimation stochastique décrits au chapitre 3. L'étude porte sur les relations non-linaires entre les structures de grande échelle présentes dans la couche limite et les petites structures générées par les rugosités dans la configuration d'une canopée de cubes. Un résumé (en français) de ce chapitre est proposé ci-après.

La couche limite turbulente qui se développe sur une paroi rugueuse ou une zone urbaine contient des structures cohérentes complexes qui consistent en: 1) des structures organisées turbulentes à grande échelle de basse ou haute vitesse qui se situent au-dessus des éléments de rugosité dans la sous-couche inertielle et qui proviennent de groupes de tourbillons en épingle à cheveux; 2) des couches de cisaillement qui se forment dans la sous-couche de rugosité le long de la partie haute des éléments de rugosité et contiennent des structures à petite échelle induites par la présence de la rugosité; 3) des zones de recirculation dans la couche de canopée. De plus, des événements turbulents intermittents, tels que les éjections (Q2: $u' < 0$ et $w' > 0$) et les balayages (Q4: $u' > 0$ et $w' < 0$), qui agissent pour ventiler la canopée urbaine se produisent à l'interface entre la couche canopée et la couche inertielle.

Dans la couche limite urbaine, ces structures dans la sous-couche de rugosité et dans la couche inertielle ainsi que leurs interactions sont particulièrement intéressantes car elles régissent le transport de chaleur, de quantité de mouvement et de pollution (Takimoto et al., 2011; Perret et Savory, 2013). Bien que ces structures aient été bien identifiées qualitativement (Coceal et al., 2007; Lee et al., 2011; 2012; Inagaki et Kanda, 2008; 2010), la relation quantitative entre les régions de basse ou haute vitesse et les petites échelles induites par la présence de la rugosité n'est pas entièrement comprise (Perret et Savory, 2013).

Les travaux antérieurs portant sur la couche limite en paroi rugueuse ont montré grâce à la décomposition triple que les interactions entre les régions de basse ou haute vitesse et les petites échelles induites par la présence de la rugosité induisent une influence (non linéaire) des grandes échelles sur les petites échelles de l'écoulement (Perret et Rivet, 2013). En outre, la preuve d'une rétroaction des petites échelles sur les grandes échelles a également été mise en évidence (Perret et Rivet, 2013). Pour la couche limite en paroi lisse, l'influence non linéaire des grandes échelles s'est révélée être un mécanisme de modulation d'amplitude (Mathis et al., 2009). En outre, une étude récente en simulation directe (DNS) pour la couche limite en paroi rugueuse a établi que, bien que le comportement quantitatif de la modulation diffère de celui de la couche limite de paroi lisse, la nature du mécanisme reste la même (Nadeem et al., 2015).

L'analyse proposée est basée sur les données expérimentales obtenues pour une couche limite en paroi rugueuse consistant en un réseau de cubes décalés, avec un nombre de Reynolds élevé (le nombre de Reynolds, basé sur l'épaisseur de la couche limite δ et la vitesse de frottement u_*, est $\mathrm{Re}_\delta = 2.4 \times 10^4$) et des propriétés de turbulence similaires à celles d'une couche limite urbaine, afin de répondre aux questions spécifiques suivantes:

1) La relation non linéaire entre les structures de grande échelle de la sous-couche inertielle et les structures de petite échelle de la sous-couche rugueux peut-elle être quantifiée lorsque l'information temporelle des petites échelles proches de la paroi n'est pas disponible?
2) Est-ce que la relation non linéaire est régie par le même mécanisme de modulation d'amplitude que dans la couche limite de paroi lisse?
3) Quelle est l'influence qualitative des éléments de rugosité sur cette relation non linéaire?

En raison des contraintes de mesure, les informations temporelles des petites échelles proches de la paroi ne sont pas disponibles et les méthodes traditionnelles telles que le filtrage spatial et temporel ne peuvent pas être utilisées pour décomposer l'écoulement en grandes et petites échelles. Au lieu de cela, le modèle d'estimation stochastique décrit au chapitre 3 est utilisé. Les fluctuations prédites par le modèle stochastique montrent qu'elles excluent les petites échelles à l'intérieur de la canopée et contiennent plutôt des

structures de grande échelle qui traversent plusieurs fois la hauteur de la couche limite. En outre, l'évolution temporelle des fluctuations prédites ressemble à des régions à grande échelle à basse et haute vitesse. Ainsi, les fluctuations prédites peuvent être considérées comme des fluctuations de grande échelle alors que les fluctuations restantes contiennent les petites échelles.

Le coefficient d'asymétrie (ou skewness), décomposé en utilisant les fluctuations de petite échelle (u'_S) et de grande échelle (u'_L) peut être utilisé pour étudier la relation non linéaire entre grandes et petites échelles. Il présente un niveau maximum dans la couche de cisaillement se formant en aval d'un obstacle cubique, qui est principalement dû à des fluctuations de petite échelle ($\overline{u'^3_S}$). Ceci suggère que ces échelles sont les principales responsables des mouvements de balayage les plus intenses dans cette région. La quantité $\overline{u'^3_S}$ devient négative au-dessus de la couche de cisaillement, et présente des similitudes avec le profil du coefficient d'asymétrie d'une couche de mélange, ce qui correspond aux résultats de travaux antérieurs (Perret et Rivet, 2013).

Les grandes échelles contribuent pour une partie négligeable au coefficient d'asymétrie dans toute la couche limite, tandis que le terme croisé $\overline{\widetilde{u'}_L u'^2_S}$ contribue de manière significative à l'asymétrie avec un maximum se situant juste au-dessus de la couche de cisaillement, à $z/h = 1.5$. Le terme $\overline{\widetilde{u'}_L u'^2_S}$ représente l'interaction non linéaire entre les grandes échelles et les petites échelles et pourrait suggérer un mécanisme descendant, tel que la modulation d'amplitude. En outre, dans le présent travail, les interactions non linéaires entre les grandes régions de basse ou haute vitesse et les fluctuations transversale ($\overline{\widetilde{u'}_L v'^2}$) et verticales ($\overline{\widetilde{u'}_L w'^2}$) sont similaires à $\overline{\widetilde{u'}_L u'^2_S}$, ce qui indique que les régions à grande échelle de basse ou haute vitesse dans la couche limite influencent les petites échelles par une interaction non linéaire des trois composantes de la vitesse.

Le modèle d'estimation stochastique utilisé dans le présent travail, qui s'appuie sur la haute résolution temporelle permise par les mesures HWA, permet une extrapolation temporelle des fluctuations de vitesse. Les interactions d'échelle peuvent ainsi être également étudiées temporellement sans avoir accès au signal temporel à petite échelle

proche de la rugosité. Grâce aux corrélations temporelles et spatiales, une vision qualitative des interactions non linéaires peut être décrite. Les régions de basse ou haute vitesse dans la couche limite sont légèrement inclinées. À partir d'une corrélation spatio-temporelle, nous constatons un angle d'inclinaison (θ) d'environ 11.5^{o}, confirmant que les structures à grande échelle inclinées de basse ou haute vitesse dans la couche logarithmique laissent leur empreinte sur les petites échelles près de la surface par une relation non linéaire. La structure inclinée se déplaçant dans la couche limite, elle passe sur les structures à petite échelle proches de la rugosité. Ainsi, les structures à petite échelle rencontrent les effets de la structure à grande échelle qui est située légèrement en aval de leur position. Plus l'emplacement de la référence à grande échelle est élevé, plus la distance entre la structure à petite échelle et la région de basse ou haute vitesse augmente, ce qui entraîne une augmentation du délai de corrélation maximale.

Les résultats des analyses de décomposition du coefficient d'asymétrie et de la corrélation fournissent les preuves quantitatives d'un mécanisme descendant d'interaction non linéaire depuis la couche limite vers l'intérieur de la paroi rugueuse. La méthode de filtrage par le modèle d'estimation stochastique (LSE) utilisée ici fournit des informations spatio-temporelles, ce qui améliore notre compréhension de la nature des interactions non linéaires. Les résultats concordent bien, qualitativement, avec ceux trouvés dans la couche limite de paroi lisse (Mathis et al., 2009) et pourraient suggérer un mécanisme de modulation d'amplitude.

Les principales conclusions de ce travail sont les suivantes :

1) Etant donné que des mesures temporelles proches de la rugosité ne sont pas directement accessibles avec le dispositif PIV utilisé, l'estimation stochastique linéaire (LSE) est utilisée pour décomposer l'écoulement. La décomposition du coefficient d'asymétrie a confirmé que, dans la région proche de la paroi rugueuse, les interactions entre échelles se produisent selon un mécanisme non linéaire illustré par le terme $\overline{\widetilde{u'_L}u'^2_S}$, ce qui représente l'influence non linéaire des grandes échelles sur les petites échelles. Le terme non linéaire, $\overline{\widetilde{u'^2_L}u'_S}$, qui représente l'influence des petites échelles sur les grandes échelles, a été jugé

négligeable. Il a été démontré que l'interaction non linéaire se produit au travers des trois composantes de la vitesse de manière similaire.

La méthode LSE appliquée ici permet d'analyser les corrélations spatio-temporelles des grandes et petites échelles, sans pour autant avoir accès au signal temporel à petite échelle proche de la rugosité. La corrélation temporelle du terme non linéaire $\overline{\widetilde{u'}_L u'^2_S}$ a démontré quantitativement que les régions de basse ou haute vitesse à grande échelle influencent les petites échelles dans toute la couche limite, ce qui correspond bien aux résultats de l'étude DNS de la couche limite de paroi rugueuse par Nadeem et al. (2015).

2) Les valeurs positives de la corrélation spatio-temporelle en deux points confirment qu'un mécanisme non linéaire descendant similaire à la modulation d'amplitude existe dans la couche limite de paroi rugueuse de même que dans les configurations de paroi lisse.
3) La méthode LSE actuelle à retard multi-temps contribue à améliorer notre compréhension du mécanisme non linéaire de modulation d'amplitude dans la couche limite de paroi rugueuse par des corrélations spatio-temporelles qui permettent d'identifier la nature des structures impliquées. La présence des éléments de rugosité, qui créent une recirculation de l'écoulement dans la canopée, se traduit par une corrélation spatio-temporelle négative entre les fluctuations à grande échelle et à petite échelle près de la paroi, modifiant ainsi l'interaction non linéaire.

4 Non-linear interactions between a cube canopy and the overlying boundary layer

The following chapter is work that was published as an article in Physics of Fluids on the non-linear relationship between large-scale structures present in the overlying boundary layer and small-scales close to the roughness (Blackman, K., Perret, L., "Non-linear interactions in a boundary layer developing over an array of cubes using stochastic estimation," Phys Fluid 28, 095108 (2016)). This work was completed using data from combined Particle Image Velocimetry (PIV) and Hot-Wire Anemometry (HWA) measurements within a staggered cube array (Rcu) as described in Chapter 2 (Figure 2.4a) and by using the Linear Stochastic Estimation (LSE) method as explained in Chapter 3. First an introduction to the topic is provided, followed by the results including characteristics of the fluctuations predicted by the Stochastic Estimation model and non-linear scale interactions and finally, conclusions.

4.1 Introduction

As detailed in Chapter 1 the turbulent boundary layer developing over a rough wall or urban area contains the canopy layer that ranges from the ground to roughly the height of the roughness elements and is part of the roughness sub-layer (Rotach et al., 2005). The depth of the roughness sub-layer depends on the density and height of the roughness elements and is followed by the inertial layer where the turbulence contains large-scale structures that are influenced by the surface characteristics (Rotach et al., 2005). Within these regions the flow is comprised of complex coherent structures that have been identified through Direct Numerical Simulation (DNS) (Coceal et al., 2007a; 2007b; Lee et al., 2011; 2012), wind tunnel experiments (Castro et al., 2006, Takimoto et al., 2013) and field experiments (Inagaki and Kanda, 2008; 2010). As discussed in Chapter 1 these coherent structures consist of 1) large-scale turbulent organized structures of either high

or low momentum that form well above the roughness in the inertial layer from groups of hairpin vortices; 2) shear layers that form within the roughness sub-layer along the top of the upstream roughness elements and contain small-scale structures induced by the presence of the roughness; and 3) a recirculation region within the canopy layer (Figure 1.13) (Coceal et al., 2007b). As well, intermittent turbulent events, such as ejections (Q2: $u' < 0$ and $w' > 0$) and sweeps (Q4: $u' > 0$ and $w' < 0$), that act to ventilate the urban canopy occur between the canopy layer and inertial layer. In the urban boundary layer these structures within the roughness sub-layer and inertial layer and their interactions are of particular interest as they govern the transport of heat, momentum and pollution (Takimoto et al., 2011; Perret and Savory, 2013). Although these structures have been well identified qualitatively (Coceal et al., 2007b; Lee et al., 2011; 2012; Inagaki and Kanda, 2008; 2010) the quantitative relationship between the large-scale momentum regions and the small-scales induced by the presence of the roughness is not fully understood (Perret and Savory, 2013). The present review and work will focus on the roughness sub-layer and beginning of the inertial layer, as this is where scale interactions important to the ventilation of urban areas are expected to occur.

As described in Chapter 3 the investigation of scale interactions requires the use of triple decomposition to separate the instantaneous velocity (U) into a time-averaged mean ($\overline{U}$), large-scale fluctuations (u'_L) and small-scale fluctuations (u'_S) as in Equation 3.1 (Hussain, 1983; 1986). Several methods have been used to identify and separate large-scale fluctuations within the rough-wall boundary layer such as Proper Orthogonal Decomposition (Perret and Rivet, 2013), wavelength spectral filtering (Nadeem et al., 2015) and spatial filtering (Inagaki and Kanda, 2010; Castillo et al., 2011). Perret and Rivet (2013) used Proper Orthogonal Decomposition (POD) to decompose the flow over a staggered cube array with plan area packing density (λ_p) of 25% in a configuration identical to the Rcu roughness studied here. The first mode was found to represent the large-scale momentum regions, which contributed 55% and 70% to the streamwise velocity variance ($\overline{u'u'}$) and shear stress ($\overline{u'w'}$), respectively, within the boundary layer, but closer to the canopy had low contribution. This is supported by Castillo et al. (2011) who used Large-Eddy Simulation (LES) to model the flow over an aligned cube array

with $\lambda_p = 25\%$. They found that the majority of $\overline{u'u'}$, approximately 90%, was due to small-scales at $z/h < 2$. For $z/h > 2$ the contribution of the large-scales gradually increased with height in the boundary layer to approximately 75% at $z/h = 3$. Inagaki and Kanda (2008; 2010) used moving average spatial filtering within an array of aligned cubes with $\lambda_p = 25\%$ immersed in the near-neutral atmospheric boundary layer and decomposed the flow into active (u'_S) and inactive turbulence (u'_L). The filter size for inactive turbulence was chosen to be equal to the boundary layer thickness, which agrees with the filter size used in the present work as detailed in Chapter 3. The authors stated that active turbulence is responsible for vertical transport and momentum transfer while inactive turbulence is not. The inactive turbulence was found to contain very large streaks of low momentum suggesting that these inactive structures are large-scale. Finally, Inagaki and Kanda (2008; 2010) showed that u'_S contributes the majority, approximately 60%, 90% and 90%, to $\overline{u'u'}$, $\overline{w'w'}$and $\overline{u'w'}$, respectively, within the roughness sub-layer at a height of $z/h = 2$.

As discussed in Chapter 3 decomposed skewness (Equation 3.2) can be used to investigate non-linear interactions between large- and small-scales (Schlatter and Orlü, 2010; Mathis et al., 2011b). Skewness decomposition analysis was first performed within the smooth-wall boundary layer in one experimental study by Mathis et al. (2011b). The small-scales were found to account for the majority, approximately 90%, of the skewness within the region of peak skewness close to the wall. The cross-term $\overline{u'_L u'^2_S}$, which represents the influence of the large-scales onto the small-scales, was found to be non-negligible, while the cross-term $\overline{u'^2_L u'_S}$, which represents the influence of the small-scales onto the large-scales, was negligible (Mathis et al., 2011b).

Within the smooth-wall boundary layer the non-linear interaction ($\overline{u'_L u'^2_S}$) has been linked to a mechanism of amplitude modulation (Hutchins and Marusic, 2007; Mathis et al., 2009; Mathis et al., 2011a; Mathis et al., 2011b; Marusic et al., 2011; Inoue et al., 2012). Previous work investigating amplitude modulation found that when large-scale momentum structures within the overlying boundary layer exhibit high streamwise turbulent fluctuations or high momentum, small-scale turbulent fluctuations near the wall

will have higher amplitude. Similarly, when large-scale low momentum structures are present the small-scale fluctuations near the wall will be suppressed (Mathis et al., 2009). Thus, as outlined in Equation 3.3 in Chapter 3 the near wall velocity (u'^{NW}), which contains small-scale structures, is influenced by the large-scale low or high momentum regions in the overlying boundary layer ($u_L'^{BL}$).

Amplitude modulation within the smooth-wall boundary layer has been shown to increase with increasing Reynolds number (Re) as large-scale structures become more turbulent thereby contributing more to turbulent interactions at higher Re (Mathis et al., 2009). It has also been shown that all three components of velocity are modulated in a similar manner (Talluru et al., 2014). Furthermore, the amplitude modulation coefficient has been shown to be related to the skewness, confirming that skewness can be used to investigate the non-linear interaction between scales (Schlatter and Orlu, 2010). Finally, the study of amplitude modulation within the smooth-wall boundary layer has been extended and applied to the develop a predictive model for u'^{NW} using $u_L'^{BL}$ (Mathis et al., 2011a; Inoue et al., 2012). This allows for prediction of the small-scales without direct measurement, which is useful when measurements in this region are difficult to obtain.

The flow structure in smooth-wall boundary layers differs significantly from that of rough-wall boundary layers. Furthermore, the nature of the roughness, whether d-type or k-type (Jimenez, 2004) and two-dimensional (2D) or three-dimensional (3D), will also have an important influence on the structure of the boundary layer. However, the coherent structures, such as momentum regions and hairpin vortices, present in d-type and k-type rough-wall boundary layers have been shown to be qualitatively similar to those found in the smooth-wall boundary layer (Volino et al., 2007). Volino et al. (2007) compared a smooth-wall boundary layer with a rough-wall boundary layer generated using a 3D mesh and found hairpin vortices accompanied by large-scale momentum regions in both cases. Takimoto et al. (2013) investigated flows over a 3D aligned cube array with $\lambda_p = 25\%$, a 2D bar array with $\lambda_p = 50\%$ and a smooth-wall. The scaling laws applied to large-scale turbulence or low momentum regions showed independence of the coherent structures from the wall roughness. This supports the top down theory, which

states that the nature of the roughness only affects the boundary conditions, not the nature of the turbulence in the inertial sub-layer (Takimoto et al., 2013). When comparing rough-wall boundary layers generated using 2D bars with $\lambda_p = 25\%$ and 3D cubes with $\lambda_p = 12.5\%$ with a smooth-wall boundary layer Lee et al. (2011; 2012) found similar patterns of large-scale low momentum regions and hairpin vortices in smooth and 2D rough walls. However, in 3D rough walls the hairpin vortices are accompanied by large packets of ejections (Q2) identified through quadrant analysis. These ejections intensify the large-scale momentum regions causing shorter length scales throughout the entire boundary layer (Lee et al., 2011; 2012). Due to the existence of qualitatively similar coherent structures in the rough-wall boundary layer, methods used to investigate scale interactions in the smooth-wall boundary layer can be applied to the rough-wall boundary layer as well.

Only one previous study has used skewness decomposition to investigate scale-interactions in the k-type rough-wall boundary layer and the results agreed qualitatively with the results from the smooth-wall boundary layer (Mathis et al., 2011a; Mathis et al., 2011b; Perret and Rivet, 2013). Using skewness decomposition Perret and Rivet (2013) showed that $\overline{u'^3_L}$ has a negligible influence within the canopy, whereas $\overline{u'^3_S}$ contributes significantly, approximately 55%, specifically in the region of peak skewness within the shear layer generated by the roughness elements. The profile of this term was also shown to exhibit features similar to a mixing layer with positive values found on the low speed side and negative values found on the high-speed side of the shear layer. Consistent with the results in the smooth-wall boundary layer, the cross term $\overline{u'_L u'^2_S}$ contributed 50% within the region of peak skewness within the shear layer, which demonstrates the existence of a non-linear interaction between the large- and small-scales in the flow. The value of $\overline{u'^2_L u'_S}$, although small within the shear layer, was shown to be non-zero, which suggests the existence of a feedback interaction of the small-scales onto the large-scales. This term became significant at a height of $z/h = 2.5$ when it contributed 50% to the skewness. In the smooth-wall boundary layer this term was shown to be negligible throughout the boundary layer, thus suggesting that the presence of the roughness induces a feedback mechanism from the small-scales to the large-scales within the flow (Perret

and Rivet, 2013). Finally, analysis by Perret and Rivet (2013) using the cross terms of u'_L with spanwise (v') and vertical (w') fluctuations showed profiles similar to the cross term $\overline{u'_L u'^2_S}$, illustrating that the interaction of the large- and small-scales involves all three components of velocity through the same type of non-linear mechanism. This supports the amplitude modulation results of Talluru et al. (2014) who state that all three components of velocity are modulated in a similar manner.

Evidence of amplitude modulation in the rough-wall boundary layer has been studied using DNS of a d-type 2D bar roughened wall with $\lambda_p = 12.5\%$, aspect ratio $(W/h) = 8$ and $\mathrm{Re}_\delta = 3.1 \times 10^3$ (Nadeem et al., 2015). In order to overcome the relationship between the amplitude modulation coefficient and the skewness a method of amplitude modulation covariance was used to describe the interaction (Bernardini and Pirozzoli, 2011; Nadeem et al., 2015). The presence of the roughness caused a wall-normal shift in the position of the peak spectral energy of the near-wall small-scales from $z/\delta = 0.005$ in a smooth-wall boundary layer to $z/\delta = 0.0135$ in a rough boundary layer. As a result, the amplitude modulation behaviour in both the near-wall and outer-wall regions was changed. The large-scale structures in the outer region were modified and interacted with both the near-wall small-scales and small-scales throughout the boundary layer (Nadeem et al., 2015). The investigation of non-linear interactions using the predictive model outlined by Mathis et al. (2011a) has been expanded to the study of a sand-roughened wall (Squire et al., 2016) and this predictive model has recently been improved using Spectral LSE to eliminate the need of user inputted scale separation (Baars et al., 2016). Using the predictive model it was found that, when compared to a smooth-wall boundary layer, the linear interaction or superposition was weaker in the rough-wall despite the large-scale structures in both boundary layers having similar shape and extent (Squire et al., 2016). The amplitude modulation within the rough-wall was found to be stronger suggesting that the small-scales generated by the presence of the roughness contribute significantly to this phenomenon. This agrees with the results from a LES study of homogenous roughness that found stronger amplitude modulation in the roughness sublayer of the homogenous roughness than in the log region of the smooth-wall (Anderson, 2016). Furthermore, a time-lag between the passage of a large-scale structure

and the suppression or amplification of the small-scales close to the roughness was observed and found to be related to advection. The study of a heterogeneous roughness consisting of staggered cubes with $\lambda_p = 25\%$ revealed significant spatial variation of the amplitude modulation, but correlations used to measure the strength of the amplitude modulation were found to be significant within each region.

The relationship between large-scale momentum regions and small-scale structures induced by the presence of the roughness in the rough-wall boundary layer remains unclear. Through triple decomposition it has been shown that this relationship is a non-linear influence of the large-scales onto the small-scales in the flow (Perret and Rivet, 2013). Furthermore, evidence of a feedback of the small-scales onto the large-scales has also been indicated (Perret and Rivet, 2013). Within the smooth-wall boundary layer the non-linear influence of the large-scales has been shown to be a mechanism of amplitude modulation (Mathis et al., 2009). Additionally, recent numerical (Nadeem et al., 2015; Anderson, 2016;) and experimental (Squire et al., 2016) studies in the rough-wall boundary layer have established that, although the quantitative behaviour of the modulation differs from that of a smooth-wall boundary layer, the nature of the mechanism remains the same. Although there is limited work on the topic within the literature evidence suggests that both k-type and d-type rough-wall boundary layers experience a non-linear interaction between large- and small-scales similar to that in the smooth-wall boundary layer. The present work aims to use experimental evidence from a rough k-type boundary layer consisting of a staggered cube array with high Reynolds number and turbulence properties similar to an urban boundary layer to answer the following specific questions:

1) Can the non-linear relationship between large-scale structures in the inertial layer and small-scale structures induced by the presence of the roughness in the roughness sub-layer be quantified when temporal information of the near wall small-scales is not available?
2) Is the non-linear relationship governed by the same mechanism of amplitude modulation as found in the smooth-wall boundary layer?

3) What is the qualitative influence of the roughness elements on this non-linear relationship?

In the present work the investigation will focus on the roughness sub-layer and beginning of the inertial layer in the area directly behind a roughness obstacle, as this is where the small-scale structures of the shear layer form through interaction with the roughness. The present work is focused on the investigation of a single flow mechanism; as such detailed analysis of the 3D flow structure including quadrant analysis is not included as it is out of the scope of the present work.

The cube-roughened boundary layer has been well-studied experimentally within the literature with λ_p ranging from 6.25% (Macdonald, 2000; Macdonald et al., 1998; 2002; Cheng and Castro, 2002) to 44% (Takimoto et al., 2011). Typically, these studies focus on the mean flow characteristics and turbulence statistics, such as mean velocity, turbulence intensity and shear stress, within and above the cube roughness (Blackman, 2014; Blackman et al., 2015a). Some work has extended this analysis to include two-point statistics and correlations to investigate the characteristics of sweep and ejection events that occur within the shear layer (Takimoto et al., 2011). Rivet (2014) used spatially resolved flow measurements to study the small-scale vortical structures present within the shear layer, in particular the separation distance between consecutive structures. However, temporal information of these structures is limited as no previous experimental work has conducted temporally resolved flow measurements within a cube roughness and its shear layer. The highly turbulent nature of these regions makes traditional measurement techniques such as HWA unreliable (Tutu and Chevray, 1975; Tagawa et al., 1992; Djenidi et al., 2014). Numerical methods such as DNS can provide temporal information of the small-scale structures, but computational limitations prevent the modeling of large Re flows such as the urban boundary layer (Lee et al., 2011; 2012). Therefore, traditional filtering methods, such as spectral filtering used by Mathis et al. (2011a), cannot be applied to a high Re cube-roughened wall boundary layer. The present experimental work at high Re number relies on LSE as described in Chapter 3 to decompose the flow into large and small-scale fluctuations, as temporal information within the shear layer is not available.

The following section will comprise the results and discussion including characteristics of the predicted and remaining fluctuations and scale interactions, followed by the conclusions.

4.2 Results and Discussion

4.2.1 Characteristics of predicted and remaining fluctuations

The LSE methodology outlined in Chapter 3 was used to predict the near-wall velocity fluctuations ($\widetilde{u'_L}$) using a large-scale boundary layer reference signal (u'^{BL}_L) measured above the Rcu roughness (Chapter 2). To assess the characteristics of the predicted velocity fluctuations the mean turbulence statistics are first compared to the mean statistics of the original PIV velocity fields (u') and the remaining fluctuations (u'_S) (Figure 4.1). As in Chapter 2 the shaded areas represent the 99% confidence interval using the standard deviations of the main PIV statistics due to statistical error. The standard deviation of the streamwise velocity, σ_u, computed using the predicted velocity fluctuations ($\widetilde{u'_L}$) shows underestimation throughout the canopy and boundary layer (Figure 4.1a). The model particularly under predicts the region of strong streamwise fluctuations within the shear layer by approximately 75%. This trend continues in the standard deviation of the vertical velocity, σ_w, which is underestimated by more than 80% within the shear layer (Figure 4.1b) and the Reynolds shear stress, $\overline{u'w'}$, which is underestimated within the roughness sub-layer by 90% (Figure 4.1c).

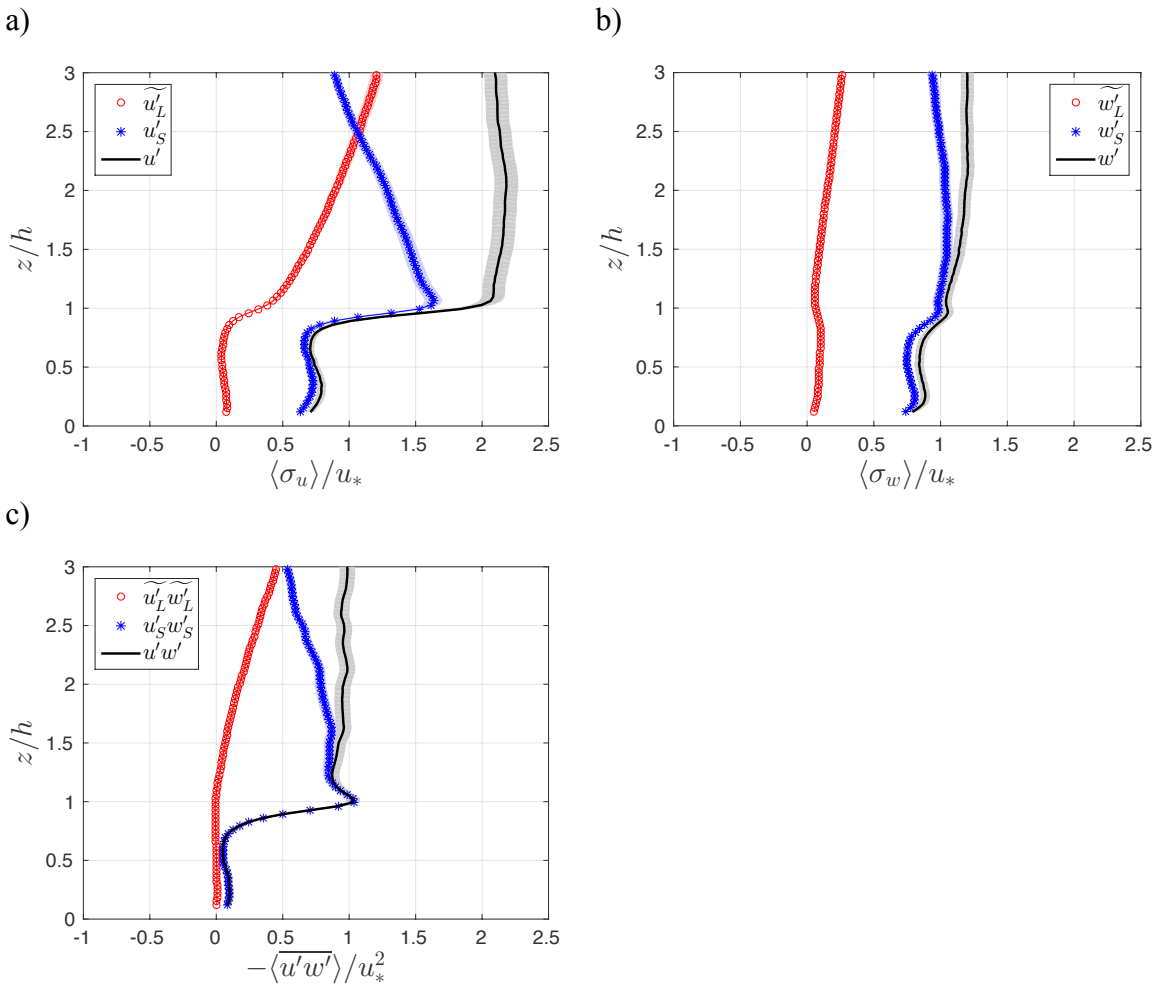

Figure 4.1. Contribution of the large-scales, $\widetilde{u'_L}$ (o) and small-scales, $\widetilde{u'_S}$ (*) to spatially averaged a) $\langle\sigma_u\rangle$, b) $\langle\sigma_w\rangle$ and c) $\langle\overline{u'w'}\rangle$.

As demonstrated above, the fluctuations estimated by the LSE model do not capture the small-scale turbulent flow within the canopy and shear layer. The spatial correlation of the predicted streamwise velocity fluctuations ($R_{\widetilde{u}'_L\widetilde{u}'_L}$) is calculated using Equation 4.1 with a reference (x_{ref}, z_{ref}) located at $x_{ref}/h = 0$ or $x_{ref}/h = -0.25$ and $z_{ref}/h = 2.5$ or $z_{ref}/h = 0.25$.

$$R_{\widetilde{u}'_L\widetilde{u}'_L}(x_{ref}, z_{ref}, x, z) = \frac{\overline{\widetilde{u'}_L(x_{ref},z_{ref})\widetilde{u'}_L(x,z)}}{\sqrt{\overline{\widetilde{u'}_L{}^2(x_{ref},z_{ref})}}\sqrt{\overline{\widetilde{u'}_L{}^2(x,z)}}} \tag{4.1}$$

The spatial correlation contours show high correlation within the boundary layer above the canopy with rapidly decaying correlation within the shear layer while within the

canopy the correlation becomes negative (Figure 4.2). The spatial correlation of the predicted vertical fluctuations ($R_{\widetilde{w}_L'\widetilde{w}_L'}$) shows similarly large structures within the boundary layer (Figure 4.3). Although these correlations indicate that large-scale structures are present within the overlying boundary layer the limited spatial extent of the PIV region prevents the direct calculation of streamwise integral length scales. Instead the streamwise length scales ($L_{\widetilde{u_L}}$) are calculated using temporal correlation and invoking Taylor's hypothesis of frozen turbulence as described in Chapter 1 (Equation 1.3). The size of these structures in the streamwise direction spans several times (up to 6) the height of the boundary layer (Figure 4.4). Finally, the temporal evolution of the estimated fluctuations is shown in Figure 4.5 and shows structures that resemble large-scale momentum regions, which are found in both rough-wall and smooth-wall boundary layers (Volino et al., 2007). The angle of inclination (θ) of these structures can be estimated using Figure 4.5 with $\theta = tan^{-1}\left({\Delta z}/{(\Delta \tau U_\infty)}\right)$ and is shown to fall between 11^o and 15^o, which agrees well with previous work (Castro et al., 2006; Coceal et al., 2007a; Guala et al., 2011; Rivet 2014). In conclusion, the fluctuations predicted by the LSE represent elongated, large-scale regions of low or high momentum that are present within the overlying boundary layer above the roughness.

a) b)

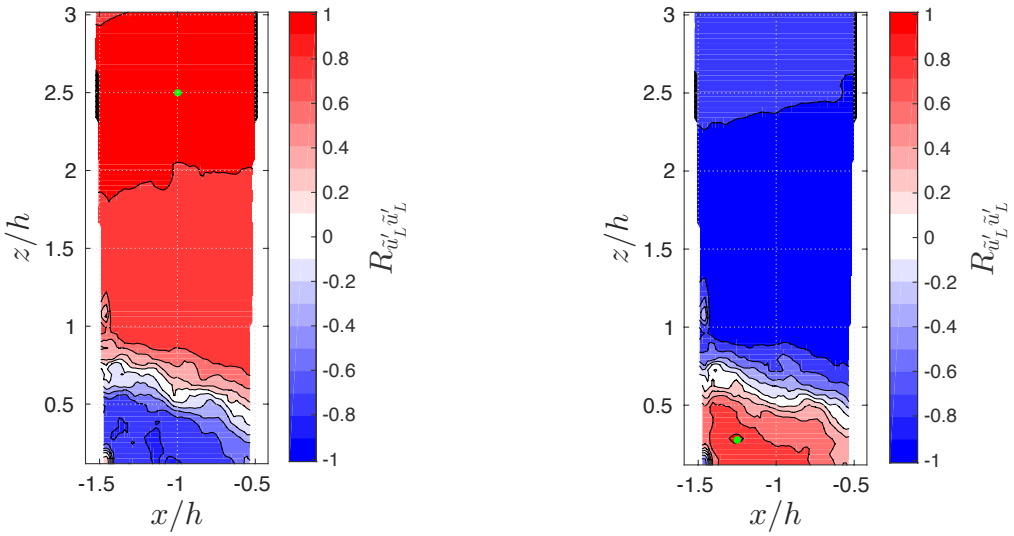

Figure 4.2. Spatial correlation coefficient ($R_{\tilde{u}_L'\tilde{u}_L'}$) of the streamwise velocity fluctuations predicted by the LSE model ($\widetilde{u'}_L$) with reference point (•) of a) x/h = -1, z/h = 2.5 and b) x/h = -1.25, z/h = 0.25.

a) b)

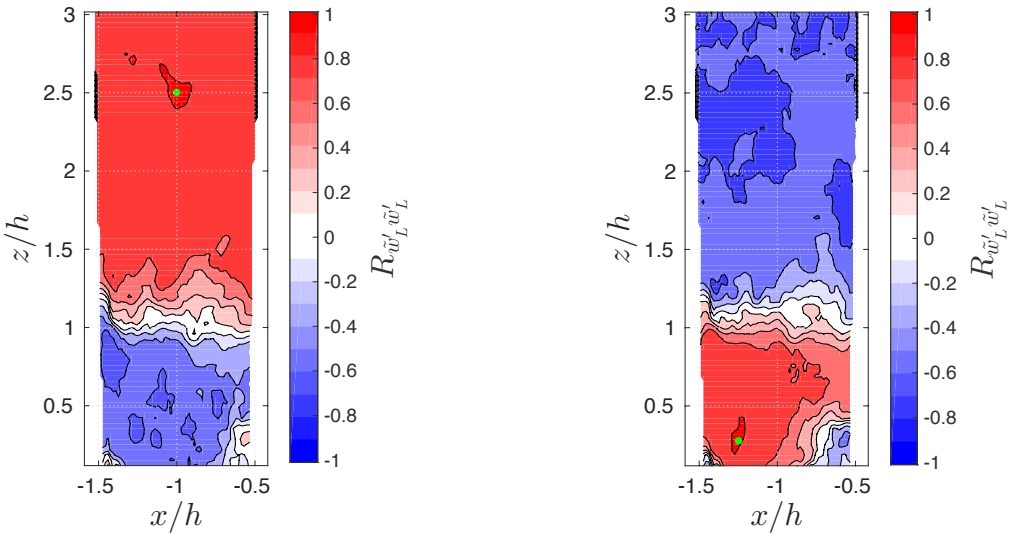

Figure 4.3. Spatial correlation coefficient ($R_{\tilde{w}_L'\tilde{w}_L'}$) of the vertical velocity fluctuations predicted by the LSE model ($\widetilde{w'}_L$) with reference point (•) of a) x/h = -1, z/h = 2.5 and b) x/h = -1.25, z/h = 0.25.

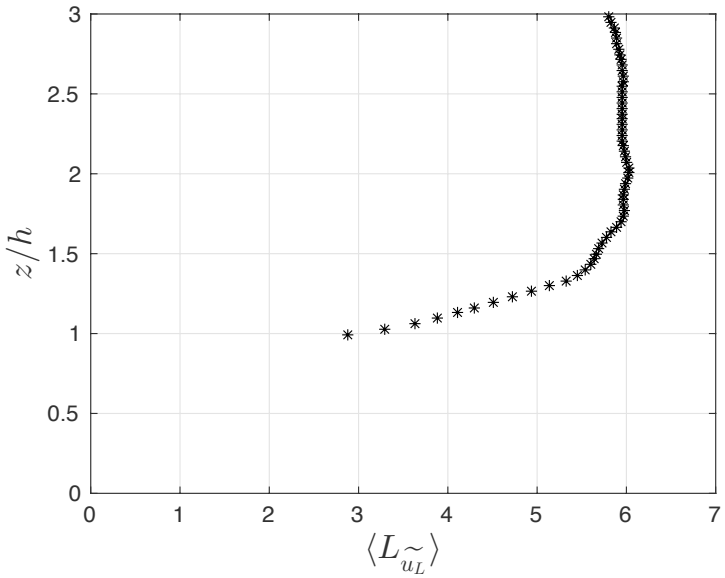

Figure 4.4. Spatially averaged streamwise integral length scales ($L_{\widetilde{u_L}}$) of streamwise velocity fluctuations predicted by the LSE model ($\widetilde{u'_L}$).

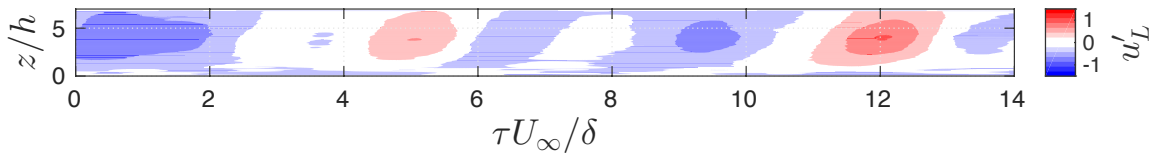

Figure 4.5. Temporal evolution of streamwise velocity fluctuations predicted by the LSE model ($\widetilde{u'_L}$) at $x/h = 0$.

We can use these same analyses to investigate the characteristics of the remaining fluctuations (u'_S and w'_S) determined through triple decomposition (Equation 3.1). The spatial correlation coefficients of u'_S and w'_S show high correlation near the reference location. The correlation level rapidly decays within the roughness sub-layer and canopy (Figure 4.6 and Figure 4.7). Therefore, these fluctuations represent small-scale structures and include those influenced by the presence of the roughness.

a) b)

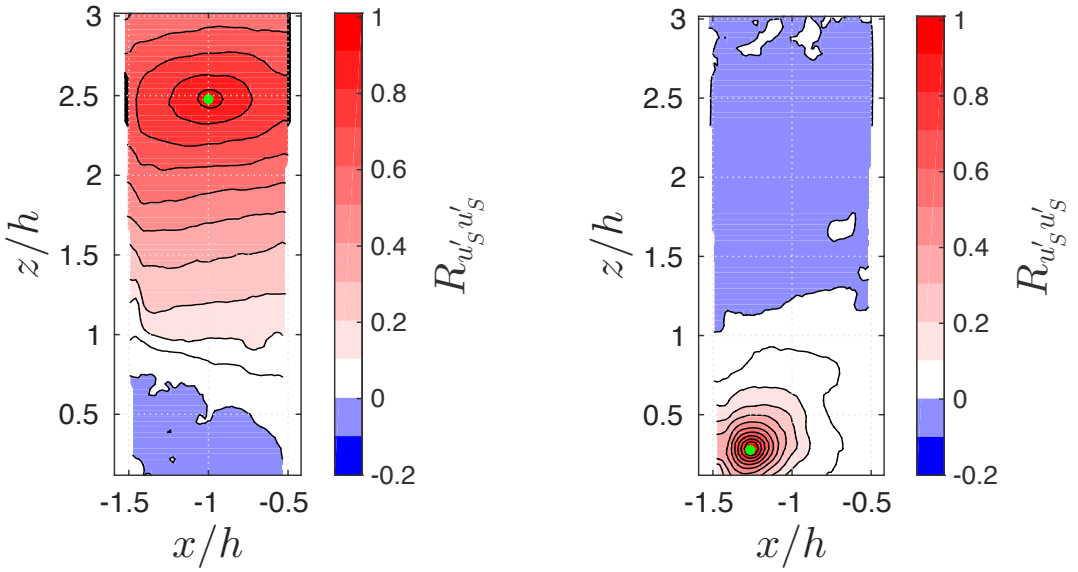

Figure 4.6. Spatial correlation coefficient ($R_{u'_S u'_S}$) of the streamwise velocity fluctuations predicted by the LSE model (u'_S) with reference point (•) of a) x/h = -1, z/h = 2.5 and b) x/h = -1.25, z/h = 0.25.

a) b)

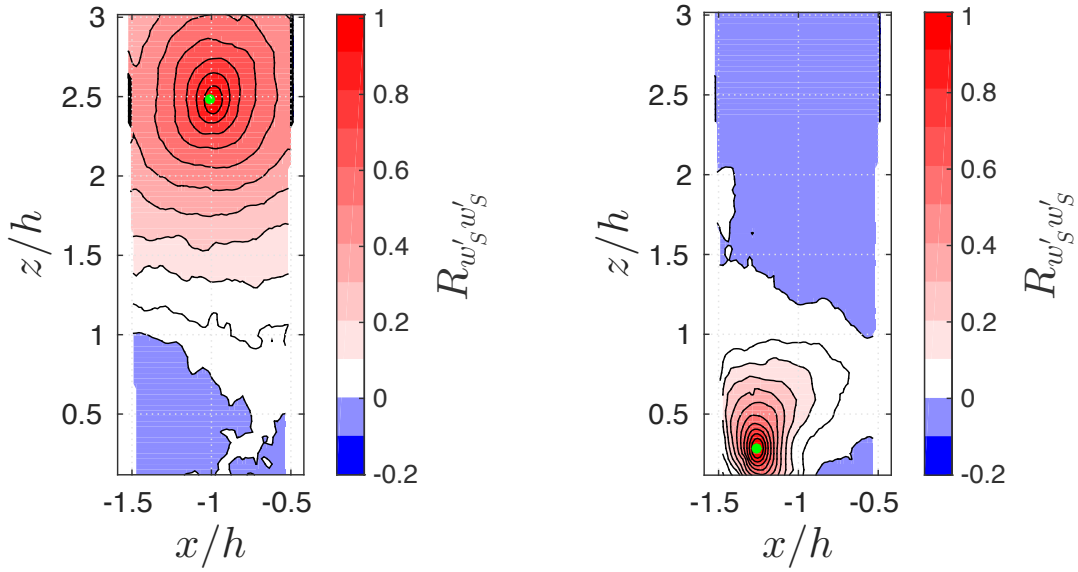

Figure 4.7. Spatial correlation coefficient ($R_{w'_S w'_S}$) of the vertical velocity fluctuations predicted by the LSE model (w'_S) with reference point (•) of a) x/h = -1, z/h = 2.5 and b) x/h =-1.25, z/h = 0.25.

4.2.2 Scale interactions

The LSE model driven by a low-pass filtered reference signal within the overlying boundary layer was able to estimate large-scale velocity fluctuations correlated with large-scale structures present in the overlying boundary layer while the remaining fluctuations have been shown to be small-scale structures. Figure 4.1 shows the contribution of the large- and small-scales to the total σ_u, σ_w and $\overline{u'w'}$. Within the roughness sub-layer and canopy, the small-scales capture the majority of the variances and shear stress while within the overlying boundary layer at $z/h = 3$ the large-scale contribution becomes significant for all quantities, but particularly for the σ_u. The contributions of the large-scales to the σ_u and $\overline{u'w'}$ agree well qualitatively with previous work (Inagaki and Kanda, 2010; Perret and Rivet, 2013) where any discrepancy can be attributed to dissimilarities of filtering methods or roughness configuration.

Skewness decomposition as outlined in Chapter 3 (Equation 3.2) can be used to investigate the existence of non-linear interactions between large- and small-scales in turbulent flows. Figure 4.8 shows the skewness decomposition spatially averaged over the width of the PIV field. The decomposed skewness exhibits a peak within the shear layer forming downstream of a cubical obstacle which is predominately due to $\overline{u'^3_S}$. This suggests that the energetic downward sweeping motions in this region are predominately a result of small-scale fluctuations. The quantity $\overline{u'^3_S}$ becomes negative above the shear layer exhibiting similarities to the skewness profile of a mixing layer, which agrees with results from previous work (Perret and Rivet, 2013). The large-scales contribute a negligible amount to the skewness throughout the boundary layer, whereas, the cross-term $\overline{\widetilde{u'}_L u'^2_S}$ has a significant contribution to the skewness with its maximum occurring just above the shear layer at $z/h = 1.5$. Within the literature the peak of this term occurs closer to the roughness within the region of peak skewness at approximately $z/h = 1$ (Perret and Rivet, 2013). Above a height of $z/h = 1.5$ the profile of $\overline{\widetilde{u'}_L u'^2_S}$ closely resembles that of the total skewness with slightly larger magnitude. The term $\overline{\widetilde{u'}_L u'^2_S}$ represents the non-linear interaction between the large-scales and the small-scales and could suggest a top-down mechanism such as amplitude modulation. The cross-term

$\overline{\widetilde{u'^2_L}u'_S}$ is negligible throughout the boundary layer contradicting the results of Perret and Rivet (2013) who stated that this term is non-negligible and could represent a feedback mechanism. The discrepancy between the present work and the work of Perret and Rivet (2013) is likely a result of different decomposition methods, POD and LSE, applied to identical flows. POD is an energy driven decomposition method with some modes containing mostly large-scale energy, but will likely encompass some small-scale energy as well. Conversely, the LSE method employed here using a cutoff filter specifically removes all small-scale energy. This fundamental difference in decomposition can cause significant changes in the results. The present work agrees with that of Mathis et al. (2011b) who demonstrated that this cross-term has a negligible influence within the smooth-wall boundary layer. The results of the skewness decomposition of the present work indicate that large- and small-scales could be phase-coupled through a mechanism such as amplitude modulation (Perret and Rivet, 2013).

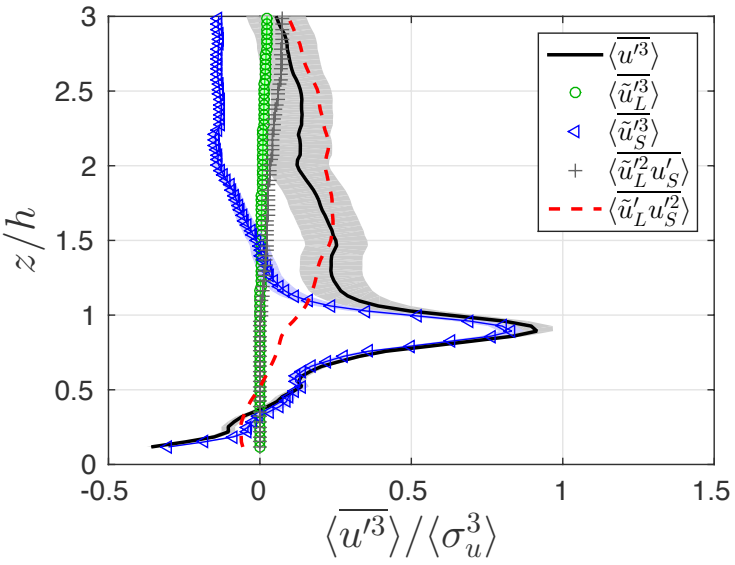

Figure 4.8. Triple decomposition of streamwise skewness, $\langle\overline{u'^3}\rangle$(-) including $\langle\overline{\widetilde{u'_L}^3}\rangle$ (o),$\langle\overline{u'^3_S}\rangle$ (◁), $3\,\langle\overline{\widetilde{u'_L}^2u'_S}\rangle$ (+), $3\,\langle\overline{\widetilde{u'_L}u'^2_S}\rangle$ (--) all spatially averaged and normalized by $\langle\sigma_u^3\rangle$.

Within the literature, it has been previously observed that the non-linear interaction between the large-scale momentum regions and the small-scales close to the roughness occurs in a similar manner for all velocity components (Perret and Rivet, 2013). In the present work the non-linear interaction between the large-scale momentum regions and

the spanwise ($\overline{\widetilde{u'_L}v'^2}$) and vertical ($\overline{\widetilde{u'_L}w'^2}$) fluctuations are computed and compared with $\overline{\widetilde{u'_L}u'^2_S}$ (Figure 4.9). In this case the spanwise and vertical fluctuations used are the raw fluctuations with no LSE filtering applied. The current results are in agreement with those of Perret and Rivet (2013) as all three components of velocity have similar profiles particularly within the canopy. The largest difference between the profiles in the present work, approximately 25%, occurs at a height of $z/h = 1.5$. This indicates that the large-scale momentum regions within the boundary layer influence the small-scale structures through a non-linear interaction of all three components of velocity.

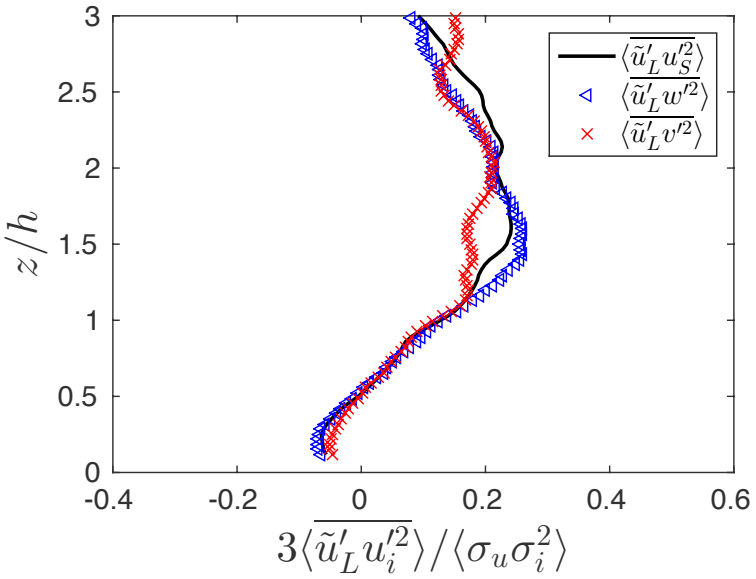

Figure 4.9. Non-linear skewness terms $3\langle\overline{\widetilde{u'_L}u'^2_S}\rangle$ (-), $3\langle\overline{\widetilde{u'_L}w'^2}\rangle$ (◁) and $3\langle\overline{\widetilde{u'_L}v'^2}\rangle$ (×) all spatially averaged and normalized by $\langle\sigma_u\sigma_i^2\rangle$.

The LSE model used in the present work with high-temporal resolution HWA allows for the temporal extrapolation of velocity fluctuations. Scale-interactions can, thus, also be investigated temporally without having access to the temporal small-scale signal close to the roughness. Using this technique we will focus on the cross-correlation of the large-scale component with the squared small-scale fluctuations, $R_{\tilde{u}'_L u'^2_S}$, which represents the non-linear interaction of the scales. This analysis is performed by introducing time lags to the $\widetilde{u'_L}$ fluctuations (Equation 4.2). Figure 4.10 shows the temporal evolution of the spatially averaged cross-correlation. The cross-correlation $R_{\tilde{u}'_L u'^2_S}$ exhibits a strong peak within the roughness sub-layer, which gradually decreases in magnitude with height in

the boundary layer. This peak tends to align with a zero time delay until a height of $z/h = 3$ is reached where the peak shifts to approximately $\tau\overline{U}_\infty/\delta = 0.5$. This positive peak shift is a result of small-scales interacting with large-scales that occur upstream in the flow and has been previously documented in the literature (Guala et al., 2011). Although the reason for this shift is unknown it suggests that the behaviour of the non-linear interaction between large- and small-scale structures is modified between the roughness sub-layer and above. Similarly, within the canopy at $z/h = 0.5$ the relationship between large- and small-scale structures is modified where a positive correlation changes to a negative correlation near the wall. In this region there is a recirculation of the flow within the wake and, as shown in Figure 4.2a, large-scales within the canopy are opposite in sign to the large-scales above the canopy. This results in a modification of the relationship between large- and small-scales within the canopy.

$$R_{\widetilde{u}'_L u'^2_S}(x_S, z_S, x_L, z_L, \tau_L) = \frac{\overline{\widetilde{u'}_L(x_L,z_L,t+\tau_L)u'^2_S(x_S,z_S,t)}}{\sqrt{\overline{\widetilde{u'}_L{}^2(x_L,z_L)}}\sqrt{\overline{u'_S{}^2(x_S,z_S)}^2}} \tag{4.2}$$

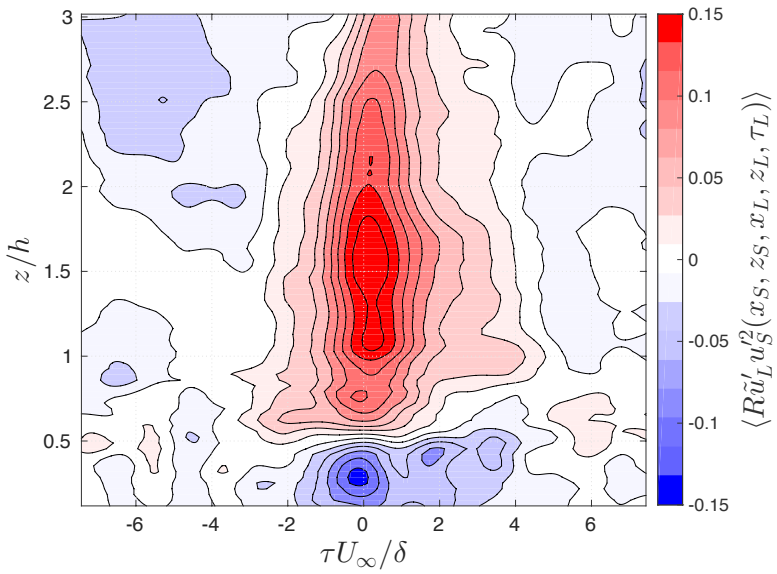

Figure 4.10. Spatially averaged Correlation Coefficient $\langle R_{\widetilde{u}'_L u'^2_S}\rangle$ where $x_L = x_S$ and $z_L = z_S$.

A spatially averaged two-point spatio-temporal correlation of the term $\widetilde{u'}_L u'^2_S$ provides further insight into this non-linear interaction (Figure 4.11). The correlation is computed using a fixed small-scale point (z_S) within the canopy at a height of $z/h = 0.75$ (Equation 4.2). Above a height of $z/h = 0.5$ there is a clear peak present with positive

correlation even for large time delays. A positive correlation suggests that when large-scale, low momentum regions are present above the canopy the small-scales are suppressed, whereas, when large-scale high momentum regions are present above the canopy the small-scales are amplified. Thus, these results support a top-down mechanism of non-linear interaction. Within the canopy the relationship is modified, there is negative correlation between large-scale near-wall fluctuations and the small-scale fluctuations at $z/h = 0.75$. As mentioned above, this is likely caused by the recirculation of the flow within the wake resulting in negative large-scale fluctuations occurring with amplification of the small-scales in the shear layer. As well, the peak of correlation tends to shift temporally as the large-scale reference location in the boundary layer increases in height. When the large-scale reference location is close to the small-scale reference at $z/h = 1$ the peak occurs at approximately $\tau\overline{U}_\infty/\delta =$ - 0.1, which becomes $\tau\overline{U}_\infty/\delta =$ - 0.6 with large-scale reference at $z/h = 3$. This is likely a consequence of the shape of the large-scale structures. Figure 4.12 shows a qualitative cartoon of a low or high momentum region passing over small-scale structures close to the roughness. The momentum regions within the boundary layer are slightly inclined. An inclination angle (θ) can be estimated using Figure 4.11 with $\theta = tan^{-1}\left(\Delta z/(\Delta\tau U_\infty)\right)$ and corresponds to approximately 11.5^{o}. This agrees well with the angle extracted from Figure 4.5, confirming that the inclined large-scale structures of high or low momentum detected in the logarithmic layer leave their footprint on the small-scales close to the wall through a non-linear relationship. As the structure moves within the boundary layer it will pass over the small-scale structures close to the roughness. Thus, small-scale structures experience effects from the large-scale structure that is slightly downstream of them. As the large-scale reference location increases in height the distance in the streamwise direction between the small-scale structure and the low momentum region increases resulting in an increase in time-delay of the peak correlation.

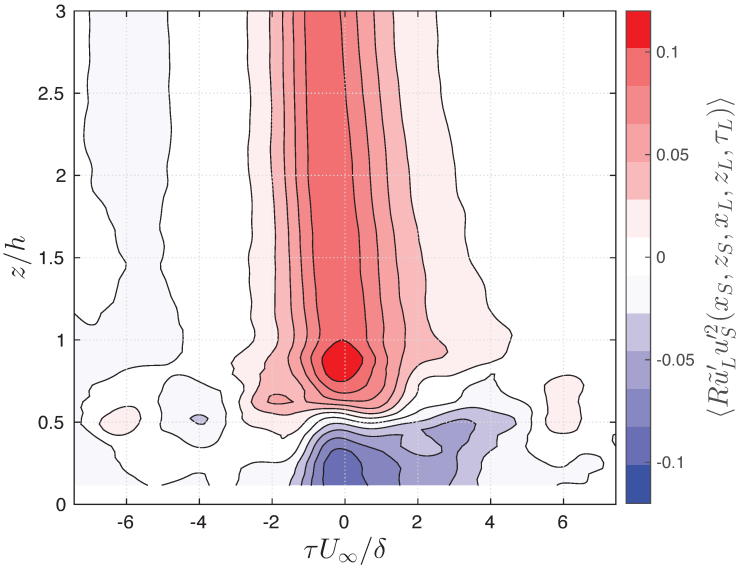

Figure 4.11. Spatially averaged spatial Correlation Coefficient $\langle R_{\tilde{u}_L' u_S'^2} \rangle$ where $x_L = x_S$ and z_S =.0.75 .

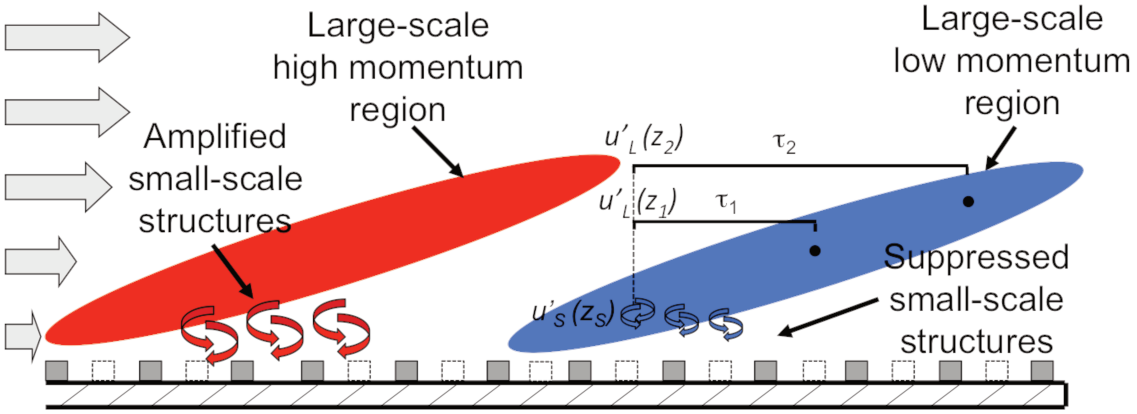

Figure 4.12. Qualitative cartoon illustrating time-delayed influence of large-scale low momentum structure (blue) and high momentum structure (red) on small-scales generated by the roughness.

The results of the skewness decomposition and correlation analysis provide quantitative evidence of a top-down mechanism of non-linear interaction within the rough-wall boundary layer. The LSE filtering method employed here provides spatio-temporal information, which improves our understanding of the nature of this non-linear interaction. The results agree well, qualitatively, with those found in the smooth-wall boundary layer (Mathis et al., 2009) and could suggest a mechanism of amplitude modulation.

4.3 Conclusions

Within the rough-wall boundary layer the relationship between the large-scale structures present in the overlying boundary layer and the small-scale structures induced by the presence of the roughness is not fully understood. Previous work in the smooth-wall boundary layer focused on this interaction has linked it to a non-linear mechanism of amplitude modulation (Mathis et al., 2009; 2011a; 2011b). Both numerical (Nadeem et al., 2015; Anderson, 2016) and experimental (Squire et al., 2016) studies using homogeneous and heterogeneous roughness have established the presence of amplitude modulation in the rough-wall boundary layer.

The present work used experimental evidence from a rough k-type boundary layer developing over a rough wall consisting of a staggered cube array to answer the specific questions listed in Section 4.1.

1) As temporally resolved measurements close to the roughness are not feasible in the present work, LSE outlined in Chapter 3 was used to decompose the flow. Through triple decomposition it is clear that the small-scales contribute the majority of the streamwise velocity standard deviation, vertical standard deviation and shear stress. Skewness decomposition confirmed that in the near-wall region of the rough-wall boundary layer, the scale interaction occurs through a non-linear mechanism shown in the term $\overline{\widetilde{u'}_L u'^2_S}$, which represents the non-linear influence of the large-scales onto the small-scales. The non-linear term, $\overline{\widetilde{u'^2_L} u'_S}$, which represents the influence of the small-scales onto the large-scales was found to be negligible. It was shown that the non-linear interaction occurs through all three components of velocity similarly.

   The LSE method applied in the present work allows for analysis of spatio-temporal correlations of large- and small-scales without having access to the temporal small-scale signal close to the roughness. Temporal correlation of the non-linear term $\overline{\widetilde{u'}_L u'^2_S}$ demonstrated quantitatively that the large-scale momentum regions influence the small-scales throughout the boundary layer, which agrees with the results of the DNS study of the rough-wall boundary layer by Nadeem et

al. (2015).

2) A two-point spatial-temporal correlation showed positive correlation, which confirms that a top-down non-linear mechanism similar to amplitude modulation exists in the rough-wall boundary layer as in smooth-wall configurations.
3) The present multi-time delay LSE method helps to improve our understanding of the non-linear mechanism of amplitude modulation in the rough-wall boundary layer through spatio-temporal correlations that help to identify the nature of the structures involved. Through spatio-temporal correlations the presence of the roughness elements, which create a recirculation of the flow within the wake of the obstacles, is shown to result in a negative correlation between the large-scale and small-scale near-wall fluctuations thereby modifying the non-linear relationship.

The present work has led to some important findings on the nature of the non-linear interaction in the rough-wall boundary layer. However, the influence of geometry and packing density (λ_p) of the roughness on the mechanism remains to be studied. In the following chapter other roughness configurations outlined in Chapter 2 using street canyons will be used to investigate the influence of roughness geometry and street canyon aspect ratio on the non-linear relationship that exists between large-scale structures present in the overlying boundary layer and small-scales close to the roughness.

Résumé du Chapitre 5: Influence du régime d'écoulement incident et du rapport d'aspect de la rue sur les interactions non linéaires entre l'écoulement de rue canyon et la couche limite

Le Chapitre 5 présente les résultats de l'analyse réalisée en utilisant la décomposition triple et le modèle d'estimation stochastique décrits au chapitre 3. On s'intéresse ici à l'influence de l'écoulement incident, qui diffère selon les configurations d'éléments rugueux, et du rapport d'aspect de la rue canyon sur les relations non-linaires entre l'écoulement de rue canyon et la couche limite. Un résumé (en français) de ce chapitre est proposé ci-après.

Un modèle simple de rue canyon permet de reproduire les caractéristiques d'écoulement dans des configurations de rue les plus communes, en particulier dans le cas où le vent incident est perpendiculaire à l'axe de la rue (Savory and Perret, 2013). Il permet de reproduire les structures cohérentes complexes, telles que les grandes régions de basse vitesse qui se produisent dans la couche limite au-dessus de la canopée et les structures à petite échelle proches de la rugosité, qui sont reliées par un mécanisme non linéaire similaire à la modulation d'amplitude (Chapitre 4).

Les écoulements dans des rues ayant un rapport d'aspect variable AR $= W/h$ (où W est la largeur du canyon et h est sa hauteur) ont été largement étudiés, en particulier pour classifier les régimes d'écoulement : écoulements rasant, écoulements avec interférences de sillages et écoulements de type obstacle isolé (Oke, 1988). Cependant, très peu d'études ont examiné l'influence sur la dynamique de la turbulence (i) du rapport d'aspect de la rue et (ii) de la géométrie (2D ou 3D) des éléments de rugosité amont (et par conséquent, de l'écoulement de la couche limite). Les configurations utilisées dans les études antérieures fournissent des informations limitées, car elles n'utilisent pas différentes configurations avec une densité surfacique λ_p variable pour chaque type de rugosité, 2D et 3D. L'étude la plus exhaustive s'est appuyée sur six configurations différentes, dont trois configurations de rugosité en amont (cubes ou barres 2D avec un

espacement différent) et deux rapports d'aspect de rue, et il a été constaté que la géométrie de la rugosité avait une influence non négligeable sur les caractéristiques de la couche limite (Blackman et al., 2015). Cependant, il n'est pas clairement établi que ces facteurs ont un impact significatif sur les relations entre les structures de la couche limite et les petites échelles induites par la présence de la rugosité.

L'existence d'une modulation d'amplitude a été prouvée expérimentalement (Squire et al., 2016; Blackman et al., 2016) et numériquement (Nadeem et al., 2015; Anderson, 2016) dans des couches limites de paroi rugueuse constituées d'une rugosité homogène et hétérogène, mais les travaux antérieurs se sont limités à un ou deux types de rugosité. Le présent travail vise à utiliser des données expérimentales des six configurations de Blackman et al. (2015) avec un nombre de Reynolds élevé pour répondre aux questions suivantes:

1) Quelle est l'influence quantitative de la configuration de rugosité sur la relation non linéaire entre les structures à grande échelle dans la couche inertielle et les structures à petite échelle induites par la présence de la rugosité dans la sous-couche de rugosité?
2) Quelle est l'influence quantitative du rapport d'aspect de la rue sur cette relation non linéaire?

Comme au chapitre 4, un modèle d'estimation stochastique est utilisé pour décomposer l'écoulement de chacune des six configurations de canyon en grandes et petites échelles. Ceci se fait à l'aide d'un signal HWA temporellement résolu filtré provenant de la couche limite supérieure, en conjonction avec des mesures PIV spatialement résolues. Les signaux de vitesse prédits montrent qu'ils contiennent des structures à grande échelle similaires aux régions de basse et haute vitesse tandis que les fluctuations restantes montrent qu'elles englobent les petites échelles.

Tout d'abord, l'influence de la configuration de rugosité en amont sur les interactions non linéaires entre grandes et petites échelles en écoulement turbulent est étudiée en utilisant la décomposition du coefficient d'asymétrie. Le terme croisé $\overline{\widetilde{u_L'}u_S'^2}$ a une contribution significative au coefficient d'asymétrie dans chacune des trois couches limites.

Cependant la position à laquelle le coefficient est maximum diffère selon la configuration de la rugosité. Un changement de 3D (cubes) à 2D (rue infinie) avec la même densité surfacique donne lieu à un décalage du maximum dans la couche de cisaillement de $z/h = 1.5$ à $z/h = 1$. En revanche, l'augmentation de la densité surfacique déplace le maximum du terme croisé $\widetilde{u_L'}\widetilde{u_S'^2}$ à $z/h = 1.2$. Cependant, la contribution relative de ce terme non linéaire ne dépend pas de la configuration de rugosité car les trois couches limites présentent des grandeurs similaires. À partir de cette analyse, il est clair que dans les trois configurations de rugosité, il y a une influence significative du terme $\widetilde{u_L'}\widetilde{u_S'^2}$, ce qui montre l'existance d'interactions non linéaires entre les grandes échelles et les petites échelles, telles que la modulation d'amplitude. Une étude des interactions non linéaires à travers les composantes transversales et verticales montre que les trois composantes sont influencées de manière similaire. Cependant, dans le cas d'écoulement rasant 2D, le terme transversal diffère du terme longitudinal et vertical, mais cette différence peut résulter d'une erreur ou d'une mauvaise convergence des statistiques.

Enfin, le modèle LSE utilisé dans le présent travail avec la haute résolution temporelle HWA permet l'extrapolation temporelle des fluctuations de vitesse. Les interactions d'échelle peuvent donc également être étudiées temporellement sans avoir accès au signal temporel à petite échelle proche de la rugosité. À partir de cette analyse, il est clair qu'une modification significative de la relation non linéaire se produit dans les cas de rugosité 2D, en particulier pour le régime d'interférence de sillages. Dans le cas en 3D, un changement de la corrélation dans la couche limite à $z/h = 3$ suggère une modification de la relation non linéaire dans cette région. Cependant, dans le cas de l'interférence de sillages, ce changement se produit aussi dans la couche de cisaillement mais à une hauteur de $z/h = 1$, suggérant une modification significative de la relation selon le type de rugosités pour ce régime d'écoulement.

L'analyse de l'influence du rapport d'aspect de la rue sur cette interaction non linéaire en utilisant la décomposition du coefficient d'asymétrie montre que le terme croisé $\widetilde{u_L'}\widetilde{u_S'^2}$ dépend uniquement de la rugosité en amont qui, comme discuté ci-dessus, modifie la position du maximum de ce terme. En outre, l'augmentation du rapport d'aspect de la rue

entraîne une augmentation de la contribution de ce terme, ce qui suggère que cette interaction non linéaire devient plus importante dans le régime d'écoulement d'interférence de sillages. Enfin, le rapport d'aspect a une influence négligeable sur la relation non linéaire au travers des composantes transversale et verticale qui se révèlent similaires à l'interaction longitudinale.

Les principales conclusions de ces analyses sont données ci-dessous :

1) La configuration de la rugosité en amont, qu'elle soit 2D ou 3D, et la densité surfacique, ont une influence non négligeable sur les interactions non linéaires avec la couche limite en paroi rugueuse. Grâce à la décomposition du coefficient d'asymétrie, il est démontré que le niveau du maximum du terme $\overline{\widetilde{u_L'}u_S'^2}$, qui représente l'influence des des grandes échelles sur les petites échelles, se rapproche de la couche de cisaillement avec une modification de la rugosité de 3D à 2D. Les travaux antérieurs ont montré que l'interaction non linéaire se produit de manière similaire à travers les trois composantes de la vitesse (Perret et Rivet, 2013; Blackman et Perret, 2016), ce qui a été confirmé dans le présent travail sauf dans le cas de d'une rugosité 2D de rapport d'aspect égal à 1, pour lequel le régime d'écoulement rasant induit une modification de la relation non linéaire avec la composante de vitesse transversale. Toutefois, cette modification pourrait résulter d'une mauvaise convergence statistique et d'une erreur. Par la corrélation temporelle, il est évident que le comportement non linéaire est modifié plus près de la couche de cisaillement en rugosité 2D par rapport à la rugosité 3D. Enfin, une corrélation spatio-temporelle en deux points a démontré que la relation non linéaire est modifiée de manière significative dans le régime d'écoulement interférence de sillages.
2) Le rapport d'aspect de la rue influence peu les interactions non linéaires. Une augmentation du rapport d'aspect réduit le rôle des petites échelles. En parallèle, il augmente la contribution du terme $\overline{\widetilde{u_L'}u_S'^2}$ non linéaire au coefficient d'asymétrie total. Cependant, l'interaction non linéaire au travers des composantes transversale et verticale de la vitesse ne dépend que de la configuration de rugosité amont et non du rapport d'aspect de la rue.

5 Effect of upstream flow regime and canyon aspect ratio on non-linear interactions between a street canyon flow and the overlying boundary layer

The following chapter is work that was submitted as an article to Boundary Layer Meteorology (Blackman, K., Perret, L., Savory, E., "Effect of upstream flow regime and canyon aspect ratio on non-linear interactions between a street canyon flow and the overlying boundary layer," submitted to Bound Layer Meteorol (2017)). This work was completed using data from combined Particle Image Velocimetry (PIV) and Hot-Wire Anemometry (HWA) measurements within the six street canyon configurations (Figure 2.5) as well as the staggered cube array (Figure 2.4a) described in Chapter 2 and using the Linear Stochastic Estimation (LSE) method detailed in Chapter 3. First an introduction to the topic is provided, followed by the results including the influence of the upstream roughness configuration and the influence of the canyon aspect ratio and finally, conclusions.

5.1 Introduction

A simple street canyon model reproduces the flow features of most common street configurations, specifically for the case for which the upstream wind is perpendicular to the street axis (Savory and Perret, 2013). As described in Chapter 1 the flow is comprised of several regions, such as the roughness sub-layer, which contain complex coherent structures (Rotach et al., 2005; Coceal et al., 2007b). These coherent structures consist of large-scale regions of either high or low momentum, shear layers that contain small-scales induced by the presence of the roughness and a recirculation region within the canyon (Coceal et al., 2007b). As discussed in Chapter 4 these structures, especially how they interact with one another, are of particular interest as they govern the intermittent

turbulent events, such as ejections and sweeps that influence the transport of heat, momentum and pollution between the street canyon and the overlying roughness sublayer and inertial layer (Takimoto et al., 2011; Perret and Savory, 2013).

As reviewed in Chapter 1 the steady flow regimes of street canyons, with varying aspect ratio (AR $= W/h$, where W is the streamwise width and h is the height of the canyon) have been well studied, including the steady flow regimes; "skimming", "wake interference" and "isolated roughness" (Figure 1.7) (Oke, 1988). However, very few studies have examined the influence on the turbulent dynamics of varying (i) canyon AR and (ii) geometry (2D or 3D) of the upstream roughness elements (hence, the boundary layer flow). The configurations used in these studies provide limited information, as they do not use multiple configurations with varying plan area density (λ_p) for each type of roughness, 2D and 3D. The most comprehensive study incorporated six different configurations, including three upstream roughness configurations (cubes or 2D bars with different streamwise spacing) and two canyon AR, and it was found that the geometry of the roughness had a non-negligible influence on the characteristics of the boundary layer (Blackman et al., 2015a). The mean streamwise velocity for configurations of equal λ_p was found to be higher in 3D than 2D configurations, which agrees with previous work (Salizzoni et al., 2011; Huq and Franzese, 2013). It was also shown that the integral length scale is larger in 2D than 3D cases of equal λ_p and confirmed that the integral length scale also increases with increasing AR in 2D configurations as previously found by Volino et al., (2009). Finally, the canyon ventilation flow rate was shown to increase from 3D to 2D configurations of equal λ_p, increase with decreasing λ_p and increase with increasing canyon AR. This is due to the transition from skimming to wake interference flow regimes (Blackman et al., 2015a). It is clear that the geometry of both the upstream roughness and the street canyon have a non-negligible influence on the turbulence. However, it is unclear whether these factors have a significant impact on the relationship between the large-scale momentum regions within the inertial layer and the small-scales induced by the presence of the roughness (Perret and Savory, 2013).

As discussed in Chapter 4 skewness decomposition (Equation 3.2) has been used to investigate the non-linear relationship between large-scales within the overlying

boundary and near-wall small-scales both within the smooth-wall (Mathis et al., 2011b) and rough-wall (Perret and Rivet, 2013; Blackman and Perret, 2016) boundary layer. In Chapter 4 through skewness decomposition it was shown that in the near-wall region of the rough-wall boundary layer, the scale interaction occurs through a non-linear mechanism shown in the term $\overline{\widetilde{u'_L}u'^2_S}$, which represents the non-linear influence of the large-scales onto the small-scales. Furthermore, it was demonstrated, using the cross terms of $\widetilde{u'_L}$ with spanwise, v', and vertical, w', fluctuations, that all three components of velocity interact non-linearly in a similar manner, which agrees within the results of Perret and Rivet (2013) (Blackman and Perret, 2016).

As detailed in Chapter 4 this non-linear interaction was linked to a mechanism of amplitude modulation (Equation 3.3) within the smooth-wall boundary layer (Hutchins and Marusic, 2007; Mathis et al., 2009; Mathis et al., 2011a; Mathis et al., 2011b; Marusic et al., 2011; Inoue et al., 2012), which has recently been expanded to the study of a sand-roughened wall (Squire et al., 2016). Furthermore, evidence of a top-down non-linear mechanism of amplitude modulation has been confirmed in a 2D bar-roughened wall using DNS (Nadeem et al., 2015) and both a homogenous and cube roughened-wall using LES (Anderson, 2016). These studies noted that although amplitude modulation differs quantitatively between the smooth- and rough-wall the nature of the mechanism remains the same (Nadeem et al., 2015; Anderson, 2016; Squire et al., 2016).

Chapter 4 described work conducted using experimental evidence from a rough-wall boundary layer consisting of staggered cubes with $\lambda_p = 25\%$ (Rcu) to investigate the non-linear interactions between large-scale momentum regions and the small-scales induced by the presence of the roughness (Blackman and Perret, 2016). The use of LSE to decompose the flow when temporal information of the near-wall small-scales is not available was demonstrated. The use of a two-point spatio-temporal correlation showed positive correlation confirming that a top-down mechanism similar to amplitude modulation exists in the rough-wall boundary layer resembling that found in the smooth-wall boundary layer. This correlation demonstrated the existence of a time lag between the large-scale momentum regions and their influence on the small-scales within the roughness sublayer, agreeing with the results of Anderson (2016). The time lag was

found to correspond to an angle of inclination, 11.5^{o}, typical of large-scale momentum regions in the rough-wall boundary layer (Blackman and Perret, 2016). Finally, through the use of spatio-temporal correlations the presence of the roughness elements, which create a recirculation of the flow within the wake of the obstacles, was shown to result in a negative correlation between the large-scale and small-scale fluctuations thereby modifying the non-linear relationship.

Although the existence of amplitude modulation has been proven experimentally and numerically in rough-wall boundary layers consisting of homogenous and heterogeneous roughness, previous work is limited to one or two types of roughness (Nadeem et al., 2015; Anderson, 2016; Squire et al., 2016; Blackman and Perret, 2016). The present work aims to use experimental evidence from the six rough-wall boundary layer configurations used by Blackman et al. (2015a) with high Reynolds number to answer the following questions:

1) What is the quantitative influence of the roughness configuration on the non-linear relationship between large-scale structures in the inertial layer and small-scale structures induced by the presence of the roughness in the roughness sub-layer?
2) What is the quantitative influence of the street canyon AR on this non-linear relationship?

The following section will detail the results and discussion, including the influence of both the upstream roughness and the canyon AR on scale interactions, followed by the conclusions.

5.2 Results and Discussion

5.2.1 Influence of the upstream roughness configuration

As in Chapter 4, the present work uses the LSE model detailed in Chapter 3 to perform triple decomposition. It was demonstrated in Chapter 4 that the current LSE model driven by a low-pass filtered reference signal within the overlying boundary layer has the ability to estimate large-scale velocity fluctuations ($\widetilde{u'_L}$) while the remaining fluctuations have been shown to be small-scale structures (u'_S) (Blackman and Perret, 2016).

The statistics presented in the following are spatially averaged in the x-direction over the width of the PIV measurement region shown in Figure 2.4a (Rcu) and Figure 2.5 (R1h and R3h) in each of the three roughness configurations. Spatially averaging the statistics provides better convergence of higher order statistics while retaining important flow features.

The streamwise length scales ($L_{\widetilde{u_L}}$) are calculated for each of the three upstream roughness configurations using temporal correlation and invoking Taylor's hypothesis of frozen turbulence as described in Chapter 1 (Equation 1.3). The sizes of these structures in the streamwise direction are very large compared to the height of the roughness (Figure 5.1) and span a streamwise length several times the height of the boundary layer. Furthermore, it is shown that both an increase in packing density and a change from 3D to 2D roughness result in an increase in the size of these structures. The temporal evolution of the estimated fluctuations for each roughness configuration is shown in Figure 5.2. Structures that resemble large-scale momentum regions, which are found in both rough-wall and smooth-wall boundary layers (Volino et al., 2007), are shown and span a length on the order of 2δ. As in Chapter 4 the angle of inclination (θ) of these structures can be estimated using Figure 5.2 with $\theta = tan^{-1}\left({}^{\Delta z}/_{(\Delta\tau U_\infty)}\right)$ and is shown to fall between 11^o and 15^o for the 3D roughness and between 16^o and 20^o for the 2D roughnesses. In conclusion, as demonstrated in Chapter 4, the fluctuations predicted by the LSE represent elongated, large-scale regions of low or high momentum that are present within the overlying boundary layer above the roughness while the remaining fluctuations represent small-scale structures.

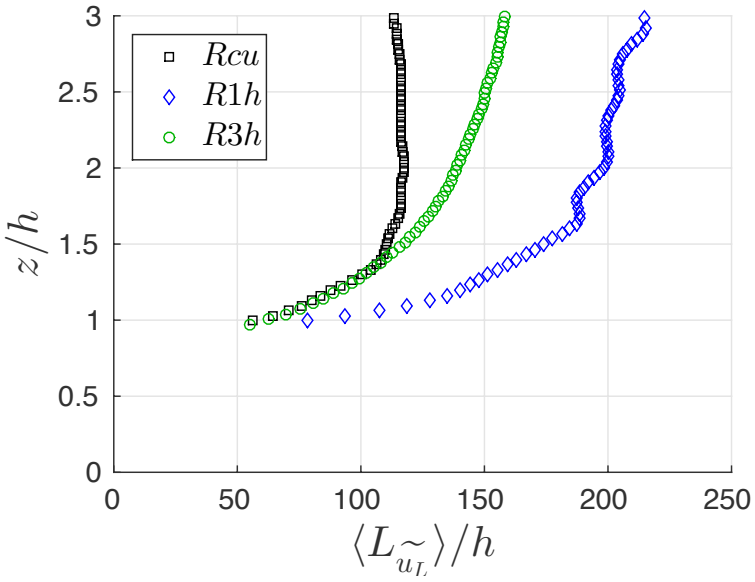

Figure 5.1 Spatially averaged streamwise integral length scales ($L_{\widetilde{u_L}}$) of streamwise velocity fluctuations predicted by the LSE model ($\widetilde{u'}_L$) in Rcu, R1h and R3h roughness configurations.

a)

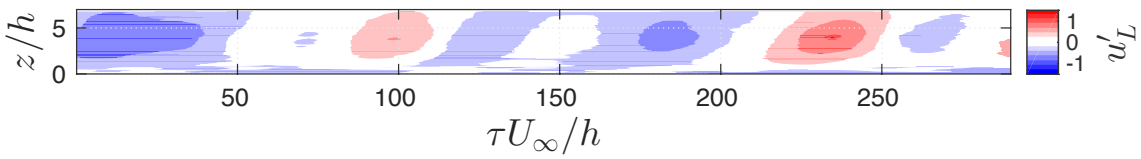

b)

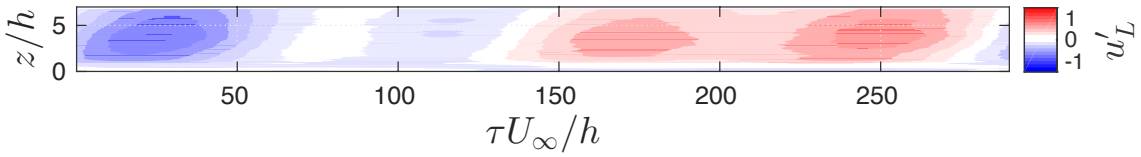

c)

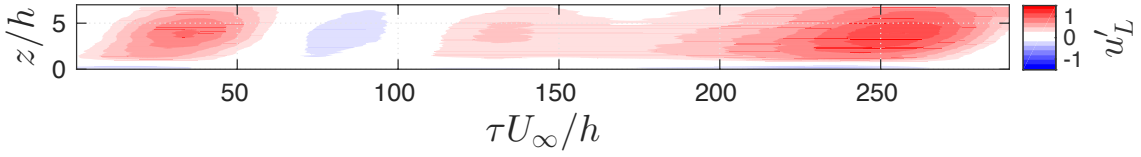

Figure 5.2 Temporal evolution of streamwise velocity fluctuations predicted by the LSE model ($\widetilde{u'}_L$) at $x/h = 0$ for a) Rcu; b) R1h; c) R3h.

Figure 5.3 shows the contribution of the large-scales to the total σ_u, σ_w and $\overline{u'w'}$ within the three roughness configurations studied in the present work. In all boundary layers within the canopy, the small-scales capture the majority of the variances and shear stress while within the overlying boundary layer the large-scale contribution becomes significant for all quantities, but particularly for σ_u. This significance is even larger for the 2D roughness cases, which show large-scale contribution to σ_u greater than 50% above a height of $z/h = 1.5$. As well, the R1h case is shown to have greater large-scale contribution (approximately two times) to the σ_w within the canopy compared to the other roughness cases. As the spatial averaging in each of these boundary layers covered the extent of the PIV measurement region the R1h and R3h statistics encompass the recirculation region within the canopy as well as the flow separation that occurs near the downstream canyon obstacle, whereas the Rcu statistics only encompass the recirculation region.

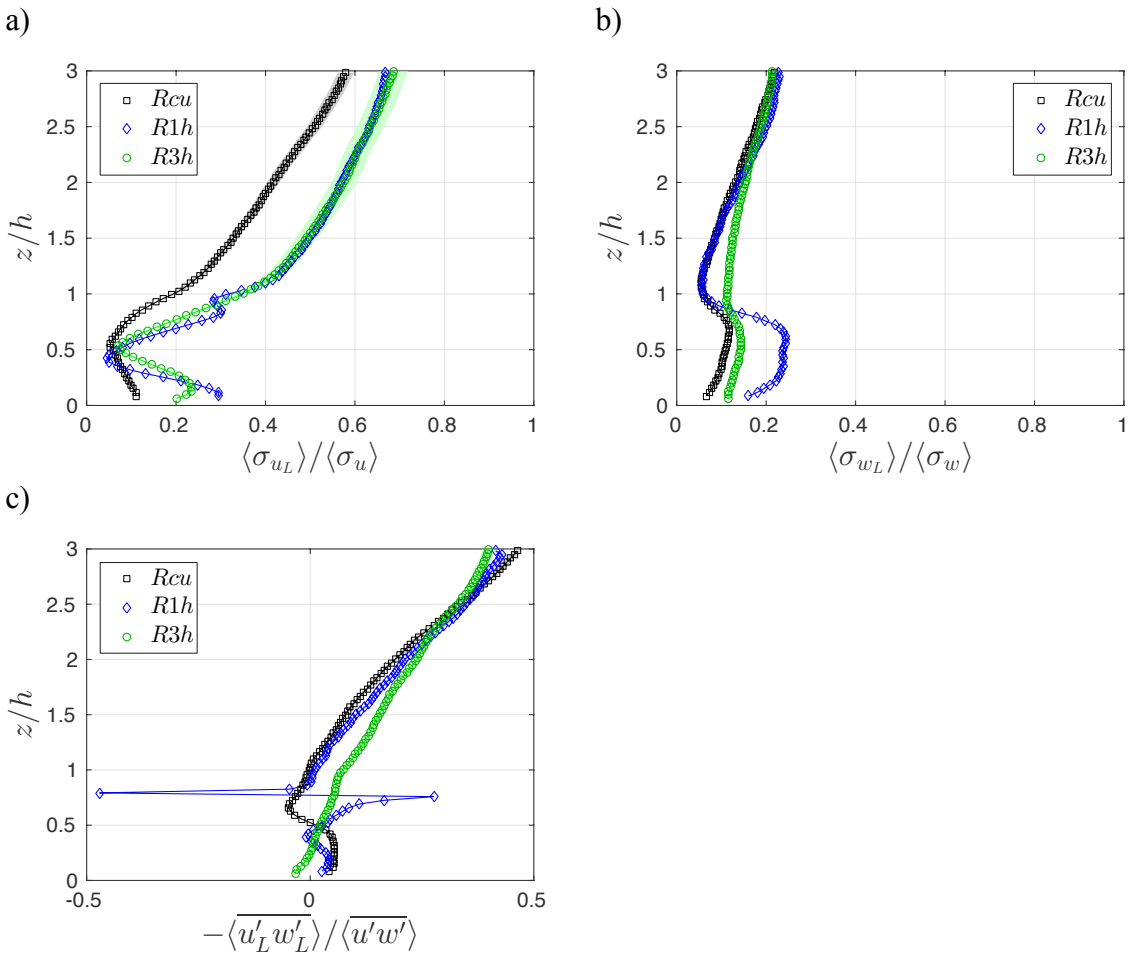

Figure 5.3 Contribution of the large-scales, $\widetilde{u'_L}$ to spatially averaged a) $\langle\sigma_{u_L}\rangle$, b) $\langle\sigma_{w_L}\rangle$ and c) $\langle\overline{u'_L w'_L}\rangle$. Outlying points in $\langle\overline{u'_L w'_L}\rangle$ are due to normalization by zero.

Skewness decomposition as outlined in Chapter 3 (Equation 3.2) has been previously used in Chapter 4 to investigate the existence of non-linear interactions between large- and small-scales in turbulent flows. Figure 5.4 shows the spatially averaged skewness decomposition of the three upstream roughness configurations, Rcu, R1h and R3h. In all three roughness configurations, the decomposed skewness exhibits a peak within the shear layer which is predominately due to $\overline{u'^3_S}$ suggesting that energetic downward sweeping motions in this region are predominately a result of small-scale fluctuations. The quantity $\overline{u'^3_S}$ becomes negative above the shear layer exhibiting similarities to the skewness profile of a mixing layer, which agrees with results from previous work (Perret and Rivet, 2013). The large-scales and the cross-term $\overline{\widetilde{u'^2_L}u'_S}$ contribute a negligible amount to the skewness throughout all three boundary layers, which agrees with previous

work in the smooth-wall boundary layer (Mathis et al., 2011a). The cross-term $\overline{\widetilde{u'}_L u'^2_S}$ has a significant contribution to the skewness in each of the three boundary layers and the location of its maximum shifts depending on the configuration of the roughness. A change from 3D to 2D roughness with the same packing density (λ_p) results in a shift of the maximum from just above the shear layer at $z/h = 1.5$ to within the shear layer at $z/h = 1$. In contrast, increasing λ_p shifts the maximum of the cross-term $\overline{\widetilde{u'}_L u'^2_S}$ to $z/h = 1.2$. However, the relative strength of this non-linear term is not dependent on the roughness configuration as all three boundary layers exhibit similar magnitudes. From this analysis, it is clear that within all three roughness configurations there is significant influence of the term $\overline{\widetilde{u'}_L u'^2_S}$, which represents the non-linear interaction between the large- and small-scales and could suggest a top-down mechanism such as amplitude modulation.

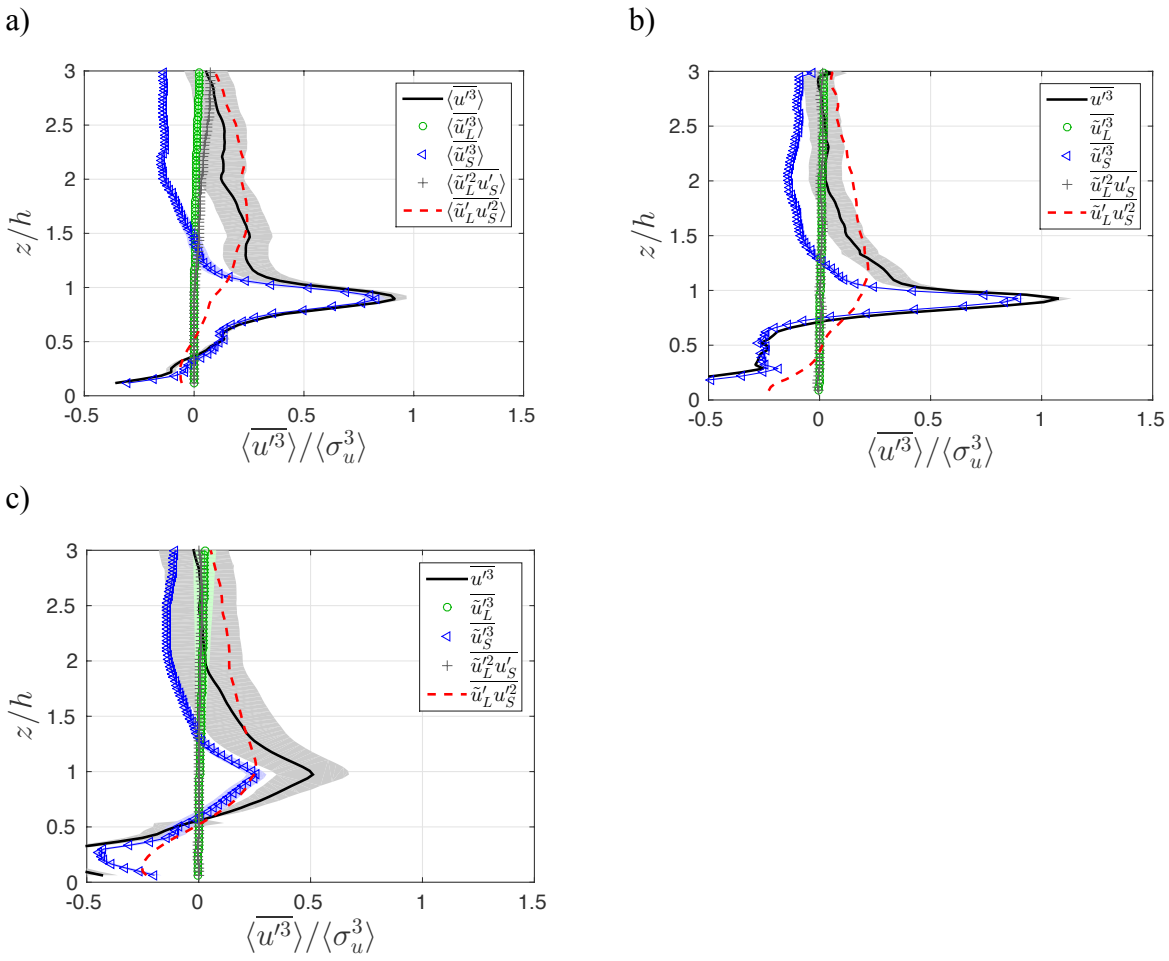

Figure 5.4 Triple decomposition of streamwise skewness, $\langle \overline{u'^3} \rangle$(-) including $\langle \overline{\tilde{u}_L'^3} \rangle$ (o),$\langle \overline{u_S'^3} \rangle$ (◁), $3\,\langle \overline{\tilde{u}_L'^2 u_S'} \rangle$ (+), $3\,\langle \overline{\tilde{u}_L' u_S'^2} \rangle$ (--) all spatially averaged and normalized by $\langle \sigma_u^3 \rangle$ for a) Rcu; b) R1h; c) R3h spatially averaged over a width of $1h$; d) R3h spatially averaged over a width of $3h$.

Within the literature and Chapter 4 of the present work, it has been observed that the non-linear interactions between large-scale momentum regions and small-scales close to the roughness occur in a similar manner for all velocity components (Perret and Rivet, 2013; Blackman and Perret, 2016). In the present work the non-linear interaction between the large-scale momentum regions and the spanwise ($\overline{\tilde{u}_L' v'^2}$) and vertical ($\overline{\tilde{u}_L' w'^2}$) fluctuations are computed for each roughness configuration and compared with $\overline{\tilde{u}_L' u_S'^2}$ (Figure 5.5). In this case the spanwise and vertical fluctuations used are the raw fluctuations with no LSE filtering applied. The results of the 3D cube roughness are in agreement with those of Perret and Rivet (2013) as all three components of velocity have

similar profiles particularly within the canopy. This similarity within and above the canopy is reiterated in the 2D roughness cases; however, there is a modification of the flow above the canopy in the R1h case. In this case the spanwise term differs from the streamwise and vertical profiles. This significant difference (confirmed through analysis of the 99% confidence interval, not shown here) is a result of the 2D skimming flow regime.

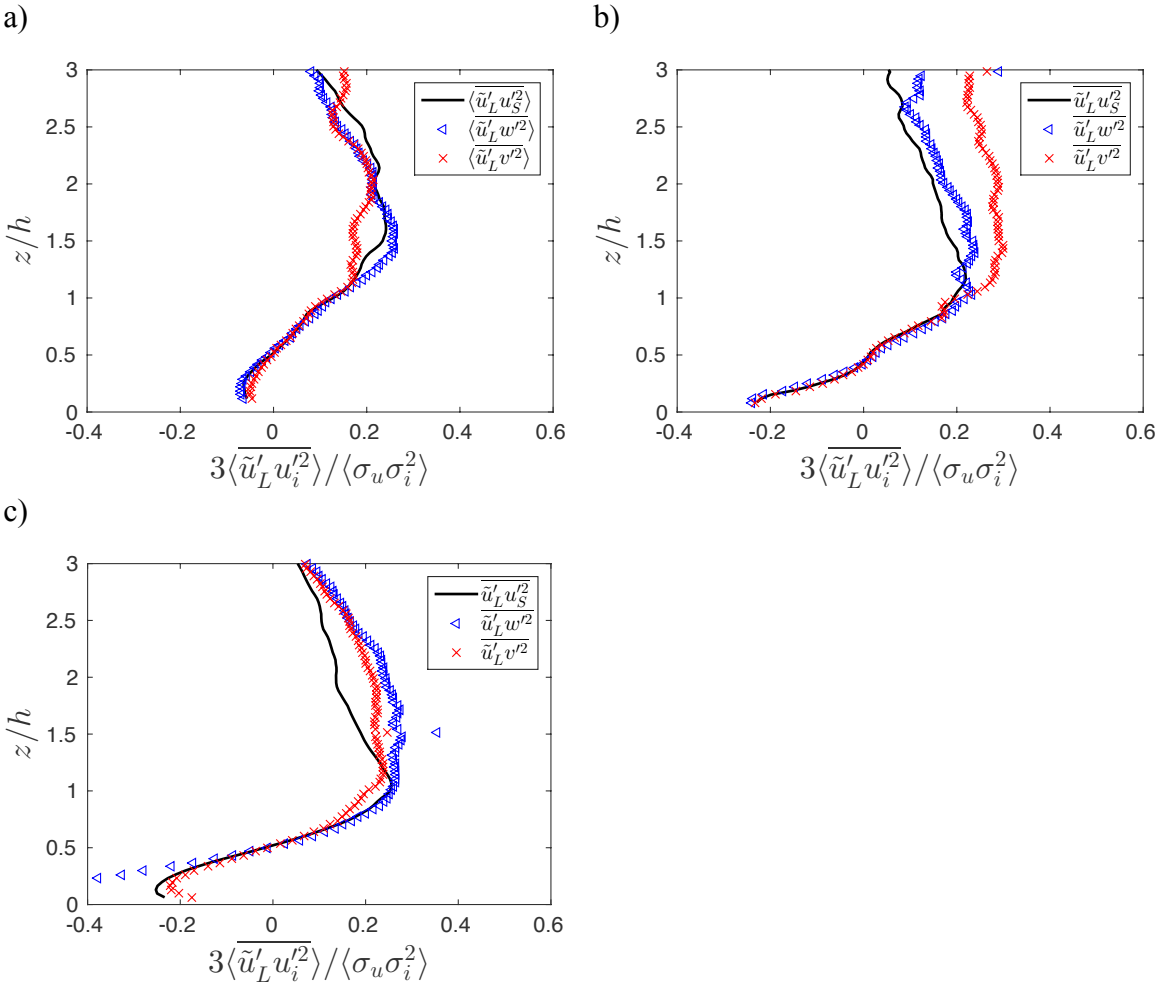

Figure 5.5 Non-linear skewness terms $3\langle\widetilde{u'_L}u'^2_S\rangle$ (-), $3\langle\widetilde{u'_L}w'^2\rangle$ (◁) and $3\langle\widetilde{u'_L}v'^2\rangle$ (×) all spatially averaged and normalized by $\langle\sigma_u\sigma_i^2\rangle$ for a) Rcu; b) R1h; c) R3h.

As described in Chapter 4 the LSE model used in the present work with high-temporal resolution HWA allows for the temporal extrapolation of velocity fluctuations and scale-interactions can, thus, also be investigated temporally without having access to the temporal small-scale signal close to the roughness. Using this technique we will focus on the cross-correlation of the large-scale component with the squared small-scale

fluctuations, $R_{\tilde{u}_L' u_S'^2}$ defined in Chapter 4 (Equation 4.2), which represents the non-linear interaction of the scales. Figure 5.6 shows the temporal evolution of the spatially averaged cross-correlation. In all three boundary layers $R_{\tilde{u}_L' u_S'^2}$ exhibits a strong peak within the roughness sub-layer, which gradually decreases in magnitude with height in the boundary layer. Within the Rcu boundary layer this peak tends to align with a zero time delay until a height of $z/h = 3$ is reached where the peak shifts to approximately $\tau\overline{U}_\infty/\delta = 0.5$. However, in the case of 2D roughness the peak shift increases to approximately $\tau\overline{U}_\infty/\delta = 1.5$ and 1.1 above a height of $z/h = 1.5$ and $z/h = 1$ for the R1h and R3h cases, respectively. As discussed in Chapter 4 this positive peak shift is a result of small-scales interacting with large-scales that occur upstream in the flow and has been previously documented in the literature (Guala et al., 2011). Although the reason for this shift is unknown it suggests that the behaviour of the non-linear interaction between large- and small-scale structures is modified between the roughness sub-layer and above. The present work indicates that this modification becomes more significant within 2D boundary layers, especially in the wake interference flow, which shows modification occurring even within the shear layer. The relationship between large- and small-scale structures is also modified within the canopy at $z/h = 0.5$ where a negative correlation occurs consistently in all three boundary layers. In this region, regardless of roughness configuration, there is a recirculation of the flow within the wake where large-scales within the canopy are opposite in sign to the large-scales above the canopy. This results in a modification of the relationship between large- and small-scales within the canopy.

a)

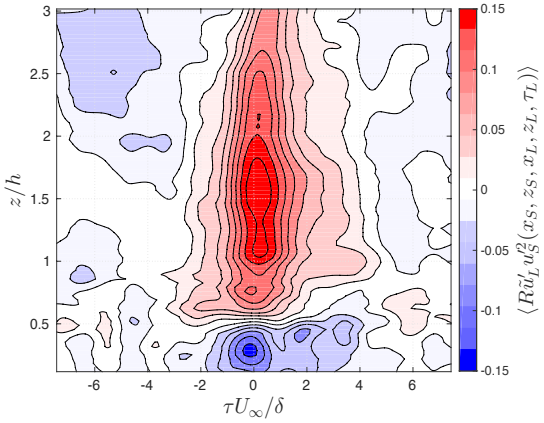

b)

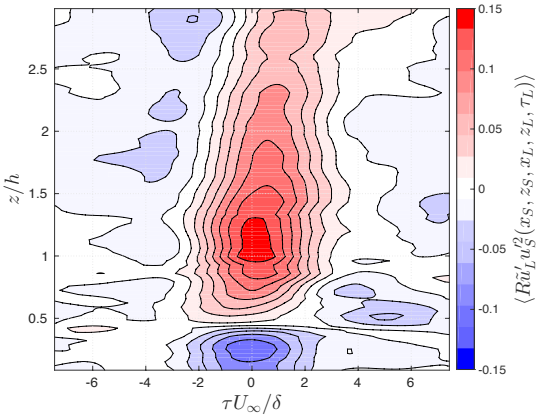

c)

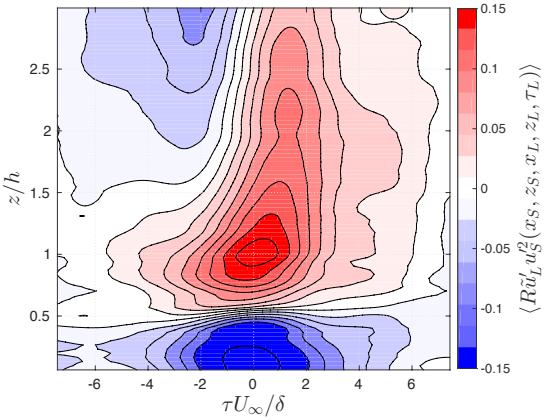

Figure 5.6 Spatially averaged Correlation Coefficient $\langle R_{\tilde{u}'_L u'^2_S} \rangle$ where $x_L = x_S$ and $z_L = z_S$ .of a) Rcu; b) R1h; c) R3h.

A spatially averaged two-point spatio-temporal correlation of the term $\widetilde{u'}_L u'^2_S$ defined in Chapter 4 (Equation 4.2) provides further insight into this non-linear interaction (Figure 5.7). The correlation is computed using a fixed small-scale point (z_S) within the canopy at a height of $z/h = 0.75$.

a)

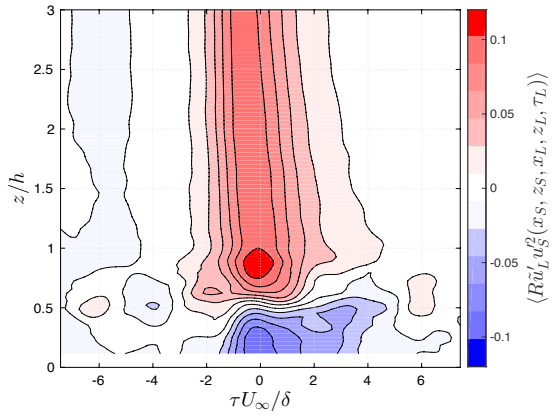

b)

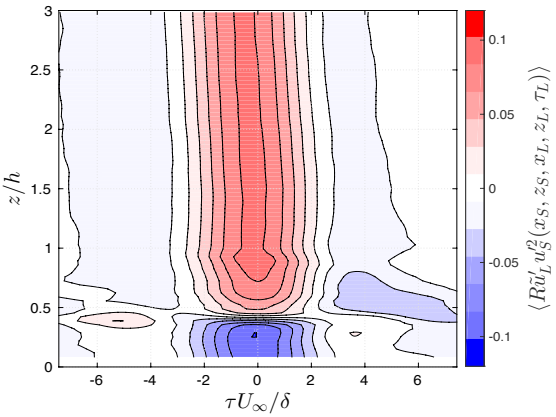

c)

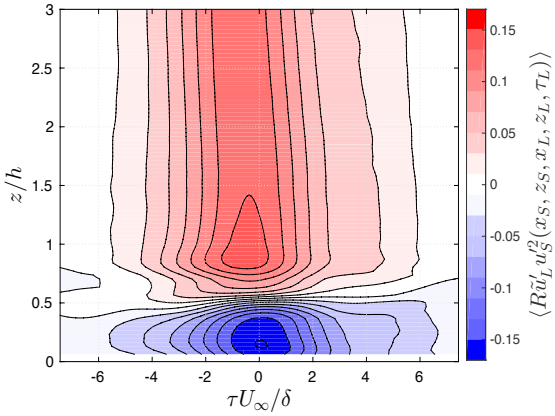

Figure 5.7 Spatially averaged spatial Correlation Coefficient $\langle R_{\tilde{u}_L' u_S'^2} \rangle$ where $x_L = x_S$ and z_S =.0.75 of a) Rcu; b) R1h; c) R3h.

At a height of $z/h = 0.75$ there is a clear peak present with positive correlation even for large time delays in all three boundary layers. A positive correlation suggests that when large-scale, low momentum regions are present above the canopy the small-scales are suppressed, whereas, when large-scale high momentum regions are present above the canopy the small-scales are amplified. Thus, these results support a top-down mechanism of non-linear interaction. Within the canopy the relationship is modified, there is negative correlation between large-scale near-wall fluctuations and the small-scale fluctuations at $z/h = 0.75$. As mentioned above, this is likely caused by the recirculation of the flow within the wake resulting in negative large-scale fluctuations occurring with amplification of the small-scales in the shear layer. As noted above a significant

modification of the nonlinear mechanism occurs in the R3h case. The strong peak at a height of $z/h = 0.75$ and the peak occurring within the canopy are temporally shifted to approximately $\tau\overline{U}_\infty/\delta =$ - 1, whereas in the other roughness cases this peak occurs at approximately $\tau\overline{U}_\infty/\delta =$ - 0.1. As well, in all three boundary layers the peak of correlation tends to shift temporally as the large-scale reference location in the boundary layer increases in height. When the large-scale reference location is close to the small-scale reference at $z/h = 1$ the peak occurs at approximately $\tau\overline{U}_\infty/\delta =$ - 0.1 for R1h and Rcu and $\tau\overline{U}_\infty/\delta =$ -0.6 for R3h, which becomes $\tau\overline{U}_\infty/\delta =$ -0.6, -0.5 and -1.2 for Rcu, R1h and R3h, respectively, with large-scale reference at $z/h = 3$. As discussed in Chapter 4 an inclination angle (θ) can be estimated using Figure 5.7 with $\theta = tan^{-1}\left(\Delta z/_{(\Delta\tau U_\infty)}\right)$ and corresponds to approximately 11.5^o, 14.4^o and 13.8^o for Rcu, R1h and R3h, respectively, which agrees well with the angles extracted from Figure 5.2. Figure 5.8 is a qualitative representation of the non-linear relationship in the R1h and R3h cases. A qualitative representation for Rcu is shown in Chapter 4 of the present work (Figure 4.12). As discussed in Chapter 4 in each of the three roughness configurations the large-scale structures within the boundary layer pass over the small-scale structures close to the roughness at an inclination. Thus, small-scale structures experience effects from the large-scale structure that is slightly downstream of them, which causes an increase in the time-delay of the peak correlation. This confirms that the inclined large-scale structures of high or low momentum detected in the logarithmic layer leave their footprint on the small-scales close to the wall through a non-linear relationship. However, local differences in the flow, such as the thin shear layer within the skimming flow regime (R1h) and the strong flapping shear layer that occurs in the wake interference regime (R3h), result in a modification of the non-linear relationship. The present work demonstrates that the relationship between the large- and small-scale structures occurs in each of the different rough-wall configurations, although significant modification of the relationship occurs in the wake interference 2D roughness case (R3h).

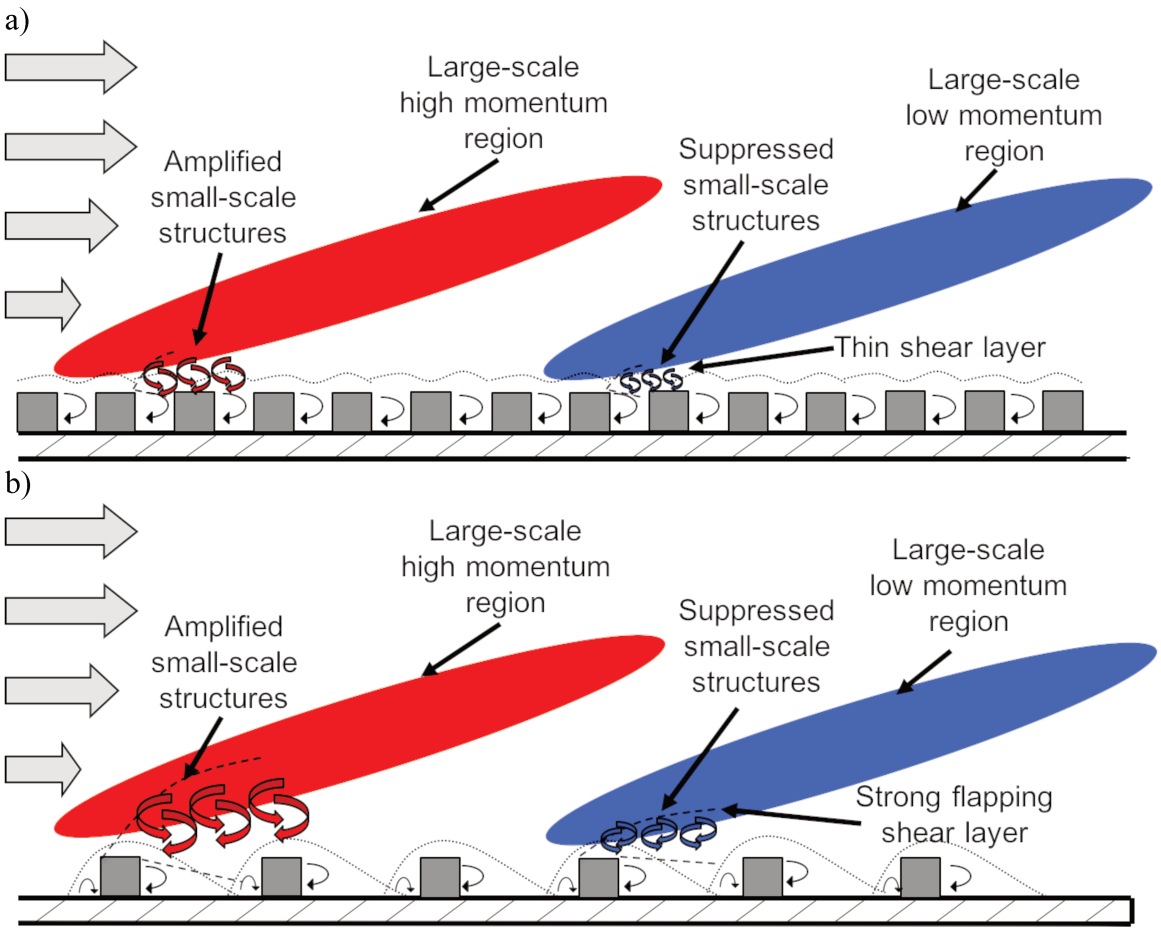

Figure 5.8 Qualitative cartoon illustrating influence of large-scale low momentum structure (blue) and high momentum structure (red) on small-scales generated by the roughness in a) R1h 2D skimming flow regime; b) R3h 2D wake interference flow regime.

5.2.2 Influence of Canyon Aspect Ratio

The LSE model was used to estimate the large-scale contribution to the total σ_u, σ_w and $\overline{u'w'}$ for all six configurations studied in the present work (Figure 5.9). The large-scale contribution to the total σ_u within the canyon is similar for all configurations, whereas, above the canyon this contribution is shown to increase with increasing canyon AR regardless of the upstream roughness configuration. An increase in canyon AR also increases the large-scale contribution to the $\overline{u'w'}$ above the canyon, but within the canyon there is a significant difference between configurations due to the occurrence of negative skewness within the C1h configurations. The large-scale contribution to the total σ_w depends only on the canyon AR where an increase in AR results in decreased

contribution within the canyon. Finally, in all cases within the canyon, the small-scales capture the majority of the variances and shear stress while within the overlying boundary layer the large-scale contribution becomes significant for all quantities, but particularly for the σ_u.

a)

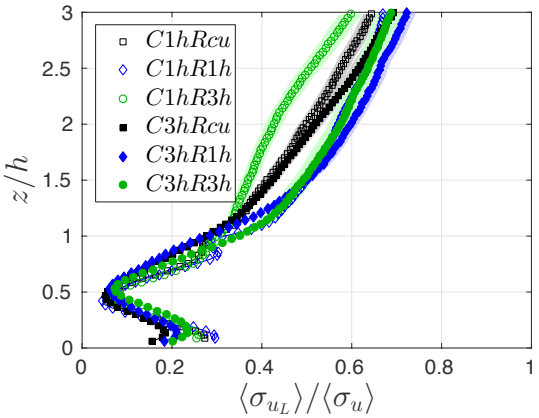

b)

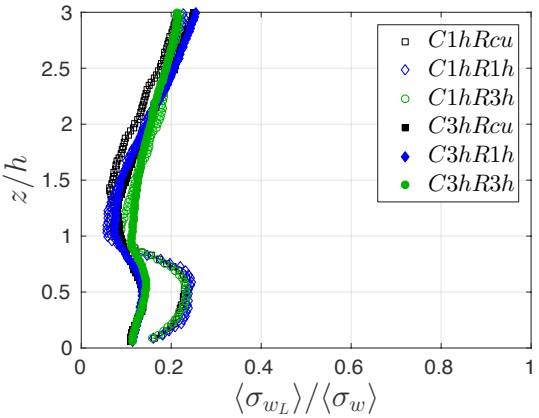

c)

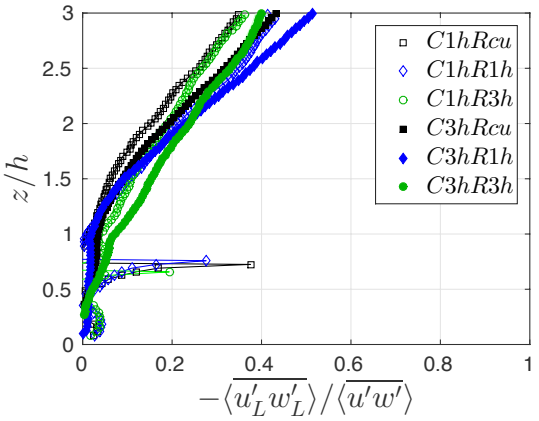

Figure 5.9. Contribution of the large-scales, $\widetilde{u'}_L$ to a) $\langle \sigma_u \rangle$, b) $\langle \sigma_w \rangle$ and c) $\langle \overline{u'w'} \rangle$ spatially averaged over canyon width. Outlying points in $\langle \overline{\widetilde{u'}_L \widetilde{w'}_L} \rangle$ are due to normalization by zero.

The skewness decomposition of the three upstream roughness configurations was discussed above and showed that the large-scales and the cross-term $\overline{\widetilde{u'^2}_L u'_S}$ contribute a negligible amount to the total skewness. Thus, in this section only the contribution of $\overline{u'^3_S}$ and $\overline{\widetilde{u'}_L u'^2_S}$ will be discussed (Figure 5.10). It is clear that an increase in canyon AR decreases the contribution of the small-scales to the total skewness suggesting that there is a reduction in the dominance of energetic downward sweeping motions in the shear

layer within the wake interference flow regime. The cross-term $\widetilde{\overline{u'_L u'^2_S}}$ is shown to be dependent on upstream roughness which, as discussed above, modifies the location of the maximum of this term. As well, increasing the canyon AR results in an increase in the contribution of this term suggesting that this non-linear interaction becomes more important in the wake interference flow regime.

a) b)

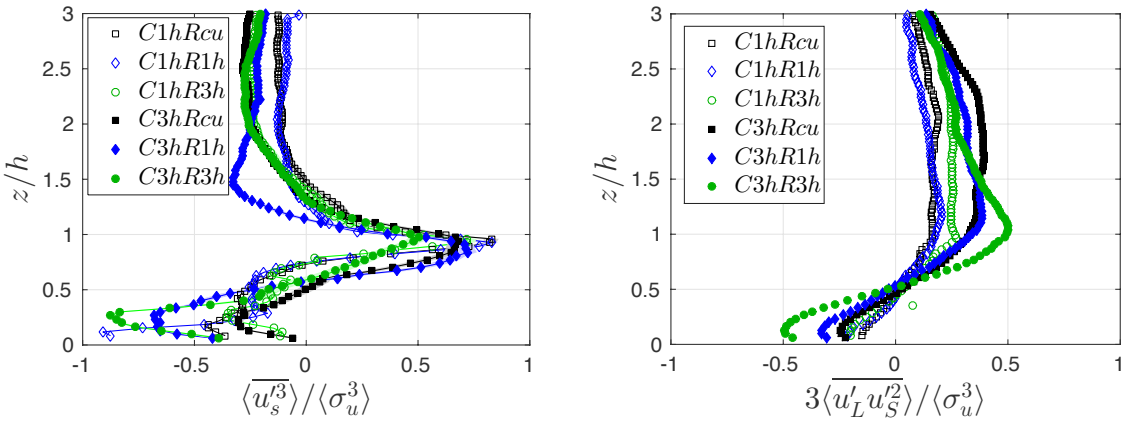

Figure 5.10 Contribution of a) $\langle \overline{u'^3_S} \rangle$ and b) $3\langle \widetilde{\overline{u'_L u'^2_S}} \rangle$ to the streamwise skewness spatially averaged over canyon width and normalized by the value of maximum skewness.

Figure 5.11 shows the non-linear interaction between the large-scale momentum regions and the spanwise ($\widetilde{\overline{u'_L v'^2}}$) and vertical ($\widetilde{\overline{u'_L w'^2}}$) fluctuations compared with $\widetilde{\overline{u'_L u'^2_S}}$. As discussed above, previous work has shown that these non-linear interactions occur in a similar manner for all velocity components of the flow (Perret and Rivet, 2013; Blackman and Perret, 2016). It is evident that the canyon AR has little influence on these relationships, which are predominantly a result of the upstream roughness configuration. Those configurations with R1h roughness upstream have 2D flow resulting in a modified interaction between the large-scale streamwise and the small-scale spanwise fluctuations. This phenomenon requires further investigation through additional roughness configurations and measurements to analyze the 2D flow.

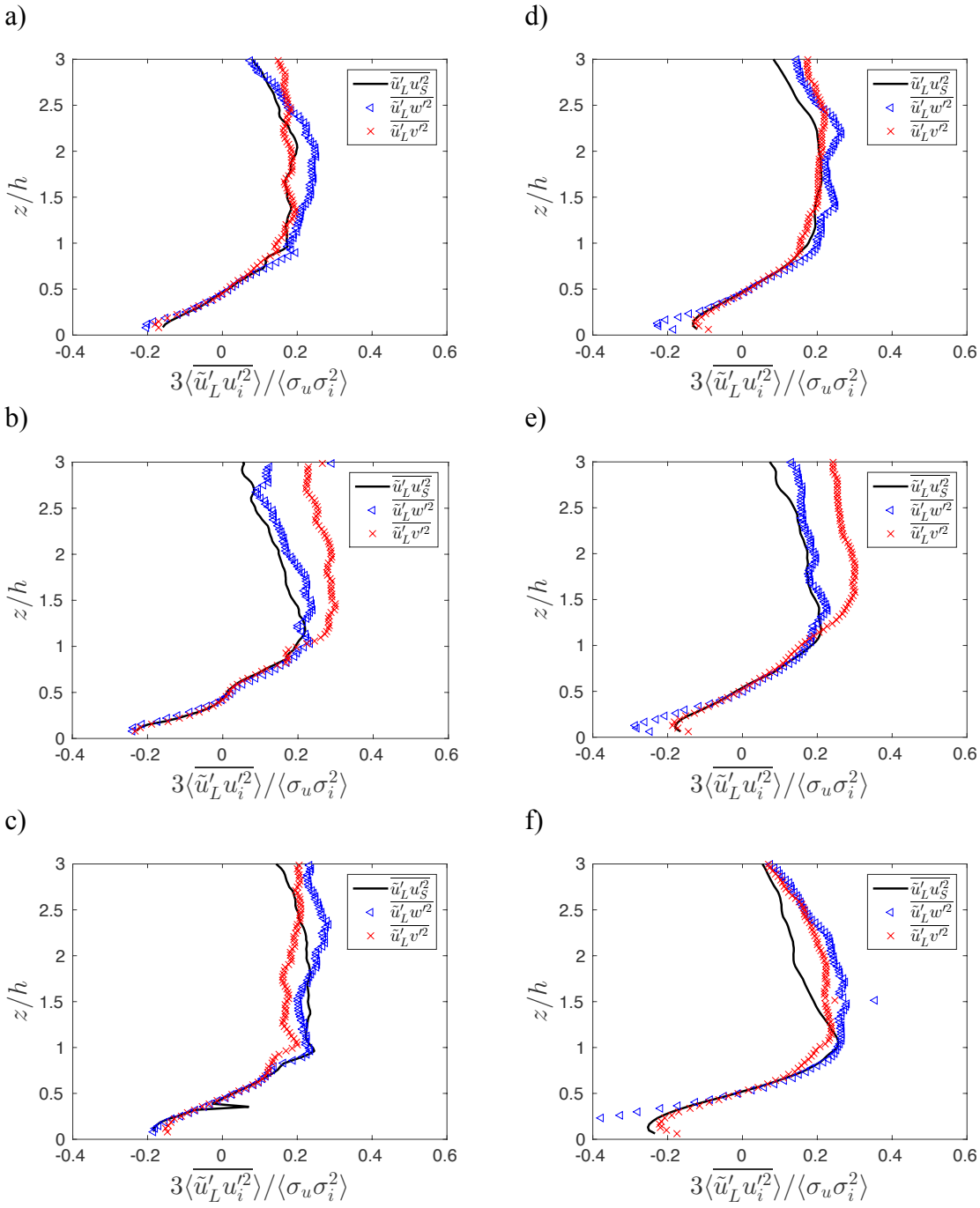

Figure 5.11. Non-linear skewness terms $3\langle\overline{\widetilde{u'_L}u'^2_S}\rangle$ (-), $3\langle\overline{\widetilde{u'_L}w'^2}\rangle$ (◁) and $3\langle\overline{\widetilde{u'_L}v'^2}\rangle$ (×) all spatially averaged over canyon width and normalized by $\langle\sigma_u\sigma_i^2\rangle$ for a) C1hRcu; b) C1hR1h; c) C1hR3h; d) C3hRcu; e) C3hR1h; f) C3hR3h.

5.3 Conclusions

Coherent structures within the rough-wall boundary layer, such as low momentum regions and hairpin vortices, have been well identified within the literature. However, within the rough-wall boundary layer the quantitative relationship between the large-scale momentum regions and the small-scales induced by the presence of the roughness is not fully understood. A simple street canyon model reproduces the main flow features present in most common street configurations, such as coherent structures. However, previous work has demonstrated the non-negligible influence of both the upstream roughness configuration (packing density λ_p and whether 2D or 3D) and the canyon AR on the turbulence phenomena (Blackman et al., 2015a). Recently, work within the rough-wall boundary layer has established that the relationship between the large-scale and small-scale structures is linked to a mechanism of amplitude modulation (Nadeem et al., 2015, Squire et al., 2016; Blackman and Perret, 2016). Specifically, Chapter 4 of the present work demonstrated the use of LSE for triple decomposition and confirmed, through the use of a two-point spatial-temporal correlation, that a top-down mechanism similar to amplitude modulation exists in the rough-wall boundary layer. The present work used experimental evidence from six rough-wall boundary layer configurations consisting of three upstream roughness (cubes or 2D bars with different streamwise spacing) and two street canyon AR configurations with high Reynolds number to answer the specific questions listed in Section 5.1.

1) The upstream roughness configuration geometry and planform packing density, have an influence on the non-linear interactions in the rough-wall boundary layer. Through skewness decomposition it is shown that the peak of the term $\overline{u_L' u_S'^2}$, which represents the influence of the large-scale momentum regions on the small-scales, shifts closer to the shear layer with a change from 3D to 2D roughness. Previous work had shown that the non-linear interaction occurs similarly through all three components of velocity (Perret and Rivet, 2013; Blackman and Perret, 2016), which was confirmed in the present work except in the case of the closely-spaced 2D bar roughness (R1h) whose skimming flow regime induces a modification of the non-linear relationship with the spanwise velocity component.

Through temporal correlation it is evident that the non-linear behaviour is modified closer to the shear layer in 2D wake interference roughness. Finally, a two-point spatio-temporal correlation demonstrated that the non-linear relationship is significantly modified in the wake interference flow regime.

2) The canyon AR was shown to have minimal influence on the non-linear interactions. An increase in canyon AR was shown to decrease the dominance of small-scales and increase the contribution of the non-linear term $\overline{u_L' u_S'^2}$ to the total skewness. However, the appearance of the non-linear interaction through the vertical and spanwise components of velocity was shown to be dependent only on upstream roughness configuration.

The present work, in conjunction with that described in Chapter 4, has confirmed the presence of a top-down mechanism similar to amplitude modulation in rough-wall boundary layers developing over both 2D and 3D roughness. Although the non-linear relationship confirmed by this work shows that large-scale coherent structures interact with and influence the small-scales close to the roughness it is unknown how energy is transferred between scales of structures in the rough-wall boundary layer. The following chapter will focus on quantifying the Turbulent Kinetic Energy (TKE) budget including the dissipation in a cube-roughened wall to better understand energy production and dissipation in the rough-wall boundary layer.

Résumé du Chapitre 6: Bilan d'énergie cinétique turbulente

Le chapitre 6 porte sur la détermination et l'analyse du bilan d'énergie cinétique dans une couche limite se développant au-dessus d'une canopée de cubes à partir des mesures PIV. On s'intéresse ici à l'influence des éléments de rugosité sur le bilan d'énergie cinétique ainsi qu'à la relation entre les structures cohérentes et le phénomène de retour d'énergie vers les grandes échelles. Pour cela, une méthode d'estimation de la dissipation basée sur les principes de la simulation des grandes échelles de la turbulence est utilisée. Un résumé (en français) de ce chapitre est proposé ci-après.

La modélisation précise du transport turbulent dans la couche limite urbaine est essentielle pour améliorer notre compréhension des processus qui régissent le transport de la chaleur, de la quantité de mouvement et de la pollution (Takimoto et al., 2011; Perret et Savory, 2013). Cependant, peu d'études DNS ou LES de la couche limite urbaine ont inclus une analyse détaillée du bilan de l'énergie cinétique turbulente (TKE) et peu d'études expérimentales sont en mesure de proposer une analyse complète en raison de contraintes expérimentales (Castro et al., 2006; Roth et al., 2015).

Typiquement, les méthodes expérimentales se limitent à des bilans s'appuyant uniquement les composantes de vitesse verticale et longitudinale et excluent le calcul direct du transport par les fluctuations de pression et de la dissipation définie par $\varepsilon = \frac{1}{2}\nu\overline{\left(\frac{\partial u_i'}{\partial x_j} + \frac{\partial u_j'}{\partial x_i}\right)^2}$. La dissipation est souvent estimée en utilisant des spectres de vitesse longitudinale (Castro et al., 2006). D'autres méthodes de quantification de la dissipation ont été proposées, comme l'estimation de l'équation de transport de l'énergie cinétique à échelle résolue (Natrajan et Christensen, 2006) et les modèles LE-PIV basés sur l'utilisation d'un modèle de sous-maille (SGS) suivant la méthodologie utilisée dans les approches de simulations des grandes échelles ou LES (Sheng et al., 2000). Cette méthode combine l'utilisation de données de PIV qui, dans la plupart des cas, ne permet pas de capturer les échelles dissipatives, avec un modèle SGS qui rend compte de l'influence de ces échelles. L'utilisation de ces modèles pour examiner le transfert

intermittent d'énergie entre les échelles est d'une importance particulière pour la compréhension de la dynamique de l'écoulement. En effet, il a été démontré récemment que les transferts se produisaient non seulement depuis les grandes échelles vers les petites échelles (transfert direct ou forward scatter), mais aussi des petites échelles vers plus grandes échelles (retour d'énergie ou backscatter) (Natrajan et Christensen, 2006).

Dans le cadre de cette thèse, les données expérimentales pour une couche limite développée au-dessus d'un réseau de cubes décalés ayant des propriétés de turbulence similaires à celles d'une couche limite urbaine sont utilisées pour répondre aux questions spécifiques suivantes:

1) Le bilan de TKE, y compris la dissipation, peut-il être quantifié à l'aide de mesures PIV dans une canopée urbaine?
2) Quelle est l'influence de la présence des éléments de rugosité sur les termes du bilan TKE?
3) Quelles structures cohérentes présentes dans la couche limite urbaine sont liées à l'apparition du phénomène de retour d'énergie?

La résolution spatiale des mesures PIV actuelles est trop faible pour résoudre les échelles dissipatives pour lesquelles les gradients dans le terme de dissipation ε doivent être calculés. Au lieu de cela, la dissipation est déterminée à l'aide d'une méthode qui repose sur l'hypothèse que, à grand nombre de Reynolds, la TKE est produite par les grandes échelles de la turbulence et est transférée en cascade vers les petites échelles, qui dissipent l'énergie (Sheng et al., 2000). Dans cette hypothèse, la TKE est produite par des tourbillons dont la taille caractéristique est l'échelle intégrale tandis que l'énergie est dissipée par les échelles de Kolmogorov au même taux qu'elle est produite. Ainsi, dans le sous-domaine inertiel la TKE n'est ni produite ni dissipée et les tourbillons transfèrent simplement de l'énergie des grandes vers petites échelles sans changement (Sheng et al., 2000). Par conséquent, la dissipation turbulente est égale au transfert d'énergie dans la gamme inertielle. Pour appliquer cette méthode, nous suivons le formalisme de LES, qui utilise le filtrage spatial, ce qui entraîne une séparation des échelles dans la gamme inertielle du spectre de la vitesse. Pour calculer le tenseur de sous-maille τ_{ij} deux méthodes sont utilisées: la méthode directe de transfert d'énergie décrite par Natrajan et

Christensen (2006) et la méthode LE-PIV proposée par Sheng et al. (2000), qui utilise un modèle de sous-maille comme dans les calculs de LES.

La dissipation estimée par les deux modèles est en bon accord, à moins de 10% près, dans la couche limite et à l'intérieur de la canopée. Cependant, à proximité du cube en amont, dans la couche de cisaillement et dans la canopée, il existe un écart important, jusqu'à 40%, entre les deux modèles. Cet écart résulte de la faible résolution de la PIV négligeant les structures à petite échelle qui sont importantes pour la dissipation au sein de la région de recirculation qui existe dans le sillage du cube en amont. Ces structures ne sont pas prises en compte par la méthode directe de transfert d'énergie alors que leur influence est modélisée dans le modèle LE-PIV.

La forme générale du bilan TKE pour un écoulement stationnaire inclut l'advection (Adv), la production (P_d), le transport turbulent (T), le transport par la pression (ψ), la diffusion visqueuse (D_μ) et la dissipation (ε). Dans le présent travail, Adv, P_d et T sont calculés directement à partir des mesures PIV, ε est estimé à l'aide des méthodes décrites ci-dessus, D_μ est considéré comme négligeable pour les écoulements à nombre de Reynolds élevé et, enfin, ψ est estimé comme le reste du bilan.

L'analyse du bilan de TKE indique que l'énergie est transportée loin du cube en amont par la couche de cisaillement, tandis que plus loin en aval, à mesure que la couche de cisaillement se développe, le terme d'advection est positif. L'énergie est produite dans la couche de cisaillement. On observe une diminution de P_d lorsque la couche de cisaillement se développe et aux frontières de la couche de cisaillement. Près du cube en aval, il existe une forte production d'énergie liée la formation d'une couche de cisaillement et de la séparation de l'écoulement. La couche de cisaillement qui se forme au sommet du cube en amont provoque un changement rapide de la vitesse de l'écoulement et une recirculation dans le sillage du cube, ce qui entraîne des termes de production négative. De plus, il est clair que la couche de cisaillement agit pour transporter l'énergie vers la canopée par le biais du transport turbulent. Les régions situées le long du bord de l'obstacle du cube contiennent des structures tourbillonnaires et gagnent de l'énergie grâce au transport turbulent et à l'advection. La dissipation est plus

élevée dans les régions où les structures à petite échelle contrôlent la dynamique de l'écoulement, comme la couche de cisaillement et le sillage du cube en amont. Au fur et à mesure que la couche de cisaillement s'épaissit, la taille des structures augmente et moins d'énergie est produite et dissipée. Le transport par les fluctuations de pression est positif dans la zone de recirculation, tandis qu'il est négatif dans la couche de cisaillement, la zone de séparation d'écoulement sur le cube en aval et les structures tourbillonnaires se produisant sur les bords du cube.

Des travaux récents sur la couche limite de paroi lisse ont démontré que la dissipation instantanée se produit non seulement depuis les grandes échelles vers les petites échelles (forward scatter), mais aussi des petites échelles vers plus grandes échelles (backscatter) (Carper et Porté-Agel, 2004; Natrajan et Christensen, 2006). Pour déterminer si ces événements instantanés de transfert d'énergie sont associés à des structures tourbillonnaires individuelles dans la couche limite, des moyennes conditionnelles à partir d'une estimation stochastique sont utilisées. Il apparait clairemeut que les structures tourbillonnaires à petite échelle dans la couche de cisaillement contribuent directement aux transferts (forward et backscatter) dans cette région. Cependant, en raison de la forme de la couche de cisaillement, la diffusion vers les petites échelles et vers les grandes échelles a tendance à se produire en amont et en aval de l'événement tourbillonnaire. Dans la couche limite, les pics localisés de transfert direct (forward) sont aussi visibles devant et derrière l'événement tourbillonnaire, alors que de forts retours d'énergie se produisent à la fois au-dessus et en amont, et au-dessous et en aval de l'événement tourbillonnaire. Ceci est cohérent avec ce qui a été trouvé dans la couche limite de paroi lisse reliant ces événements de forward et de backscatter à des tourbillons en épingle à cheveux (Carper et Porté-Agel, 2004; Natrajan et Christensen, 2006).

Les principales conclusions de cette analyse sont données ci-dessous:

1) Dans le présent travail, ε est estimé en utilisant deux méthodes, un modèle de gradient LE-PIV (Sheng et al., 2000) et un calcul direct de transfert d'énergie (Natrajan et Christensen, 2006). Les deux méthodes estiment ε en utilisant un filtre spatial passe-bas avec une longueur d'onde de coupure supérieure à la microéchelle de Taylor, ce qui garantit que la séparation entre les grandes échelles

et les petites échelles se situe dans la gamme inertielle des spectres de vitesse (Sheng et al. 2000). Cependant, un écart a été montré entre les deux méthodes, qui peut s'expliquer par le fait que la méthode directe de transfert d'énergie sous-estime la quantité d'énergie à dissiper, de sorte que la méthode LE-PIV est préférée car elle modélise les petites échelles. Les autres termes de bilan ont été calculés directement à partir des mesures PIV, avec le transport par les fluctuations de pression comme résidu du bilan.

2) La couche de cisaillement induite par la présence de la rugosité joue un rôle important dans la production et la dissipation de l'énergie, ainsi que pour transporter l'énergie par l'advection, le transport turbulent et le transport par la pression. Plus la couche de cisaillement se développe au-dessus de la canopée, plus les valeurs de la production et de la dissipation d'énergie diminuent, jusqu'à ce que la séparation se produise près du cube en aval entraînant une forte production. Une région de recirculation, qui se forme dans le sillage du cube en amont en raison de l'interaction entre la couche de cisaillement et la couche de canopée, crée un transport par la pression positif et contient des structures de petite échelle qui dissipent l'énergie. En outre, cette région entraîne une augmentation rapide de la composante de vitesse de façon continue dans la direction longitudinale, générant ainsi des termes de production négative.
3) Enfin, grâce à une estimation stochastique de la moyenne conditionnelle, nous avons montré, comme pour la couche limite en paroi lisse, que des régions localisées de transfert direct (forward scatter) se produisent devant et derrière la tête des tourbillons en épingle à cheveux, alors que les retours d'énergie se produisent dans des régions situées au-dessus et en amont, et en dessous et en aval d'une tête de tourbillons en raison du terme $\tau_{11}S_{11}$. La présence des éléments de rugosité induit une couche de fort cisaillement contenant des structures tourbillonnaires à petite échelle qui contribuent de manière significative aux événements de forward et de backscatter. En outre, les moyennes conditionnelles du champ de vitesse basées sur ces événements ont démontré la nécessité de considérer l'estimation tridimensionnelle de la dissipation.

6 Turbulent Kinetic Energy Budget using PIV

The following chapter is work that was published in Physics of Fluids on the Turbulent Kinetic Energy (TKE) budget in a boundary layer developing over cube roughness (Blackman, K., Perret, L., Calmet, I., Rivet, C., "Turbulent kinetic energy budget in the boundary layer developing over an Urban-like rough wall using PIV," Phys Fluid 29, 085113 (2017)). This work was completed using Particle Image Velocimetry (PIV) measurements aligned in the streamwise (Figure 2.4b) and spanwise direction (Figure 2.4c) within a staggered cube array (Rcu) as described in Chapter 2. The labels A, B, C, D and E shown in Figure 2.4b,c are used in the current chapter to define profile locations. First an introduction to the topic is provided, followed by a description of the dissipation estimation method. The results including the TKE budget, influence of the cube roughness on the budget and the relationship between coherent structures and the occurrence of backscatter are then presented, followed by conclusions.

6.1 Introduction

As discussed in Chapter 4 accurately modeling the turbulent transport in the urban boundary layer is essential to improving our understanding of the processes that govern the transport of heat, momentum and pollution (Takimoto et al., 2011; Perret and Savory, 2013). However, the turbulent boundary layer developing over an urban area is comprised of complex flow structures, such as large-scale regions of either high or low momentum that are believed to be formed by groups of hairpin vortices and a strong shear layer containing small-scale structures induced by the presence of the roughness (Coceal et al., 2007b). Several methods have been used to study the complex turbulent structure of the urban boundary layer such as field experiments (Inagaki and Kanda, 2008; Christen et al., 2009; Inagaki and Kanda, 2010; Takimoto et al., 2011; Roth et al., 2015; Blackman et al., 2015b; Perret et al., 2016), wind tunnel experiments (Takimoto et

al., 2011; Takimoto et al., 2013; Blackman et al., 2015a) and numerical models such as Direct Numerical Simulation (DNS) (Coceal et al., 2007a; 2007b) and Large-Eddy Simulation (LES) (Kanda et al., 2004; Kanda, 2006; Inagaki et al., 2012; Michioka and Sato, 2012). LES is a powerful tool as it can simulate three-dimensional (3D), unsteady turbulence more efficiently than DNS. LES uses spatial filtering, which removes small-scales (unresolved scales) and their effect on the resolved scales is parameterized using a subgrid-scale (SGS) model thereby reducing the computing cost (Carper and Porté-Agel, 2004). However, few DNS or LES studies of the urban boundary layer have included detailed analysis of the TKE budget, as well, few experimental studies are able to include significant analysis due to experimental restraints (Castro et al., 2006; Christen et al., 2009; Roth et al., 2015).

Typically, experimental methods, such as PIV, limit the budget to include only the streamwise and vertical velocity components and exclude the direct calculation of the pressure transport and dissipation defined by $\varepsilon = \frac{1}{2}\nu\overline{\left(\frac{\partial u_i'}{\partial x_j} + \frac{\partial u_j'}{\partial x_i}\right)^2}$. In previous work the pressure transport was the residual of the TKE budget with the dissipation estimated using analysis of longitudinal velocity spectra (Castro et al., 2006; Zhu et al., 2007). This method is typically used, as the spatial resolution of experimental methods is normally too coarse to resolve the dissipative scales at which the gradients in ε must be calculated (Sheng et al., 2000). Perhaps due to this limitation, there are few experimental studies of urban boundary layers that include TKE budget calculations in their work (Castro et al., 2006; Christen et al., 2009; Roth et al., 2015). Of these studies, Castro et al. (2006) provide the most detailed analysis and include analysis of each of the TKE budget terms. The measurements were conducted above a canopy composed of staggered cubes with a plan area packing density $\lambda_p = 25\%$. The dissipation was estimated from the power spectral density in the inertial range with a maximum error of 20% (Castro et al., 2006). As expected, the dissipation rate is approximately balanced by the shear production in the inertial layer of the boundary layer. Near the tops of the cubes the turbulent transport term is an energy sink. The residual of the budget is negative and has a large magnitude, which suggests that pressure transport away from the shear layer is significant (Castro et

al., 2006). To the authors' knowledge no other experimental study has sufficient results for comparison with the present work.

Other methods for quantifying ε have been proposed including estimation from the transport equation of the resolved-scale kinetic energy (Natrajan and Christensen, 2006) and Large-Eddy Particle Image Velocimetry (LE-PIV) models based on the use of a SGS model following the methodology used in Large-Eddy Simulations (Sheng et al., 2000). This method combines the use of PIV that in most cases is unable to resolve the dissipative scales with a SGS model, which takes into account the influence of those scales. As in LES, any of the SGS models, such as the Smagorinsky model, Similarity model or Gradient model, can be used in the LE-PIV analysis. Further details on how these models are applied to PIV are provided in Section 6.2 below.

Examining the intermittent energy transfer between scales is of specific importance to understanding the flow dynamics and has recently been demonstrated to occur not only in the direction of large-scales to small-scales (forward scatter), but also from small-scales to larger-scales (backscatter) (Natrajan and Christensen, 2006). LES sub-grid scale models that don't take this intermittent backscatter into account have been shown to overestimate the mean dissipation in the atmospheric boundary layer (Porté-Agel et al., 2001). Recent work within the smooth-wall turbulent boundary layer has linked intermittent backscatter to the occurrence of hairpin vortices (Natrajan and Christensen, 2006). It was shown through stochastic estimation of the conditional averages of forward and backscatter based on a swirling event that regions of forward scatter occur in front of and behind a hairpin head, whereas, localized backscatter occurs above and upstream and below and downstream of a hairpin head. Finally, through the conditional average of velocity it is shown that converging ejection (Q2) and sweep (Q4) events are linked to the occurrence of forward scatter, while backscatter is linked to diverging Q2 and Q4 events. These results agree with those of a field experiment conducted in the Great Salt Lake Desert of Western Utah by Carper and Porté-Agel (2004). Conditional averages of the vorticity based on either a forward scatter or backscatter event demonstrates that localized forward scatter occurs behind a hairpin head at a convergence of the flow, while backscatter is located below and downstream of a hairpin head at a divergence of the

flow. Although evidence of these localized forward and backscatter events has been found in the smooth-wall turbulent boundary layer and atmospheric boundary layer, this relationship, to the authors' knowledge, has not yet been demonstrated in the rough-wall or urban boundary layer (Carper and Porté-Agel, 2004; Natrajan and Christensen, 2006).

The present work aims to use experimental evidence from a boundary layer developing over a staggered cube array with turbulence properties similar to an urban boundary layer, to answer the following specific questions:

1) Can the TKE budget, including dissipation be quantified using PIV measurements in an urban canopy?
2) What is the influence of the presence of the roughness elements on the TKE budget terms?
3) Which coherent structures present in the urban boundary layer are related to the occurrence of backscatter?

The following section will outline the dissipation estimation method. Next, the results and discussion including the TKE budget, the influence of the roughness elements on the TKE budget terms and an investigation of backscatter and coherent structures are presented, followed by the conclusions.

6.2 Dissipation estimation

As demonstrated later, the spatial resolution of the present PIV measurements is too coarse to resolve the dissipative scales at which the gradients in the dissipation term ε must be computed. Instead the dissipation was determined using Equation 6.1 where S_{ij} is the resolved strain rate tensor calculated using Equation 6.2 and τ_{ij} is the SGS stress tensor.

$$\varepsilon = -\overline{\tau_{ij} S_{ij}} \tag{6.1}$$

$$S_{ij} = \frac{1}{2}\left(\frac{\partial \widetilde{U_j}}{\partial x_i} + \frac{\partial \widetilde{U_i}}{\partial x_j}\right) \tag{6.2}$$

In these equations $\overline{}$ denotes temporal averaging while $\sim$ denotes spatial filtering. This method is based on the assumption that in high Reynolds number flows TKE is produced by large-scales and cascades to small-scales, which dissipate energy (Sheng et al., 2000). It states that TKE is produced by the integral scales while energy is dissipated by the Kolmogorov scales at the same rate that it is produced, thus within the inertial subrange TKE is neither produced nor dissipated and these structures simply transfer energy from large to small-scales without changing (Sheng et al., 2000). Therefore, the turbulent dissipation is equal to the energy transfer in the inertial range. For a mathematical explanation of the method the reader is referred to Appendix A.

To apply this method to the present work we follow the LES formalism, which uses spatial filtering resulting in scale separation within the inertial range of the velocity spectrum. In this formalism, the SGS stress tensor, τ_{ij}, is defined as

$$\tau_{ij_{ET}} = \widetilde{u_i u_j} - \widetilde{u}_i \widetilde{u}_j \tag{6.3}$$

The direct energy transfer (ET) method outlined by Natrajan and Christensen (2006) directly calculates the energy transfer between the large-scale filtered turbulence and the small-scale structures using Equation 6.3. Due to the low spatial resolution of the PIV the small-scale structures in the flow are not fully captured. This method thus may neglect small-scale structures important to energy transfer in urban boundary layers contained in the term $\widetilde{u_i u_j}$ in Equation 6.3.

Sheng et al. (2000) proposed to model the energy transfer with the use of a subgrid scale model, as in LES computations, referred to as the LE-PIV method. In the present work the gradient model as outlined by Clark et al. (1979) is used to estimate ε of the SGS (Equation 6.4).

$$\tau_{ij_{LE-PIV}} = \frac{1}{12}\Delta^2 \left(\frac{\partial \widetilde{U_i}}{\partial x_k}\right)\left(\frac{\partial \widetilde{U_j}}{\partial x_k}\right) \tag{6.4}$$

In this equation Δ denotes the size of the spatial filter used.

As detailed in Chapter 2 the streamwise aligned stereoscopic PIV measurements (Figure 2.4b) used in the present work have been performed in one plane making it impossible to compute the spatial gradient of the instantaneous velocity in the three directions of space but allows for computation in the plane of measurement (x-z). For both the direct energy transfer and LE-PIV methods the missing term $\frac{\partial U_2}{\partial x_2}$ is estimated using the divergence-free condition with the remaining estimated invoking an isotropy condition (Sheng et al., 2000). Similarly, in the case of the spanwise aligned measurements (Figure 2.4c) which were performed in one plane at a time, the divergence-free and isotropy condition were used to compute the missing terms. To justify the assumption of isotropy the missing velocity gradients in each plane were compared with the measured velocity gradients at point *D* in the other measurement plane and good agreement, to within 10%, was found. For further details the reader is referred to Appendix B.

Estimation of the dissipation using the two methods, direct ET and LE-PIV, requires special treatment of the data. The PIV technique acts as a low-pass filtering operation on the velocity field. However, the size and the type of the filter are not well defined, especially when performing stereoscopic PIV. Moreover, the spatial resolution obtained with the PIV processing algorithm does not necessarily lie in the inertial range of the velocity spectrum, which is required for estimation of the dissipation. Thus, in the present work, a low-pass filter is applied to the data prior to the computation of the velocity gradients, using a cut-off wavelength larger than the Taylor micro-scale (λ). This ensures a clear cut-off in the inertial range where the equivalence between the scale energy transfer and the dissipation holds (Sheng et al., 2000).

To determine the cut-off wavelength required for the low-pass filter the dissipation was estimated using both the LE-PIV and ET methods with different low-pass filter sizes applied. The dissipation estimate should be independent of the filter cut-off wavelength if this parameter lies within the inertial range of the turbulent energy spectrum and will be used here as a criterion to validate the choice of the low-pass filter size. Due to differences in the nature of the turbulence within the canopy and within the overlying boundary layer two different filter sizes are applied. From Figure 6.1 at heights $z/h <$

0.8 a filter of size $\Delta_1(x,z) = (0.58h, 0.13h)$ must be applied while at heights $z/h \geq 0.8$ a filter of size $\Delta_2(x,z) = (0.44h, 0.13h)$ is sufficient. In the present work the same low-pass filter was applied for both the LE-PIV and direct ET estimations. In addition, the Taylor microscale λ is estimated using Equation 6.5 and compared with the low-pass filter size to ensure that the chosen cut-off wavelength is larger than λ. Figure 6.2 shows λ along with the low-pass filter size used (Δ_1^x, Δ_2^x), the Kolmogorov scale (η) estimated using Equation 6.6 and the spatial resolution of the PIV (Δx). The estimation of the scales λ and η was performed with the dissipation calculated using the LE-PIV method as it is expected due to the low spatial resolution of the PIV that the direct ET method will neglect some small-scale structures important to energy transfer. It is clear from Figure 6.2 that the spatial resolution of the PIV is too coarse to capture the scales of the order of η necessary for direct calculation of ε and too fine to fall within the inertial range necessary for the calculation of ε using the LE-PIV or ET equations.

$$\lambda = \left(15\overline{u'^2}\,\nu / \varepsilon_{LE-PIV}\right)^{1/2} \tag{6.5}$$

$$\eta = \left(\nu^3 / \varepsilon_{LE-PIV}\right)^{1/4} \tag{6.6}$$

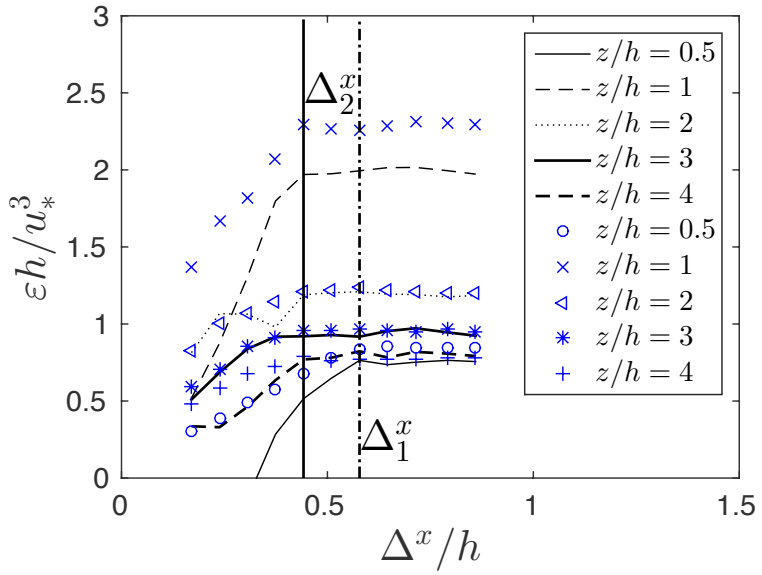

Figure 6.1. Mean dissipation at B calculated using direct energy transfer (lines) and LE-PIV gradient model (symbols) with varying low-pass filter size Δ, all terms normalized by h/u_*^3. The chosen filter sizes Δ_1^x (dotted line) and Δ_2^x (solid line) are also shown.

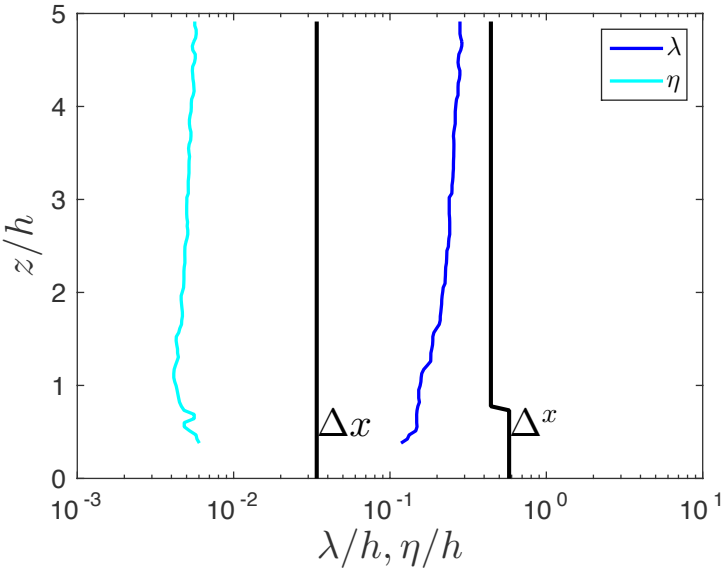

Figure 6.2. Estimation of the Taylor (λ) and Kolmogorov (η) microscales at B using LE-PIV method showing spatial resolution of PIV (Δx) and low-pass filter (Δ^x), all normalized by h.

The longitudinal spatial spectra computed from both PIV and by invoking Taylor's hypothesis of frozen turbulence with Hot-Wire Anemometry (HWA) measurements conducted by Rivet (2014) in the overlying boundary layer can be used to verify the low-

pass filter size and are shown in Figure 6.3. The spectra within the canopy are unavailable so this method can only be used to confirm the size of Δ_2^x. Within the inertial subrange the spectra exhibit a plateau and the chosen cut-off filter should be located on the edge of this plateau to ensure it falls within the inertial subrange. In the present work the chosen filter is shown to be within this range confirming that the filter size is appropriate for the calculation of ε using the LE-PIV or ET equations.

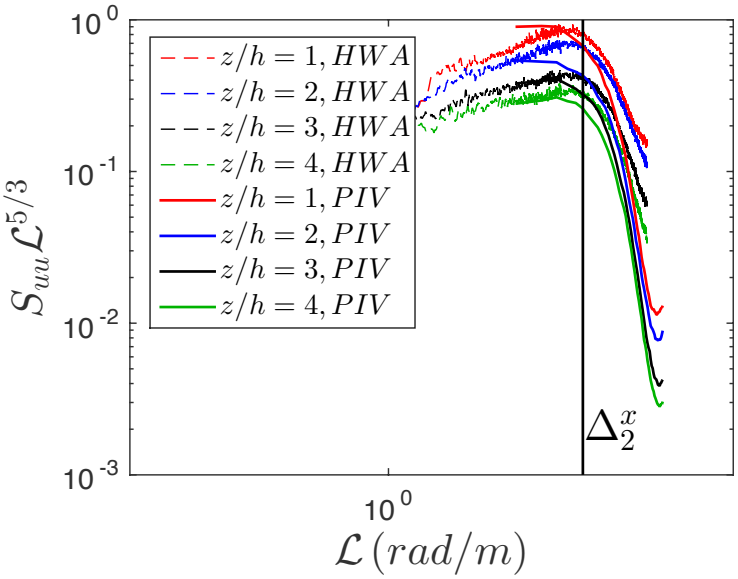

Figure 6.3. Longitudinal spectra calculated at B using PIV (solid lines) and HWA by invoking Taylor's hypothesis (dotted lines). Vertical solid black line: low-pass filter size above the canopy (Δ_2^x).

The longitudinal spectra are also frequently used to estimate the dissipation (Castro et al., 2006) using Equation 6.7,

$$\varepsilon_{Spectral} = \left(\frac{1}{C_1} S_{uu} \mathcal{L}^{5/3}\right)^{3/2} \tag{6.7}$$

where $C_1 \approx 0.52$. In the present work the comparison between the spectral estimate of the dissipation using the longitudinal spatial spectra determined from the PIV, the LE-PIV and ET methods shows good agreement above the canopy at B (Figure 6.4).

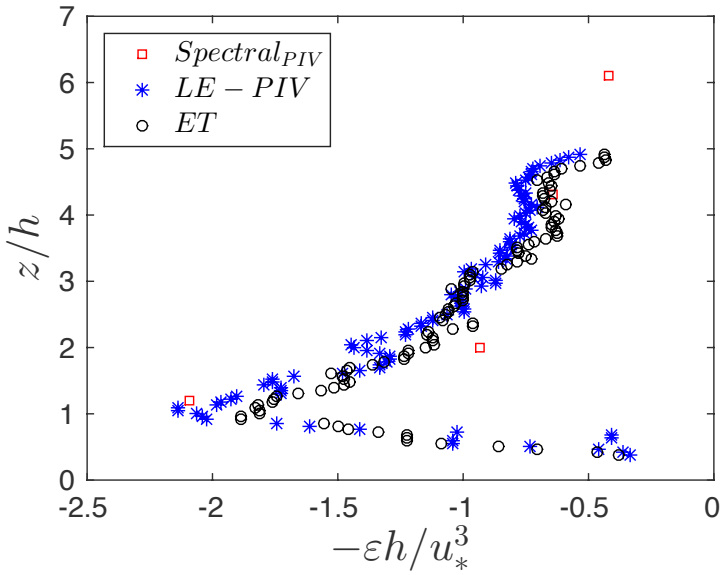

Figure 6.4. Comparison of dissipation estimates at B using longitudinal spatial spectra determined from the PIV (□), LE-PIV gradient model (*) and direct energy transfer, ET (o) methods, all terms normalized by h/u_*^3.

Figure 6.5 shows ε calculated using both the LE-PIV method and the direct ET method at A, B, C, D and E as indicated in Figure 2.4b,c. The dissipation estimated by both models agrees well, to within 10%, within the overlying boundary layer and within the canopy at B and C. However, close to the upstream cube at A there is a significant discrepancy, up to 40%, between the two models within the shear layer and canopy (Figure 6.5a). This discrepancy is a result of the low PIV resolution neglecting small-scale structures important to the dissipation within the recirculation region existing in the wake of the upstream cube. Those structures are not taken into account by the direct ET method while their influence is modelled within the LE-PIV model. Therefore, the gradient SGS LE-PIV model will be used in the remaining analysis of the present work.

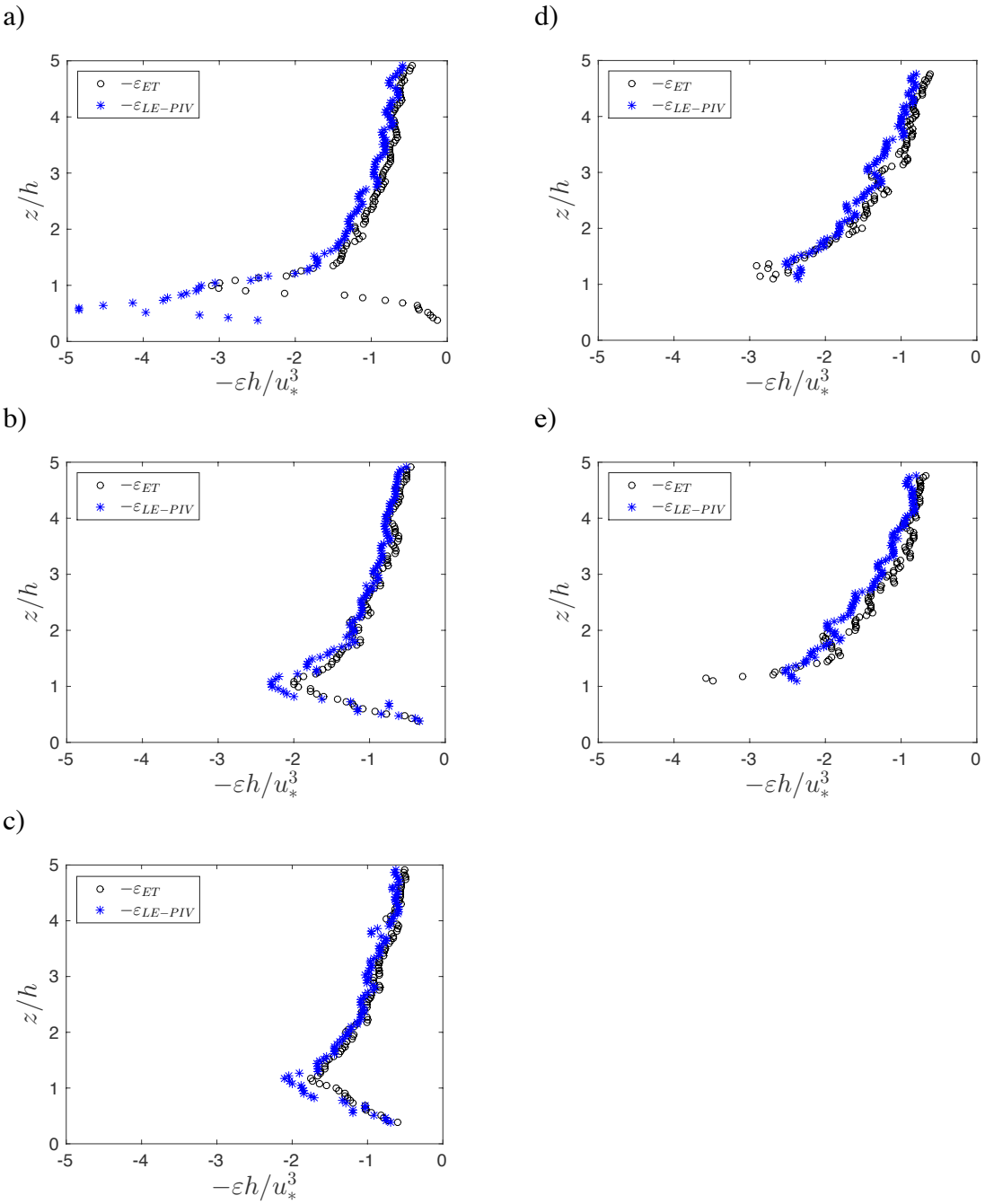

Figure 6.5 Mean dissipation from the *x*-*z* plane (left column) at a) A; b) B; c) C and from the *y*-*z* plane (right column) at d) D; e) E calculated using direct energy transfer, ET (o) and LE-PIV gradient model (*) with all terms normalized by h/u_*^3.

6.3 Results and discussion

6.3.1 Turbulent Kinetic Energy Budget

The general form of the TKE budget for a stationary flow is described in Equation 6.8, where Adv is advection, P_d is production, T is turbulent transport, Ψ is pressure transport, D_μ is viscous transport and ε is dissipation.

$$0 = \underbrace{-\overline{u}_j \frac{\partial \overline{k}}{\partial x_j}}_{Adv} \underbrace{- \overline{u_i' u_j'} \frac{\partial \overline{u_i}}{\partial x_j}}_{P_d} \underbrace{- \frac{1}{2} \frac{\partial \overline{u_i' u_i' u_j'}}{\partial x_j}}_{T} \underbrace{- \frac{1}{\rho} \frac{\partial \overline{P' u_j'}}{\partial x_j}}_{\Psi} \underbrace{+ \nu \frac{\partial}{\partial x_j} \left[\overline{u_i' \left(\frac{\partial u_i'}{\partial x_j} + \frac{\partial u_j'}{\partial x_i} \right)} \right]}_{D_\mu} - \varepsilon \qquad (6.8)$$

In the present work Adv, P_d and T are calculated directly from the PIV measurements. The missing terms in Adv and P_d are assumed to be negligible from symmetry except the missing term $-\overline{v'v'} \frac{\partial \overline{V}}{\partial y}$ in P_d which is estimated using the divergence-free condition. The terms in T involving spanwise gradients cannot be estimated. Finally, ε is estimated using the methods described in Section 6.2, D_μ is considered negligible for high Reynolds number flows and ψ is estimated as the residual of the budget.

Figure 6.6 shows the TKE budget at A, B, C, D and E behind a cube obstacle. Above the roughness sublayer ($z/h > 2$) the production of energy is balanced by the dissipation, while all other terms are negligible. Close to the obstacles (Figure 6.6a), the strong shear layer induced by the presence of the roughness elements produces energy. This production term decreases in magnitude with downstream distance as the shear layer develops over the canopy (Figure 6.6c). Energy is also dissipated within the shear layer and transported to the canopy and overlying boundary layer through advection, turbulent transport and pressure transport by the shear layer. Finally, within the canopy pressure transport is a significant energy sink and is balanced by production and turbulent transport (Figure 6.6b,c) except close to the upstream cube where pressure transport becomes an energy source (Figure 6.6a). This region, which contains a recirculation region, also exhibits high magnitudes of dissipation and weakly positive production. Away from the shear layer in Figure 6.6d,e the production is still balanced by the

dissipation, however, the pressure transport becomes weakly positive within the overlying boundary layer suggesting that energy from the shear layer is transported to these regions.

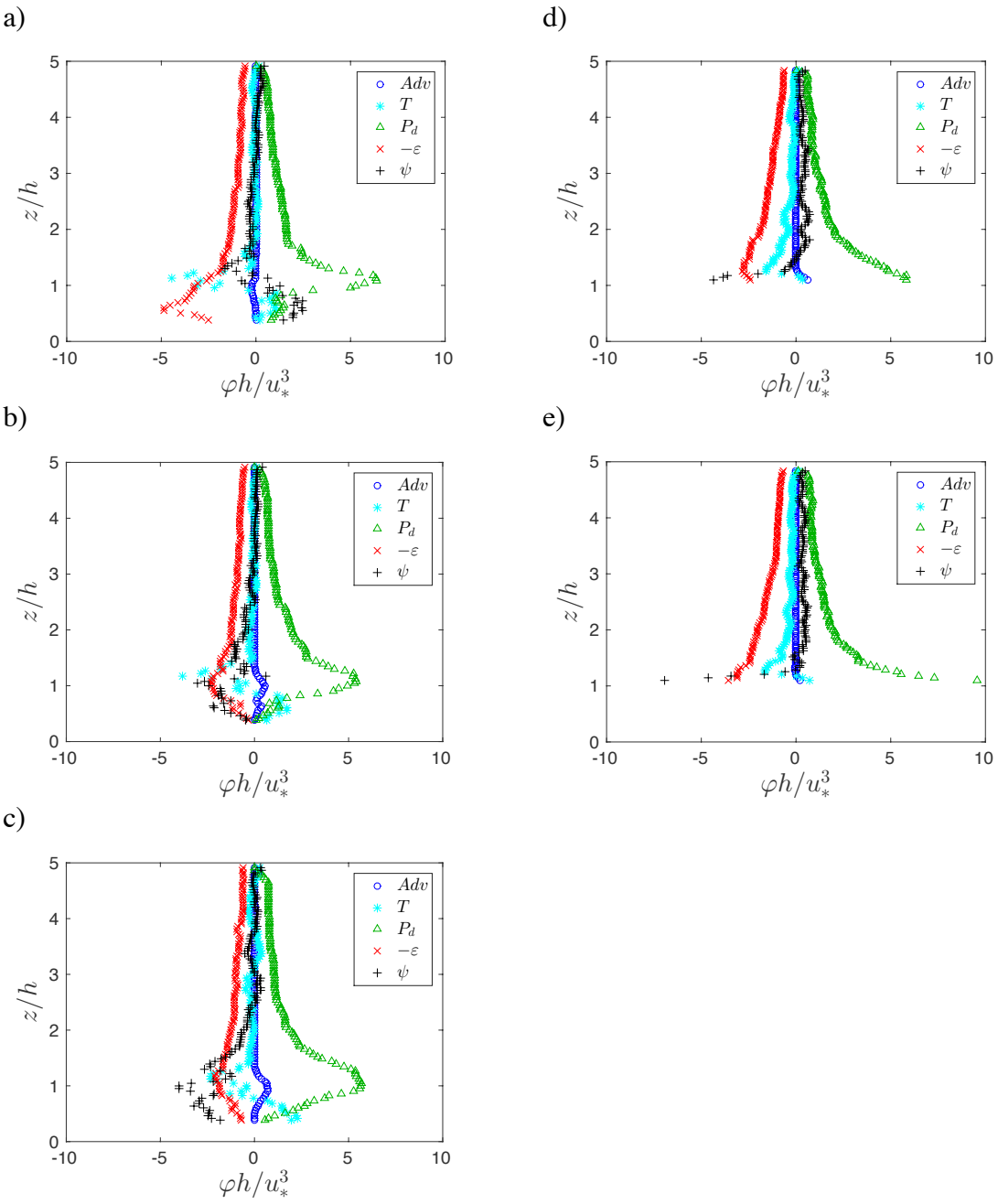

Figure 6.6. Turbulent Kinetic Energy Budget with $\varepsilon_{LE\text{-}PIV}$ dissipation from the *x*-*z* plane (left column) at a) A; b) B; c) C and from the *y*-*z* plane (right column) at d) D; e) E with all terms normalized by h/u_*^3.

There are few experimental studies that can be used for comparison with the present work. Castro et al. (2006) provide the TKE budget of a 25% staggered cube array where ε is estimated using the longitudinal velocity spectra computed with Taylor's hypothesis of frozen turbulence (Equation 1.3). Figure 6.7 shows the TKE budget terms of the present work with those of Castro et al. (2006) at B (only production, ε and pressure transport are shown for clarity). There is good agreement in the production of energy; however, the present work results in a lower magnitude of ε throughout the boundary layer. The estimates obtained in the present work agree well with those from Leonardi and Castro (2010) who performed a DNS of staggered cube roughness with $\lambda_p = 25\%$. These authors stated that unlike smooth-wall boundary layers the ratio of production to ε is significantly higher than unity especially near the cubes. Spatial averages show that just above the cubes within the shear layer the ratio of production to ε is approximately 2.8, while in the present work a spatial average in the x-direction results in a ratio of approximately 2.7. Therefore, the discrepancy between the present work and that of Castro et al. (2006) suggests that there is an over estimation of the dissipation in Castro et al. (2006) as the ratio of production to dissipation is close to unity. This discrepancy is likely due to the relative height of the boundary layer, which is approximately $19.5h$ in the present work, but only $7.5h$ in Castro et al. (2006). A relatively low boundary layer thickness causes changes in the relationship between inner and outer layer flow structures resulting in changes to energy production and dissipation (Jiménez, 2004). Furthermore, the discrepancy could be due to the limitation of Taylor's hypothesis in regions of highly turbulent flow, such as the shear layer and demonstrates the benefit of using the present approach to obtain a more accurate dissipation rate.

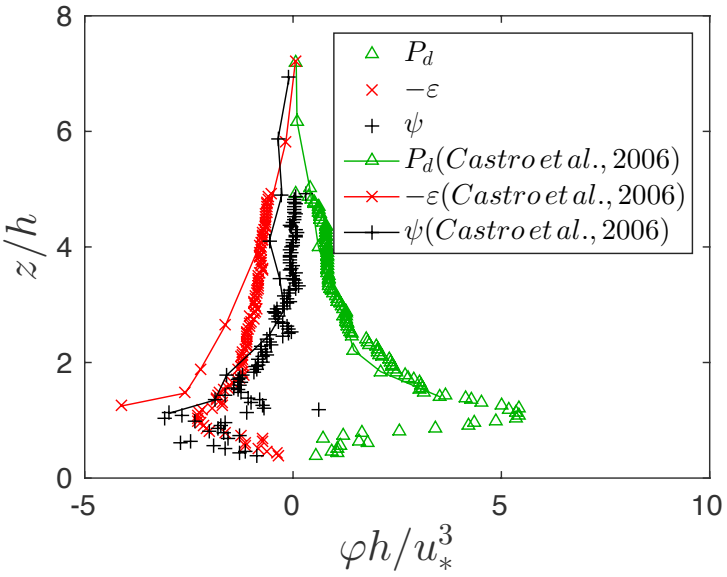

Figure 6.7. Production, ε and pressure transport of Turbulent Kinetic Energy budget compared with results from Castro et al. (2006) at *B*, all terms normalized by h/u_*^3.

In the present work the variation of production with x/h warrants further examination. Figure 6.8 shows the production decomposed into the contribution of each velocity gradient term (negligible terms not shown for clarity). At all locations the largest contribution is the term $-\overline{u'w'}\,\partial\overline{U}/\partial z$ which is a result of the strong shear layer that is induced by the presence of the roughness. However, within the canopy close to the upstream cube there is a large contribution of the term $-\overline{u'u'}\,\partial\overline{U}/\partial x$ which is balanced by the term $-\overline{v'v'}\,\partial\overline{V}/\partial y$ causing weakly positive production in this region (Figure 6.8a). The negative production in the term $-\overline{u'u'}\,\partial\overline{U}/\partial x$ suggests that flow is not in equilibrium and it has been previously shown to occur in asymmetric flows such as, the wake of a thin plate (Hayakawa et al., 1992), the wake of two cylinders of different diameters (Beguier et al., 1978) and around a wall-mounted cube (Yakhot et al., 2006). The negative term $-\overline{u'u'}\,\partial\overline{U}/\partial x$ is attributed to a rapid change of the flow in the recirculation region, resulting in positive $\partial\overline{U}/\partial x$ (Hayakawa et al., 1992; Yakhot et al., 2006). In the present work this rapid increase occurs within the wake of the upstream cube at *A* (Figure 6.8d) where the shear layer interacts with the canopy layer forming a recirculation region with large positive $\partial\overline{U}/\partial x$. Downstream of the wake the term $-\overline{u'u'}\,\partial\overline{U}/\partial x$ becomes positive reaching a maximum just above the canopy layer suggesting that in this region

this term is related to the growth of the shear layer.

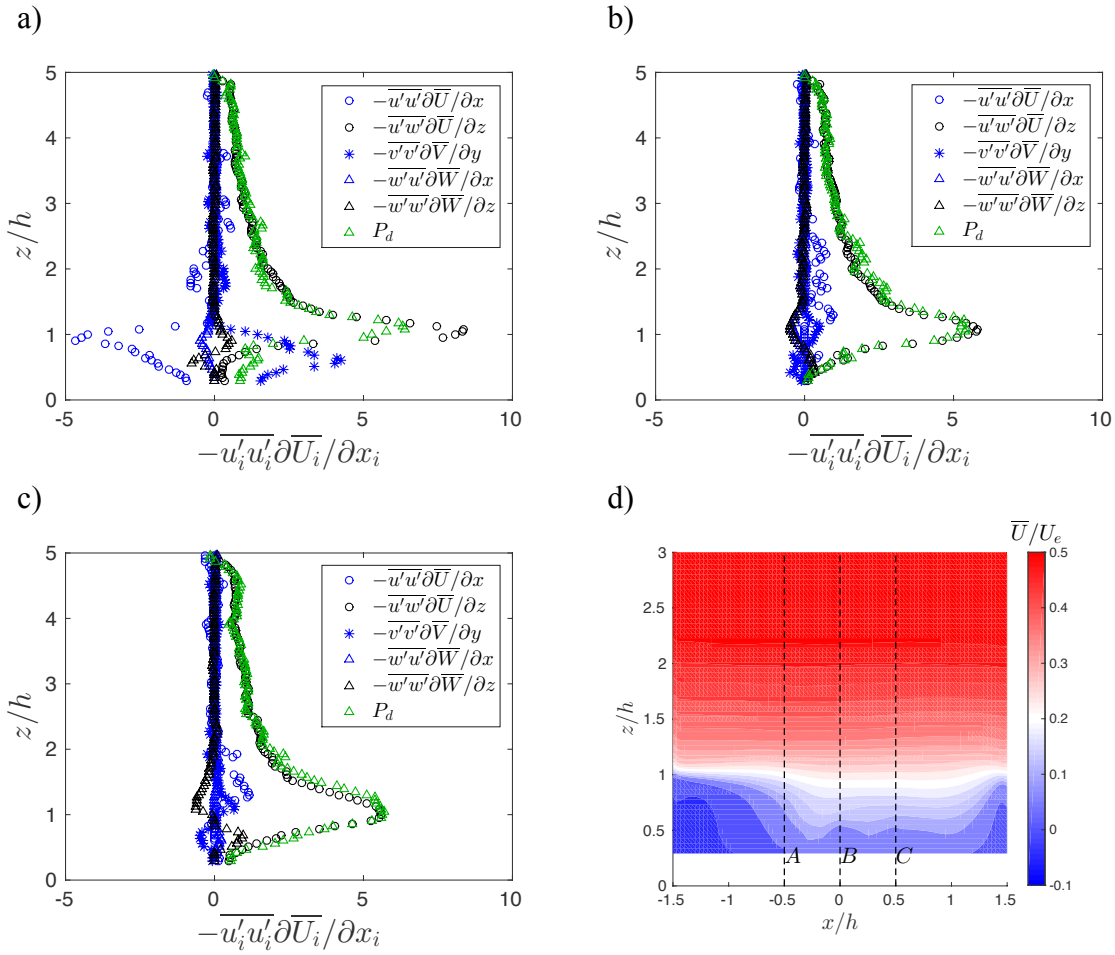

Figure 6.8. Decomposed turbulence production with total production (Δ) at a) A; b) B; c) C where negligible terms are not shown for clarity and all terms normalized by h/u_*^3; d) Mean streamwise velocity normalized by U_e.

The decomposition of the advection and turbulent transport into the contribution of each velocity gradient is shown in Figure 6.9. Advection is due to the vertical velocity and vertical TKE gradient that exists within the shear layer. The turbulent transport is more difficult to interpret due to the noise of the 3rd order statistics. However, close to the shear layer the peak of turbulent transport is a result of the vertical gradients of $\overline{u'u'w'}$ and $\overline{w'w'w'}$.

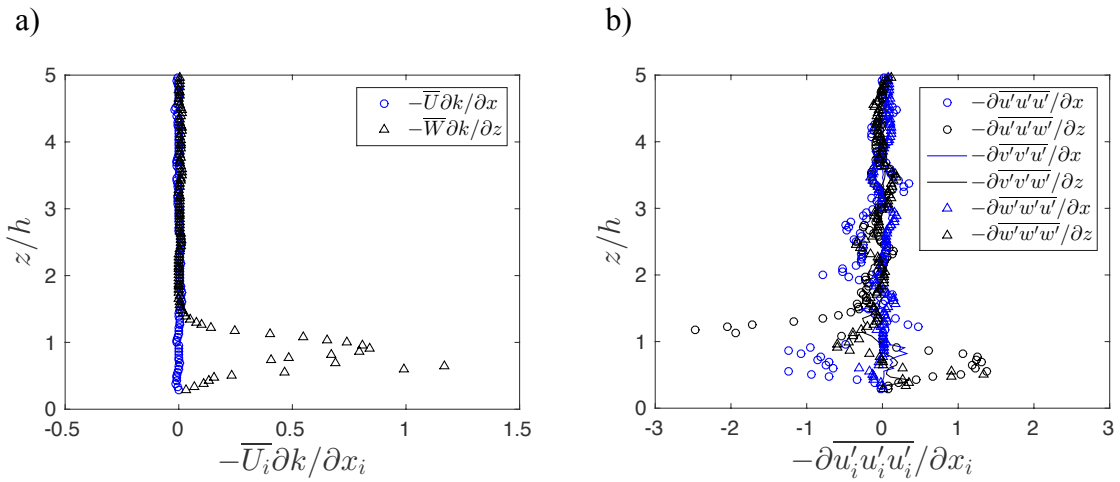

Figure 6.9. Decomposition of a) advection; b) turbulent transport at B, all terms normalized by h/u_*^3.

6.3.2 Influence of cube roughness

The influence of the cube roughness on the TKE budget terms is important to understanding energy transfer within the urban boundary layer. Figure 6.10 shows the mean contours of each term in the x-z (left column) and y-z (right column) planes. Energy is advected away from the upstream cube by the region of strong shear, while further downstream, as the shear layer develops, the advection term is positive (Figure 6.10a). Energy is produced within the shear layer with the magnitude decreasing as the shear layer grows and at the edges of the shear layer at $y/h = 0.5$ and 1.5 (Figure 6.10b). Near the downstream cube at $x/h = 1.25$ there is strong energy production from the formation of a shear layer and separation of the flow. As well, it is clear that the shear layer acts to transport energy away through turbulent transport to the canopy (Figure 6.10c). The regions along the edge of the cube obstacle at $y/h = 0.5$ and 1.5 contain vortical structures formed along the sides and edges of the cube that obtain energy through turbulent transport and advection (Figure 6.10a,c). Dissipation is highest in regions where small-scale structures control the flow dynamics, such as the shear layer and the wake of the upstream cube (Figure 6.10d). As the shear layer grows the size of the structures within increase and less energy is produced and dissipated. The recirculation region forms an area of positive pressure transport, whereas the shear layer, the flow separation on the downstream cube and the vortical structures occurring at the

edges of the cube induce negative pressure transport (Figure 6.10e). Lumley (1978) proposed to model the pressure transport as $\psi = {}^{-2}/_{5}\, T$ resulting in a pressure transport of opposite sign to the turbulent transport. In the present work the pressure transport is non-negligible with a magnitude exceeding that of the turbulent transport. This non-negligible pressure transport within the wake has been previously noted in the wake of a wake generating body (Liu and Thomas, 2004) and a permeable rib plate (Panigraphi et al., 2008) and has been shown to be a result of an adverse pressure gradient. This implies that the simplified model proposed by Lumley (1978) cannot account for the strong pressure gradients present in the urban canopy.

a)

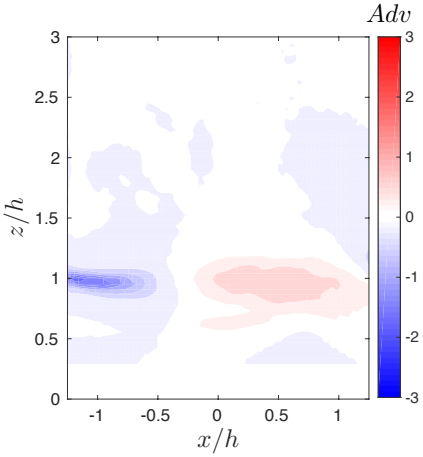

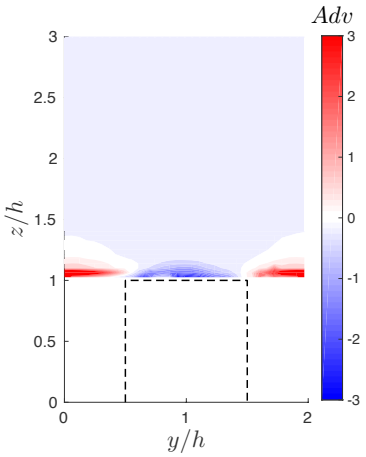

b)

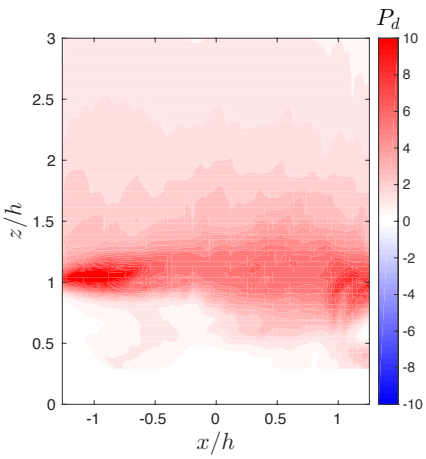

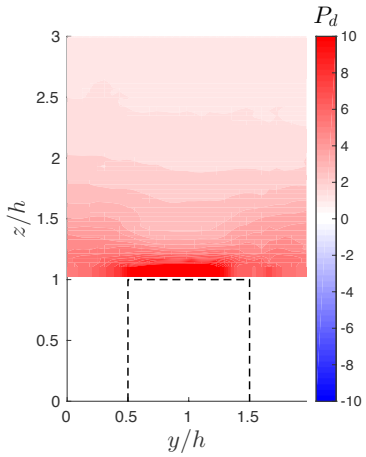

c)

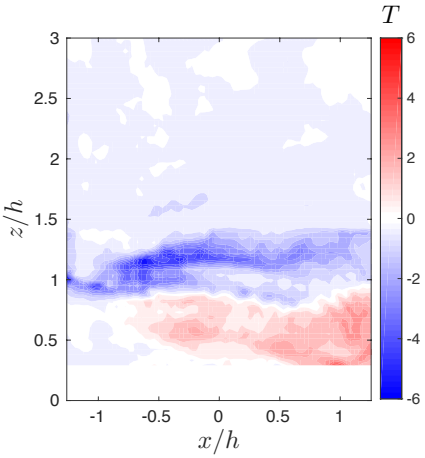

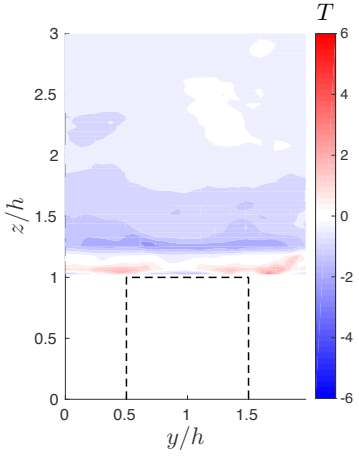

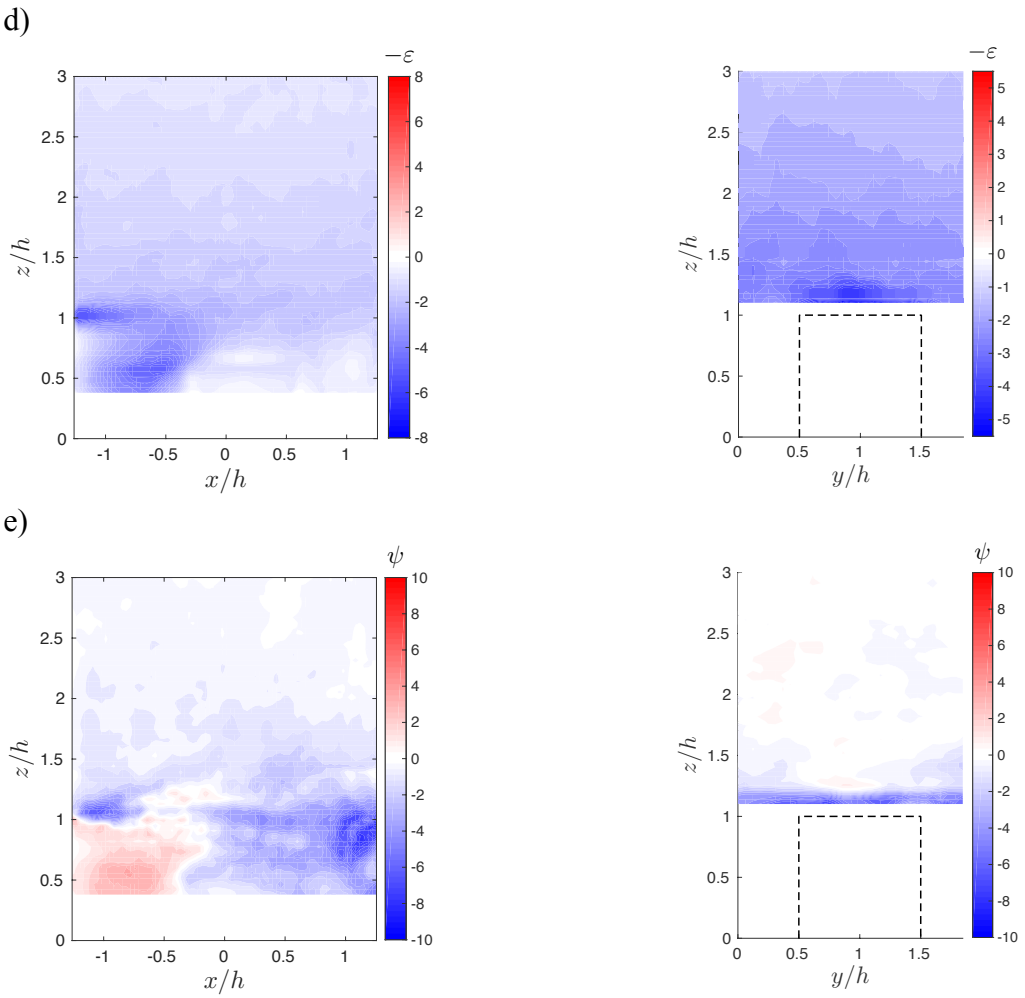

Figure 6.10. Spatial variability of TKE budget terms a) advection; b) production; c) turbulent transport; d) dissipation; e) pressure transport in the *x*-*y* plane (left column) and *y*-*z* plane (right column), all terms normalized by h/u_*^3.

6.3.3 Backscatter and coherent structures

As mentioned above, recent work in the smooth-wall boundary layer has demonstrated that instantaneous dissipation occurs not only in the direction of large-scales to small-scales (forward scatter), but also from small-scales to larger-scales (backscatter) (Carper and Porté-Agel, 2004; Natrajan and Christensen, 2006). In the present work this is confirmed from the PDF of the instantaneous dissipation spatially averaged over the extent of the PIV measurement plane (Figure 2.4b), which shows significant backscatter ($-\epsilon > 0$). Like the PDF of instantaneous dissipation, the PDFs of τ_{ij} computed using the LE-PIV gradient model and spatially averaged over the extent of the PIV field exhibit

non-gaussian behaviour with non-zero and asymmetric PDF tails agreeing with the behaviour found in the atmospheric boundary layer (Figure 6.12) (Carper and Porté-Agel, 2004).

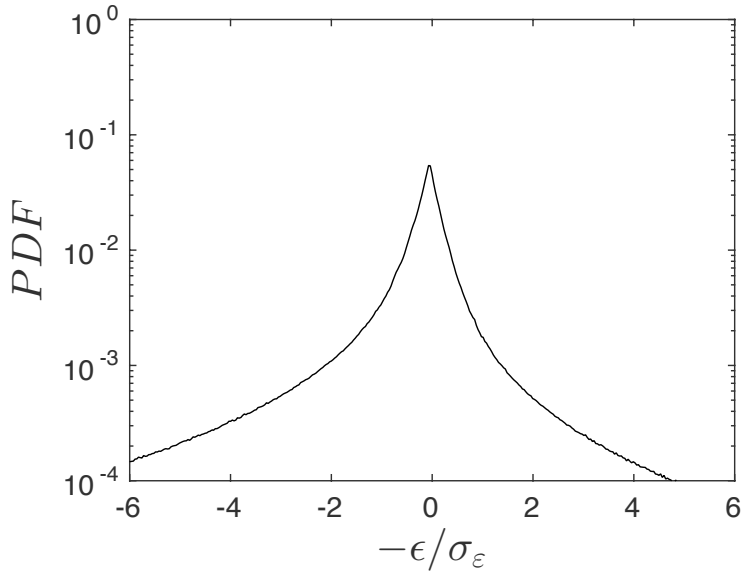

Figure 6.11. PDF of instantaneous dissipation (ϵ) normalized by σ_ε.

a) b)

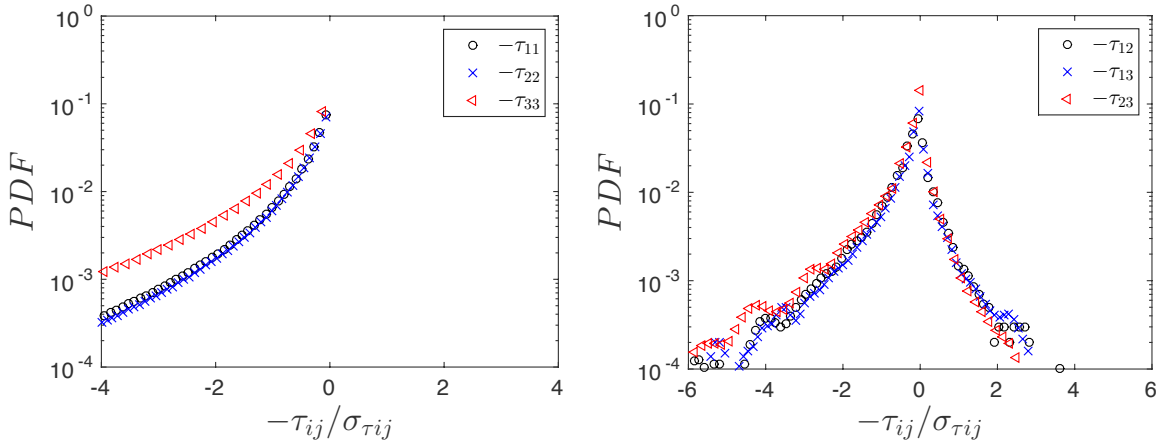

Figure 6.12. PDF of instantaneous stress tensor τ_{ij} normalized by $\sigma_{\tau_{ij}}$ with every third point shown for clarity.

Backscatter events within the smooth-wall boundary layer and atmospheric boundary layer have been linked to coherent hairpin vortices that occur within the overlying boundary layer and have been shown to be qualitatively similar to those found in the rough-wall boundary layer (Carper and Porté-Agel, 2004; Natrajan and Christensen,

2006). Conditional averages will be used to determine the nature of the flow structure related to these backscatter events in the rough-wall boundary layer.

To ensure only significant forward scatter (ϵ_f) and backscatter (ϵ_b) events are included in this analysis, a threshold is first imposed at each grid location thereby minimizing any decorrelation caused by weak or insignificant dissipation events (Natrajan and Christensen, 2006). The threshold used in the present work corresponds to that applied by Natrajan and Christensen (2006) in the smooth-wall boundary layer and is based on the mean forward scatter (ε^+) and backscatter (ε^-) at each grid location. Thus, the instantaneous dissipation at each grid location is

$$\phi(x,y) = \begin{cases} \epsilon_f = \epsilon & if \ \ \epsilon > \varepsilon^+ \\ \epsilon_b = \epsilon & if \ \ \epsilon < \varepsilon^- \\ 0 & otherwise \end{cases} \tag{6.9}$$

To determine whether these instantaneous forward and backscatter events occur consistently with individual vortical structures in the boundary layer, conditional averages are used. Due to the large number of events that must be included for statistical convergence direct computation of the conditional average is not possible, instead Stochastic Estimation will be used to estimate the conditional average (Adrian, 1975). Stochastic Estimation estimates the conditional average from unconditional correlations by minimizing the mean-square error between the true conditional average and a given estimate. The conditional average of the forward scatter or backscatter associated with a vortical structure is therefore,

$$\overline{\phi(x,y)|\lambda_{cl}(x_r,y_r)} = \frac{\overline{\phi(x,y,z)\lambda_{cl}(x_r,y_r)}}{\overline{\lambda_{cl}(x_r,y_r)\lambda_{cl}(x_r,y_r)}}\lambda_{ci}(x_r,y_r) \tag{6.10}$$

where (x_r, y_r) is the chosen reference location and λ_{ci} is the swirling strength, which is the imaginary part of the complex eigenvalues of the velocity gradient tensor.

The average velocity field associated with the swirling event can also be estimated as

$$\overline{u'_j(x,y)|\lambda_{ci}(x_r,y_r)} = \frac{\overline{u'_j(x,y,z)\lambda_{ci}(x_r,y_r)}}{\lambda_{ci}(x_r,y_r)\lambda_{ci}(x_r,y_r)}\lambda_{ci}(x_r,y_r) \quad (6.11)$$

where u'_j is the jth fluctuating velocity component.

Figure 6.13 shows the conditionally averaged forward and back scatter contours along with the streamwise and vertical velocity fluctuations associated with a swirling event at $z/h = 1$ within the shear layer and $z/h = 4$ within the boundary layer. To improve the estimate the conditional average was computed using a reference location (x_r) at each x/h grid location and then spatially averaged in the x-direction so that $\delta x = x - x_r$. It is clear that the small-scale vortical structures within the shear layer contribute directly to both strong forward and backscatter in this region (Figure 6.13a,b). However, due to the shape of the shear layer the forward and backscatter tend to occur in front of and behind the swirling event. Contrarily, within the boundary layer localized peaks of forward scatter are shown to occur in front of and behind the swirling event, while strong backscatter occurs above and upstream of the swirling event and below and downstream of the vortex core (Figure 6.13c,d). This is consistent with what has been found in the smooth-wall boundary layer linking these forward and backscatter events to coherent hairpin vortices (Carper and Porté-Agel, 2004; Natrajan and Christensen, 2006). The regions of forward scatter in the boundary layer have an angle of inclination between 10^o and 18^o. These angles agree well with the angle of inclination of large-scale low and high momentum regions, which are believed to be formed by groups of hairpin vortices, found in Chapter 4 of the present work and previous work (Castro et al., 2006; Coceal et al., 2007a; Guala et al., 2011; Rivet, 2014; Blackman and Perret, 2016). The presence of the roughness elements induces a strong shear layer containing small-scale structures that produce both strong forward and backscatter resulting in two distinct flow regions with distinct relationships to the dissipation of energy.

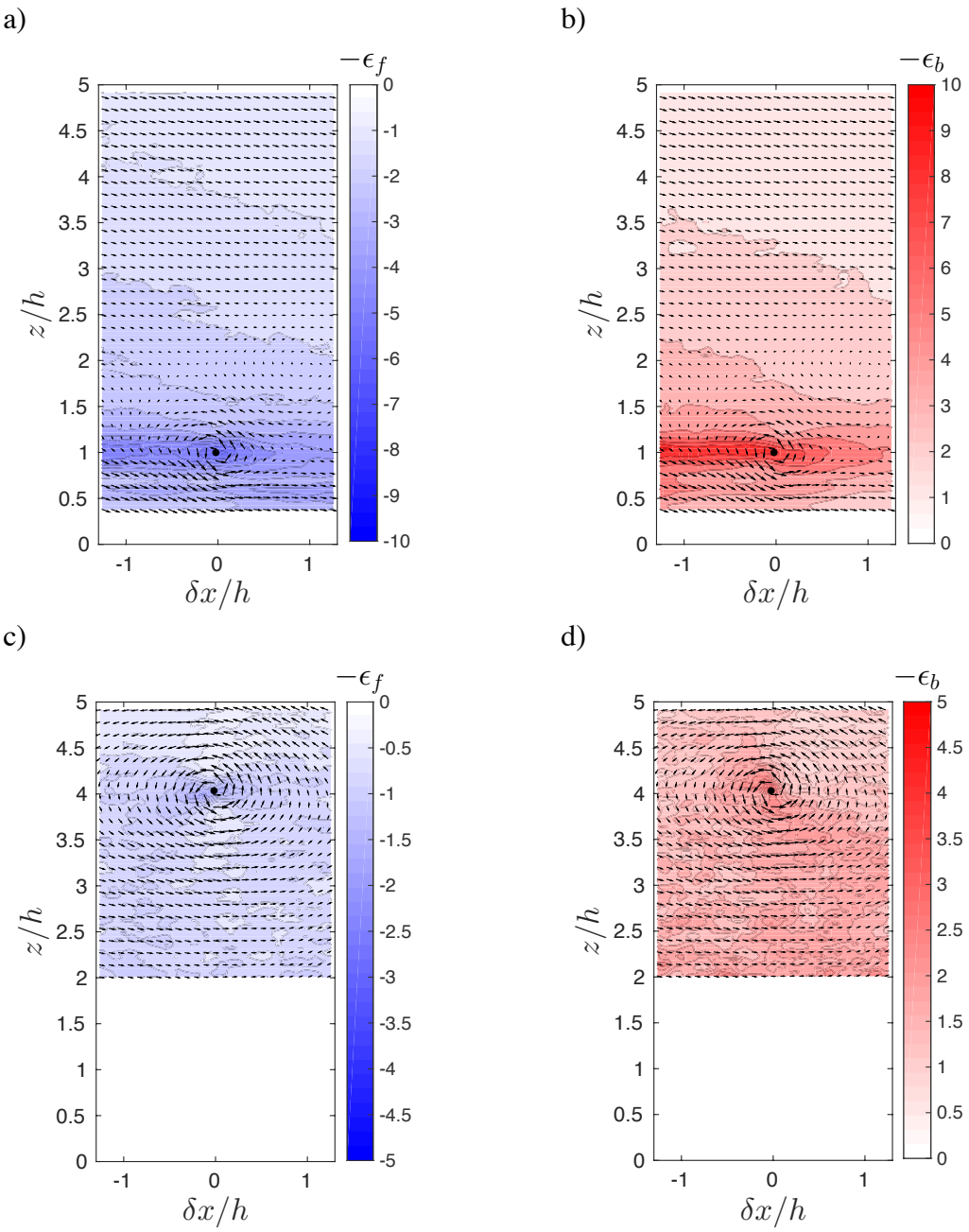

Figure 6.13. Conditional average of dissipation a) forward scatter and b) backscatter based on swirling event at $z/h = 1$; c) forward scatter and d) backscatter based on swirling event at $z/h = 4$.

The calculation of the dissipation is based on the shear stress and strain products $\tau_{ij}S_{ij}$. The conditional average of each product is computed and shown for a height of $z/h = 1$ in Figure 6.14 and $z/h = 4$ in Figure 6.15. Within the shear layer strong forward scatter is mainly a result of $\tau_{13}S_{13}$ and $\tau_{33}S_{33}$, while $\tau_{11}S_{11}$ contributes significantly to

backscatter in this region (Figure 6.14). The term $\tau_{11}S_{11}$ also exhibits a localized region of forward scatter downstream of the swirling event (Figure 6.14a). Within the overlying boundary layer it is evident that the strong localized forward scatter in front of and behind the swirling event is a result of the term $\tau_{11}S_{11}$ (Figure 6.15a). In addition, $\tau_{11}S_{11}$ generates significant backscatter both above and upstream and below and downstream of the swirling event, which is not found in any other term. The term $\tau_{12}S_{12}$ is negligible and the remaining terms are shown to not contribute to the dominant energy transfer around swirling events (Figure 6.15). Instead, the remaining terms are shown to contribute significant backscatter spatially coincident with the intense forward scatter and significant forward scatter spatially coincident with the intense backscatter shown in Figure 6.13, especially for the term $\tau_{33}S_{33}$ (Figure 6.15f). The term $\tau_{13}S_{13}$ differs significantly from previous work in the literature that found it contributed to the dominant forward scatter in front of and behind a swirling event (Figure 6.15c) (Natrajan and Christensen, 2006). This discrepancy is likely not a result of a change in flow dynamics between smooth-wall and rough-wall boundary layers, but instead a result of the influence of the spanwise gradients in the calculation of the dissipation, which were not taken into account in the work of Natrajan and Christensen (2006). This was confirmed using a two-dimensional (2D) estimation of the dissipation, considering only streamwise and vertical velocity gradients, where the conditional average of $\tau_{13}S_{13}$ (not shown) exhibited localized forward scatter corresponding to the regions of intense forward scatter found in the conditional average and the work of Natrajan and Christensen (2006). Finally, although the conditional averages of forward scatter and backscatter differ significantly in shape between the shear layer and overlying boundary layer the patterns within the terms $\tau_{11}S_{11}$and $\tau_{33}S_{33}$ are comparable in each region of the flow.

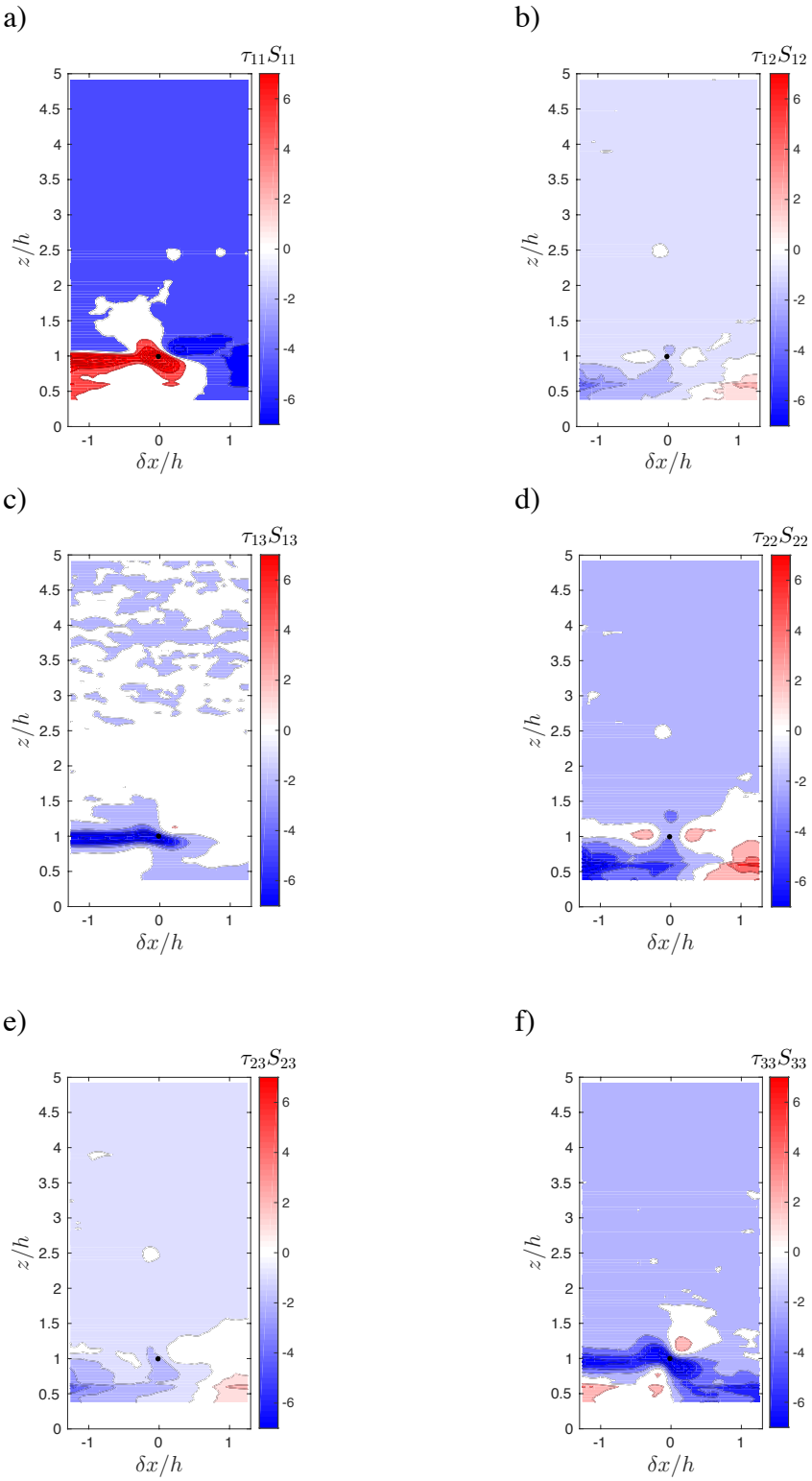

Figure 6.14. Conditional average of dissipation terms a) $\tau_{11}S_{11}$; b) $\tau_{12}S_{12}$; c) $\tau_{13}S_{13}$; d) $\tau_{22}S_{22}$; e) $\tau_{23}S_{23}$; f) $\tau_{33}S_{33}$ based on swirling event at $z/h = 1$.

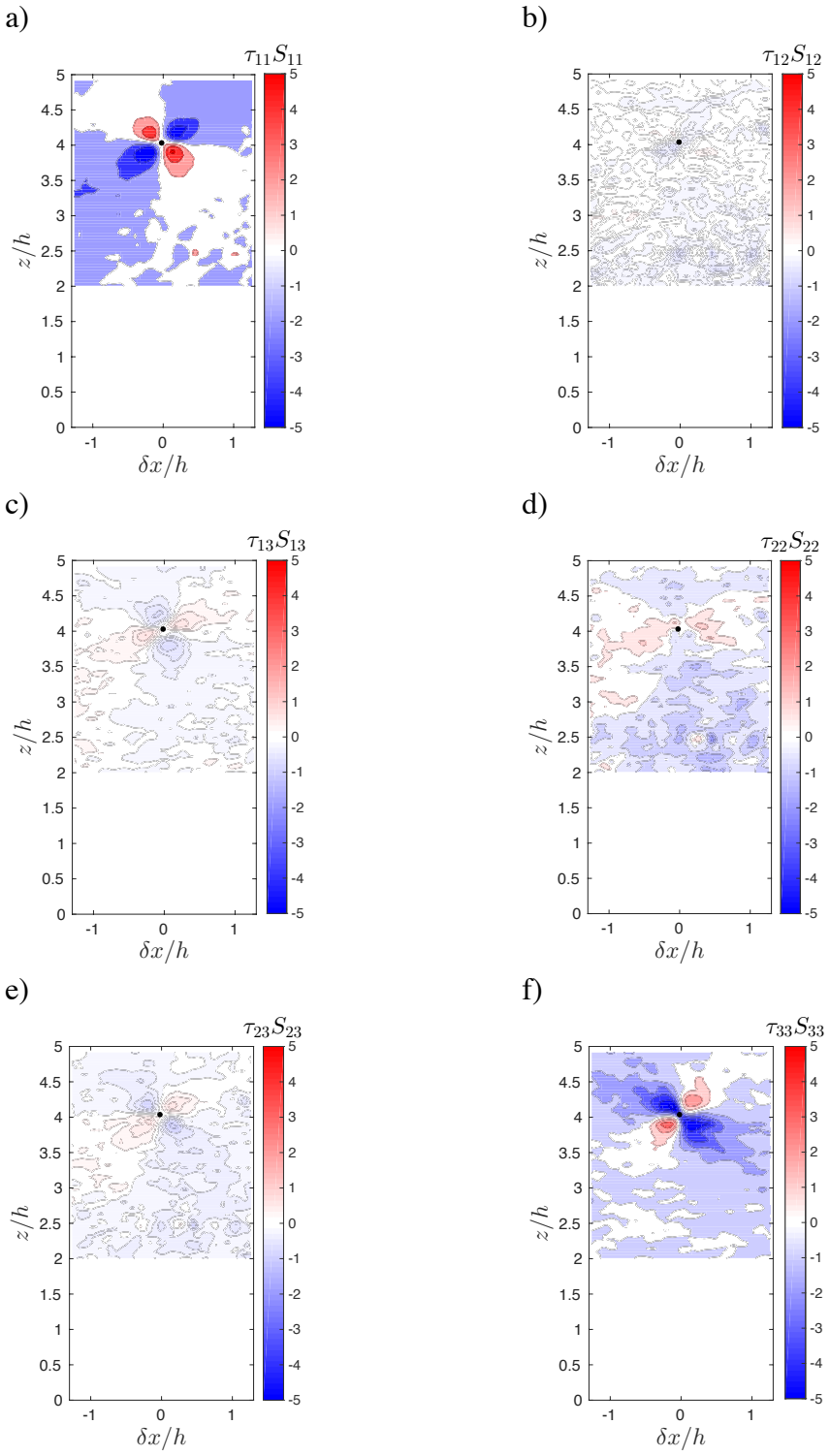

Figure 6.15. Conditional average of dissipation terms a) $\tau_{11}S_{11}$; b) $\tau_{12}S_{12}$; c) $\tau_{13}S_{13}$; d) $\tau_{22}S_{22}$; e) $\tau_{23}S_{23}$; f) $\tau_{33}S_{33}$ based on swirling event at $z/h = 4$.

The results previously indicate that swirling events like hairpin vortices generate significant energy transfer from large-scales to small-scales, but also from small-scales to large-scales. Although individual vortices have been shown to be correlated with energy transfer events it is unknown whether these structures are the most dominant flow structure associated with forward scatter and backscatter. Thus, we present the conditionally averaged fluctuating streamwise and vertical velocity using either a forward scatter or backscatter event in the shear layer (Figure 6.16 and Figure 6.17) and in the boundary layer (Figure 6.18 and Figure 6.19) as the condition. The average velocity field associated with a forward or backscatter event can be estimated as

$$\overline{u'_j(x,y)|\phi(x_r,y_r)} = \frac{\overline{u'_j(x,y,z)\phi(x_r,y_r)}}{\phi(x_r,y_r)\phi(x_r,y_r)}\phi(x_r,y_r) \tag{6.12}$$

where u'_j is the jth fluctuating velocity component.

Within the shear layer the conditionally averaged velocity shows an elongated vortex rotating clockwise in the case of a forward scatter event and counter-clockwise in the case of a backscatter event (Figure 6.16 and Figure 6.17). This confirms that the most important flow mechanisms for energy transfer in the shear layer are the vortices that form as a result of the roughness elements. The conditionally averaged velocity based on a forward scatter event in the overlying boundary layer shows a region of converging flow at the point of strong forward scatter (Figure 6.18). This is consistent with previous work in the smooth-wall boundary layer that found forward scatter occurring at an opposing Q2-Q4 interface (Natrajan and Christensen, 2006) and a converging flow pattern (Carper and Porte-Agel, 2004). As well, it corresponds to results from the rough-wall boundary layer, which also exhibited strong dissipation at the interface between opposing Q2-Q4 events (Hong et al., 2012). However, in the present work there is also a vortex occurring in front of the forward scatter event, which was not present in the smooth-wall boundary layer (Figure 6.18). As discussed above this difference is due to the three-dimensional (3D) estimation of the dissipation including spanwise velocity gradients. The forward scatter within the smooth-wall boundary layer was shown to occur within a large shear layer spanning a length of 1.5 times the boundary layer thickness (δ) suggesting that significant energy transfer occurs along the backbone of a hairpin vortex

packet due to the induced sweep and ejection events (Natrajan and Christensen, 2006). Due to the restricted extent of the PIV field in the present work it is clear we are unable to capture this large shear layer. Within the smooth-wall boundary layer the backscatter was shown to occur most predominantly at the trailing edges of the hairpin packets where there are diverging Q2-Q4 events, not at the vortex core (Natrajan and Christensen, 2006). However, the conditional average of the present work using a backscatter event shows a swirling flow at the location of backscatter (Figure 6.19). Again, this is due to the estimation of the spanwise velocity gradients in the dissipation estimation.

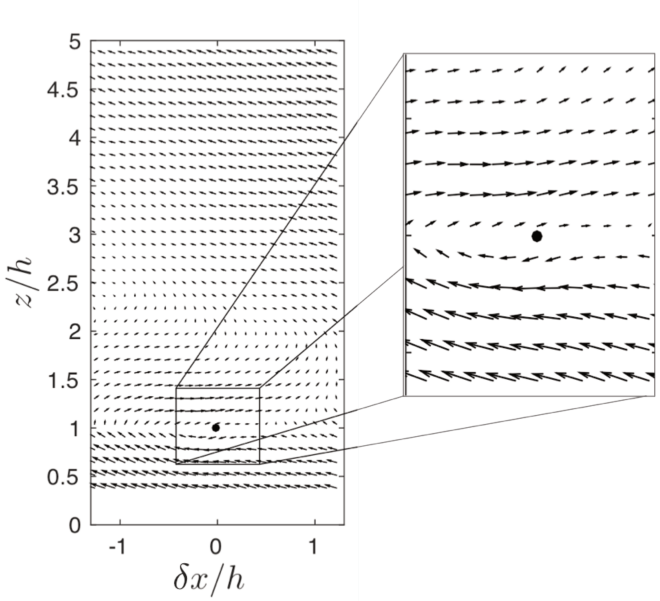

Figure 6.16. Conditional average of u' and w' based on a forward scatter event at $z/h = 1$.

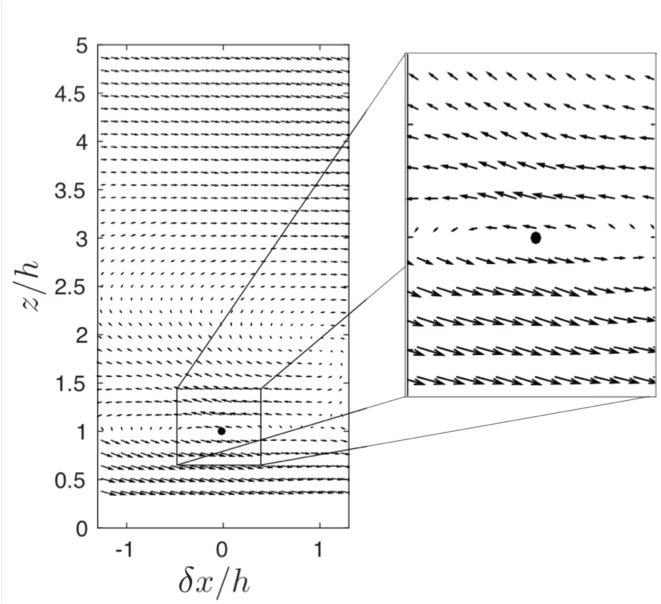

Figure 6.17. Conditional average of u' and w' based on a backscatter event at $z/h = 1$.

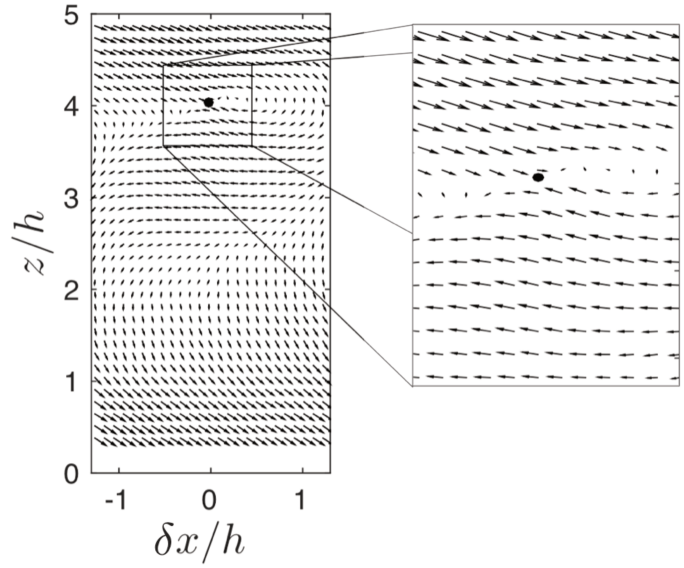

Figure 6.18. Conditional average of u' and w' based on a forward scatter event at $z/h = 4$.

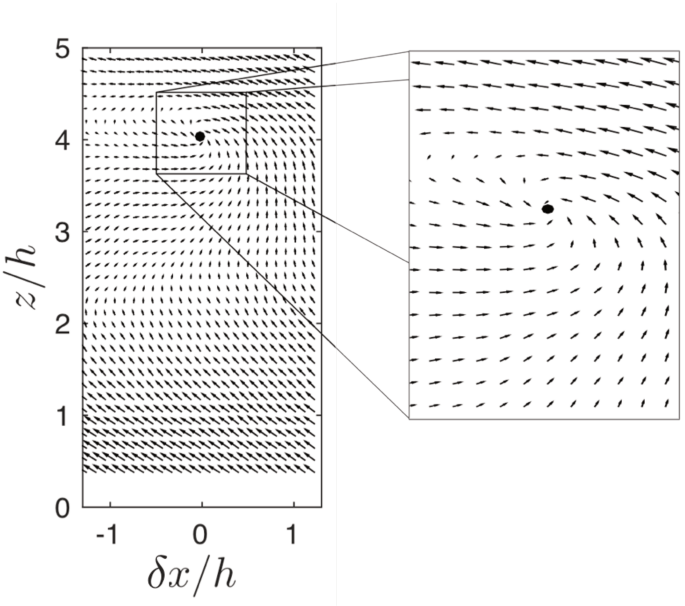

Figure 6.19. Conditional average of u' and w' based on a backscatter event at $z/h = 4$.

6.4 Conclusions

Within the urban boundary layer few experimental studies have attempted to calculate the TKE budget, particularly ε, which is typically estimated using longitudinal spectra (Castro et al., 2006; Zhu et al., 2007; Roth et al., 2015). Previous work in the smooth-wall boundary layer has highlighted the importance of modeling backscatter, which is the transfer of energy from the small-scales to the large-scales, to accurately capture the dissipation (Natrajan and Christensen, 2006). Furthermore, it has been demonstrated that localized forward and backscatter are linked to coherent hairpin vortices (Carper and Porte-Agel, 2004; Natrajan and Christensen, 2006).

In the present work experimental evidence from a rough-wall boundary layer consisting of a staggered cube array was used to answer the specific questions listed in Section 6.1 and the following conclusions found.

1) In the present work ε is estimated using two methods, an LE-PIV gradient model (Sheng et al., 2000) and a direct ET calculation (Natrajan and Christensen, 2006). Both methods estimate ε using a low-pass spatial filter with a cut-off wavelength larger than the Taylor microscale ensuring that the separation between the large-scales and the small-scales occurs within the inertial range of the velocity spectra

(Sheng et al., 2000). However, a discrepancy was shown between the two methods as a result of the direct ET method neglecting some small-scales important to the dissipation, thus, the LE-PIV method is preferred as it models these scales. The other budget terms were calculated directly from the PIV measurements with pressure transport as the residual of the budget.

2) The shear layer induced by the presence of the roughness is shown to produce and dissipate energy, as well as, transport energy through advection, turbulent transport and pressure transport. As the shear layer develops over the canopy the magnitudes of the production and dissipation of energy decrease until separation occurs at the downstream cube causing strong production. A recirculation region that forms within the wake of the upstream cube through interaction of the shear layer and the canopy layer creates positive pressure transport and contains small-scale structures that dissipate energy. Furthermore, this region results in a rapid increase of the streamwise velocity component in the longitudinal direction as well as a significant contribution of the spanwise component thereby generating significant spatial variation of the production.
3) Finally, through stochastic estimation of the conditional average it was found that, similar to the smooth-wall boundary layer, localized regions of forward scatter occur in front of and behind a hairpin head, whereas, backscatter occurs above and upstream and below and downstream of a hairpin head a result of the term $\tau_{11}S_{11}$. However, the presence of the roughness elements induces a layer of strong shear containing small-scale vortical structures that contribute significantly to both forward and backscatter events within the shear layer. Furthermore, conditional averages of the velocity field based on either a forward scatter or backscatter event demonstrated the need to consider the 3D estimation of the dissipation.

Although the nature of energy production and dissipation in the urban boundary layer is now better understood, previous work detailed in Chapter 4 has shown that large-scale coherent structures interact and influence small-scale structures within the shear layer through a non-linear interaction. In the following chapter the cube array described in

Chapter 2 (Rcu) will be used to investigate the non-linear energy transfer that occurs between small-scales close to the roughness and large-scales present in the overlying boundary layer.

Résumé du Chapitre 7

Le chapitre 7 tente d'apporter un éclairage sur le lien entre le mécanisme non linéaire de modulation d'amplitude mis en évidence dans le chapitre 4 pour une couche limite au-dessus d'une canopée de cubes, et les transferts d'énergie entre structures de grandes et petites échelles. Pour cela, la méthode de décomposition triple est appliquée à l'équation de bilan d'énergie cinétique turbulente afin d'analyser les termes dominants dans les transferts d'énergie et d'évaluer les interactions entre échelles. Un résumé (en français) de ce chapitre est proposé ci-après.

La couche limite turbulente d'une zone urbaine est composée de plusieurs régions, telles que la sous-couche de rugosité et la couche inertielle, qui contiennent des structures cohérentes complexes. Ces structures sont liées à l'apparition d'événements turbulents intermittents tels que les balayages (Q4 : $u' > 0$ et $w' < 0$) et les éjections (Q2 : $u' < 0$ et $w' > 0$) qui régissent le transport de la chaleur, de la quantité de mouvement et de la pollution entre la sous-couche de rugosité et la couche inertielle (Takimoto et al., 2011 Perret et Savory, 2013). Ainsi, comprendre ces structures et leurs interactions d'un point de vue quantitif est d'une grande importance.

Les travaux antérieurs dans la couche limite de paroi lisse ont identifié une relation non linéaire entre les structures à grande échelle se produisant dans la couche limite et les structures à petite échelle proches de la paroi (Mathis et al., 2011a). La modulation d'amplitude a également été étudiée expérimentalement dans le cas d'une paroi faiblement rugueuse recouverte de sable (Squire et al., 2016), et numériquement pour une paroi fortement rugueuse recouverte de cubes (Anderson, 2016) ou d'élements 2D (Nadeem et al., 2015). Récemment, Blackman et Perret (2016) ont utilisé des données expérimentales de couches limites se développant au-dessus de parois rugueuses (constituées d'éléments 3D et 2D) pour étudier les interactions non linéaires. Ils ont constaté un mécanisme descendant similaire à la modulation d'amplitude dans tous les cas de rugosité (voir aussi chapitre 5). La façon dont ce mécanisme influence le transfert d'énergie entre les échelles reste encore non élucidée. Hussain (1983; 1986) a introduit une décomposition triple qui décompose l'écoulement en une moyenne ($\overline{U}$), des

fluctuations à grande échelle (u_L') et des fluctuations à petite échelle (u_S'). Cette méthode peut également être appliquée à l'équation de bilan d'énergie cinétique turbulente pour mettre en évidence les termes de transfert d'énergie entre échelles : le premier terme (*I*) traduit le transfert d'énergie du mouvement moyen vers les grandes échelles de la turbulence, le deuxième terme (*II*) correspond à l'énergie transférée du mouvement moyen vers les petites échelles et le troisième terme (*III*) décrit l'énergie transférée depuis les grandes échelles vers les petites échelles.

Nous nous basons sur les données expérimentales pour une couche limite de paroi rugueuse consistant en une canopée de cubes pour répondre à la question spécifique suivante: Est-ce que la relation non linéaire entre grandes et petites échelles mise en évidence précédemment est liée au transfert d'énergie entre les échelles?

Étant donné que l'information temporelle du signal proche de la paroi n'est pas disponible, le modèle d'estimation stochastique décrit au chapitre 3 est utilisé à nouveau pour effectuer la décomposition triple. Une fois l'écoulement décomposé en fluctuations de grande et petite échelles, les trois termes de transfert d'énergie, I, II, et III sont calculés.

La majorité du transfert d'énergie provient de l'interaction entre les petites échelles et l'écoulement moyen, mais même si le terme III est nettement plus faible, il affiche de plus fortes valeurs dans la couche de cisaillement. Dans cette région, des petites échelles sont présentes, ainsi que des tourbillons qui se forment le long du cube en amont. Le transfert d'énergie vers les structures de petite échelle se concentre autour de ces tourbillons dans la couche de cisaillement. Ce terme III, qui représente le transfert d'énergie vers les structures de petite échelle, est principalement le résultat de $III_{11} = -\overline{\langle u_S' u_S' \rangle \frac{\partial u_L'}{\partial x}}$ et $III_{31} = -\overline{\langle u_S' w_S' \rangle \frac{\partial u_L'}{\partial z}}$.

Pour étudier le lien entre la relation non linéaire qui existe entre les structures à grande échelle et les structures à petite échelle et le transfert d'énergie entre ces structures, on utilise des corrélations spatio-temporelles. Ces corrélations permettent une description qualitative des mécanismes. Quand une région de haute vitesse passe au-dessus des

petites structures présentes à proximité des éléments de rugosité, les petites échelles sont modifiées grâce à une interaction non linéaire avec les grandes échelles. Cela provoque un transfert d'énergie de la région de haute vitesse vers les petites échelles dont l'énergie est amplifiée à travers le terme III_{31}. Dans le même temps une partie de l'énergie est transférée des petites échelles vers la région de haute vitesse à travers le terme III_{11}. Cette relation est inversée dans le cas où il y a présence d'une région de basse vitesse : les petites échelles transfèrent de l'énergie aux grandes échelles à travers le terme III_{31} et reçoivent de l'énergie travers le terme III_{11}. Comme on l'a vu au chapitre 4, ces régions de basse ou haute vitesse sont légèrement inclinées. Ainsi, les structures à petite échelle dans la couche de cisaillement subissent des effets de la structure à grande échelle située légèrement en aval. Lorsque l'emplacement de référence à grande échelle augmente en hauteur, la distance entre la structure à petite échelle et la région à faible quantité de mouvement augmente, ce qui entraîne une augmentation du délai de la corrélation maximale. Le retard dans la corrélation maximale est conservé dans la relation de transfert d'énergie. Ainsi, la relation non linéaire entre les régions de basse ou haute vitesse à grande échelle et les petites échelles dans la couche de cisaillement à vraissemblablement une influence sur le transfert d'énergie entre les échelles.

Des structures cohérentes à grande échelle ont pu être reliées par une relation non linéaire aux structures à petite échelle induites par la présence de la rugosité dans une couche limite de paroi rugueuse (Squire et al., 2016, Blackman et al., 2016). Cependant, la façon dont cette relation influence le transfert d'énergie entre les structures était encore inconnue. Le présent travail a permis d'avancer sur cette question et les principaux résultats sont donnés ci-dessous.

Le transfert moyen d'énergie entre l'écoulement moyen, les grandes échelles et les petites échelles a été quantifié en utilisant la décomposition triple du bilan TKE. Nous avons pu constater que, bien que le transfert d'énergie entre l'écoulement moyen et les petites échelles soit le plus important, un transfert d'énergie non-négligeable entre grandes échelles et petites échelles (III) existe. Les deux principaux contributeurs à ce terme sont III_{11} et III_{31}. Grâce à une corrélation spatio-temporelles entre u_L' et III_{11} ou III_{31} il a été confirmé que la relation non linéaire est liée au transfert d'énergie entre les structures

cohérentes à grande échelle et les petites échelles induites par la présence de la rugosité.

7 Energy transfer and non-linear interactions

In the previous chapters the non-linear relationship between large-scales in the overlying boundary layer and small-scales close to the roughness and the Turbulent Kinetic Energy (TKE) Budget have been studied within a cube canopy (Rcu) using Particle Image Velocimetry (PIV) and Hot-Wire Anemometry (HWA). However, it is still unclear how this non-linear relationship influences energy transfer between scales in the rough-wall boundary layer. The following chapter is an analysis of the energy transfer between large- and small-scale structures using a triple decomposition of the TKE budget. This work uses combined PIV and HWA measurements within a staggered cube array (Rcu) as detailed in Chapter 2 (Figure 2.4a). First an introduction to the topic is provided, followed by a description of the triple decomposition of the TKE budget. The results, including the mean energy transfer between scales and the link between the non-linear relationship and energy transfer between structures, are then presented followed by conclusions.

7.1 Introduction

As described in Chapter 1 the turbulent boundary layer developing over a rough-wall or urban area is comprised of several regions such as the roughness sublayer and inertial layer that contain complex coherent structures. These coherent structures, such as large-scale low momentum regions occurring within the inertial layer, have been linked to the occurrence of intermittent sweep and ejection events that govern the transport of heat and momentum between the canopy and above (Coceal et al., 2007b; Takimoto et al., 2011; Perret and Savory, 2013). Thus, understanding these structures and their interactions quantitatively is essential to understanding pollutant transport in the urban canopy.

As detailed in Chapter 4 previous work in the smooth-wall boundary layer identified a non-linear relationship between large-scale structures occurring in the boundary layer and small-scale structures close to the wall, which was investigated using skewness decomposition (Mathis et al., 2011a) and also linked to a mechanism of amplitude modulation (Hutchins and Marusic, 2007; Mathis et al., 2009; Mathis et al., 2011a; Mathis et al., 2011b; Marusic et al., 2011; Inoue et al., 2012). Amplitude modulation has also been investigated experimentally (Squire et al., 2016) and numerically (Nadeem et al., 2015; Anderson, 2016) in the rough-wall boundary layer and although the amplitude modulation was modified in the rough-wall the nature of the mechanism remained the same.

In Chapter 4 of the present work experimental evidence from a rough-wall boundary layer consisting of staggered cubes with $\lambda_p = 25\%$ (Rcu) was used to investigate the non-linear interactions between large-scale momentum regions and the small-scales induced by the presence of the roughness (Blackman and Perret, 2016). As temporal information of the near-wall small-scales was not available Linear Stochastic Estimation (LSE), as described in Chapter 3, was used to decompose the flow. This work confirmed through two-point spatio-temporal correlations that a top-down mechanism similar to amplitude modulation exists in the rough-wall boundary layer. As detailed in Chapter 4 the non-linear relationship in the rough-wall boundary layer can be described qualitatively by Figure 4.12, which shows a low or high momentum region passing over small-scale structures close to the roughness. As the slightly inclined large-scale structure moves within the boundary layer, it passes over the small-scale structures close to the roughness. Thus, small-scale structures experience effects from the large-scale structure that is slightly downstream of them. Investigation of this non-linear relationship was expanded within Chapter 5 to street canyon flow using six rough-wall boundary layer configurations consisting of three upstream roughness configurations (cubes or 2D bars with different streamwise spacing) and two street canyon aspect ratios (AR) as detailed in Chapter 2 (Figure 2.5). The canyon AR was found to have a negligible influence on the non-linear relationship, but the upstream roughness when changed from 3D to 2D resulted in a modification of the non-linear relationship closer to the shear layer.

However, a top-down non-linear relationship similar to amplitude modulation was confirmed in all of the roughness cases. What still remains unclear is how this non-linear relationship relates to energy transfer between scales in the turbulent boundary layer.

As stated in Chapter 6, few studies within the rough-wall boundary layer have investigated the TKE budget due to experimental restraints (Castro et al., 2006; Blackman et al., 2017). The most complete study to date is described in Chapter 6 and includes quantification and detailed analysis of all the TKE budget terms including dissipation (Blackman et al., 2017). However, to investigate the relationship between the non-linear interactions and TKE one must use triple decomposition, as described in Chapter 3, of the TKE budget.

The total kinetic energy is the sum of the kinetic energy from the movement of the mean flow (E), the large-scales (ξ) and the small-scales (e) (Equation 7.1).

$$\frac{1}{2}\overline{U_\iota U_\iota} = \underbrace{\frac{1}{2}\overline{U}_\iota\overline{U}_\iota}_{E} + \underbrace{\frac{1}{2}\overline{u'_{L\iota}u'_{L\iota}}}_{\xi} + \underbrace{\frac{1}{2}\overline{u'_{S\iota}u'_{S\iota}}}_{e} \tag{7.1}$$

The energy interactions between scales are then determined by examining the kinetic energy budgets for each of the scales where Equations 7.2, 7.3, 7.4 are the kinetic energy budget for the movement of the mean flow, the large-scales and the small-scales, respectively. Within these equations ⌈ ⌉ is a large-scale filter used to determine the large-scale structures induced by small-scale interactions. The detailed derivation of these equations can be found in Hussain (1983).

$$\frac{D\bar{E}}{Dt} = \frac{\partial\overline{PU_i}}{\partial x_i} \underbrace{- \left(-\overline{u'_{L\iota}u'_{LJ}}\right)\frac{\partial U_i}{\partial x_j}}_{-I} \underbrace{- \left(-\overline{u'_{S\iota}u'_{SJ}}\right)\frac{\partial U_i}{\partial x_j}}_{-II} - \frac{\partial}{\partial x_j}\left[\overline{U}_\iota\left(\overline{u'_{L\iota}u'_{LJ}} + \overline{u'_{S\iota}u'_{SJ}}\right)\right] + \frac{1}{Re}\frac{\partial}{\partial x_j}\left(\overline{U}_\iota\overline{S_{\iota J}}\right) - \varepsilon \tag{7.2}$$

$$\frac{D\bar{\xi}}{Dt} = \frac{\partial}{\partial x_j}\left[\overline{u'_{Lj}\left(P_L + \frac{1}{2}u'_{Li}u'_{Li}\right)}\right] \underbrace{- \overline{u'_{Li}u'_{Lj}}\frac{\partial \bar{U}_i}{\partial x_j}}_{I} \underbrace{- \left(-\overline{\left[u'_{Si}u'_{Sj}\right]\frac{\partial u'_{Li}}{\partial x_j}}\right)}_{-III} - \frac{\partial}{\partial x_j}\left(\overline{u'_{Li}\langle u'_{Si}u'_{Sj}\rangle} + \right.$$

$$\left. \frac{1}{Re}\frac{\partial}{\partial x_j}\left(\overline{u'_{Li}S_{ij}}\right) - \varepsilon_L \right. \tag{7.3}$$

$$\frac{D\bar{e}}{Dt} = \frac{\partial}{\partial x_j}\left[\overline{u'_{Sj}\left(P_S + \frac{1}{2}u'_{Si}u'_{Si}\right)}\right] \underbrace{- \overline{u'_{Si}u'_{Si}}\frac{\partial \bar{U}_i}{\partial x_j}}_{II} \underbrace{- \overline{\left[u'_{Si}u'_{Sj}\right]\frac{\partial u'_{Li}}{\partial x_j}}}_{III} - \overline{u'_{Lj}\frac{\partial}{\partial x_j}\langle\frac{1}{2}u'_{Si}u'_{Sj}\rangle} +$$

$$\frac{1}{Re}\frac{\partial}{\partial x_j}\left(\overline{u'_{Si}S_{ij}}\right) - \varepsilon_S \tag{7.4}$$

Within these equations there are three terms that represent energy exchange between scales, *I*, *II* and *III*, and each of these terms can be found in two equations albeit with opposite signs. *I* captures the energy transferred from the movement of the mean flow to the large-scales, *II* describes the energy production of the small-scales by the movement of the mean flow and *III* describes the energy production of small-scales as a result of the large-scales. This final term, *III*, is of particular interest as it captures the interaction between large- and small-scales which may be related to the non-linear relationship described above. These equations have been previously used to investigate kinetic energy scale interactions using LES in a plane mixing layer excited with periodic perturbation (König et al. 1996; 1997; Sarkar and Schlüter, 2013a) and the wake of an oscillating cylinder (Sarkar and Schlüter, 2013b). It was found in the plane mixing layer that the majority of energy production was a result of interactions between the mean flow and large-scale coherent structures while the smallest contribution was a result of interactions between large-scale coherent motions and random small-scales (König et al. 1996; 1997; Sarkar and Schlüter, 2013a). However, to the author's knowledge these equations have not previously been applied within the rough-wall or urban boundary layer.

As stated above the large-scale structures present in the turbulent boundary layer developing over a rough-wall have been linked through a non-linear relationship with the small-scale structures induced by the presence of the roughness (Squire et al., 2016; Blackman and Perret, 2016). However, it is still unknown how this relationship relates to

energy transfer between scales. The present work aims to use experimental evidence from a rough-wall boundary layer consisting of a staggered cube array (Rcu) to answer the following specific question: Is the non-linear relationship between large- and small-scales related to energy transfer between scales?

7.2 TKE Triple Decomposition

In the present work the LSE method as described in Chapter 3 is used to perform triple decomposition separating the flow into large- (u'_L) and small-scales (u'_S). To investigate the energy transfer between scales in the present work three terms are analyzed from the decomposed TKE equations presented above: *I*, *II* and *III* (Equations 7.5, 7.6, 7.7).

$$I = \left(-\overline{u'_{L\iota}u'_{L\jmath}}\right)\frac{\partial \overline{U_\iota}}{\partial x_j} \tag{7.5}$$

$$II = \left(-\overline{u'_{S\iota}u'_{S\jmath}}\right)\frac{\partial \overline{U_\iota}}{\partial x_j} \tag{7.6}$$

$$III = -\overline{\left[u'_{S\iota}u'_{S\jmath}\right]\frac{\partial u'_{L\iota}}{\partial x_\jmath}} \tag{7.7}$$

As stated above these terms describe the energy transferred from the mean flow to the large-scales, from the mean flow to the small-scales and from the large-scales to the small-scales, respectively. ⌈ ⌉ within *III* represents the large-scale structures resulting from interactions between small-scale structures and is determined using the Stochastic Estimation approach described in Chapter 3. As in Chapter 3 a low-pass filtered HWA signal is used with a time-delay. However, instead of the raw near-wall PIV signal, the near-wall squared small-scale signal ($\widetilde{u'_{S\iota}u'_{S\jmath}}$) is used to determine the LSE coefficients (A_i^n) (Equation 7.8).

$$\overline{\widetilde{u'_{S\iota}u'_{S\jmath}}(x,y,z,t)v\left(x_\jmath,y_\jmath,z_\jmath,t+m\Delta\tau\right)} = \sum_{i=1}^{N_{ref}}\sum_{n=-N_t}^{N_t} A_i^n \overline{v(x_\iota,y_\iota,z_\iota,t+n\Delta\tau)v(x_\iota,y_\iota,z_\iota,t+m\Delta\tau)}\,, j \in \left[1,N_{ref}\right], m \in [-N_t,N_t] \tag{7.8}$$

As the measurements were conducted in a single streamwise aligned stereoscopic PIV plane it is impossible to compute the spatial gradient of the instantaneous velocity in three directions of space as required for the full computation of I, II and III. Furthermore, the LSE method used for triple decomposition cannot be used to predict the large-scales of the spanwise velocity. Therefore, I, II and III are calculated using streamwise and vertical components only. For example the four terms included in the calculation of III are $III_{11} = -\overline{\lceil u_S' u_S' \rceil \frac{\partial u_L'}{\partial x}}$, $III_{13} = -\overline{\lceil w_S' u_S' \rceil \frac{\partial w_L'}{\partial x}}$, $III_{31} = -\overline{\lceil u_S' w_S' \rceil \frac{\partial u_L'}{\partial z}}$ and $III_{33} = -\overline{\lceil w_S' w_S' \rceil \frac{\partial w_L'}{\partial x}}$. Using this method the mean energy transfer between scales is investigated in the following section.

7.3 Results and Discussion

7.3.1 Mean Energy Transfer

Using the method described above the mean energy transfer from the mean flow to the large-scales (I), from the mean flow to the small-scales (II) and from the large-scales to the small-scales (III) are calculated and shown in Figure 7.1 at three positions in the streamwise direction. The sign of these terms describes the direction of energy transfer where positive I is energy transfer from the mean flow to the large-scales, and negative I is energy transfer from the large-scales to the mean flow. Similarly, positive II is energy transfer from the mean flow to the small-scales and positive III is energy transfer from the large-scales to the small-scales. At each streamwise location the majority of the energy transfer occurs at the top of the canopy within the shear layer and is from interaction between the small-scales and the mean flow (II). II along with I represents the mean TKE production $\left(P_d = -\overline{u_i' u_j'} \frac{\partial \overline{U_i}}{\partial x_j}\right)$ which was analyzed in Chapter 6. The magnitude of $II + I$ is greater than that of P_d within the shear layer, which is a result of neglecting the spanwise velocity terms in the calculations of II and I. III is shown to be negligible throughout the boundary layer except within the shear layer where it reaches a maximum. This region contains small-scale structures, but also within this region coherent vortices are formed along the top of the upstream cube and shed downstream. The interaction between the small-scales and these coherent vortices may contribute to

the energy transfer between large- and small-scale structures (*III*). The negligible mean energy transfer between large-scale coherent structures and small-scales agrees with previous work stating that large-scale structures within the overlying boundary layer don't exchange energy with other scales as they are self-sustaining (Rawat et al., 2015).

a)

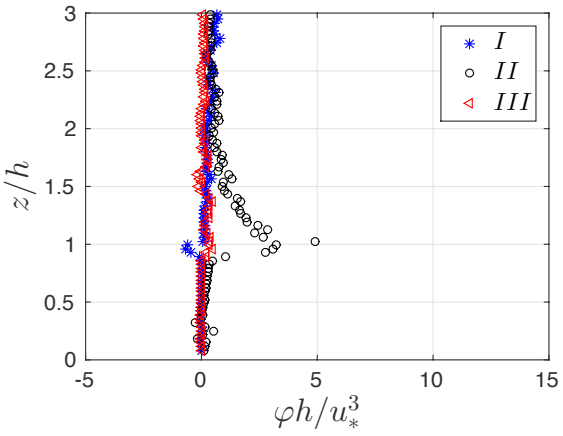

b)

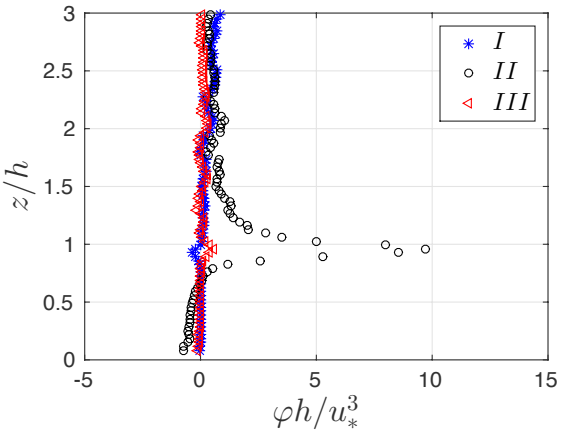

c)

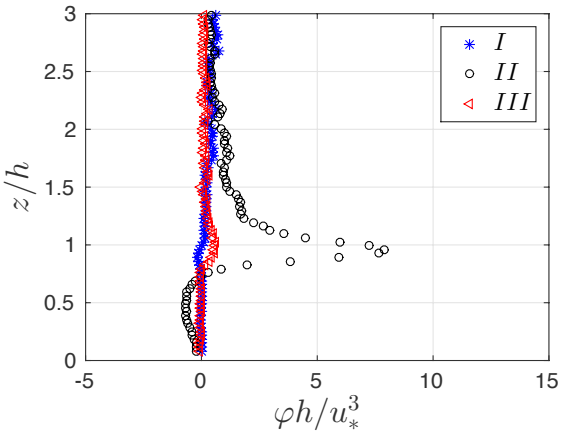

Figure 7.1. Mean I, II and III at a) x/h = -0.25; b) x/h = 0; c) x/h = 0.25, all terms normalized by h/u_*^3.

To determine which regions of the flow are most important to each type of energy transfer the contours of I, II and III are shown in Figure 7.2. The energy transfer from the movement of the mean flow to large-scale coherent structures (I) occurs mostly in the overlying boundary layer where large-scale coherent structures move with the advection

velocity. Whereas within the shear layer and the canopy energy is transferred from the large-scales to the mean flow through interaction of the shear layer with the wake. The small-scale production of energy from movement of the mean flow (*II*) occurs mostly in the shear layer where small-scale structures are induced by the presence of the roughness. Similarly to *I*, the recirculation within the wake causes energy transfer from the small-scales to the mean flow as they are entrained into this region from the shear layer. This phenomenon of negative energy transfer within the wake contradicts the positive production of TKE shown in Chapter 6 as the estimation of the TKE production included the term $-\overline{v'v'}\frac{\partial \bar{V}}{\partial y}$, which is not available in the present analysis. The negative energy transfer is therefore likely a result of the term $-\overline{u'u'}\frac{\partial \bar{U}}{\partial x}$that was shown in Chapter 6 to be a result of the rapidly increasing streamwise velocity present in the wake. Finally, the energy transfer from large-scale coherent structures to small-scales (*III*) is shown to be strongest within the shear layer. Within this region there are vortices that form along the upstream cube and shed downstream. The transfer of energy to the small-scale structures is shown to be concentrated around these vortices within the shear layer. However, this may be a result of a lack of convergence in the statistics.

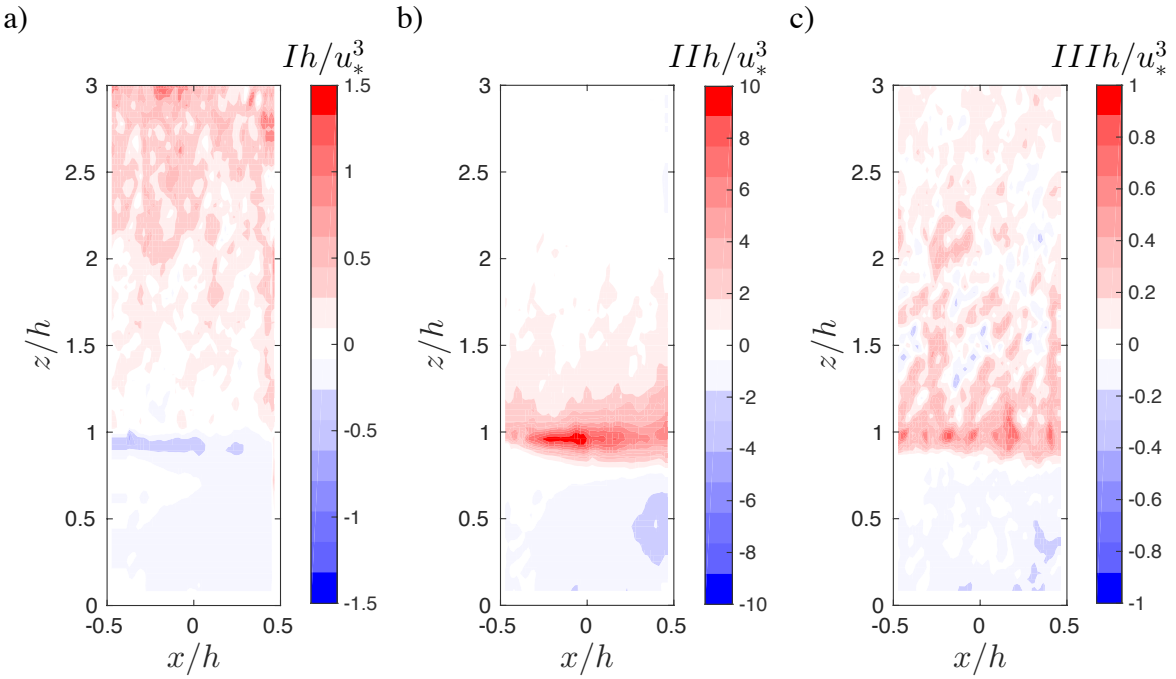

Figure 7.2. Contours of mean a) *I*; b) *II*; c) *III*, all terms normalized by h/u_*^3.

7.3.2 Large and small-scale interactions

To investigate the link between energy transfer and the non-linear relationship between large- and small-scales the term III, which represents the energy transfer from large- to small-scales, will be further analyzed. Figure 7.3 shows the mean and standard deviation of this term spatially averaged in the x-direction over the width of the PIV measurement plane. The standard deviation is approximately two times the magnitude of III exhibiting the largest magnitude within the shear layer. This suggests that although the mean energy transfer between large- and small-scales is negligible there is significant energy transfer between these structures instantaneously.

The mean contribution of each of the velocity components to III spatially averaged over the x-direction is shown in Figure 7.4. The largest contributor to III, III_{31}, exhibits a peak within the shear layer as it directly depends on the shear stress. The standard deviations of these terms reach a maximum within the shear layer particularly for the term III_{31}, while the term III_{11} shows large magnitudes of standard deviation for a significant portion of the roughness sublayer (Figure 7.5). As discussed above this suggests that although the mean energy transfer through these terms is negligible the instantaneous energy transfer for the terms III_{11} and III_{31} is non-negligible and warrants further investigation. Therefore, in the following section the instantaneous energy transfer between large- and small-scales will be further investigated including the instantaneous energy transfer as a result of the terms III_{11} and III_{31}.

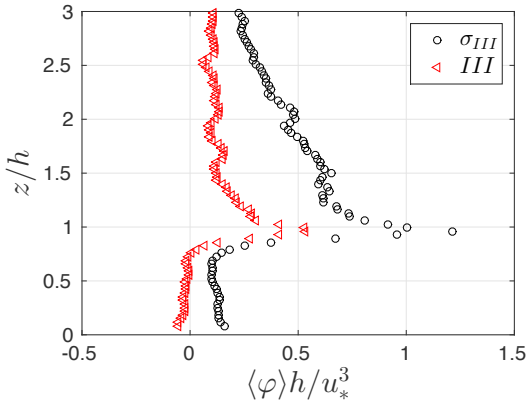

Figure 7.3. Mean and standard deviation of III spatially averaged and normalized by h/u_*^3.

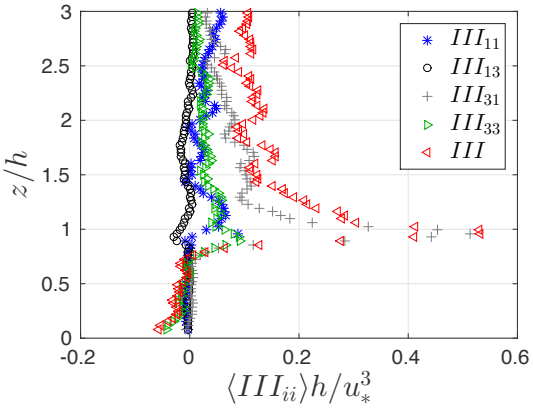

Figure 7.4. Contribution of each velocity term to total spatially averaged III, all terms normalized by h/u_*^3.

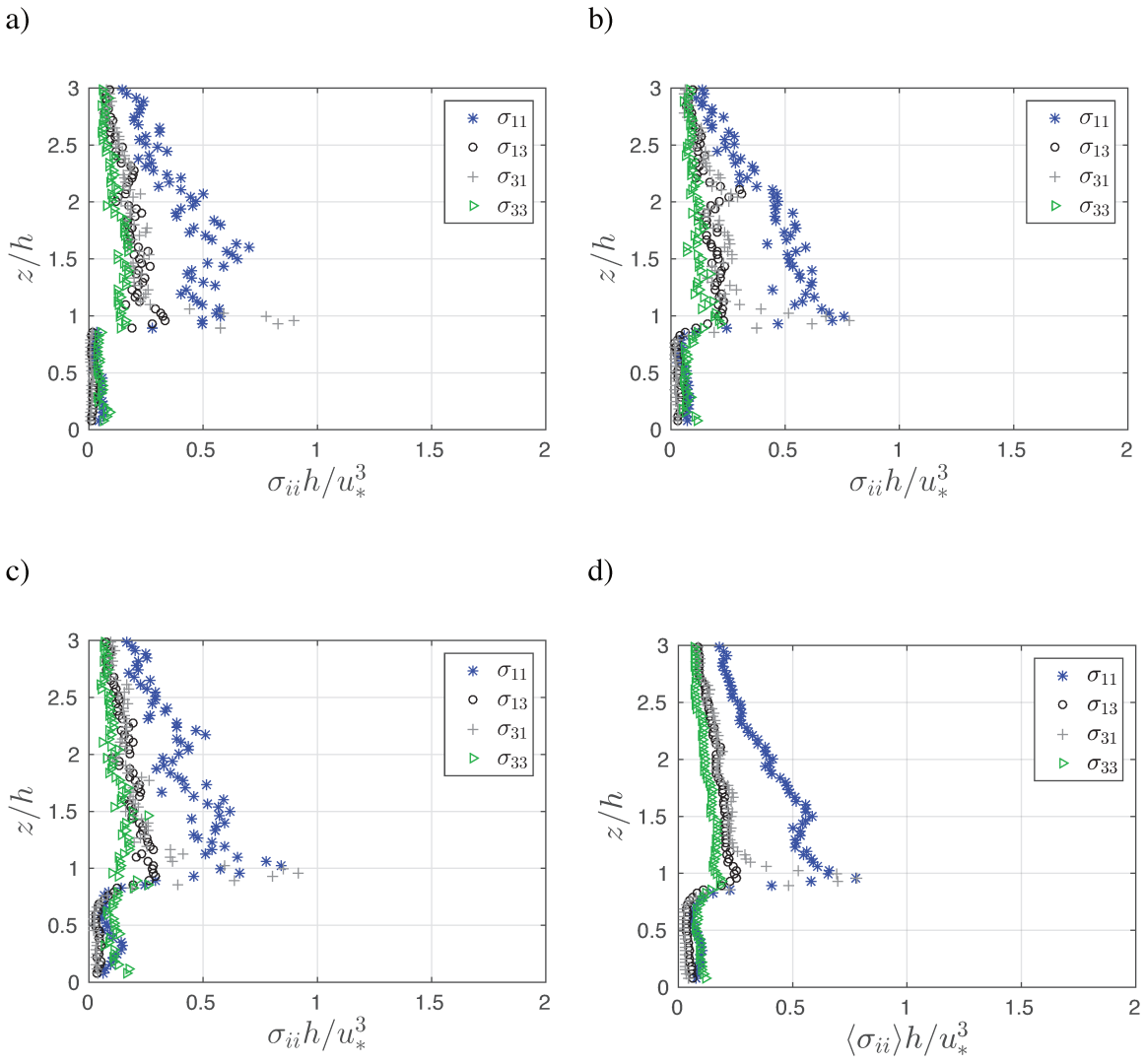

Figure 7.5. Standard deviation of velocity contribution to III at a) x/h = -0.25; b) x/h = 0; c) x/h = 0.25; d) spatially averaged, all terms normalized by h/u_*^3.

As described in Chapter 4 the LSE model used in the present work allows for the temporal extrapolation of velocity fluctuations and the energy transfer can, thus, also be investigated temporally. Using this technique we will focus on the cross-correlation of the large-scale component with the term III, $R_{\widetilde{u}'_L III}$, which represents the influence of the non-linear interaction between large-scale coherent structures and small-scales on the

energy transfer between those scales. As in Chapter 4 this analysis is performed by introducing time lags to the $\widetilde{u'}_L$ fluctuations (Equation 7.9).

$$R_{\widetilde{u}'_L III}(x_S, z_S, x_L, z_L, \tau_L) = \frac{\overline{\widetilde{u'}_L(x_L, z_L, t+\tau_L) III(x_{III}, z_{III}, t)}}{\sqrt{\overline{\widetilde{u'}_L{}^2(x_L, z_L)}}\sqrt{\overline{III(x_{III}, z_{III})}^2}} \tag{7.9}$$

The correlation exhibits positive values at zero and positive time delays within the shear layer and the overlying boundary layer (Figure 7.6). A positive correlation suggests that large-scales transfer energy to small-scales when the large-scales are high momentum and small-scales transfer energy to large-scales when large-scales are low momentum. The positive time shift is a result of small-scales interacting with large-scales that occur upstream in the flow and has been previously noted in Chapters 4 and 5 of the present work and documented within the literature (Guala et al., 2011; Blackman and Perret, 2016). A modification of the relationship occurs within the overlying boundary layer at $z/h = 3$ where a positive correlation at a positive time delay is countered by negative correlation at a negative time delay. This negative correlation, which represents a low momentum region triggering energy transfer from large-scales to small-scales or a high momentum region triggering energy transfer from small-scales to large-scales, suggests that the behavior of the interaction is modified between the roughness sub-layer and above. Previously in Chapter 4, a modification of the non-linear relationship above the roughness sublayer was related to a phenomenon of small-scales interacting with upstream large-scales, which was shown to occur only within the overlying boundary layer. Although the reason for this is unknown it suggests that the modification within the energy transfer interactions is related to the modification of the non-linear relationship between scales.

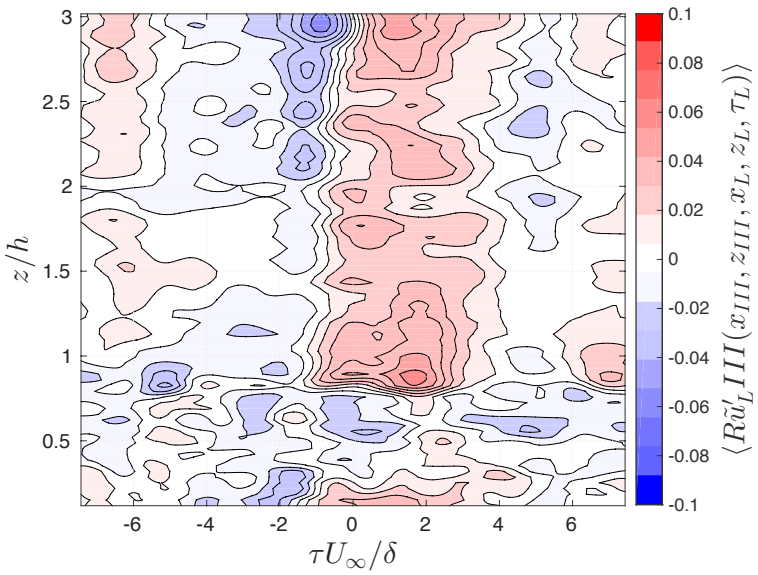

Figure 7.6. Spatially averaged Correlation Coefficient $\langle R_{\tilde{u}'_L III}\rangle$ where $x_L = x_{III}$ and $z_L = z_{III}$.

To further investigate the relationship between energy transfer and large-scale structures the cross-correlation is also computed for the III_{11} and III_{31} terms (Figure 7.7). Of the four terms used for the computation of III, these terms were shown to have the largest magnitude of standard deviation in Figure 7.5 and will therefore contribute most to the instantaneous energy transfer. The modification within the correlation $R_{\tilde{u}'_L III}$ at $z/h = 3$ is shown to be a result of III_{11}, which also shows negligible correlation throughout the roughness sublayer. This indicates that the modification that occurs within $R_{\tilde{u}'_L III}$ may be an artificial correlation due to near zero values of correlation being normalized by near-zero values of standard deviation. The correlation between large-scales and III_{31} exhibits positive correlation for positive time delays and negative correlation for negative time delays suggesting that this term governs the relationship between large-scales and energy transfer between large- and small-scales (III). These results confirm that energy transfer between large- and small-scales is a result of large-scale coherent structures occurring both upstream and downstream of the small-scales and suggests there could be a time-delay between the non-linear interaction and the energy transfer response.

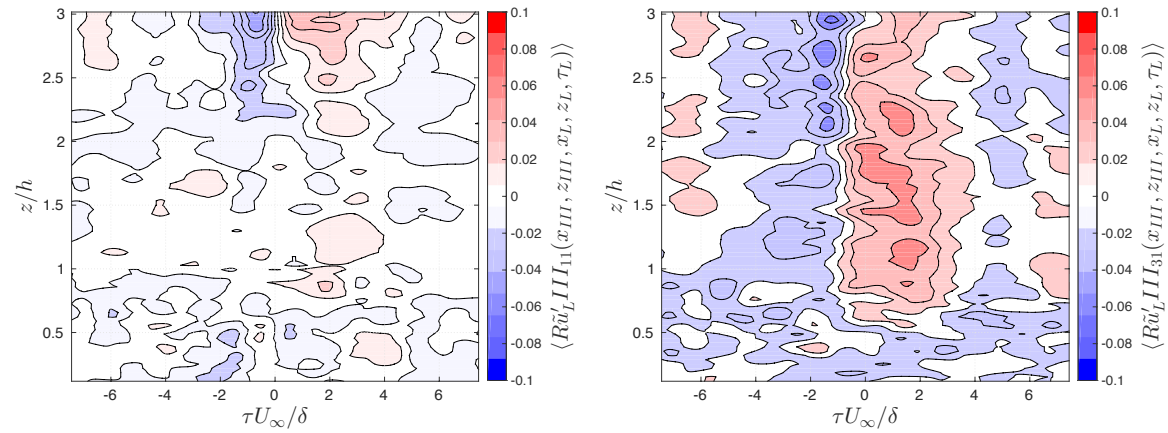

Figure 7.7. Spatially averaged Correlation Coefficient $\langle R_{\widetilde{u}'_L III}\rangle$ where $x_L = x_{III}$ and $z_L = z_{III}$ of a) III_{11}; b) III_{31}.

The spatially averaged two-point spatio-temporal correlation $R_{\widetilde{u}'_L III}$ provides further insight into this non-linear interaction (Figure 7.8a). The correlation is computed using a fixed point of III (z_{III}) within the shear layer at a height of $z/h = 1$ where the instantaneous energy transfer between large- and small-scales is most prominent (Equation 7.9). The correlation is positive throughout the boundary layer for both negative and positive time delays indicating there is a significant relationship between large-scale momentum regions and the energy transfer between scales. As previously described a positive correlation means that high momentum regions cause energy transfer to the small-scales while low momentum regions cause energy transfer from the small-scales. Thus, these results show that the top-down non-linear mechanism previously confirmed in Chapter 4 is related to energy transfer between scales. The shape of this correlation is similar to that of the correlation used to confirm the non-linear relationship ($R_{\widetilde{u}'_L u'^2_S}$), which is shown in Figure 7.8b. Both of the correlations exhibit positive values throughout the boundary layer and negative correlation within the canopy. As well, the peak of the correlation tends to shift temporally as the large-scale reference location in the boundary layer increases in height. When the large-scale reference is close to the shear layer at $z/h = 1$ the peak correlation occurs at approximately $\tau\overline{U}_\infty/\delta = 1.66$ and 0.18 for $R_{\widetilde{u}'_L III}$ and $R_{\widetilde{u}'_L u'^2_S}$, respectively. The peak then shifts to $\tau\overline{U}_\infty/\delta = 1.10$ and -0.38 for $R_{\widetilde{u}'_L III}$ and $R_{\widetilde{u}'_L u'^2_S}$, respectively, at a height of $z/h = 3$. As described in Chapter 4 this

is a consequence of the shape of the large-scale momentum regions which are inclined. The inclination angle can be estimated from these correlations as described in Chapter 4 and is found to be approximately 10.4° and 10.3° for $R_{\widetilde{u}_L' III}$ and $R_{\widetilde{u}_L' u_S'^2}$, respectively.

a) b)

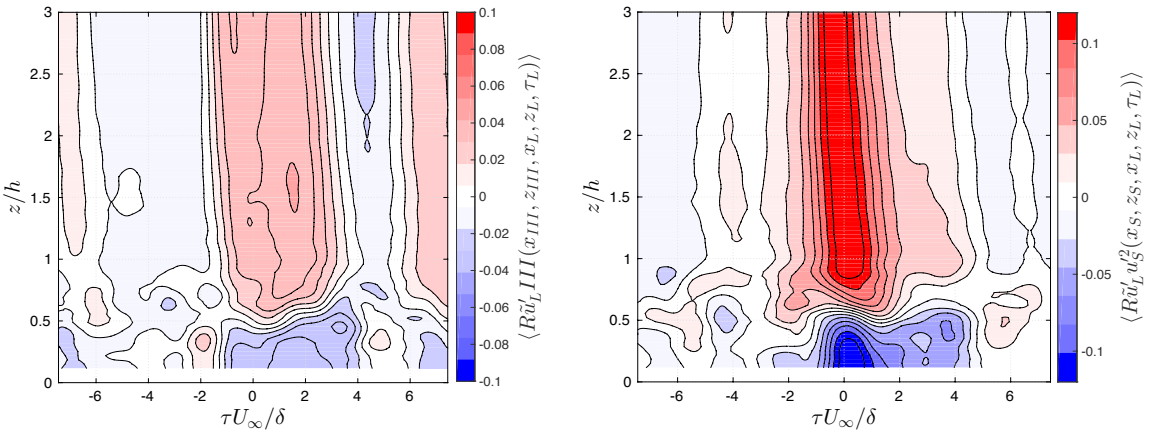

Figure 7.8. a) Spatially averaged spatial Correlation Coefficient $\langle R_{\widetilde{u}_L' III} \rangle$ where $x_L = x_{III}$ and $z_{III} = 1$; b) Spatially averaged spatial Correlation Coefficient $\langle R_{\widetilde{u}_L' u_S'^2} \rangle$ where $x_L = x_S$ and $z_S = 1$.

To determine which terms used to compute III contribute the most to this non-linear interaction the spatio-temporal correlations of u_L' with III_{11} and III_{31} are computed and shown in Figure 7.9. It is clear that III_{11} does not contribute significantly to the energy transfer between large-scales present within the overlying boundary layer and small-scales within the shear layer. The correlation computed with III_{31} is positive throughout the boundary layer, which corresponds to $R_{\widetilde{u}_L' III}$ and $R_{\widetilde{u}_L' u_S'^2}$, confirming that the energy transfer between scales is related to the shear stress within the shear layer. This suggests that although the footprint of the large-scales onto the small-scales through a non-linear interaction can be seen in the streamwise fluctuations the actual underlying cause could be predominantly due to energy interactions through the term III_{31}.

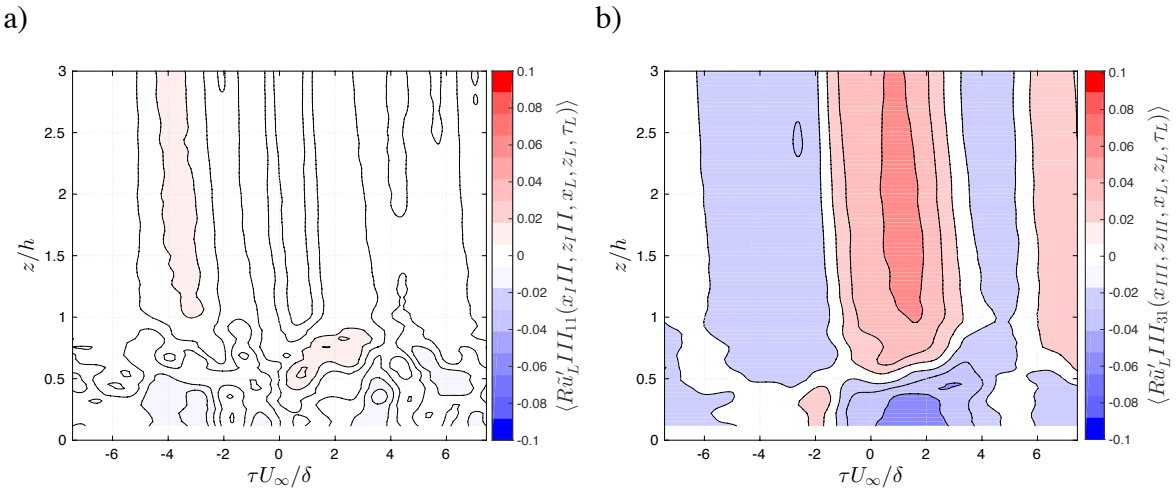

Figure 7.9. Spatially averaged spatial Correlation Coefficient $\langle R_{\tilde{u}'_L III}\rangle$ where $x_L = x_{III}$ and $z_{III} = 1$ of a) III_{11}; b) III_{31}.

As in Chapters 4 and 5, the present work provides further information about the flow dynamics in the rough-wall boundary layer that can be summarized in a qualitative cartoon (Figure 7.10). As a high momentum region passes over the small-scales close the roughness the small-scales are amplified through a non-linear interaction. This interaction corresponds to a transfer of energy from the high momentum region to the amplified small-scales through the term III_{31}. This relationship is reversed in the presence of a low momentum region when suppressed small-scales transfer energy to the large-scales through term III_{31}. However, due to limitations of the LSE method applied in the present work some terms in III were not computed and may be non-negligible and contribute to the energy transfer between scales. As discussed in Chapter 4 the momentum regions are slightly inclined which results in small-scale structures within the shear layer experiencing effects from the large-scale structure that is slightly downstream of them. As the large-scale reference location increases in height the distance in the streamwise direction between the small-scale structure and the low momentum region increases resulting in an increase in time-delay of the peak correlation. As shown above this time-delay is conserved in the energy transfer relationship. Thus, the non-linear relationship between large-scale momentum regions and small-scales within the shear layer is confirmed to be connected to a top-down mechanism of energy transfer between the scales.

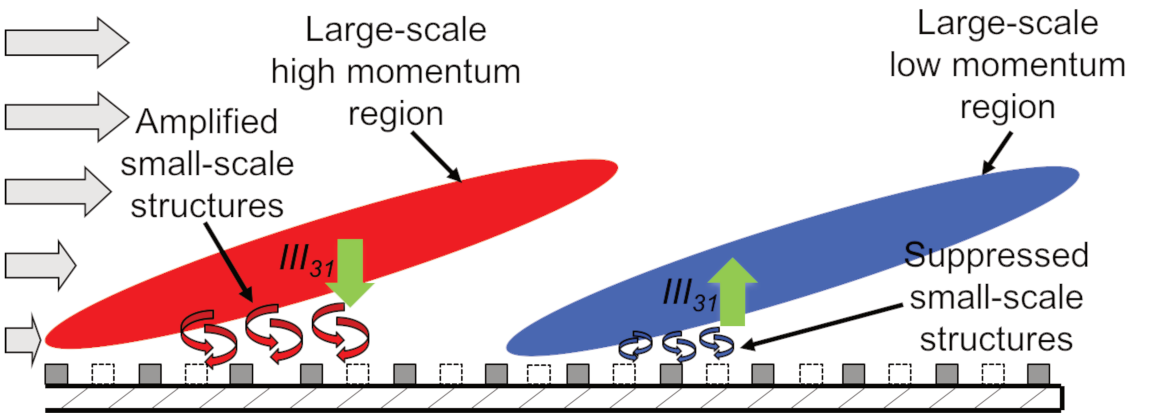

Figure 7.10. Qualitative cartoon illustrating time-delayed influence of large-scale low momentum structure (blue) and high momentum structure (red) on small-scales generated by the roughness showing energy transfer III_{31}. (green).

7.4 Conclusions

Large-scale coherent structures have been linked through a non-linear relationship to small-scale structures induced by the presence of the roughness in a rough-wall boundary layer (Squire et al., 2016; Blackman and Perret, 2016). However, how this relationship influences the energy transfer between structures is still unknown. The present work used experimental evidence from a rough-wall boundary layer consisting of a staggered cube array to answer the specific question posed in Section 7.1 above and the following conclusion found. The mean energy transfer between the mean flow, large-scales or ABL scales and small-scales or canopy scales was quantified using triple decomposition of the TKE budget and it was found that although the greatest mean energy transfer occurs between the mean flow and the small-scales, a non-negligible instantaneous energy transfer between large- and small-scales (III) exists. Through spatio-temporal cross-correlation between $\widetilde{u_L'}$ and III it was confirmed that the non-linear relationship is linked to energy transfer between large-scale coherent structures and small-scales induced by the presence of the roughness. Furthermore, this non-linear relationship has been shown to be a top-down mechanism as hypothesized in Chapter 4. In the following chapter the results from Chapters 4 through 7 will be discussed and final conclusions and perspectives drawn.

Résumé du Chapitre 8

Le chapitre 8 détaille les conclusions du présent travail et discute des conséquences de cette thèse sur notre comprehension de la couche limite urbaine. Un résumé (en français) de ce chapitre est proposé ci-après.

Ce travail a constaté que les régions à grande échelle de basse et haute vitesse interagissaient de manière non linéaire avec des structures à petite échelle dans la couche de cisaillement grâce à un mécanisme descendant, similaire à la modulation d'amplitude qui a été identifiée précédemment dans la paroi lisse (Mathis et al. 2009; 2011a; 2011b) et les couches limites des parois rugueuses (Nadeem et al., 2015; Anderson, 2016; Squire et al., 2016). Dans le présent travail, cette relation non linéaire a été étudiée à l'aide de différents types de rugosités (2D et 3D) et il a été confirmé que bien que la configuration de rugosité ait une influence non négligeable sur la relation quantitative entre les échelles, le mécanisme de base de la relation non-linéaire reste la même. Le lien entre ce mécanisme non linéaire et le transfert d'énergie entre les échelles a également été étudié et bien que le transfert d'énergie le plus important se soit produit entre le flux moyen et les petites échelles, un transfert d'énergie instantané non négligeable s'est produit entre les grandes et les petites échelles. Ce transfert d'énergie instantanée s'est également révélé être lié à la relation non linéaire qui existe entre les régions à grande échelle et les petites échelles. Enfin, la méthode LE-PIV (Large-Eddy PIV) utilisée avait pour but d'estimer la dissipation et de quantifier le bilan complet de l'énergie cinétique turbulente (TKE). L'analyse de la dissipation instantanée a confirmé la nécessité d'un modèle de dissipation qui considère à la fois la diffusion vers l'avant (transfert d'énergie de grandes à petites échelles) et la rétrodiffusion (transfert d'énergie de petites à grandes échelles) et a montré que ces phénomènes sont liés à des tourbillons qui se produisent dans la couche de cisaillement et la couche limite située au dessus. Le présent travail a conduit à des résultats importants sur les relations qui régissent l'échange de l'énergie entre des structures cohérentes dans la couche de limite urbaine. Cependant, comme le montrent les travaux actuels, ces relations sont complexes et nécessitent une étude approfondie.

Dans la couche limite de la paroi lisse, la modulation d'amplitude non linéaire a été utilisée pour développer un modèle prédictif pour les fluctuations à petite échelle près de la paroi, basé sur les fluctuations à grande échelle dans la couche limite située au dessus (Mathis et al., 2009, Mathis et al., 2011a). Récemment, ce modèle prédictif a été étendu à l'étude d'une paroi rugueuse (Squire et al., 2016). Cependant, le modèle prédictif utilisé dans ces cas n'est qu'un modèle statistique et n'intègre pas de processus dynamiques. Les travaux antérieurs ont montré que les structures à grande échelle présentes dans la couche limite située au dessus sont autosuffisantes et, par conséquent, n'échangent pas d'énergie avec d'autres échelles au sens moyen (Rawat et al., 2015). Ceci a été confirmé dans le présent travail, mais il a également été montré au chapitre 7 que ces structures échangent instantanément de l'énergie avec d'autres échelles. Cela a des conséquences importantes pour la dynamique du flux, qui ne sont pas pris en compte dans un modèle statistique prédictif. Par conséquent, il est impératif qu'un modèle dynamique soit développé pour la couche limite de paroi rugueuse où l'échange d'énergie et de polluants est régi par des processus turbulents. Un modèle LES qui résout les structures à grande échelle combinées à un modèle prédictif dynamique a le potentiel de réduire considérablement le coût de calcul des modèles dans des couches limites complexes comme la couche limite urbaine.

La nature hétérogène de la canopée urbaine présente un défi majeur pour le développement d'un modèle prédictif car l'interaction entre petites et grandes échelles est une dépendance spatiale. De plus, comme l'a démontré, la classification de la rugosité, que l'écoulement de type rasant, d'interférence de sillages ou de sillages isolés aient un effet significatif sur la relation non linéaire qui existe entre les petites échelles proches et les grandes échelles dans la couche limite. Par conséquent, les modèles prédictifs à la fois statistiques et dynamiques devraient être développés séparément pour chaque type de classification de flux. Enfin, le présent travail s'est concentré sur des configurations de rugosité simplifiées consistant soit en éléments de rugosité 2D ou 3D d'une hauteur égale. D'autres configurations de rugosité non étudiées dans le présent travail, telles que celles avec une hauteur de rugosité variée et des densités aléatoires, avec des profils de couches limites proches de celles d'une zone urbaine réelle devraient être utilisées pour étudier des

mécanismes de modulation d'amplitude non linéaire et des mécanismes de transfert d'énergie complexes zones urbaines.

8 Conclusions and Perspectives

Coherent structures, which govern the transport of heat, momentum and pollution within the urban boundary layer (Takimoto et al., 2011), have been well identified qualitatively, but their quantitative interactions and organization are still poorly understood. The purpose of this thesis was to investigate the quantitative relationships that exist between large-scale structures occurring in the boundary layer and small-scales induced by the presence of the roughness in the rough-wall boundary layer in order to improve our understanding of the fundamental turbulent dynamics that govern the transport of pollutants in urban areas.

This work was carried out using a combination of Particle Image Velocimetry (PIV) and Hot-Wire Anemometry (HWA) measurements within simplified wind tunnel roughness configurations. Large-scale low and high momentum regions were found to interact non-linearly with small-scale structures within the shear layer through a top-down mechanism similar to amplitude modulation which has been found previously in the smooth-wall (Mathis et al., 2009; 2011a; 2011b) and rough-wall boundary layers (Nadeem et al., 2015; Anderson, 2016; Squire et al., 2016). In the present work this non-linear relationship was investigated using several different roughness types (2D and 3D) and it was confirmed that although the roughness configuration has a non-negligible influence on the quantitative relationship between scales, the basic mechanism of the non-linear relationship remains the same. The link between this non-linear mechanism and energy transfer between scales was also investigated and although the greatest energy transfer was found to occur between the mean flow and small-scales a non-negligible instantaneous energy transfer was found to occur between large- and small-scales. This instantaneous energy transfer was also found to be linked to the non-linear relationship that exists between large-scale momentum regions occurring in the overlying boundary layer and small-scales induced by the presence of the roughness. This is a significant finding as although previous work has identified amplitude modulation in turbulent boundary layers (Mathis et al., 2009; 2011a; 2011b; Nadeem et al., 2015; Anderson,

2016; Squire et al., 2016) the relationship between the top-down non-linear mechanism and energy transfer between structures shown in Chapter 7 has not previously been investigated. Finally, the Large-Eddy PIV (LE-PIV) method was used to estimate the dissipation and quantify the full Turbulent Kinetic Energy (TKE) budget. Analysis of the instantaneous dissipation confirmed the need for a dissipation model that considers both forward scatter (energy transfer from large- to small-scales) and backscatter (energy transfer from small- to large-scales) and showed that these phenomena are linked to vortices that occur within the shear layer and overlying boundary layer. The present work has led to some important findings on the relationships that govern the exchange of momentum and energy between coherent structures in the urban boundary layer. However, as seen from the present work these relationships are complex and require further investigation.

Although the presence of a non-linear mechanism similar to amplitude modulation has been found and linked to energy transfer in the rough-wall boundary layer it is still not clear whether the non-linear mechanism is the underlying cause of the energy transfer or simply a result. The non-linear mechanism was found to occur consistently through the streamwise velocity component however amplitude modulation may be only a consequence of other important energy interactions. Therefore, future work should focus on quantifying the non-linear interactions of other velocity components to determine how they relate to the energy transfer between scales. As well, quantifying other terms within the triple decomposition of the TKE budget, such as the turbulent transport, may provide evidence of other important energy interactions.

Within the smooth-wall boundary layer non-linear amplitude modulation has been used to develop a predictive model for the near-wall small-scale fluctuations based on the large-scale fluctuations within the overlying boundary layer (Mathis et al., 2009, Mathis et al., 2011a) and recently this predictive model has been expanded to the study of a sand-roughened wall (Squire et al., 2016). However, the predictive model used in these cases is only a statistical model and does not incorporate dynamic processes. Previous work has shown that large-scale structures present within the overlying boundary layer are self-sustaining and therefore don't exchange energy with other scales in the mean sense

(Rawat et al., 2015). This has been confirmed in the present work, however, it was also shown in Chapter 7 that these structures do exchange energy with other scales instantaneously. This has significant consequences for the dynamics of the flow, which are not taken into account in a predictive statistical model. Therefore, it is imperative that a dynamic model be developed for the rough-wall boundary layer where energy and pollutant exchange is governed by turbulent processes. A coarsely resolved LES model that resolves the large-scale structures combined with a dynamic predictive model has the potential to significantly reduce the computation cost of models in complex boundary layers like the urban boundary layer. The exchange of pollutants between the urban canopy and the overlying boundary layer has been linked to intermittent turbulent processes, such as sweeps and ejections. A predictive model that accounts for dynamic processes such as these turbulent exchanges could be adapted for application in dispersion models used to predict pollutant concentrations in complex urban areas.

The heterogeneous nature of the urban canopy presents a significant challenge for the development of a predictive model as the interaction between small- and large-scales is spatially dependent. As well, as demonstrated, the classification of roughness whether skimming flow, wake interference flow or isolated flow has a significant effect on the non-linear relationship that exists between near-wall small-scales and large-scales within the boundary layer. Therefore, predictive models both statistical and dynamical would need to be developed separately for each type of flow classification. Finally, the present work has focused on simplified roughness configurations consisting of either 2D or 3D roughness elements of equal height. Other roughness configurations not studied in the present work, such as those with varied roughness height and random packing densities, with boundary layer profiles close to those of a real urban area should be used to investigate non-linear amplitude modulation and energy transfer mechanisms in complex urban areas.

Due to the constantly evolving urban landscape, increased emissions and threats from terrorism the need for numerical models with low computing costs is intensifying. The present work along with previous studies has shown that within the urban boundary layer there are dynamic processes that govern the exchange of energy and momentum between

large-scale structures that occur above a city and the small-scale structures induced by the presence of the urban area. This has demonstrated the potential for the development of a dynamic predictive model that could greatly reduce the computational costs of modeling the urban boundary layer allowing for detailed numerical investigations of urban flow and dispersion.

References

Adrian, R.J., in *On the role of conditional averages in turbulence theory. In Turbulence in Liquids*: *Proceedings of the Fourth Biennial Symposium*, Rolla, Missouri, 22-24 September 1975, Princeton, N.J: Science Press, pp. 323-332.

Adrian, R.J., "Hairpin vortex organization in wall turbulence," Phys Fluids 19, 041301 (2007).

Adrian, R.J., Meinhart, C.D., Tomkins, C.D., "Vortex organization in the outer region of the turbulent boundary layer," J Fluid Mech 422, 1-54 (2000).

Anderson, W., "Amplitude modulation of streamwise velocity fluctuations in the roughness sub-layer: evidence from large-eddy simulations," J Fluid Mech 789, 567-588 (2016).

Baars, W.J., Hutchins, N., Marusic, I., "Spectral stochastic estimation of high-Reynolds-number wall-bounded turbulence for a refined inner-outer interaction model," Phys Rev Fluids 1, 054406 (2016).

Beguier, C., Giralt, F., Fulachier, L., Keffer, J.F., in *Negative production in turbulent shear flows. Structure and Mechanisms of Turbulence II: Proceedings of the Symposium on Turbulence*, Berlin, 1-5 August 1978, 197.

Bernardini, M., Pirozzoli, S., "Inner-outer layer interactions in turbulent boundary layers: a refined measure for the large-scale amplitude modulation," Phys Fluids 23, 061701 (2011).

Blackman, K., "Influence of approach flow conditions on urban street canyon flow," M.E.Sc. Dissertation, University of Western Ontario, Canada, 2014.

Blackman, K., Perret, L., “Non-linear interactions in a boundary layer developing over an array of cubes using stochastic estimation,” Phys Fluid 28, 095108 (2016).

Blackman, K., Perret, L., Calmet, I., Rivet, C., “Turbulent kinetic energy budget in the boundary layer developing over an Urban-like rough wall using PIV,” Phys Fluid 29, 085113 (2017).

Blackman, K., Perret, L., Savory, E., “Effect of upstream flow regime on street canyon flow mean turbulence statistics,” Environ Fluid Mech 15, 823-849 (2015a).

Blackman, K., Perret, L., Savory, E., “Effect of upstream flow regime and canyon aspect ratio on non-linear interactions between a street canyon flow and the overlying boundary layer,” submitted to Bound Layer Meteorol (2017).

Blackman, K., Perret, L., Savory, E., Piquet, T., “Wind tunnel modeling of an idealized street canyon flow,” Atmos Environ 106, 139-153 (2015b).

Bonnet, J.P., Cole, D.R., Delville, J., Glauser, M.N., Ukeiley, L.S., “Stochastic estimation and proper orthogonal decomposition: complementary techniques for identifying structure,” Exp Fluids 17, 307-314 (1994).

Brunet, Y., Finnigan, J.J., Raupach, M.R., “A wind tunnel study of air flow in waving wheat: single-point velocity statistics,” Bound Layer Meteorol 70, 95-132 (1994).

Carper, M.A., Porté-Agel, F., “The role of coherent structures in subfilter-scale dissipation of turbulence measured in the atmospheric surface layer,” J Turbul 5, 40-64 (2004).

Castillo, M.C., Inagaki, A., Kanda, M., “The effects of inner- and outer-layer turbulence in a convective boundary layer on the near-neutral inertial sub-layer over an urban-like surface,” Bound Layer Meteorol 140, 453-469 (2011).

Castro, I., Cheng, H., Reynolds, R., “Turbulence over urban-type roughness: deductions from wind-tunnel measurements,” Bound Layer Meteorol 118, 109-131 (2006).

Cheng, H., Castro, I.P., “Near wall flow over urban-like roughness,” Bound Layer Meteorol 104, 229-259 (2002).

Christen, A., Rotach, M.W., Vogt, R., “The budget of turbulent kinetic energy in the urban roughness sublayer,” Bound Layer Meteorol 131, 193-222 (2009).

Clark, R.A., Ferziger, J.H., Reynolds, W.C., “Evaluation of subgrid-scale models using an accurately simulated turbulent flow,” J Fluid Mech 91, 1-16 (1979).

Coceal, O., Dobre, A., Thomas, T.G., Belcher, S.E., “Structure of turbulent flow over regular arrays of cubical roughness,” J Fluid Mech 589, 375-409 (2007a).

Coceal, O., Dobre, A., Thomas, T.G., “Unsteady dynamics and organized structures from DNS over an idealized building canopy,” Int J Climatol 27, 1943-1953 (2007b).

Cook, N.J., “The designer’s guide to wind loading of building structures: Part 1,” The University Press, Cambridge (1985).

DeGraaff, D.B., Eaton, J.K., “Reynolds number scaling of the flat plate turbulent boundary layer,” J Fluid Mech 422, 319-346 (2000).

Djenidi, L., Antonia, R.A., Amielh, M., Anselmet, F., “Use of PIV to highlight possible errors in hot-wire Reynolds stress data over a 2D rough wall,” Exp Fluids 55, 1830 (2014).

Druault, P., Lardeau, S., Bonnet, J.P., Coiffet, F., Delville, J., Lamballais, E., Largeau, J.F., Perret, L., “Generation of three-dimensional turbulent inlet conditions for Large-

Eddy Simulation," AIAA J 42, 447-456 (2004).

Dupont, S., Brunet, Y., Finnigan, J.J., "Large-eddy simulation of turbulent flow over a forested hill: validation and coherent structure identification," Q J R Meteorol Soc 134, 1911-1929 (2008).

ESDU, "Strong winds in the atmospheric boundary layer. Part I: mean-hourly wind speeds," Data Item 82026 (amended 1993), Engineering Sciences Data Unit International (1982).

ESDU, "Characteristics of atmospheric turbulence near the ground. Part II: single point data for strong winds (neutral atmosphere)," Data Item 852020 (amended 1993), Engineering Sciences Data Unit International (1985).

Grimmond, C.S.B., Oke, T.R., "Aerodynamic properties of urban areas derived from analysis of surface form," J Appl Meteorol 38, 1262-1292 (1999).

Guala, M., Metzger, M., McKeon, B.J., "Interactions within the turbulent boundary layer at high Reynolds number," J Fluid Mech 666, 573-604 (2011).

Hayakawa, M., Iida, S., "Behavior of turbulence in the near wake of a thin plate at low Reynolds number," Phys Fluid 4, 2282-2291 (1992).

Hong, J., Katz, J., Meneveau, C., Schultz, M.P., "Coherent structures and associated subgrid-scale energy transfer in a rough-wall turbulent channel flow," J Fluid Mech 712, 92-128 (2012).

Hussain, F., "Coherent structures – reality and myth," Phys Fluids 26, 2816-2838 (1983).

Hussain, F., "Coherent structures and turbulence," J Fluid Mech 173, 303-356 (1986).

Hutchins, N., Marusic, I., “Large-scale influences in near-wall turbulence,” Phil Trans R Soc A 365, 647-664 (2007).

Inagaki, A., Castillo, M., Yamashita, Y., Kanda, M., Takimoto, H., “Large-eddy simulation of coherent flow structures within a cubical canopy,” Bound Layer Meteorol 142, 207-222 (2012).

Inagaki, A., Kanda, M., “Turbulent flow similarity over an array of cubes in near-neutrally stratified atmospheric flow,” J Fluid Mech 615, 101-120 (2008)

Inagaki, A., Kanda, M., “Organized structure of active turbulence over an array of cubes within the logarithmic layer of atmospheric flow,” Bound Layer Meteorol 135, 209-228 (2010).

Inoue, M., Mathis, R., Marusic, I., Pullin, D.I., “Inner-layer intensities for the flat-plate turbulent boundary layer combining a predictive wall-model with large-eddy simulations,” Phys Fluids 24, 075102 (2012).

Jimenez, J., “Turbulent flows over rough walls,” Annu Rev Fluid Mech 36, 173-196 (2004).

Kanda, M., “Large-eddy simulations on the effects of surface geometry of building arrays on turbulent organized structures,” Bound Layer Meteorol 118, 151-168 (2006).

Kanda, M., Moriwaki, R., Kasamatsu, F., “Large-eddy simulation of turbulent organized structures within and above explicitly resolved cube arrays,” Bound Layer Meteorol 112, 343-368 (2004).

Kellnerova, R., Kukacka, L., Jurcakova, K., Uruba, V., Janour, Z., “PIV measurement of turbulent flow within a street canyon: detection of coherent motion,” J Wind Eng Ind Aerodyn 104, 302-313 (2012).

Klein, P., Clark, J.V., “Flow variability in a North American downtown street canyon,” Amer Meteorol Soc 46, 851-877 (2007).

König, O., Schlüter, J., Fiedler, H.E., in *The decelerated mixing layer controlled by two frequencies*. *Advances in Turbulent studies: Progress in Aeronautics. 8th Beer-Sheva International Seminar on MHD-Flows and Turbulence*, Israel, 1996.

König, O., Schlüter, J., Fiedler, H.E., in *Excitation of mixing layers with two frequencies*. *Euromech Colloquium 361, Active control of turbulent shear flows,* Berlin, Germany, 1997.

Lee, J.H., Hyung, J.S., “Very-large-scale motions in a turbulent boundary layer,” J Fluid Mech 673, 80-120 (2011).

Lee, J.H., Hyung, J.S., Krogstad, P.A., “Direct numerical simulation of the turbulence boundary layer over a cube-roughened wall,” J Fluid Mech 669, 397-431 (2011).

Lee, J.H., Abu, S., Lee, S.H., Sung, J.H., “Turbulent boundary layers over rod- and cube-roughened walls,” J Turb 13, 1-26 (2012).

Leonardi, S., Castro, I.P., “Channel flow over large cube roughness: a direct numerical simulation study,” J Fluid Mech 651, 519-539 (2010).

Liu, X., Thomas, F.O., “Measurement of the turbulent kinetic energy budget of a planar wake flow in pressure gradients,” Exp Fluids 37, 469-482 (2004).

Liu, H.Y., Bo, T.L., Wang, G.H., Zheng, X.J., “The analysis of turbulence intensity and Reynolds shear stress in wall-bounded turbulent flows at high Reynolds numbers,” Bound Layer Meteorol 150, 33-47 (2014).

Lumley, J.L., "Computational modeling of turbulent flows," Adv Appl Mech 18, 123-176 (1978).

Macdonald, R.W., "Modelling the mean velocity profile in the urban canopy layer," Bound Layer Meteorol 97, 25-45 (2000).

Macdonald, R.W., Carter Schofield, S., Slawson, P.R., "Modelling of urban roughness using arrays of roughness elements," Water Air Soil Pollut 2, 541-554 (2002).

Macdonald, R.W., Griffiths, R.F., Hall, D.J., "An improved method for the estimation of surface roughness of obstacle arrays," Atmos Environ 32, 1857-1864 (1998).

Marusic, I., Mathis, R., Hutchins, N., in *A wall-shear stress predictive model*: *Proceedings of 13th European Turbulence Conference*, Warsaw, Poland, 12-15 September 2011.

Marusic, I., McKeon, B.J., Monkewitz, P.A., Nagib, H.M., Smits, A.J., Screenivasan, K.R., "Wall-bounded turbulent flows at high Reynolds numbers: Recent advances and key issues," Phys Fluids 22, 065103 (2010).

Mathis, R., Hutchins, N., Marusic, I., "Large-scale amplitude modulation of the small-scale structures in turbulent boundary layers," J Fluid Mech 628, 311-337 (2009).

Mathis, R., Hutchins, N., Marusic, I., "A predictive inner-outer model for streamwise turbulence statistics in wall-bounded flows," J Fluid Mech 681, 537-566 (2011a).

Mathis, R., Marusic, I., Hutchins, N., Screenivasan, K.R., "The relationship between the velocity skewness and the amplitude modulation of the small scale by the large scale in turbulent boundary layers," Phys Fluids 23, 121702 (2011b).

Michioka, T., Sato, A., “Effect of incoming turbulent structure on pollutant removal from two-dimensional street canyon,” Bound Layer Meteorol 145, 469-484 (2012).

Michioka, T., Takimoto, H., Sato, A., “Large-eddy simulation of pollutant removal from a three-dimensional street canyon,” Bound Layer Meteorol 150, 259-275 (2014).

Nadeem, M., Lee, J.H., Lee, J., Sung, H.J., “Turbulent boundary layers over sparsely-spaced rod-roughened walls,” Int J Heat Fluid Flow 56, 16-27 (2015).

Naguib, A., Wark, C., Juckenhöfel, O., “Stochastic estimation and flow sources associated with surface pressure events in a turbulent boundary layer,” Phys Fluids 13(9), 2611-2626 (2001).

Natrajan, V.K., Christensen, K.T., “The role of coherent structures in subgrid-scale energy transfer within the log layer of wall turbulence,” Phys Fluids 18, 065104 (2006).

Oke, T.R., “The urban energy balance,” Prog Phys Geogr 12, 471-508 (1988).

Panigraphi, P.K., Schroeder, A., Kompenhans, J., “Turbulent structures and budgets behind permeable ribs,” Exp Therm Fluid Sci 32, 1011-1033 (2008).

Perret, L., Blackman, K., Savory, E., “Combining wind-tunnel and field measurements of street-canyon flow via stochastic estimation,” Bound Layer Meteorol 16, 491-517 (2016).

Perret, L., Rivet, C., in *Dynamics of a turbulent boundary layer over cubical roughness elements: Insight from PIV measurements and POD analysis: Proceedings of Eighth International Symposium on Turbulence and Shear Flow Phenomena*, Poitiers, France, 27-30 August 2013.

Perret, L., Savory, E., “Large-scale structures over a single street canyon immersed in an urban-type boundary layer,” Bound Layer Meteorol 148, 111-131 (2013).

Picard, C., Delville, J., “Pressure velocity coupling in a subsonic round jet,” Int J Heat Fluid Flow 21, 359-364 (2000).

Porté-Agel, F., Parlange, M.B., Meneveau, C., Eichinger, W.E., “A-priori field study of the subgrid-scale heat fluxes and dissipation in the atmospheric surface layer,” J Atmos Sci 58, 2673-2698 (2001).

Rawat, S., Cossu, C., Hwang, Y., Rincon, F, “On the self-sustained nature of large-scale motions in turbulent Couette flow,” J Fluid Mech 782, 515-540 (2015).

Rivet, C., “Étude en soufflerie atmosphérique des interactions entre canopée urbaine et basse atmosphère par PIV stéréoscopique,” Ph.D. Dissertation, École Centrale de Nantes, France, 2014.

Robinson, S., “Coherent motions in the turblent boundary layer,” Ann Rev Fluid Mech 23, 601-639 (1991).

Rotach, M.W., Vogt, R., Bernhofer, C., Batchvarova, E., Christen, A., Clappier, A., Feddersen, B., Gryning, S.E., Martucci, G., Mayer, H., Mitev, V., Oke, T.R., Parlow, E., Richner, H., Roth, M., Roulet, Y.A., Ruffieux, D., Salmond, J.A., Schatzmann, M., Voogt, J.A., “BUBBLE – an urban boundary layer meteorology project,” Theor Appl Climatol 81, 231-261 (2005).

Roth, M., “Review of atmospheric turbulence over cities,” Q J R Meteorol Soc 126, 941-990 (2000).

Roth, M., Inagaki, A., Sugawara, H., Kanda, M., “Small-scale spatial variability of turbulence statistics, (co)spectra and turbulent kinetic energy measured over a regular array of cube roughness,” Environ Fluid Mech 15, 329-348 (2015).

Salizzoni, P., Marro, M., Soulhac, L., Grosjean, N., Perkins, R.J., "Turbulent transfer between street canyons and the overlying atmospheric boundary layer," Bound Layer Meteorol 141, 393-414 (2011).

Sarkar, A., Schlüter, J.U., "Large eddy simulations of turbulent mixing layers excited with two frequencies," Flow Turbul Combust 92, 651-671 (2013a).

Sarkar, A., Schlüter, J.U., "Numerical investigation of the turbulent energy budget in the wake of freely oscillating elastically mounted cylinder at low reduced velocities," J Fluid Struct 43, 441-462 (2013b).

Savory, E., Perret, L., Rivet, C., "Modelling considerations for examining the mean and unsteady flow in a simple urban-type street canyon," Meteorol Atmos Phys 121, 1-16 (2013).

Schlatter, P., Orlu, R., "Quantifying the interaction between large and small scales in wall-bounded turbulent flows: A note of caution," Phys Fluids 22, 051704 (2010).

Sheng, J., Meng, H., Fox, R.O., "A large eddy PIV method for turbulence dissipation rate estimation," Chem Eng Sci 55, 4423-4434 (2000).

Smits, A.J., McKeon, B.J., Marusic, I., "High-Reynolds number wall turbulence," Annu Rev Fluid Mech 43, 353-375 (2011).

Squire, D.T., Baars, W.J., Hutchins, N., Marusic, I., "Inner-outer interactions in rough-wall turbulence," J Turb 17, 1468-5248 (2016).

Stewart, I., Oke, T.R., in *Classifying urban climate field sites by "local climate zones": the case of Nagano, Japan: Proceedings of the seventh International Conference on Urban Climate*, Yokohama, Japan, 29 June - 3 July 2009, pp. 1-5.

Stull, R.B., “An introduction to boundary layer meteorology,” Kluwer Academic Publishers, Dordrecht (1988).

Tagawa, M., Tsuji, T., Nagano, Y., “Evaluation of X-probe response to wire separation for wall turbulence measurements,” Exp Fluids 12, 413-421 (1992).

Takimoto, H., Inagaki, A., Kanda, M., Sato, A., Michioka, T., “Length-scale similarity of turbulent organized structures over surfaces with different roughness types,” Bound Layer Meteorol 147, 217-236 (2013).

Takimoto, H., Sato, A., Barlow, J.F., Moriwaki, R., Inagaki, A., Onomura, S., Kanda, M., “Particle Image Velocimetry measurements of turbulent flow within outdoor and indoor urban scale models and flushing motions in urban canopy layers,” Bound Layer Meteorol 140, 295-314 (2011).

Talluru, K.M., Baidya, R., Hutchins, N., Marusic, I., “Amplitude modulation of all three velocity components in turbulent boundary layers,” J Fluid Mech 746, 1-11 (2014).

Tinney, C.E., Coiffet, F., Delville, J., Hall, A.M., Jordan, P., Glauser, M.N., “On spectral linear stochastic estimation,” Exp Fluids 41, 763-775 (2006).

Tomkins, C.D., Adrian, R.J., “Spanwise structure and scale growth in turbulent boundary layers,” J Fluid Mech 490, 37-74 (2003).

Tropea, C., Yarin, A., Foss, J.F., Springer Handbook of Experimental Fluid Mechanics (Springer-Verlag, Berlin Heidelberg, 2007) p. 1403-1405.

Tutu, N.K., Chevray, R., “Cross-wire anemometry in high intensity turbulence,” J Fluid Mech 71, 785-800 (1975).

Volino, R.J., Schultz, M.P., Flack, K.A., “Turbulence structure in rough- and smooth-wall

boundary layers," J Fluid Mech 592, 263-2 (2007).

World Health Organization, "Ambient (outdoor) air quality and health: fact sheet 313," http://www.who.int/mediacentre/factsheets/fs313/en/. Accessed 14 November 2015 (2014).

Wyngaard, J.C., *Turbulence in the Atmosphere* Cambridge University Press, Cambridge (2010).

Yakhot, A., Liu, H., Nikitin, N., "Turbulent flow around a wall-mounted cube: A direct numerical simulation," Int J Heat Fluid Fl 27, 994-1009 (2006).

Zhu, W., van Hout, R., Katz, J., "On the flow structure and turbulence during sweep and ejection events in a wind-tunnel model canopy," Bound Layer Meteorol 124, 205-233 (2007).

Appendix A

The general form of the TKE budget for a stationary flow is described in Equation A.1, where *Adv* is advection, P_d is production, T is turbulent transport, Ψ is pressure transport, D_μ is viscous transport and ε is dissipation.

$$0 = \underbrace{-\overline{u_j}\frac{\partial \bar{k}}{\partial x_j}}_{Adv} \underbrace{-\overline{u_i' u_j'}\frac{\partial \overline{u_i}}{\partial x_j}}_{P_d} \underbrace{-\frac{1}{2}\frac{\partial \overline{u_i' u_i' u_j'}}{\partial x_j}}_{T} \underbrace{-\frac{1}{\rho}\frac{\partial \overline{P' u_j'}}{\partial x_j}}_{\Psi} + \underbrace{\nu \frac{\partial}{\partial x_j}\left[\overline{u_i'\left(\frac{\partial u_i'}{\partial x_j} + \frac{\partial u_j'}{\partial x_i}\right)}\right]}_{D_\mu} - \varepsilon \quad \text{(A.1)}$$

Due to the limited spatial resolution of the PIV measurements the dissipation term cannot be calculated directly and is instead calculated using the LE-PIV method, which states that the turbulent dissipation is equal to the energy transfer in the inertial range (Equation A.2) (Sheng et al., 2000):

$$\varepsilon \approx -\overline{\tau_{ij} S_{ij}} \quad \text{(A.2)}$$

A mathematical explanation of the method is provided below.

The instantaneous velocity (u_j) can be decomposed as follows

$$U_j = \widetilde{u_j} + \breve{u_j} \quad \text{(A.3)}$$

where $\widetilde{u_j}$ is the resolved-scale velocity and $\breve{u_j}$ is the unresolved-scale velocity. By applying a filter to the incompressible continuity equation and the Navier-Stokes equation, the LES equations are obtained (Equation A.4, A.5)

$$\frac{\partial \widetilde{u_j}}{\partial x_j} = 0 \quad \text{(A.4)}$$

$$\frac{\partial \widetilde{u_i}}{\partial t} + \frac{\partial \widetilde{u_i}\widetilde{u_j}}{\partial x_j} = -\frac{\partial \tilde{P}}{\partial x_j} + \nu \frac{\partial^2 \widetilde{u_i}}{\partial x_j \partial x_j} - \frac{\partial \tau_{ij}}{\partial x_j} \quad \text{(A.5)}$$

where

$$\tau_{ij} = \widetilde{u_\iota u_J} - \widetilde{u_\iota}\widetilde{u_J} \tag{A.6}$$

is the sub-grid scale stress tensor.

The resolved scale kinetic energy is defined by Equation A.7 and its budget (Equation A.8) is obtained by multiplying Equation A.5 by $\widetilde{u_\iota}$ and averaging.

$$E = \frac{1}{2}\overline{\widetilde{u_\iota}\widetilde{u_J}} \tag{A.7}$$

$$\frac{\partial E}{\partial t} + \overline{\widetilde{u_J}}\frac{\partial E}{\partial x_j} = -\frac{1}{\rho}\frac{\partial \overline{\tilde{P}\widetilde{u_J}}}{\partial x_j} + \nu\frac{\partial^2 E}{\partial x_j \partial x_j} - \frac{\partial}{\partial x_j}\overline{\overline{\tau_{\iota J}}\widetilde{u_\iota}} - \nu\overline{\frac{\partial\widetilde{u_\iota}}{\partial x_J}\frac{\partial\widetilde{u_\iota}}{\partial x_J}} + \overline{\overline{\tau_{\iota J}}S_{\iota J}} \tag{A.8}$$

$\overline{\overline{\tau_{\iota J}}S_{\iota J}}$ is the sub-grid energy transport, which models the kinetic energy transported to the small-scales from the resolved scales and $\nu\overline{\frac{\partial\widetilde{u_\iota}}{\partial x_J}\frac{\partial\widetilde{u_\iota}}{\partial x_J}}$ is the dissipation by the resolved scales. Finally,

$$S_{ij} = \frac{1}{2}\left(\frac{\partial\widetilde{u_J}}{\partial x_i} + \frac{\partial\widetilde{u_\iota}}{\partial x_j}\right) \tag{A.9}$$

is the resolved scale strain rate tensor.

The resolved scale velocity can be further decomposed into a mean ($\overline{\widetilde{u_j}}$) and fluctuating component (u_j'') (Equation A.10).

$$\widetilde{u_J} = \overline{\widetilde{u_j}} + u_j'' \tag{A.10}$$

Similarly the resolved kinetic energy (E) is decomposed into a contribution from the movement of the mean flow (ξ) and turbulent flow (e) (Equation A.11).

$$E = \xi + e \tag{A.11}$$

The resolved scale kinetic energy from the movement of the mean flow is then defined by Equation A.12 and its budget by Equation A.13.

$$\xi = \frac{1}{2}\overline{\widetilde{u_\iota}}\overline{\widetilde{u_J}} \tag{A.12}$$

$$\frac{\partial \xi}{\partial t} + \widetilde{\bar{u}_j}\frac{\partial \xi}{\partial x_j} = -\frac{1}{\rho}\frac{\partial \bar{\bar{P}}\widetilde{\bar{u}_j}}{\partial x_j} + \nu\frac{\partial^2 \xi}{\partial x_j \partial x_j} - \frac{\partial}{\partial x_j}\overline{\tau_{ij}\widetilde{u_i}} - \nu\frac{\partial \widetilde{\bar{u}_i}}{\partial x_j}\frac{\partial \widetilde{\bar{u}_i}}{\partial x_j}$$

$$+\overline{\tau_{ij}}\,\overline{S_{ij}} - \overline{u_i'' u_j''}\frac{\partial \widetilde{\bar{u}_i}}{\partial x_j} \tag{A.13}$$

where $\overline{\tau_{ij}}\,\overline{S_{ij}}$ and $\nu\frac{\partial \widetilde{\bar{u}_i}}{\partial x_j}\frac{\partial \widetilde{\bar{u}_i}}{\partial x_j}$ are the sub-grid energy transport and the dissipation from the movement of the mean flow, respectively. Finally, the resolved scale turbulent kinetic energy and its budget are shown in Equations A.14 and A.15.

$$e = \frac{1}{2}\overline{u_i'' u_j''} \tag{A.14}$$

$$\frac{\partial e}{\partial t} + \widetilde{\bar{u}_j}\frac{\partial e}{\partial x_j} = -\overline{u_i'' u_j''}\frac{\partial \widetilde{\bar{u}_i}}{\partial x_j} - \frac{1}{2}\frac{\partial \overline{u_i'' u_i'' u_j''}}{\partial x_j} - \frac{1}{\rho}\frac{\partial \overline{P'' u_j''}}{\partial x_j} + \nu\frac{\partial^2 e}{\partial x_j \partial x_j} - \frac{\partial}{\partial x_j}\overline{u_i'' \tau_{ij}''} - \nu\overline{\frac{\partial u_i''}{\partial x_j}\frac{\partial u_i''}{\partial x_j}} + \overline{\tau_{ij}'' S_{ij}''} \tag{A.15}$$

where $\overline{\tau_{ij}'' S_{ij}''}$ and $\nu\overline{\frac{\partial u_i''}{\partial x_j}\frac{\partial u_i''}{\partial x_j}}$ are the sub-grid energy transport and dissipation of the turbulent flow.

From Equations A.8, A.13, A.15 the total sub-grid energy transport and dissipation of kinetic energy is composed of contributions from the movement of the mean flow and the turbulent flow (Equation A.16).

$$\underbrace{-\nu\overline{\frac{\partial \widetilde{\bar{u}_i}}{\partial x_j}\frac{\partial \widetilde{\bar{u}_i}}{\partial x_j}} + \overline{\tau_{ij}}\,\overline{S_{ij}}}_{dissipation\ of\ kinetic\ energy} = \underbrace{\overline{\tau_{ij}}\,\overline{S_{ij}} - \nu\frac{\partial \widetilde{\bar{u}_i}}{\partial x_j}\frac{\partial \widetilde{\bar{u}_i}}{\partial x_j}}_{dissipation\ from\ movement\ of\ the\ mean\ flow} + \underbrace{\overline{\tau_{ij}'' S_{ij}''} - \nu\overline{\frac{\partial u_i''}{\partial x_j}\frac{\partial u_i''}{\partial x_j}}}_{dissipation\ from\ turbulent\ flow} \tag{A.16}$$

In high Reynolds number flows TKE is produced by the integral scales at the same rate at which energy is dissipated by the Kolmogorov scales. Furthermore, within the inertial subrange TKE is neither produced nor dissipated and these structures simply transfer energy from large- to small-scales without changing (Sheng et al., 2000). This theory is confirmed in Figure A.1, which shows each of the terms in Equation A.16 calculated from the present work, which used a spatial filter falling within the inertial range. The

terms $\nu \overline{\frac{\partial \widetilde{u_i}}{\partial x_j}} \overline{\frac{\partial \widetilde{u_i}}{\partial x_j}}$, $\nu \overline{\frac{\partial \widetilde{\overline{u_i}}}{\partial x_j}} \overline{\frac{\partial \widetilde{\overline{u_i}}}{\partial x_j}}$, and $\nu \overline{\frac{\partial u_i''}{\partial x_j}} \overline{\frac{\partial u_i''}{\partial x_j}}$ are negligible demonstrating that scales within the inertial range do not dissipate energy. As well, it is shown that the contribution of the movement of the mean flow to the sub-grid energy transport ($\overline{\tau_{ij}} \overline{S_{ij}}$) is negligible. It then follows that dissipation of turbulent kinetic energy is equal to the sub-grid energy transport in the inertial range (Equation A.17).

$$\varepsilon \approx -\overline{\tau_{ij}'' S_{ij}''} \approx -\overline{\tau_{ij} S_{ij}} \tag{A.17}$$

a) b)

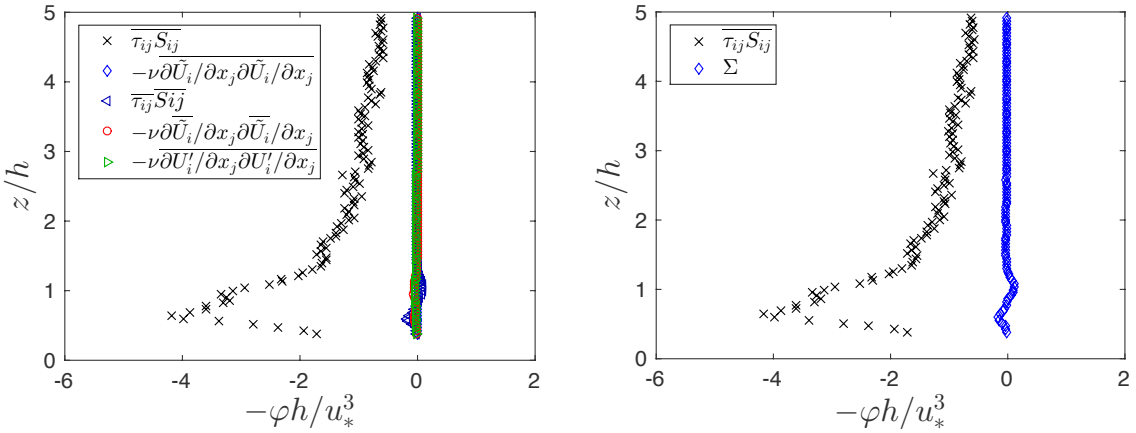

Figure A.1a) Mean dissipation terms; b) Mean dissipation and the sum of all other terms (Σ) at B, all terms normalized by h/u_*^3.

Appendix B

In the present work the streamwise aligned stereoscopic PIV measurements have been performed in one plane making it impossible to compute the spatial gradient of the instantaneous velocity in three directions of space but allows for computation in the plane of measurement (x-z). In order to compute the three-dimensional turbulent kinetic energy budget two assumptions, the divergence free condition shown in Equation B.1 and isotropy condition shown in Equation B.2 were used.

$$\frac{\partial U}{\partial x} + \frac{\partial V}{\partial y} + \frac{\partial W}{\partial z} = 0 \tag{B.1}$$

$$\frac{\partial U}{\partial y} = \frac{\partial V}{\partial y} = \frac{\partial W}{\partial y} \tag{B.2}$$

To test these assumptions the point *D* shown on Figure 2.4b,c in Chapter 2 from the *x-z* and *y-z* planes was used to compare gradients. Figure B.1 shows the gradients calculated directly from the *y-z* plane and those estimated from the assumptions listed above applied to the *x-z* plane. It shown that the estimated and directly calculated gradients agree well particularly within the overlying boundary layer, thus the assumptions are valid.

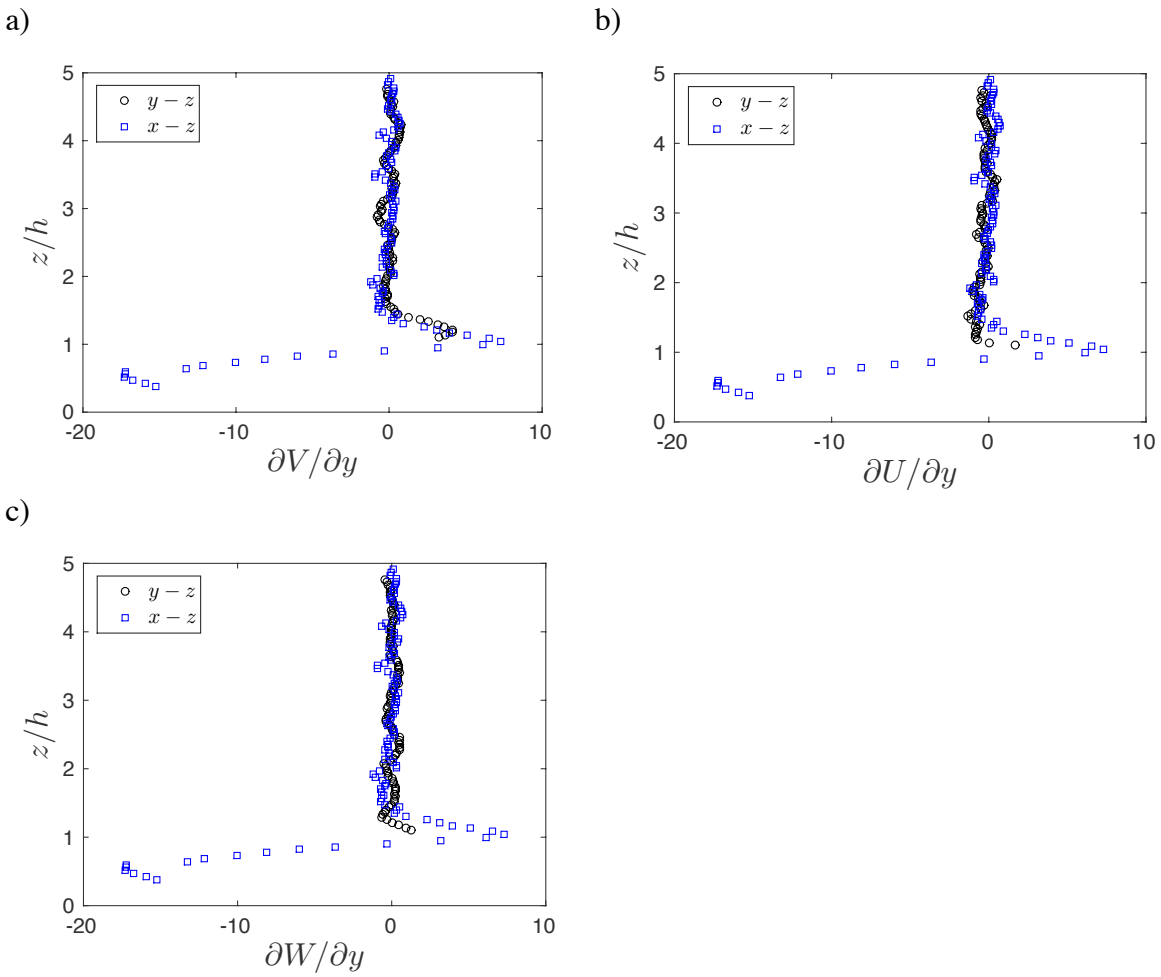

Figure B.1 a) $\partial V/\partial y$ calculated from the *y*-*z* plane compared with estimation from divergence free condition in the *x*-*z* plane; b) $\partial U/\partial y$ and c) $\partial W/\partial y$ calculated from the *y*-*z* plane compared with estimation from isotropy condition in the *x*-*z* plane.

UNIVERSITE BRETAGNE LOIRE

CENTRALE NANTES

Thèse de Doctorat

Karin BLACKMAN

Titre de la thèse : Interactions multi-échelles entre la basse atmosphère et la canopée urbaine

Title of thesis: Scale interactions between the lower atmosphere and the urban canopy

Résumé

La couche limite urbaine est caractérisée par la présence de structures cohérentes complexes, telles que des structures de grande échelle à basse vitesse, et par des processus turbulents intermittents de balayage et d'éjection, responsables du transport de masse, de chaleur et de quantité de mouvement. Ces structures sont bien identifiées qualitativement mais leurs interactions avec les petites structures induites par la présence de la canopée urbaine sont encore mal connues.
Afin d'étudier ces interactions, des écoulements de couche limite se développant sur des parois rugueuses sont étudiés en soufflerie. Le signal à petite échelle n'étant pas résolu temporellement, l'estimation stochastique linéaire est utilisée pour décomposer le champ de vitesse en grandes et petites échelles. On confirme que les structures à grande échelle dans la couche limite influencent les petites échelles proches de la rugosité à travers un mécanisme non linéaire similaire à une modulation d'amplitude. On montre également que la modification de la géométrie des éléments de rugosité entraîne une modification de cette interaction non linéaire dans la couche cisaillée.
Le bilan complet de l'énergie cinétique turbulente (TKE), incluant la dissipation, est calculé à l'aide d'un modèle LE-PIV et démontre que les structures à petite échelle dans la couche de cisaillement sont importantes pour la production, le transport et la dissipation de l'énergie. Enfin, la décomposition triple du bilan de TKE confirme que la relation non linéaire qui existe entre les structures à grande échelle et les petites échelles proches de la rugosité est liée au transfert d'énergie entre ces structures.

Mots-clés
Mécanique des fluides, Couche limite atmosphérique, Canopée urbaine, Vélocimétrie par Images de Particules, Soufflerie, Bilan TKE, Interactions multi-échelles

Abstract

The urban boundary layer consists of complex coherent structures, such as large-scale low momentum regions and intermittent turbulent sweeps and ejections, which are responsible for the transport of heat, momentum and pollution. Although these structures have been well identified, their quantitative relationship with the flow inside the canopy is still unknown.
Wind tunnel modelling of flow over simplified rough terrain consisting of either three-dimensional or two-dimensional roughness elements are able to reproduce these structures and are used to investigate the non-linear relationship between large-scale momentum regions and small-scales induced by the presence of the roughness. As the temporally resolved small-scale signal is not available Linear Stochastic Estimation is used to decompose the flow into large and small-scales and confirm that the large-scale structures within the overlying boundary layer influence the small-scales close to the roughness through a non-linear mechanism similar to amplitude modulation. Changing terrain configuration from 3D to 2D roughness results in a modification of the non-linear relationship closer to the shear layer that develops near the top of the obstacles.
The full turbulent kinetic energy (TKE) budget including dissipation is calculated using an LE-PIV model and demonstrates that small-scale structures within the shear layer are important to the production, transport and dissipation of energy. Finally, triple decomposition of the TKE budget confirms that the non-linear relationship that exists between large-scale momentum regions and small-scales close to the roughness is related to energy transfer between these structures.

Key Words
Fluid Mechanics, Atmospheric boundary layer, Urban canopy, Particle Image Velocimetry, Wind tunnel, TKE budget, Scale interactions